Cross-sections for charged channels in k-p interactions between 1470 and 1550 meV C.M. energy

Yaqob Ali Hamam

To my parents and my brother

Yehya Hamam

CROSS-SECTIONS FOR CHARGED CHANNELS IN K^-P INTERACTIONS BETWEEN 1470 AND 1550 MeV C.M. ENERGY

by

YAQOB ALI HAMAM

A thesis submitted to the University of Durham
for the degree of
Doctor of Philosophy

August 1978

CONTENTS

CHAPTER I

INTRODUCTION

1.1 Low Energy K^--Meson Interactions

Even at zero momentum interactions of negative kaons with protons involve several, open, two-body channels. Moreover three-body channels involving the production of an extra pion are energetically possible at zero momentum, or become possible at primary momenta about 250 MeV/C. However their contribution to the total cross-section is very small until primary momenta above about 600 MeV/C are reached. Consequently the main contribution to the reactions which take place in K^-P collisions below 600 MeV/C are:

$K^-P \rightarrow K^- + P$	1	elastic scattering
$\rightarrow \bar{K}^0 + n$	2	charge exchange
$\rightarrow \pi^- + \Sigma^+$	3	
$\rightarrow \pi^+ + \Sigma^-$	4	
$\rightarrow \pi^0 + \Sigma^0$	5	
$\rightarrow \pi^0 + \Lambda^0$	6	

A survey of the K^-P interactions at low momenta ($P_{K^-} < 2.0$ GEV/C) carried out in the last decade or so, shows that these interactions have been studied comparatively well experimentally in the region of primary momenta of 600 MeV/C upwards (1.1). Below this value of primary momentum the number of experiments performed is low and limited in statistics. Consequently the quality of the experimental data in this region is poor.

The first experiment to be performed with reasonable statistics below 600 MeV/C was by Humphrey and Ross (1.2). This was followed later by the experiment of Kim (1.3). Both measured the cross-sections for reactions 1 to 6 in the region below 300 MeV/C. Both determined the differential cross-section for elastic scattering and also determined the relative branching ratios for the production of hyperons by kaons at rest.

Other results have been reported in various works, these are summarised in Table 1.1. Here C means that cross-section has been determined and D means that the differential cross-section has been determined for that particular channel. CC denotes that the combined cross-section was calculated for the channels under consideration.

The neutral channel reactions were studied by Berly et al. (1.15), where the cross-sections for channels 2, 5 and 6 were determined in the region 350 MeV/C to 430 MeV/C and the polarisation of the Σ^0-hyperon as well as the differential cross-sections were determined. The experiment of Watson et al. (1.16) where a full analysis was carried out for all the reactions 1 to 6 including the three-body reactions, and the experiment of Mast et al. (1.17) are an attempt to study the region of K^--meson momentum between 250 to about 510 MeV/C in great detail.

Figure 1.1 is a summary of the experimental situation below 2.0 GeV/C primary kaon momentum. It shows the existing bubble chamber experiments in terms of the number of events/mb/25 MeV/C interval. In the figure it is seen that the level above 650 MeV/C primary momentum is about 3000 events/mb/25 MeV/C. This level drops an order of magnitude lower at about 300 events/mb/25 MeV/C for the region between 450 to 650 MeV/C primary momentum. In the region of 350 to 450 MeV/C (the Tripp series of experiments) this level reaches the highest value of about 5000 events/mb/25 MeV/C. Below 350 MeV/C primary momentum this level has

CHANNEL / REFERENCE		1	2	3	4	5	6	P_{K^-} in MeV/C
Kaplon	(1 - 4)	C		C	C			50 - 240
Nordin et al.	(1 - 5)	C						0 - 400
Eberhard et al.	(1 - 6)		C					90 - 430
Freden et al.	(1 - 7)	C		CC				20 - 300
Nordin	(1 - 8)	C,D	C	C	C	CC		300 and 400
Davis et al.	(1 - 9)	C						80 - 250
Sakitt et al.	(1 -10)	C		C	C			60 - 300
Thomas and Jain	(1 -11)	C						0 - 250
Csejthey-Barth et al.	(1 -12)	C						50 - 200
Abrams and Sechi-Zorn	(1 -13)	C						80 - 250
Kittel et al.	(1 -14)	C,D						100 - 300

Table 1.1: Early results of the K^-P interactions in the low K^--meson momentum region.

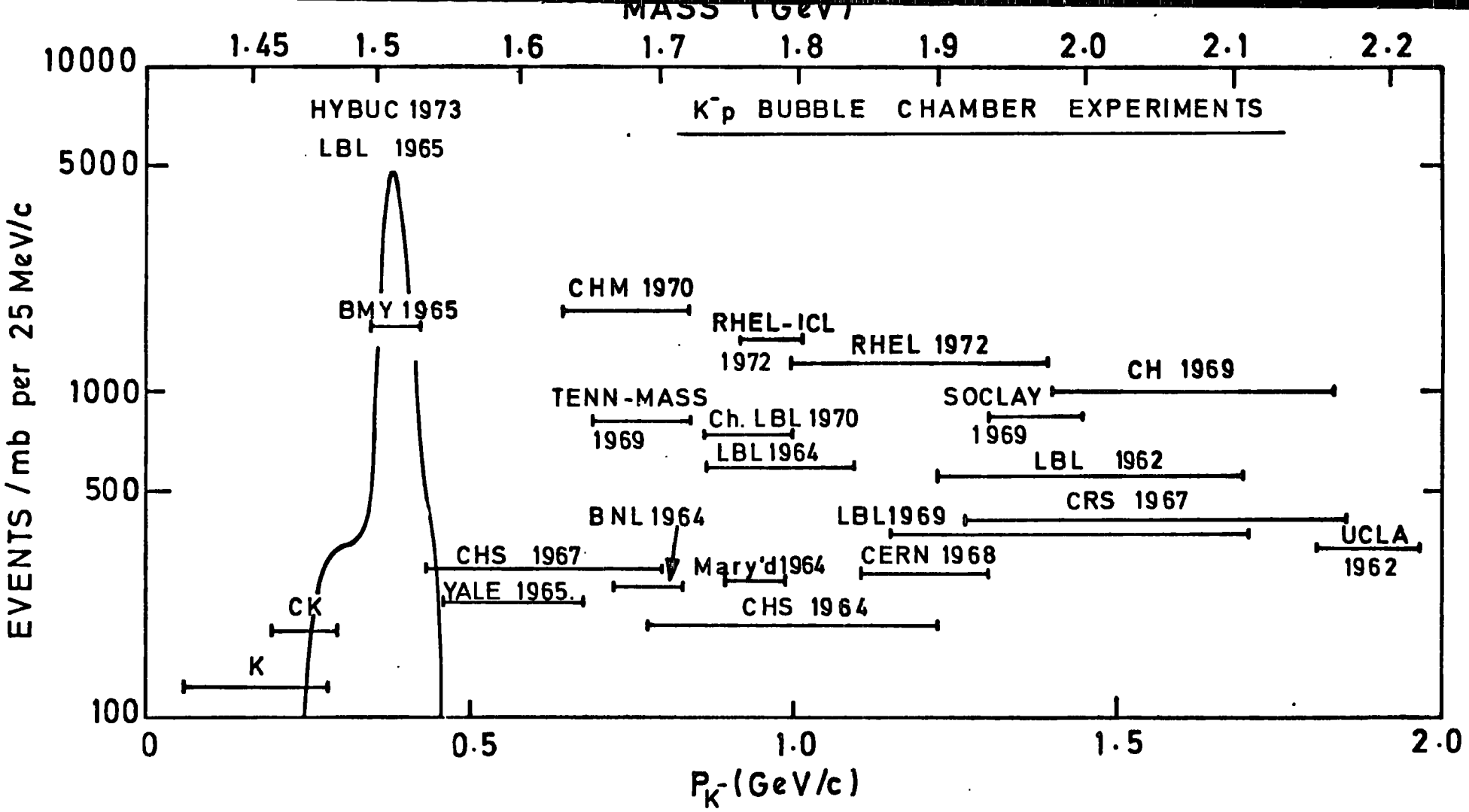

FIG. 1·1 K^-p bubble chamber path lengths below 2GeV/c. Numbers refer to the approximate date of the exposure. Horizontal lines show the momentum interval and the average level of the exposure over that interval. The path length is averaged over the indicated momentum interval of the experiment (except for LBL 1965). References are given in Ref. (1·25)

dropped to about 50 events/mb/25 MeV/C. Below 150 MeV/C primary momentum experiments are very difficult to perform, unless beams of kaons of very well defined momenta are transported through the fringing field of the bubble chamber magnets. The well defined momentum is required so that the momentum of the beam is known from its position in the bubble chamber and not by direct measurement of curvature in the presence of high energy loss. Because of this, data below 150 MeV/C are very poor and virtually non-existent except for the special case of negative kaon interactions at rest.

The lack of good experimental data in the low momentum kaon interactions below 600 MeV/C can be attributed to many reasons. Among these, in the very low momentum region, it has been difficult to produce kaon beams of well defined momentum which is needed for the detailed studies. Also in this region, the problems are many. For example, the rapid energy loss of the kaons makes momentum determinations very difficult and can produce very short tracks of interest which are difficult to detect and measure, which in turn lead to different biases on measured physical values. Furthermore over the last two decades the energy of accelerating machines has risen from a few GeV to hundreds of GeV. With this fast development the main interest of investigators has moved correspondingly to higher and higher energies to match the new developments of accelerating machines. The interest has shifted from performing experiments of the order of hundreds MeV energy; it has even moved away from a few GeV to hundreds of GeV.

These reasons, together with the fact that a superficial reading of the literature on the low energy kaon interactions would indicate a good experimental coverage, make it seem that it is unlikely that further experimental investigation will be carried out in this low

momentum region.

Apart from these reasons there are difficulties, from the physics point of view, in the low momentum region and these will be considered below.

1.2 Review of the Physics of Low Energy Kaon Interactions

As mentioned above, the three-body final state reactions are negligible below 600 MeV/C so here only the two-body final states will be considered.

The $\bar{K}N$ interaction involves isotopic spin states of I = 0 and I = 1. From SU(2) the K^-P reaction involves both these states with equal amplitudes, that is, the state vector K^-P is

$$| K^-P > = \frac{1}{\sqrt{2}} | 1,0 > + \frac{1}{\sqrt{2}} | 0,0 >$$

All reactions 1 to 6 are energetically possible at zero K^--meson momentum except charge exchange (reaction 2) where the threshold momentum of the primary K^--meson in the laboratory system is 90 MeV/C. This is due to the mass differences between the particles in the final state, $\bar{K}^0n$, and the particles in the initial state, K^-P, and represents a breaking of SU(2) symmetry (or isospin). For the moment this is ignored.

The matrix elements for the final states are expressed in terms of the transition matrix elements T_I in each total isotopic spin I as follows:

$$< K^- P \,|T|\, K^- P > \;=\; \frac{1}{2}\left[T_1 + T_o\right]$$

$$< \bar{K}^o n \,|T|\, K^- P > \;=\; \frac{1}{2}\left[T_1 - T_o\right]$$

$$< \pi^- \Sigma^+ |T|\, K^- P > \;=\; \frac{1}{\sqrt{6}}\, T_o^{\Sigma} + \frac{1}{2}\, T_1^{\Sigma}$$

$$< \pi^+ \Sigma^- |T|\, K^- P > \;=\; \frac{1}{\sqrt{6}}\, T_o^{\Sigma} - \frac{1}{2}\, T_1^{\Sigma}$$

$$< \pi^o \Sigma^o |T|\, K^- P > \;=\; -\frac{1}{\sqrt{6}}\, T_o^{\Sigma}$$

$$< \pi^o \Lambda^o |T|\, K^- P > \;=\; \frac{1}{\sqrt{2}}\, T_1^{\Lambda}$$

Note that the production of Σ^o and Λ^o hyperons involve pure $I = 0$ or $I = 1$ reactions.

If S_o and S_1 are the scattering amplitudes which are given by $S_I = -A_I/(1 - ikA_I)$, and if M_o, M_1 and N_1 are the reaction amplitudes for the Σ-hyperon and Λ-hyperon production in $I = 0$ and $I = 1$, then the cross-sections in the different channels are given by

$$\sigma_{K^- P} \;=\; 4\pi \left| \frac{\frac{1}{2}(A_1 + A_o) \;-\; i k A_1 A_o}{(1 - i k A_1)\,(1 - i k A_o)} \right|^2$$

$$\sigma_{\bar{K}^o n} \;=\; 4\pi \left| \frac{\frac{1}{2}\,(A_1 - A_o)}{(1 - i k A_1)\,(1 - i k A_o)} \right|^2$$

$$\sigma_{\pi^- \Sigma^+} \;=\; \frac{4\pi\, q_{\Sigma^+}}{k} \left| \frac{1}{\sqrt{6}}\; \frac{M_o}{1 - i k A_o} \;+\; \frac{1}{2}\; \frac{M_1}{1 - i k A_1} \right|^2$$

$$\sigma_{\pi^+ \Sigma^-} \;=\; \frac{4\pi\, q_{\Sigma^-}}{k} \left| \frac{1}{\sqrt{6}}\; \frac{M_o}{1 - i k A_o} \;-\; \frac{1}{2}\; \frac{M_1}{1 - i k A_1} \right|^2$$

$$\sigma_{\pi^o \Sigma^o} \;=\; \frac{4\pi\, q_{\Sigma^o}}{k} \left| \frac{1}{\sqrt{6}}\; \frac{M_o}{1 - i k A_o} \right|^2$$

$$\sigma_{\pi^o \Lambda^o} \;=\; \frac{4\pi\, q_{\Lambda^o}}{k} \left| \frac{1}{\sqrt{2}}\; \frac{N_1}{1 - i k A_1} \right|^2$$

Here A_o and A_1 are the complex scattering lengths in isospin $I = 0$ and $I = 1$ respectively, k is the centre of mass momentum of the kaon in the initial state and q_Σ and q_Λ are the centre of mass momenta of the Σ-hyperon and Λ^o-hyperon in the final state.

The absorption cross-sections for the isotopic spin channels $I = 0$ and $I = 1$ are

$$\sigma_o = \frac{4\pi b_o}{k} \left| \frac{1}{(1 - i k A_o)} \right|^2$$

$$\sigma_1 = \frac{4\pi b_1}{k} \left| \frac{1}{(1 - i k A_1)} \right|^2$$

where $A_I = a_I + i b_I$.

It is assumed that charge independence holds for strong interactions. Clearly the symmetry is broken because of the mass difference between the $\bar{K}^o$ and K^- mesons. Consequently the cross-section for the charge exchange process as given above is incorrect since there is a threshold momentum to be exceeded ($\sim$ 90 MeV/C) to produce charge exchange. This is a deviation from charge independence and it is a measure of the breakdown of the charge independence. Also at low momentum coulomb scattering becomes important. If this is taken into account it leads to 8% corrections to the elastic scattering cross-sections at about 100 MeV/C primary momentum and 2% corrections at about 400 MeV/C. The coulomb corrections are insignificant in comparison to the precision of experiments performed in this region. However if the charge dependent cross-sections for different channels are recalculated by introducing the $\bar{K}^o$ momentum, k_o, in the charge exchange process this leads to the introduction of

$$D^c = 1 - \frac{i}{2}(A_1 + A_o)(k + k_o) - k\,k_o\,A_1\,A_o$$

(Simplifies to $D = (1 - i\,k\,A_1)(1 - i\,k\,A_o)$ if charge independence is good).

Then the absorption cross-sections for I = 0 and I = 1 become

$$\sigma_o^c = \frac{4\pi\,B_o}{k}\left|\frac{1 - i\,k\,A_1}{D^c}\right|^2$$

$$\sigma_1^c = \frac{4\pi\,B_1}{k}\left|\frac{1 - i\,k\,A_o}{D^c}\right|^2$$

where

$$B_o = q_\Sigma\,|M_o|^2$$

$$B_1 = q_\Sigma\,|M_1|^2 + q_{\Lambda o}\,|N_1|^2$$

In terms of these charge dependent quantities D^c, σ_o^c, and σ_1^c the cross-sections become

$$\sigma_{K^-p} = \pi\left|\frac{A_1 + A_o - 2\,i\,k_o\,A_1\,A_o}{D^c}\right|^2$$

$$\sigma_{\bar{K}^o n} = \frac{\pi\,k_o}{k}\left|\frac{A_1 - A_o}{D^c}\right|^2$$

$$\sigma_{\pi^-\Sigma^+} = \frac{1}{6}\sigma_o^c + \frac{1}{4}(1-\varepsilon)\,\sigma_1^c - \sqrt{\frac{1}{6}\sigma_o^c\,\sigma_1^c\,(1-\varepsilon)}\,\cos\phi$$

$$\sigma_{\pi^+\Sigma^-} = \frac{1}{6}\sigma_o^c + \frac{1}{4}(1-\varepsilon)\,\sigma_1^c + \sqrt{\frac{1}{6}\sigma_o^c\,\sigma_1^c\,(1-\varepsilon)}\,\cos\phi$$

$$\sigma_{\pi^o\Sigma^o} = \frac{1}{6}\sigma_o^c$$

$$\sigma_{\pi^o\Lambda^o} = \frac{1}{2}\varepsilon\,\sigma_1^c$$

where

(a) $$\varepsilon = q_{\Lambda^o} |N_1|^2 \Big/ \left(q_\Sigma |M_1|^2 + q_{\Lambda^o} |N_1|^2 \right)$$

is the ratio of $\pi^o\Lambda^o$ production rate to the total hyperon production rate in the isotopic spin channel I = 1.

(b) ϕ is the phase difference between the I = 0 and I = 1 amplitudes for Σ-hyperon production.

$$\phi = \text{Arg} \left[\frac{M_o (1 - ikA_1)}{M_1 (1 - ikA_o)} \right]$$

$$= \phi_{th} + \text{Arg} \left[\frac{1 - ikA_1}{1 - ikA_o} \right]$$

$$\phi_{th} = \text{Arg} \, (M_o/M_1)$$

where ϕ_{th} is the phase difference at the charge exchange threshold (90 MeV/C primary momentum).

The most detailed analysis based on an experiment of the low momentum K^--meson interactions with the proton target (K^--meson momentum below 300 MeV/C) was carried out by Kim (1.3) using the six parameters required above defined as $A_o = a_o + i b_o$, $A_1 = a_1 + i b_1$, ϕ_{th}, and ε to fit his data (where A_o and A_1 are the complex scattering lengths). Kim finds for these six parameters the values

$$A_o = \left\{ (-1.67 \pm 0.04) + i(0.71 \pm 0.04) \right\} \quad 10^{-13} \text{ cm}$$

$$A_1 = \left\{ (-0.00 \pm 0.06) + i(0.68 \pm 0.03) \right\} \quad 10^{-13} \text{ cm}$$

$$\phi_{th} = -53.8^o$$

$$\varepsilon = 0.318 \pm 0.021$$

It should be noted that in the equations defining the cross-sections above, A_o and A_1 are involved through the terms $(1 - i k A_o)$ and $(1 - i k A_1)$ respectively and both are in the denominator. Consequently Kim's negative value of a_o, will produce a pole at $1 - i k a_o = 0$. If $k = i K$ where K is real, a singularity is produced below the $K^- P$ threshold at $1 + K a_o = 0$ or $K = -\frac{1}{a_o} = \frac{1}{|a_o|}$.

So the pole occurs at centre of mass momentum $k = i/|a_o|$. Substituting Kim's values of a_o and b_o gives a virtual bound state in the $K^- P$ system at an energy $E = 1410.7 \pm 1.0$ MeV and a half width $\Gamma = 36.2 \pm 3.2$ MeV. These values are consistent with those of the resonance $Y_o^*(1405)$ which can be interpreted as an S-wave bound state strongly coupled to the $K^- P$ system. This result is a very important one and it gives confidence in Kim's experiment. However more detailed reading of Kim's work raises doubts about its accuracy. These can be summarised in the following:

(a) from the point of view of dealing with a low momentum $K^- P$ experiment there is no evidence that energy loss has been properly taken into account. For example, primary momenta are quoted which correspond to kaons of zero-range.

(b) some of the physical values determined by Kim's experiment are discrepant with the same physical values obtained by other experiments. For example the ratio γ which is defined as

$$\gamma = K^- P \to \pi^+ \Sigma^- \; / \; K^- P \to \pi^- \Sigma^+$$

is found by Kim for K^--meson interactions at rest as (2.06 ± 0.06) whereas the value found by Tovee et al (1.18), using emulsion technique, is (2.34 ± 0.08).

(c) in an analysis by A.D. Martin (1.19) using dispersion relations to link the high and low momentum of both K^+ and K^- mesons interactions then inconsistencies appear again in Kim's work.

Because of these reasons a need for a further experiment to determine the cross-sections for different channels and to perform the analysis of the K^--meson interactions below 300 MeV/C is required. Other reasons are given in the next three sections.

1.3 Resonance Production

Resonances cannot be seen directly in the bubble chamber; they are identified by their decay into particles which are stable with respect to strong decay. The experiments in which they are produced are of two kinds. Firstly, formation experiments where the projectile particle with a specified momentum struck a target such that the total energy of the two particles in the centre of mass system is equal to the mass of the resonance. Secondly, production experiments where the resonance is produced along with other particles which are either stable or unstable.

In the momentum region up to 600 MeV/C K^--momentum resonances are produced in formation experiments largely. Baryon resonances with strangeness S = -1 and mass less than 1607 MeV/C^2 (equivalent to K^- laboratory momentum of less than 600 MeV/C) which are well accepted are $\Sigma(1385)$, $\Lambda(1405)$, and $\Lambda(1520)$. The first two resonances cannot be produced in formation experiments with K^-P because their masses lie below the K^-P threshold (1432 MeV). However they can be produced in production experiments of the type $K^-P \rightarrow Y^*\pi$ where Y^* denotes a baryon resonance with strangeness S = -1. The only well established and clearly identified resonant state of the K^-P system in formation experiments below 600 MeV/C K^--meson momentum is the $\Lambda(1520)$ resonance. Other resonances in this

region have been reported in various experiments, but they are still not verified.

Below the $\Lambda(1520)$ resonance there has been a tentative identification of a resonance at a laboratory K^--momentum 280 MeV/C (1.20). This is the $\Sigma(1480)$. Above the $\Lambda(1520)$ resonance a number of resonances have been tentatively identified. The two states P_{01} and P_{11} reported by Kim (1.21) and CHS (1.22) at laboratory momenta 480 MeV/C and 510 MeV/C respectively which are equivalent to centre of mass energies of 1554 MeV and 1568 MeV. Recently Bowen et al (1.23) have examined the K^-P interactions in hydrogen and K^-n interactions in deuterium. They found evidence for an $I = 1$ resonance at a laboratory momentum of about 500 MeV/C which may be a manifestation of the P_{11} resonance mentioned above. Also it has been reported by Carroll et al (1.24) that a structure has been seen; this is the $\Sigma(1583)$ which could be a Y^* resonance. This corresponds to primary momentum of nearly 560 MeV/C.

Because of this, again higher statistics experiments of good quality are required to clarify the situation of the existence or otherwise of resonances other than the $\Lambda(1520)$ in this region of low K^--meson momentum.

1.4 Partial Waves

The K^-P interaction at very low momentum and up to about 300 MeV/C primary momentum in the laboratory system indicates that it is dominated by an S-wave reaction. Above this momentum other partial waves begin to show themselves in a very strong way and they are no longer unimportant. For example at about 400 MeV/C the D-wave $\Lambda(1520)$ is produced quite strongly. Where P-waves and D-waves begin to be important is not clear experimentally. This needs to be known to define the region in which

the Kim analysis (S-wave analysis) is valid and it requires well founded angular distributions.

The onset of higher waves can be estimated from the examination of the polarisation for the weakly decaying Σ and Λ hyperons; the polarisation arises from the interference of the partial waves in this region.

1.5 Λ^o/Σ^o Ambiguity

As mentioned earlier, reactions 1 to 4 are a mixture of isotopic spin I = 0 and I = 1 channels. Also it has been mentioned that the neutral channels in the final state are pure isotopic spin states of I = 0 or I = 1. The Λ-hyperon production is a pure isotopic spin 1 (reaction 6) meanwhile Σ^o-hyperon production is pure isotopic spin 0 (reaction 5). Consequently, as far as these two channels are concerned, the production of the $\Lambda(1520)$ resonance (I = 0, $J^P = 3/2^-$) should be seen only in the Σ^o-hyperon channel and the existence or otherwise of the I = 1 resonances described earlier ($\Sigma(1480)$, P_{11}, and I = 1 at 580 MeV/C) should clearly manifest themselves in the Λ^o-hyperon production channel only. Although the Λ^o-hyperon is clearly identified in the bubble chamber, this unfortunately does not give any information whether the Λ^o-hyperon was produced directly or indirectly via the Σ^o-hyperon since both interactions 5 and 6 look similar in the bubble chamber. This is the well known Λ^o/Σ^o ambiguity which exists at all energies. Unambiguous identification of the two reactions 5 and 6 can only be made if the associated gamma rays convert in the chamber. This is discussed in more detail later.

1.6 The Present Experiment

This is an exposure of high statistics (about a million frames) in

the K^--meson momentum range between 0 - 600 MeV/C. The exposure was carried out in a composite chamber for the first time where the low momentum kaons were produced by the interaction of protons from the NIMROD proton synchrotron with a copper target. The kaons are transported into the chamber where interactions on protons only can occur. The composite chamber effectively constitutes two chambers, the hydrogen chamber which is a slice of hydrogen embodied in a larger chamber filled with a neon-hydrogen mixture. The outer neon-hydrogen chamber is needed for the interaction of gamma rays with heavy nuclei so that some of these would materialise into electron-positron pairs and be seen. The effective radiation length is about 45 cms. This improves the gamma rays conversion by a factor of 20 over a conventional hydrogen bubble chamber.

The high statistics should lead to the determination of cross-sections with good precision and to angular distributions and polarisations of fair precision. The enhanced gamma rays should help towards the separation of the I = 0 and I = 1 channels (reactions 5 and 6). Since it is a low momentum experiment special attention needs to be given to several factors. Firstly to the determination of the momenta and secondly to the corrections for short tracks which are very difficult to be seen. Further, because it is the first time to have an experiment in the composite chamber the technique has to be demonstrated to work. It is also necessary to understand the technical problems and the limitations of the technique and to make sure that these are properly dealt with. Because of this it is essential to have a clear well known signal to measure relative to it; this signal is the $\Lambda(1520)$ resonance.

The experiment will undergo three phases. Firstly it has to be shown that the technique works in a satisfactory way. This includes understanding its limitations and how to handle them properly. This is

done by demonstrating that cross-sections, angular distributions, and polarisations in the region of the $\Lambda(1520)$ do not lead to systematic differences from known values.

The second phase is to re-examine the data at low momenta specially in the region of Kim's work and to repeat the analysis of the six parameters, so that eventually the results of A.D. Martin on dispersion relations can also be examined.

The third phase is to complete the investigation of the region from 450 - 650 MeV/C where little has been done in this region so that the existence or otherwise of the I = 1 resonances can be checked.

This thesis is concerned with phase I of the experiment. In Chapter II the experiment is described where a review of the advantages and disadvantages of the conventional bubble chamber is given; this is followed by the description of the composite chamber, the beam line and the exposure. In Chapter III a general review of the experimental and processing of the data is described. It is followed in Chapter IV with a technical assessment in terms of scanning efficiencies, the determination of the detection efficiency of gamma rays and an estimate of the neon concentration in the outer region of neon-hydrogen mixture. In Chapter V the event/mb as a function of momentum interval is determined and corrections for various losses of events are given so that eventually in Chapter VI the cross-sections can be calculated. Besides the cross-sections in Chapter VI, the ratio $\gamma = K^-P \to \pi^+\Sigma^-/K^-P \to \pi^-\Sigma^+$ is calculated using a method independent of the cross-sections; the angular distributions of the charged sigma hyperons and the elastic scattering channels are investigated and fitted. Finally the polarisation of the Σ^+-hyperon is examined.

In Chapter VII the Σ-hyperon cross-sections are further analysed to separate them into isospin 0 and isospin 1 cross-sections using the data from this experiment and the published data of Mast et al (1.17). Finally in Chapter VII general conclusions are given.

CHAPTER II

BUBBLE CHAMBER, BEAM LINE, AND EXPOSURE

2.1 Introduction

The bubble chamber has proved to be a powerful tool for high energy physics, and since it has been put into operation it has led to a considerable increase in the knowledge of elementary particles. Bubble chambers have been made with a wide variety of pure liquids, liquid mixtures, and liquids containing dissolved gas. Pure liquid bubble chambers range from hydrogen to heavy liquids of complex nuclei such as xenon to provide targets, but the liquids which have been commonly used are those of hydrogen or deuterium. The exposure of the K^-P experiment was carried out in the composite British National Hydrogen Bubble Chamber (B.N.H.B.C.) which received kaons from the K19 beam. In the following the merits of the bubble chamber technique and its limitations as a detector are first reviewed. This is followed by a brief description of the first stage of the experiment which is by no means insignificant; this is the setting up of the experiment. This consists of the bubble chamber and the beam line. Then finally the details of the exposures are given.

2.2 The Merits and Limitations of the Bubble Chamber Technique

The conventional chamber filled with hydrogen or deuterium has been successfully operated for many years. Its success as a particle detector arises from the following reasons:

(1) hydrogen and deuterium are the most significant liquids to be used in high energy physics since hydrogen represents a pure free proton target

and deuterium represents a quasi-free neutron target.

(2) the bubble chamber is efficient over 4π steradians of solid angle. It reveals all the charged particles so that the tracks of these particles are detected irrespective of their direction. This is to be contrasted with counter systems where solid angles are always much less than 4π steradians.

(3) measurements on charged particles trajectories can be achieved with high accuracy. The precision of measurements is about 50 - 100 μ (2.1). This is after geometrical reconstruction back into chamber space and where the inherent errors of the chamber are included.

(4) the spatial resolution of the conventional bubble chamber is about 1 millimetre, so that tracks and vertices can be identified and measured if they are separated by a millimetre or more. This is important in the case of short-lived particles produced with low energy where the decay length may be of the order of a few millimetres. In the present experiment hyperons with life-times about 10^{-10} seconds are produced with velocities about 0.3 C, where C is the velocity of light. These have average decay lengths of about 1.0 cms. Consequently many would be undetected but for the good spatial resolution.

The conventional bubble chamber however is not free from limitations. These limitations are summarised in the following:

(a) most bubble chambers which have been used so far have been designed to take a picture of the target region for each expansion regardless of the interactions taking place. Consequently in cases of interactions of very low cross-sections, a very large number of pictures has to be taken and scanned to achieve reasonable statistics required for the proper

analysis. Typically about one million pictures are required. These require one or two months for exposure and about three years for scanning, measuring and analysis of the process of low cross sections.

(b) the rate of sampling beam particles is low. Whereas counter systems can work with beam intensities up to 10^5/second the bubble chamber is limited to about 10/second.

(c) because of the long radiation length in both liquid hydrogen and deuterium (about 10.0 metres in liquid hydrogen and about 9.0 metres in liquid deuterium) there is poor detection of gamma rays. Consequently this results in the lack of effective detection of the π^o-meson through the two gamma rays into which it decays with a mean life-time about 10^{-16} second. From primary momenta of a few GeV/C and upwards, the π^o-meson channels form a substantial fraction of the total cross-section. At high momenta the production of multineutral channels increases. These channels cannot be kinematically fitted, and consequently cannot be analysed in a straightforward way. Some resolution would result if gamma ray detection would be made efficient.

Lack of gamma ray detection also results in the well known ambiguity between Λ^o and Σ^o hyperons. In the present experiment this results in an ambiguity between the two following channels (channels 5 and 6).

$$K^- + P \rightarrow \Lambda^o + \pi^o \qquad (1)$$

$$K^- + P \rightarrow \Sigma^o + \pi^o \qquad (2)$$

in reaction (2) the Σ^o-hyperon decays very rapidly into $\Lambda^o + \gamma$. Then in both channels the Λ^o-hyperon decays weakly; the branching ratio into charged products ($\Lambda^o \rightarrow P + \pi^-$) is 64.2%. Consequently both reactions, in a conventional bubble chamber, appear identical. What is

seen in each case is an interacting kaon track with associated Λ^o-hyperon pointing to the end of the kaon track. It is clear that this ambiguity could be resolved with effective gamma ray detection.

Attempts have been made using two different ways to study and resolve the Λ^o-hyperon and Σ^o-hyperon channels. First data from the conventional bubble chambers was used without gamma rays detection (1.22). The method used was to study the missing mass squared to the seen recoiling Λ^o-hyperon. By imposing severe selections it is possible to separate the Σ^o signal from the Λ^o signal. But even after taking all precautions the Σ^o signal is contaminated from the $\Lambda^o\pi^o$ and $\Lambda^o\pi^o\pi^o$ channels and this signal could also be biased because of the severe selections. Second, data from heavy liquid bubble chamber experiments (2.2) were used and these demanded gamma rays to be seen. This proved to be no more satisfactory than the first method since the improve gamma ray detection is obtained at the expense of precision of measurement of momentum. Heavy liquid bubble chambers have been used to reduce the radiation length of the gamma rays by a considerable factor. For example the radiation length for xenon is 3.7 cms, about 11.0 cms for freon (CF_3Br), and 110.0 cms for propane.

Thus from the seen gamma rays which materialise into electron-positron pairs, the number of missing neutral particles will be reduced by using these gamma rays. These chambers have their own problems however such as the large error of measurements due to the multiple coulomb scattering, the background interactions in heavy nuclei, and the extraneous gamma rays coming from these background interactions.

To combine the virtues of both chambers, that is, the precision of the hydrogen bubble chamber and the gamma ray conversion of the heavy liquid bubble chamber, the idea of the track sensitive target (T.S.T.)

has been developed and successfully operated at the Rutherford Laboratory. This uses the 1.5 metre British National Hydrogen Bubble Chamber (B.N.H.B.C.) which was modified and used as a composite chamber. The track sensitive target is a target of pure liquid hydrogen or deuterium behaving as a bubble chamber contained in the middle of a heavy liquid chamber. These two chambers form the composite chamber which attempts to use the advantages from both kinds of chambers and to compensate for each other's drawbacks. Primary interactions are made to occur in the track sensitive target of hydrogen or deuterium. There the target nucleon (proton or neutron) is clearly known and measurements in the chamber are precise. Meanwhile the second region of a heavy liquid ensures good conversion of gamma rays.

2.3 Bubble Chamber

The 1.5 metre B.N.H.B.C., with the dimensions of 150 cms length, 50 cms height, and 45 cms depth, is photographed by three cameras placed on the corners of an isosceles triangle of height 480 ± 0.01 mm (= base). Illumination is from a set of flash tubes. Figure 2.1 is a plan view of the chamber optics (2.3). This chamber has been modified to enable it to be used as a composite chamber with a target of liquid hydrogen surrounded by neon-hydrogen mixture. The use of the neon-hydrogen mixture was chosen because both pure hydrogen and the neon-hydrogen mixture can be made sensitive to ionisation under the same operating conditions. Attempts have been made to operate a composite chamber since the early 1960's, but these attempts were beset by many difficulties, due to the fact that they either used pure heavy liquids or a mixture of heavy liquids to fill the second region. These have different operating conditions from those of the track sensitive target, so that as a result of

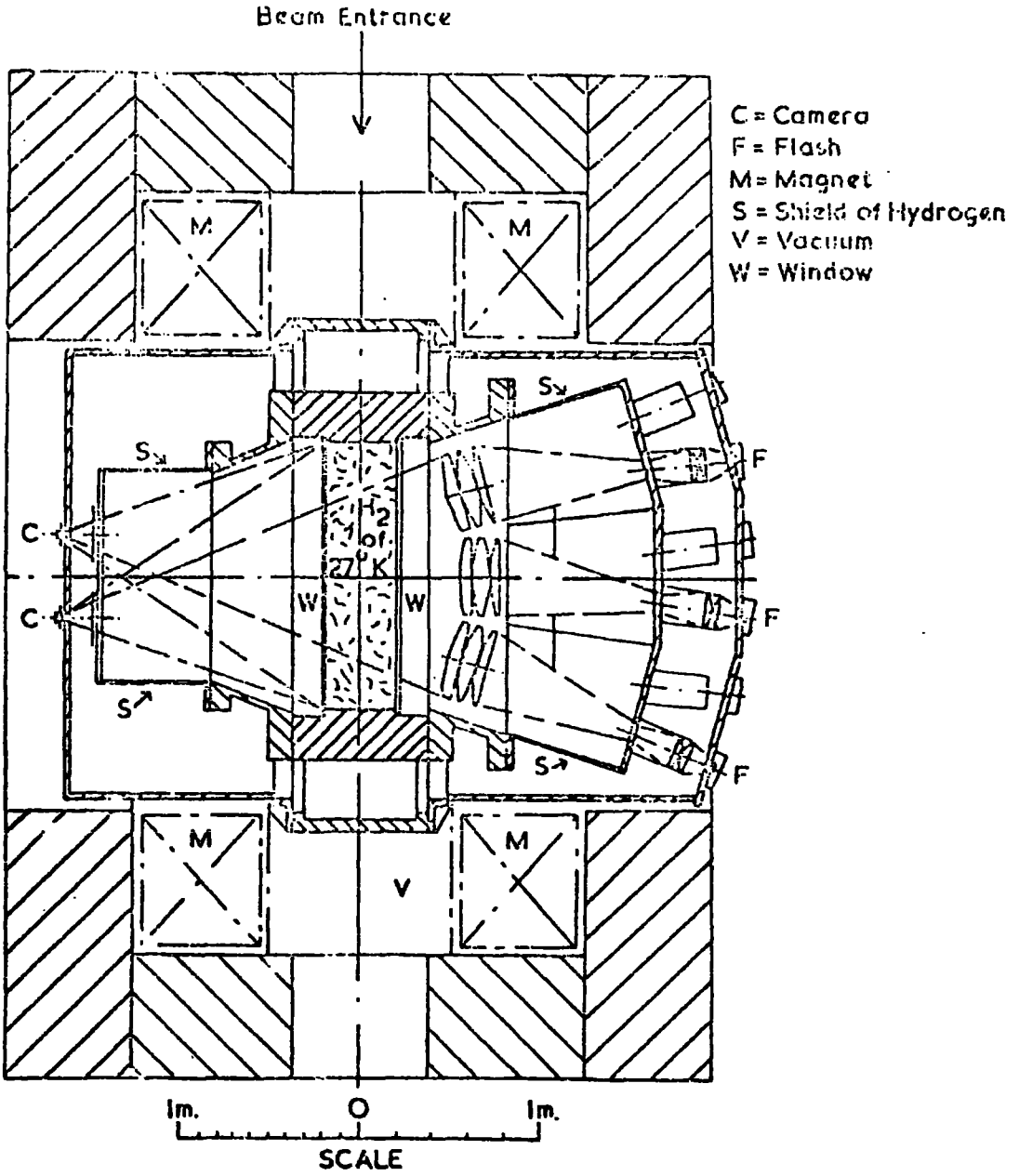

FIG.(2-1) PLAN VIEW OF B.N.H.B.C. SHOWING OPTICAL SYSTEM AND MAGNET

this the two regions have to be separated to maintain their individual operating conditions by different systems. This difficulty is avoided by using the neon-hydrogen mixture (2.4).

Figure 2.2 shows a schematic diagram of the T.S.T. together with the second region of neon-hydrogen mixture (2.5) where it is seen that the target is a slice mounted vertically in the middle of the chamber and running nearly over its full length. It is 7.8 cms deep, 45 cms high, and 140 cms long. A detailed diagram of the T.S.T. is shown in Figure 2.3 (2.1).

The primary beam of K^--mesons is injected into the target region, so that interactions occur on free protons. The gamma rays from the decay of neutral secondaries such as π^o, Σ^o etc. emerge in all directions, going through the walls containing the target to the second region of neon-hydrogen mixture where they have a greater chance of being converted into electron-positron pairs and thus being seen.

The same expansion mechanism has been used for both regions. The expansion direction is vertical, while the optical and magnetic field directions are horizontal and normal to the beam direction. With expansion the neon-hydrogen mixture is made sensitive. The fall in its hydrostatic pressure is transmitted through the flexible walls of the T.S.T. to the hydrogen which also becomes sensitive. The temperatures were set at 29.5 K for the hydrogen target and 29.8 K for the neon-hydrogen mixture.

The target has been contained between two perspex walls sealed by a frame. Two types of frames have been used to construct the target:

(1) Metal framed target:

It consists of a steel frame with two perspex windows. The metal frame is not transparent and so obscures part of the neon-hydrogen mixture

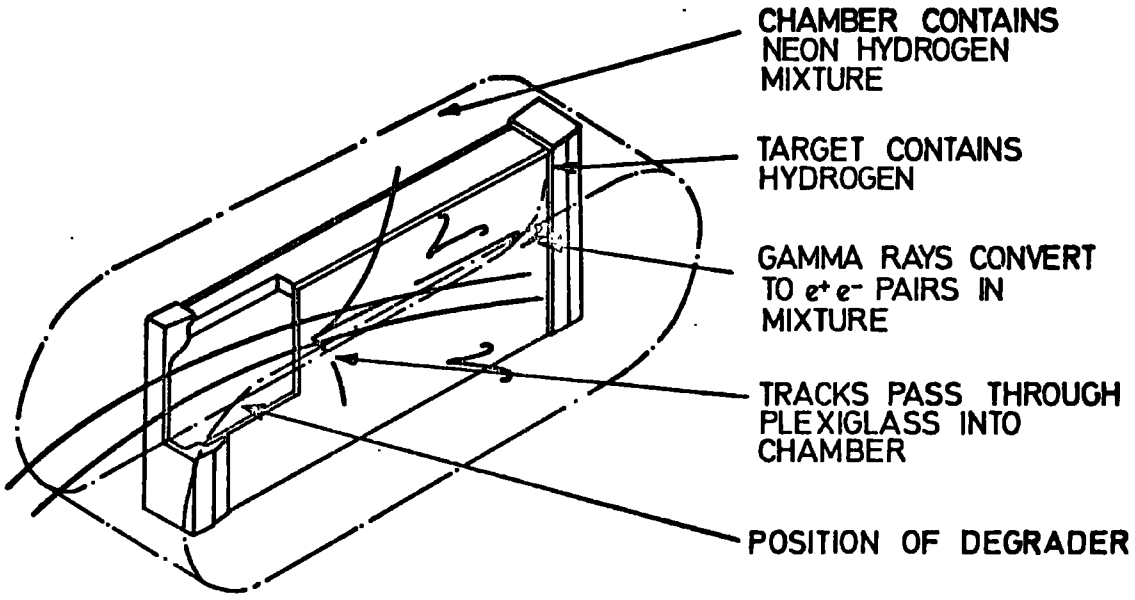

FIG.(2·2) SCHEMATIC DIAGRAM OF A TRACK SENSITIVE TARGET.

Figure 2.3: The Composite target section. The beam enters directly into the hydrogen. The magnetic field produces a curvature in the plane of the target.

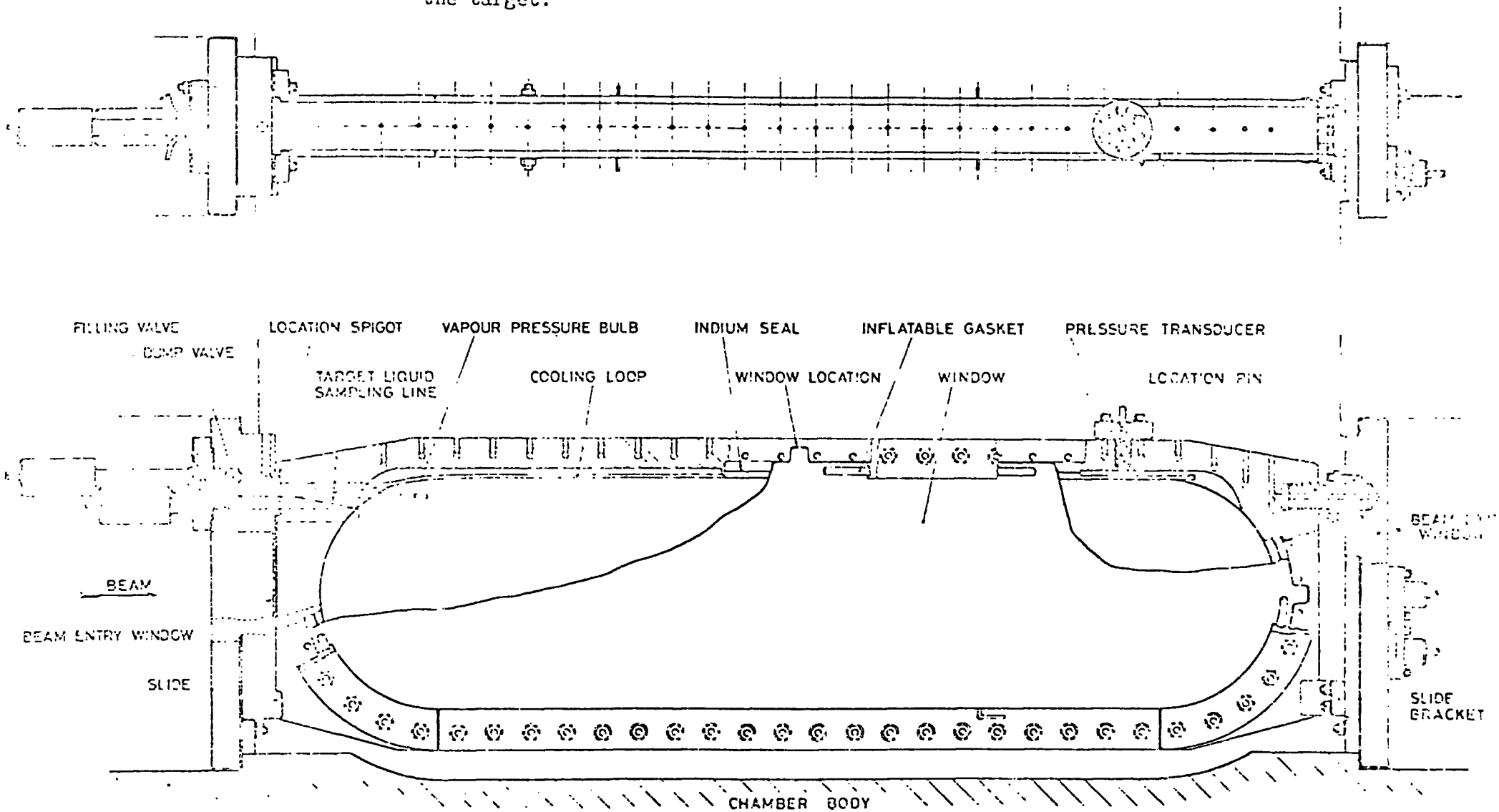

TRACK SENSITIVE TARGET FOR 1·5 METRE CHAMBER

region above and below the target. This means that the useful region of the mixture is limited and some of the gamma rays which materialise are unseen.

(2) The all perspex target:

This consists of a perspex frame together with the two perspex windows. In this case all the useful region of the chamber is seen and the gamma ray detection efficiency is improved.

The characteristics of the tracks are quite different in both regions of pure hydrogen and neon-hydrogen mixture and are very easily recognizable. Tracks in the pure hydrogen region have a high bubble density and small bubble size, meanwhile tracks in the neon-hydrogen mixture have low bubble density and large bubble size. A track which goes through one of the perspex walls from the pure hydrogen region to the neon-hydrogen region is characterised by a gap separating the two segments, where the track passed through the perspex. This gap is useful as a scanning aid. If it is short the track is steep; if it is long the track is shallow.

2.4 Beam Line

Figure 2.4 shows the layout of the beam line for experiment K19, carried out at Rutherford Laboratory. The beam of protons from the NIMROD proton synchrotron was produced at 7.0 GeV/C momentum, and the number of protons per pulse was of the order of 6×10^{11}. This beam of protons struck a copper target in which largely pions and some few kaons were produced. The production ratio of pions to kaons (π/K) is about 50. For the experiment this has to be reduced to π/K of about 1/10 by selecting kaons preferentially. Since it is a low energy experiment,

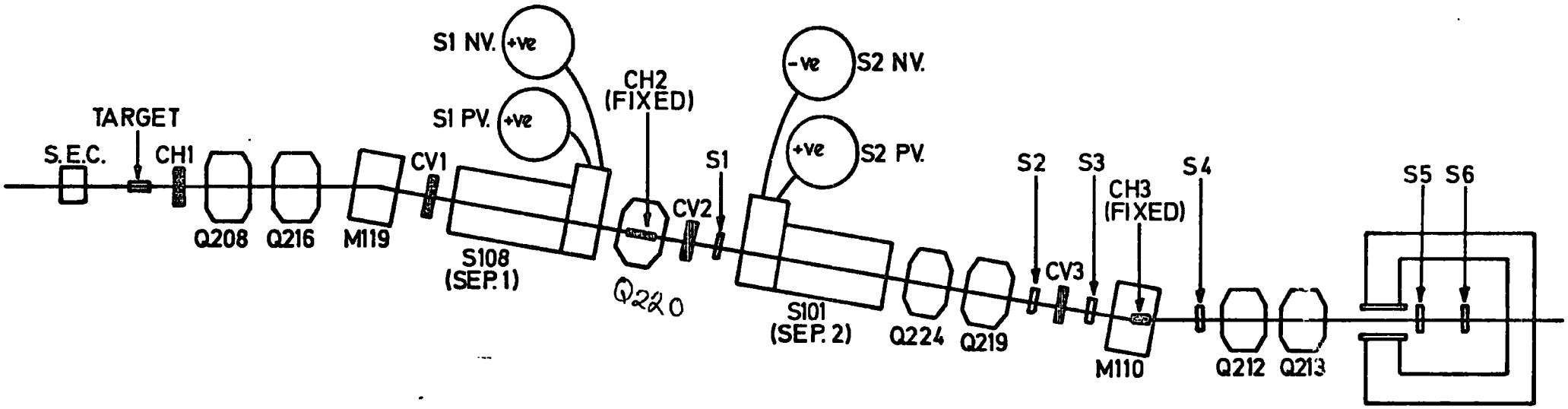

FIG. (2·4) K19 BEAM LINE

below 1.0 GeV/C K^--meson momentum, the separation is done electrostatically. This was achieved in two stages which are briefly described below:

First Stage:

The quadrupole doublet Q208/216 focuses the beam from the external target to CH2 and CV2, the horizontal and vertical collimators. The bending magnet M119 bends the beam enabling the momentum and momentum bite to be chosen by CH2, which is a fixed aperture surrounded by quadrupole magnet Q220 which acts as a field lens. CV2 is a variable aperture and serves as the first mass slit, defining the vertical image width for the second stage.

CH1 and CV1 define the angular acceptance of the beam. A fixed aperture collimator has been put near CV1 to provide rough momentum selection.

The separator S108 is capable of separating kaons and pions from the target.

Second Stage:

The quadrupole doublet Q224/219 focuses the beam to CV3 and CH3. CH3 is a fixed aperture collimator and is placed near the bending magnet M110.

The separator S101 totally separates pions and kaons at CV3. The quadrupole doublet Q212/213 is used to direct and transport the beam to the chamber. An average of about 30 kaons per pulse reached the front of the chamber.

Although the experiment was designed to run with kaon momenta in the region 0-650 MeV/C, it is not possible to transport the very low momentum kaons into the chamber easily because of the surrounding magnetic field. Instead the beam was transported through the fringing field up

to the chamber at a momentum of about 750 MeV/C. There it was degraded by a block of aluminium set in the chamber. Of the 30 kaons reaching the chamber about 10 per pulse penetrated into the fiducial region of the chamber.

2.5 Exposure

The T.S.T. chamber was exposed to the electrostatically separated K^--meson beam in the momentum range from 0 - $\sim$ 600 MeV/C. The runs were divided into two major stages; the first was devoted to K^--meson interactions at rest with the proton as a target (stopping K^--meson interactions). For this the beam was transported at 600 MeV/C momentum, and then was degraded to 260 MeV/C by an aluminium degrader mounted inside the track sensitive target region. About 229000 pictures were taken in this run, block 1, using the metal framed target. The second run using different momentum settings was devoted to K^--meson interactions in flight with the proton as a target. Again an aluminium degrader was used inside the track sensitive target region. About 204000 pictures were taken in four blocks (blocks 2-5) each at a different momentum setting. For the rest of the momentum settings, blocks 6-19, the all perspex target was used and about 473000 pictures were taken. In this case the beam momentum was also degraded by the aluminium, but it was mounted outside the track sensitive target region. The block numbers are defined in Table 2.1 where a summary of the two runs is given.

Table (2·1) K19 Data taking summary

The experiment was divided into Blocks of film with differing external beam momentum, degrader thickness and target type.

Block No.	Roll Nos.	Thousands of frames	Approx. K^- per frame	Approx. entry momen. MeV/c	Approx. exit momen. MeV/c	Degrader thickness cms. AL	Target frame
1	1-105	229	5	260	0	30	metal
2	106-126	54	8·4	315	235	30	"
3	127-147	45	10·1	370	320	30	"
4	148-168	54	12·3	405	370	30	"
5	169-188	51	8·8	445	410	30	"
6	190-210	52	8·7	320	240	27	perspex
7	211-220	26	7·9	300	190	27	"
8	221-240	51	11·6	370	320	27	"
9	241-250	26	12·2	405	360	27	"
10	251-260	25	10·0	420	380	18	"
11	261-277	44	13·4	450	410	18	"
12	278-286	22	14·2	475	435	18	"
13	287-292	16	17·3	495	455	18	"
14	293-304	28	12·6	505	465	9	"
15	305-314	25	16·6	530	490	9	"
16	315-335	49	20·0	550	510	9	"
17	336-355	49	12·6	560	525	0	"
18	356-365	25	15 7	580	545	0	"
19	366-379	35	15 2	510	475	18	"

Total frames 904000 (675000 for K^- inflight)

CHAPTER III

EXPERIMENTAL DETAILS AND PROCESSING OF THE DATA

3.1 The Processing Chain

Any bubble chamber experiment must undergo various stages before a data summary tape (D.S.T.) can be written. The K^-P experiment at low momenta (which is a collaboration among the five universities of Birmingham, Brussels, University College London, Durham and Warsaw) has gone through the following stages:

(a) the scanning stage. This includes the scanning, rescanning and recording of the events found. Scan information is eventually recorded on magnetic tape from which measuring lists were prepared.

(b) the measuring stage. Besides measuring the events this includes some preliminary processing through the two programs REAP and TRANS to prepare them for the geometrical reconstruction.

(c) geometrical reconstruction. This reconstructs the measured events in three dimensions.

(d) kinematical fitting. Here interpretations for the interactions and decays are sought through demanding balance of total energy and momentum.

(e) judging. Quite often the kinematic fitting results in an ambiguity of interpretation. To some extent these can be resolved by judging, ionisation in particular, at the scanning table.

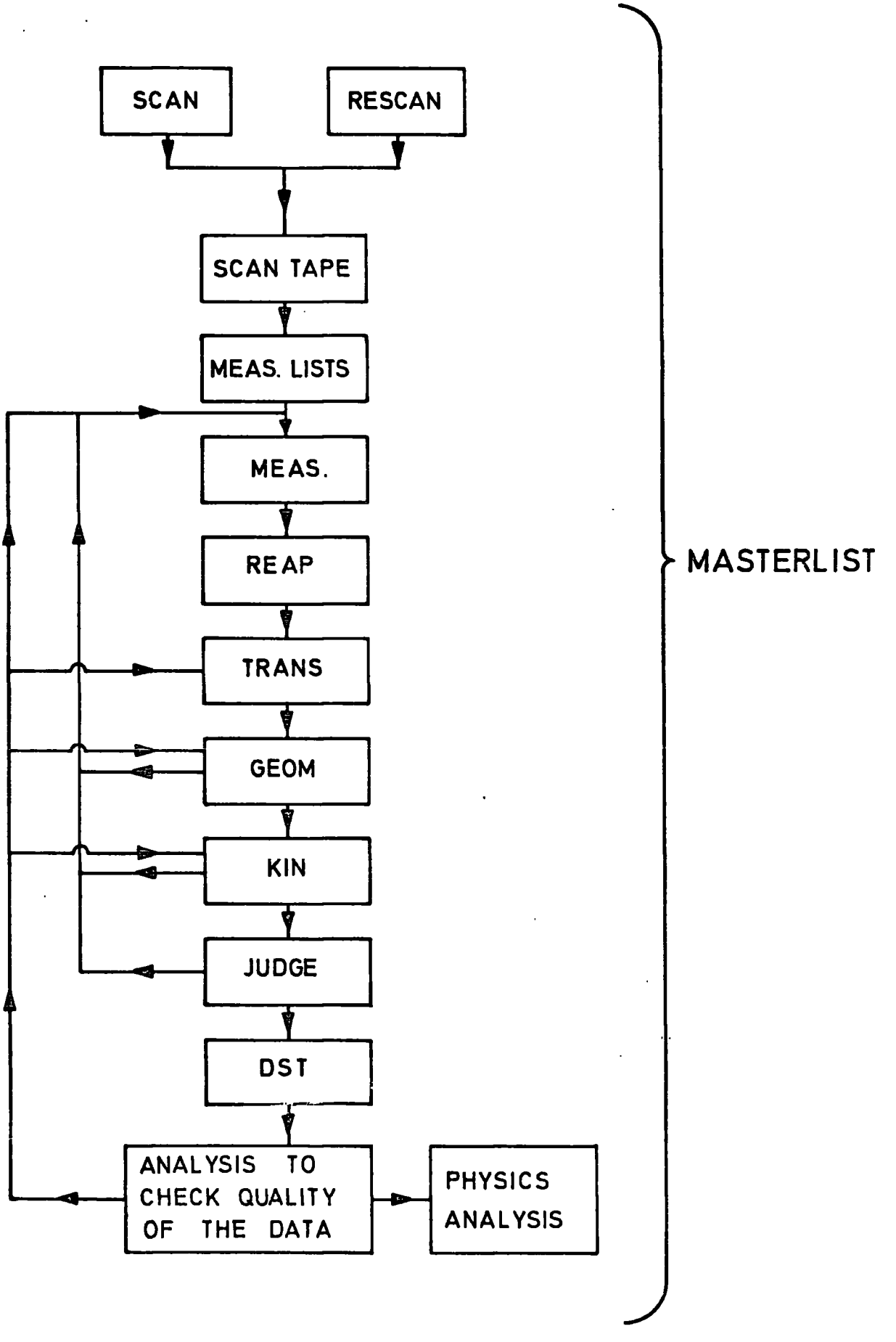

FIG. (3·1) EVENT PROCESSING CHAIN.

(f) data summary tape (D.S.T.). Finally as a result of all these stages, data in final form emerges. This is concentrated on to a data summary tape. It is at this stage that the data is analysed to check that the experimental data is of good quality and that biases are detected and understood. Finally the data is in final form for the physics analysis.

An outline of these processes is shown in Figure 3.1 and each is described in some detail in the following passages.

3.2 Scanning

The K^-P interaction is characterised by the possibility of opened channels even at zero K^--meson momentum. These channels are (reactions 3, 4, 5 and 6 mentioned in Chapter I, section 1.1).

$$K^- + P \rightarrow \pi^- + \Sigma^+$$

$$\rightarrow \pi^+ + \Sigma^-$$

$$\rightarrow \pi^o + \Sigma^o$$

$$\rightarrow \pi^o + \Lambda^o$$

also

$$K^- + P \rightarrow (2\pi)^o + \Lambda^o$$

Other reactions can take place if the K^--meson momentum is higher than zero. Table 3.1 gives some of these channels together with the K^--meson threshold momentum, P_{K^-}, in the laboratory system and their cross-sections. Only the first three are of any consequence. The first two are falling cross-sections and so are quoted at the least detectable momentum of this experiment. The latter is a rising cross-section and this is quoted at the highest momentum of this experiment.

	CHANNEL	THRESHOLD P_{K^-} (MeV/c)	CROSS-SECTION AT (MOMENTUM) mb (MeV/c)
	$K^- + P \longrightarrow K^- + P$	> 0	87.29 (110)
	$K^- + P \longrightarrow \bar{K}^0 + n$	90	19.8 (100)
	$K^- + P \longrightarrow \Sigma^{\pm}_{\mp} + (2\pi)^{\mp}_{\pm}$	250	0.23 (600)
	$K^- + P \longrightarrow \Lambda^0 + (3\pi)^0$	130	CROSS-SECTIONS ARE NEGLIGIBLE IN THE REGION OF THIS EXPERIMENT
	$K^- + P \longrightarrow K^- + P + \pi^0$	510	
	$K^- + P \longrightarrow \bar{K}^0 + n + \pi^0$	525	
	$K^- + P \longrightarrow \Sigma^{\pm}_{\mp} + (3\pi)^{\mp}_{\pm}$	590	
	$K^- + P \longrightarrow \bar{K}^0 + n + (2\pi)^0$	820	

TABLE (3.1) SOME CHANNELS OF THE REACTION $K^- P$ AT MOMENTA OTHER THAN ZERO.

The films have been scanned twice and in a restricted number of the films, three times. In the first scan the following topologies were sought in a restricted fiducial volume:

1. Zero-prong events with an associated V^0-decay.
2. Two-prong events with an associated Λ^0-hyperon.
3. Two-prong events with a $\Sigma^{\pm}$-decay.
4. Three-prong events. These will be largely due to the three pion mode of decay of the kaon (τ-decay). There will be a small admixutre from interactions in neon nuclei which have diffused into the hydrogen, and from one-prong decays with a Dalitz pair. The τ-decays are necessary to calibrate the experiment. From these the total kaon track length can be found in each momentum interval.
5. Positive pion decays in the mode $\pi^+ \rightarrow \mu^+ + \nu_\mu, \mu^+ \rightarrow e^+ + \nu_e + \bar{\nu}_e$ (π - μ - e events). These are required in hydrogen to check the extent of the diffusion of neon nuclei. If this is of any consequence the muon range should decrease. They are required in the neon-hydrogen region to determine the percentage mixture there.

Zero-prong events with seen V^0, Σ^+-hyperon events, and two prong events associated with Λ^0-hyperon were scanned for gamma rays pointing to the appropriate vertex (it is not possible at our energies to produce $n\bar{K}^0\pi^+\pi^-$, i.e. two-prong events associated with $\bar{K}^0$-meson). Nearly no gamma rays have been found pointing to the production vertex of a two-prong event associated with Λ^0-hyperon, which indicates that only reactions of the type $K^- + p \rightarrow \Lambda^0 + \pi^+ + \pi^-$ are possible at our energies and not $K^- + p \rightarrow \Lambda^0 + \pi^+ + \pi^- + \pi^0$. This is consistent with the cross-section for the production of Λ^0-hyperon and three pions which is zero up to about 620 MeV/C K^--meson momentum. Events were scanned and recorded if both the production and decay vertices were

in hydrogen. Meanwhile the gamma rays were scanned for and recorded if they were anywhere in the chamber and were associated with the event.

No attempt has been made at the scanning stage to allocate events associated with V^0s into Λ^0-hyperon and $\bar{K}^0$ meson events. They were treated as one class of events. When the film was scanned independently for a second time an extra class of events was sought. These are two prong events which comprise elastic scattering and, rather importantly, events of early classes which simulate two prong events. These are due to, in general, the decays of hyperons close to the production vertex. Because of this extra class, a third scan was carried on about 10% of the films to allow (a) the scanning efficiencies of this new class of events to be determined, and (b) to check scan efficiencies by the multiple scan method.

The scan information (the classes of events found on various scans) were processed partly manually and partly by computer program. The main function was to check the input data for faults or inconsistencies and to copy the good scan information into a permanent file on magnetic tape. At any stage scan information exists on a tape. New data is merged with the existing data and stored on new tape file. The 'old'/'new' magnetic tapes switch between themselves automatically. The merging process of the scan information is shown in Figure 3.2.

Measuring lists were produced via the computer using the information from the two main scans. Details of an event were copied on to a measuring list from the scan tape with the information whether it was seen on a single scan only, or seen in common on both scans.

3.3 Scanning Procedure

The fiducial volume was defined from camera 2. This is shown in Figure 3.3. Each charged kaon entering the fiducial volume of the T.S.T.

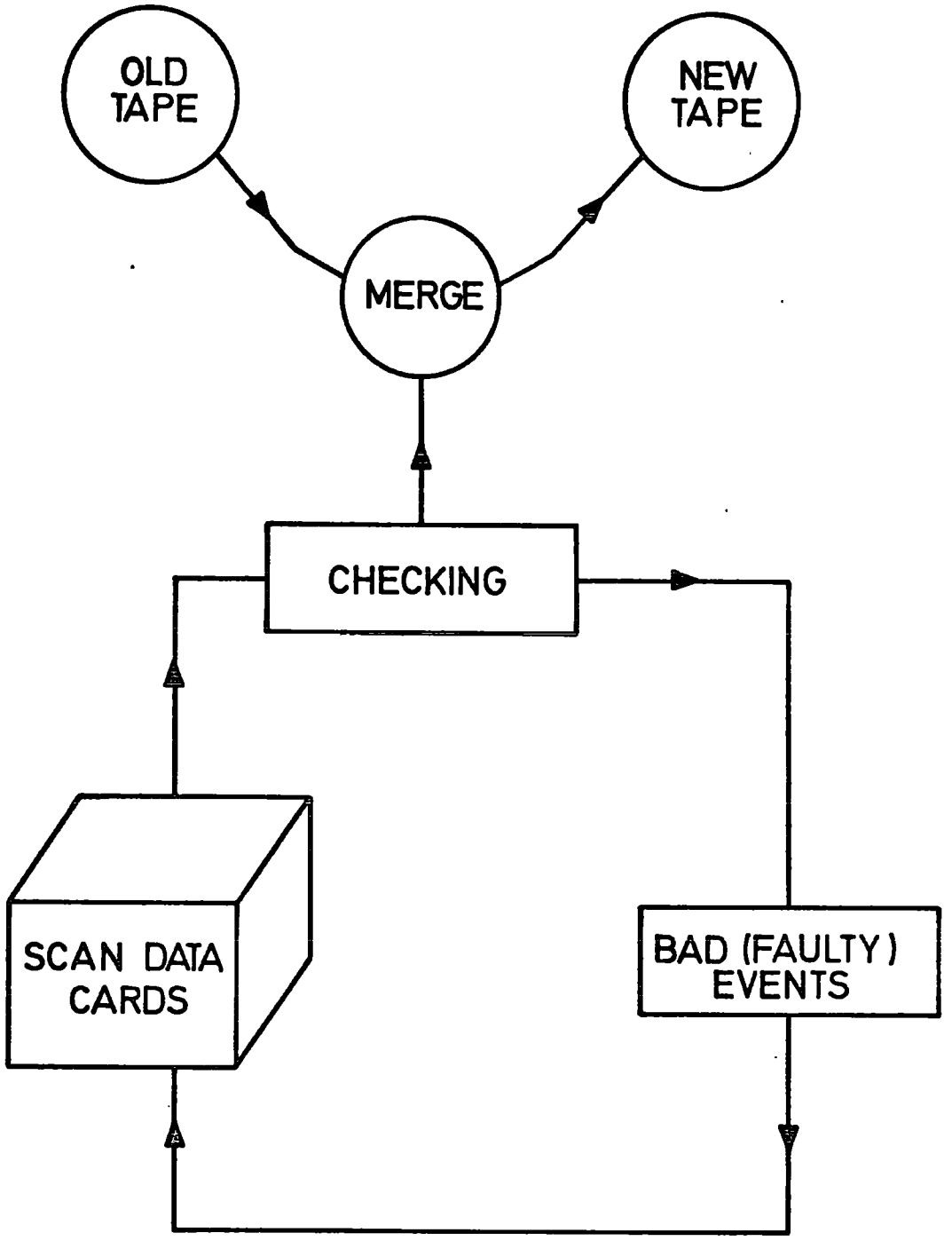

FIG. (3·2) MERGING PROCESS OF SCAN INFORMATION.

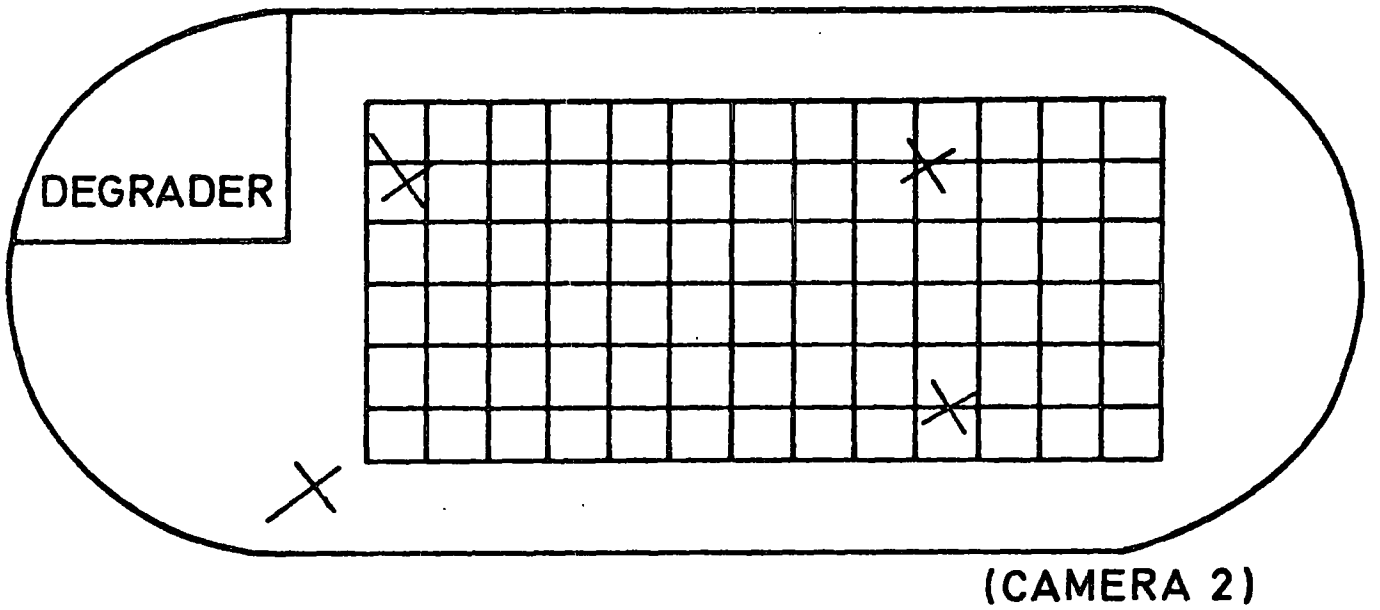

FIG. 3·3 SCANNING FIDUCIAL VOLUME

was followed until it:-

(a) left the fiducial volume,

(b) left the T.S.T. region into the perspex (and perhaps subsequently into the neon-hydrogen mixture).

(c) interacted or decayed in hydrogen.

The flow chart, Figure 3.4 is a summary of the scanning procedure.

A record of each event was made. A twenty five digit number is used to describe each event, this record is defined as

4	1	1	3	1	1	1	3	3	3	4
A	B	S	D	Y	E	Ne	G1	G2	G3	C

A is the frame number

B is the event number

S is the event size (number of prongs at the primary vertex)

D is the zone where the event is found

Y is the hyperon number

1 for Σ^+

2 for Σ^-

3 for V^0

4 for $\Sigma^+ \rightarrow P + \pi^0$ and associated with gamma ray(s)

5 for two prong elastic scatterings

6 for other two prong events

E is the code for the $\pi - \mu - e$ decay

Ne is the τ-decay code or the neon interaction code(1 for τ-decay and 2 for neon interaction)

G1, G2 and G3 are the zones of the gamma rays on the scanning grid

C is a comment code.

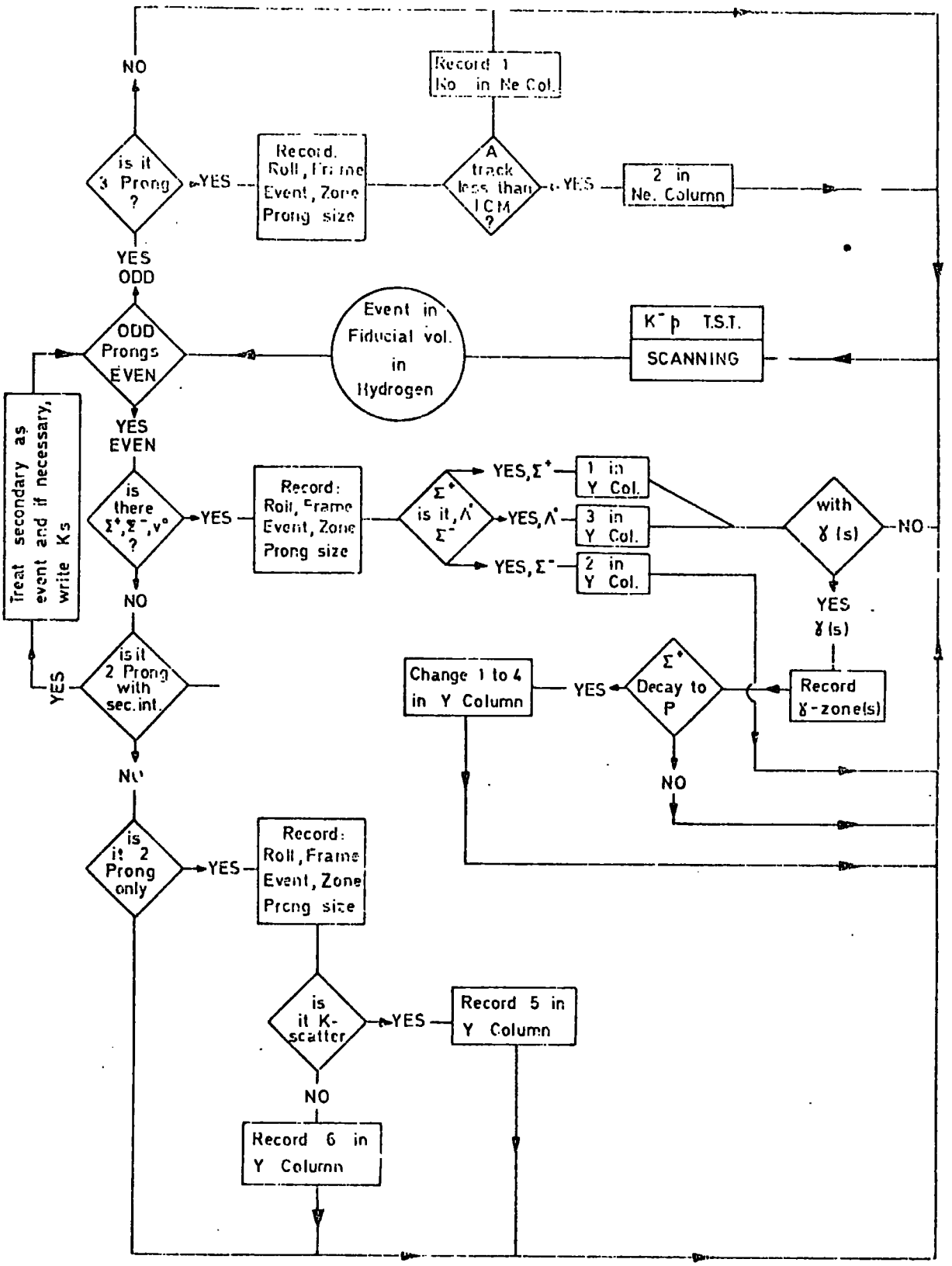

FIG. (3.4) FLOW CHART OF SCAN PROCEDURE

The length of each of these subrecords is given above it. for example A is a four digit number, B is one digit number, and so on.

3.4 Measuring of Events

All events found on the first and second scans were measured, with the exception of ordinary two prong events. With these a sample of about 1000 events was measured from each block of the metal framed target for the in-flight data. Image plane digitized machines were used which were on-line to an IBM 1130 computer. All tracks involved were measured away from the vertex they were associated with, preserving the order in which they were measured on all three views.

Split tracks, that is tracks which pass through the perspex walls to the neon-hydrogen mixture region, were not always measured in the neon-hydrogen since the information from the hydrogen section is much more accurate. The neon-hydrogen section is only useful when the hydrogen segment is very short or straight. In this case the end point of the hydrogen segment and the first point of the neon-hydrogen segment had to be measured very accurately. The end point of the hydrogen segment was measured twice (and subsequently this is used as a flag) so that this point could be used to divide the measurements of the track into two parts, one part in the pure hydrogen region and another part in the neon-hydrogen region.

Preliminary event information such as frame number, event number, topology short stopping tracks, and long stopping tracks, was entered at the beginning of measuring each event. This was used to guide the measurer through the measurement of the event. In general each event was measured per view more or less in the following order:

(a) production vertex

(b) four fiducial crosses

(c) beam track

(d) tracks associated with the production vertex

(e) secondary vertex and the track associated with this vertex, where gamma rays were treated as secondary vertices.

Precision of measurement was constantly monitored. Checks in the on-line system quickly revealed errors in the measuring system. For example, there is sufficient difference in the relative positions of the four measured fiducial marks to be able to detect immediately that a wrong view is being measured. Tolerances ensured that these relative positions never varied by more than about 0.15%. Other checks detected slackening of film gates, small movement of the projectors and so on. In this way helix fit errors on tracks and on vertices were always less than about 10 μ error on the film (3.1).

This attention to precision has also to be backed by consideration of systematic errors. At the measuring stage a systematic error of importance arises from the nature of image plane digitized machines. Since most measurements are some distance from the optic axis then lens distortions become important (the distortions are small but the measurements are very precise). Each machine is regularly calibrated. The position of twenty fiducial crosses are measured on the machines and compared with the known positions on the film. By use of a regression statistical approach the transformation coefficients from the image plane to the plane of the film may be calculated using a polynomial of the order three of the form

$$x_t = a_{11} + a_{12}\, x_m + a_{13}\, y_m + a_{14}\, x_m^2 + a_{15}\, y_m^2 + a_{16}\, x_m\, y_m +$$

higher order terms.

$$y_t = a_{21} + a_{22}\, x_m + a_{23}\, y_m + a_{24}\, x_m^2 + a_{25}\, y_m^2 + a_{26}\, x_m\, y_m +$$

higher order terms.

Here x_t and y_t are the true corrected coordinates, a_{ij} are the transformation coefficients, and x_m and y_m are the measured coordinates.

The transformation coefficients for any measured point were found to be dependent on the location of that point on the table top. The transformed points depend on rotations and distortions of the image due to lens aberrations and the angled positions of the projectors.

3.5 Pre-geometry Processing

After the measurement, events were processed through the program REAP which sorts and rearranges them in order. The program TRANS puts the events into a format readable by the reconstruction program in addition to transforming coordinates to the film plane, and to correcting the measurements by the third order polynomial transformation described above.

3.6 Geometrical Reconstruction

The output tape from TRANS contains measured coordinates of fiducial crosses and points along the tracks, in addition to other information from the measurement of events. GEOMETRY (3.2) reconstructs events in the space of the chamber. But before reconstruction can proceed, the program GEOMETRY must be supplied with preliminary information such as:

(a) coordinates of the cameras and fiducial crosses

(b) optical constants of the chamber and the range-momentum table

(c) tolerances on the coordinates of the cameras and fiducial marks

(d) tolerances on the error of the reconstructed points

(e) refractive indices of the media between the cameras and the back window of the chamber.

The standard GEOMETRY (3.2) program was used after it has been modified to handle tracks in the composite chamber. Its work is briefly described below:

(1) Light rays are first constructed on the front glass assuming that the chamber is filled with one liquid then these light rays are modified for the inclusion of more than one medium (neon-hydrogen mixture, perspex and hydrogen) to reconstruct the vertices which are treated as corresponding points. The light rays are then modified if the vertices show that they are outside the T.S.T.

(2) Light rays for points along a certain track are corrected so that the reconstructed track is in the same medium as the vertex on this track. A check is then made to see if the track has crossed the perspex to the neon-hydrogen mixture region. If so the track is cut at the point where it was measured twice and reconstruction proceeds in the normal way in both media. The method of near correspondence is used for points on the track.

Three different range momentum tables were supplied to allow for the variation of momentum due to energy loss in the three different media.

GEOMETRY reconstructs tracks with mass dependent helix fitting and vertex reconstruction using tracks and corresponding points. After helix fitting GEOMETRY provides the centre of track values ϕ, $\tan\lambda$, and $1/p$ and their correlated errors in hydrogen where ϕ is the azimuthal angle, λ is the dip angle, and p is the momentum. The centre of track values and their correlated errors are used by the kinetmatical fitting program. From the above, KINEMATICS does not need any modifications to deal with the composite chamber events.

(3) Gamma rays are mainly converted in the region of neon-hydrogen mixture. Those converted in the T.S.T. region were measured and treated in the normal way. Gamma rays in the region of neon-hydrogen mixture were measured, and the method to deal with them was incorporated in the program. For electrons the slowing down by bremstrahlung is an important factor, so electrons were fitted to helices with three different energy losses using a constant dE/dx (assumed bremstrahlung loss). The best fit was selected. Then using the first four points, the angles at the beginning of the track were calculated by correction to the point of materialisation. The angles of the electron and positron were compared and a mean value derived to define the direction of the gamma ray from the best fit. This was compared with the gamma ray direction obtained by joining the point of conversion to the origin of the gamma ray.

3.7 Kinematical Fitting

The program KINEMATICS (3.3) takes the reconstructed events by geometry program and tries either to find a unique interpretation or to find the possible interpretations for each event. These must satisfy the conservation of energy and momentum which are described by the equations

$$\sum P_x = \sum_i P_i \cos\lambda_i \cos\phi_i - P \cos\lambda \cos\phi \Longrightarrow 0$$

$$\sum P_y = \sum_i P_i \cos\lambda_i \sin\phi_i - P \cos\lambda \sin\phi \Longrightarrow 0$$

$$\sum P_z = \sum_i P_i \sin\lambda_i - P \sin\lambda \Longrightarrow 0$$

$$\sum E = \sum_i \sqrt{P_i^2 + m_i^2} - \sqrt{P^2 + m^2} \Longrightarrow 0$$

Where, P_i, λ_i, and ϕ_i are respectively the momentum, dip angle, and azimuthal angle of the ith particle of the secondaries, whereas P, λ, and ϕ are the corresponding variables for the beam track, m_i and m are the mass assignment of the secondaries and the primary mass. For example if we take the Λ^o-hyperon decay into a proton and a π^--meson then these equations can be written as

$$P_p \cos\lambda_p \cos\phi_p + P_\pi \cos\lambda_\pi \cos\phi_\pi - P_\Lambda \cos\lambda_\Lambda \cos\phi_\Lambda = 0$$

$$P_p \cos\lambda_p \sin\phi_p + P_\pi \cos\lambda_\pi \sin\phi_\pi - P_\Lambda \cos\lambda_\Lambda \sin\phi_\Lambda = 0$$

$$P_p \sin\lambda_p + P_\pi \sin\lambda_\pi - P_\Lambda \sin\lambda_\Lambda = 0$$

$$\sqrt{P_p^2 + m_p^2} + \sqrt{P_\pi^2 + m_\pi^2} - \sqrt{P_\Lambda^2 + m_\Lambda^2} = 0$$

If all three parameters (P, λ, ϕ) of the proton and the π^--meson are known and if also the origin of the Λ^o-hyperon is known then only the momentum of the Λ^o-hyperon is left unknown. In this case the event is subject to three constraints and is called a 3C-fit. If the origin of the Λ^o-hyperon is unknown then there are three variables to be determined using the four equations and in this case the decay is subject to one constraint and is called a

1C-fit. In general at any vertex the number of constraints is given by

Number of Constraints = 4 - number of unknowns.

Fits which have been tried depended on the event category. These are:

1. Zero prong events:

Fits which have been tried for this category are the following:

(a) $\bar{K}^0 \rightarrow \pi^+ + \pi^-$, $\bar{K}^0$ without origin ('floating' 1C - fit).

(b) $\bar{K}^0 \rightarrow \pi^+ + \pi^-$ with $\bar{K}^0$ meson pointing to the production vertex ('pointing' 3C - fit).

(c) knowing the direction and momentum of the $\bar{K}^0$ a fit was tried of the type $K^- + P \rightarrow \bar{K}^0 + n$ to determine the missing values of the neutron (1C - fit).

(d) multivertex fit which uses all the information from the previous fits (4C - fit).

This sequence of fits has been tried also for Λ^0-hyperon in exactly the same way. In the case of a zero prong event associated with Λ^0-hyperon and one or more gamma rays the procedure was to drop the gamma rays first using reduced topology, and then trying all combinations of the gamma rays. This will introduce an extra three constaints, for each gamma ray added, to the final fit. Events were accepted for analysis in the case of Λ^0-hyperon if they gave fit b or higher fits, whereas $\bar{K}^0$ events were accepted for analysis only if they gave the multivertex fit.

2. Two prong events $\Sigma^{\pm}$:

These have been fitted in three steps:

(a) the first fit which uses the production vertex of the reaction

$K^- + P \rightarrow \Sigma^{\pm} + \pi^{\mp}$ (3C - fit) to determine the usually unmeasured momentum of the $\Sigma^{\pm}$-hyperon.

(b) the second fit which uses only the decay vertex of the charged sigma. This uses the calculated momentum for the charged sigma from the first fit (1C - fit).

(c) the multivertex fit (4C - fit).

As in the case of zero-prong events associated with Λ^o-hyperon and gamma rays, the Σ^+-hyperon events with one or two gamma rays were tried first with the reduced topology, then the gamma rays were used. The two-prong events, $\Sigma^{\pm}$-hyperon, were accepted for analysis only if they gave the multivertex fit.

3. Two-prong events:

Most of the two-prong events are elastic scatterings, where the nature of the two outgoing particles are the same as the ingoing particles. Another group of two-prong events was that the two outgoing particles were different from the ingoing particles. This group of events does not satisfy the K^--meson elastic scattering.

The outgoing particles are:

(a) A π^--meson and a proton. This subgroup is either a result of Λ^o-hyperon decay very close to the production vertex where a gap was not seen, or Σ^+-hyperon decay to proton and neutral pion without leaving a visible track.

(b) A π^--meson and a π^+-meson. This subgroup can be the product of many channels which are:

1. The production of $\Sigma^{\pm}$-hyperons which decayed into $\pi^{\pm}$ n without leaving a visible track for $\Sigma^{\pm}$-hyperons.

2. The production of $\bar{K}^0$ meson which decayed very close to the production vertex and a gap was not observed; this is unlikely.

3. The production of $\pi^+\pi^-\Lambda^0$ where Λ^0-decayed into unseen neutral particles.

(c) A π^--meson and a positive sigma, where the decay vertex of the Σ^+-hyperon was not seen because the Σ^+-hyperon either was produced near the perspex and it disappeared inside the perspex, or it decayed to a proton where the angle between the Σ^+-hyperon and proton tracks are so small that they looked as one continuous track originating from the production vertex.

(d) A π^+-meson and a negative sigma, where the Σ^--hyperon either produced very close to the perspex that it disappeared inside it, or it was produced with low momentum and was absorbed after it came to rest.

Two prong events were tried for all these possibilities and were accepted if they gave any of the possible fits.

4. Three prong events:

These events are mainly $K^- \rightarrow \pi^+ + \pi^- + \pi^-$ (τ-decay), but some of these are either one prong K^--meson decays associated with Dalitz pairs where the scanners were not able to recognize them, or three prong neon interactions due to the diffusion of neon nuclei through the seals of the perspex walls as time went on. All three prong events were fitted to three hypotheses, the τ-decay hypothesis, the decay of $K^- \rightarrow \pi^- e^+ e^-$, and the decay of $K^- \rightarrow \pi^-\pi^0$, $\pi^0 \rightarrow \gamma\gamma$, $\gamma \rightarrow e^+e^-$. The fitted events of classes 2 and 3 were subsequently re-examined in judge and deleted from the records if the hypothesis is seen to be correct.

3.8 Judge:

Events which passed through the program KINEMATICS successfully may have unique interpretation or they may be ambiguous with more than one interpretation. Those which have unique interpretations, such as three-prong events which fitted the τ-decay, or the two-prong events with Σ^--hyperon which gave the multivertex fit, and so on, present no problems. Ambiguous events were looked at on the scanning table to be judged. Essentially, judge uses visual ionisation information to resolve track identities. In addition to the ambiguous events, certain other events which were given unique interpretations were also looked at on the scanning table. The types of these events which have been checked are:-

(a) Zero-prong events

These events were examined on the scanning table whether fitted to a unique hypothesis or not. Zero-prong events associated with Λ^o-hyperon were searched for more gamma rays (this was a third scan for associated gamma rays) and if it was found that these events were not associated with more gamma rays, they were accepted and no further action was taken, but if more gamma rays were found the events were put to be remeasured. Some of the zero-prong events associated with vees were judged to try to resolve the ambiguity between $\bar{K}^o$-meson and Λ^o-hyperon when both were fitted by the program. This sort of event was very rare, and was judged on the basis of the positive track ionisation of the vee particle.

(b) Two-prong events, $\Sigma^\pm$

Σ^+-hyperon events were looked at on the scanning table in two cases; first if the Σ^+-hyperon decay was fitted ambiguously to a proton and a π^o-meson and also to a π^+-meson and a neutron, to resolve which decay mode was the correct one using the ionisation of the charged decay track

from Σ^+-hyperon. If it was decided that the decay track is a proton the event was examined for associated gamma rays; secondly the event was examined if the decay track from the Σ^+-hyperon was fitted unambiguously to a proton. In this case the event was examined for gamma rays, or for more gamma rays associated with the decay vertex of the Σ^+-hyperon.

At this stage it has to be mentioned that the scan efficiencies for gamma rays is difficult to calculate because of the third scan for gamma rays at judging. Since if a gamma ray was found at this stage it will be added to the event and its status will be the same as the original event as far as whether the event was found on a particular scan is concerned. Because of this third scan which was in a way a special one for gamma rays, the scanning efficiency for the gamma rays should be very high.

Σ^--hyperon-events were only judged in one case, that is if they did not fit the Σ^--hypothesis but they fitted the K^-P elastic scattering followed by K^--meson decay to one prong. Here it is necessary to decide whether scanning or kinematic fitting is correct.

(c) Three prong and two prong events

Three prong and two prong events were judged only if they did not fit the τ-decay and the K^-P elastic scattering hypotheses respectively.

If an ambiguous three prong event fitted the τ-decay hypothesis it was taken as a τ-decay. Similarly if an ambiguous two prong event was consistent with the fit to elastic scattering, then this fit was accepted. This approach is justified from an initial examination of ambiguities which showed the correctness of these decisions in 99% of the ambiguous events.

Three prong events which did not fit the τ-decay hypothesis were looked at on the scanning table, and those which were not τ-decay events

were eliminated, otherwise they were considered τ-decay events and were not remeasured. The reason for not remeasuring is that the τ-mesons are required for normalisation purposes only. Only their numbers and primary momenta are needed.

Two prong events which do not give an elastic scattering fit were examined on the scanning table to see if they can be resolved. Either, by distinguishing a very short $\Sigma^{\pm}$-hyperon, a gap near the production vertex, or judging, on the basis of ionisation of one or both of the two prongs, to eliminate the wrongly fitted hypotheses.

3.9 Book-Keeping and Data Summary Tape

The book-keeping was achieved throughout this experiment by the system which is known in the processing chain, Figure 3.1, as the MASTERLIST. This consists of a set of files which contain summary information on each event as it progressed through the processing chain. Each event has an entry of twenty bits of information giving the frame number, event number, the fitted hypotheses, and a status word. This word gives the stage the event has reached. The entry of twenty words was used to control the writing of the Data Summary Tape. Separate Data Summary Tapes were produced on the basis of the topologies to facilitate the analysis. The length of the record for each event on the D.S.T. contains all information of measured and fitted values (ϕ, $\tan\lambda$, $1/p$, and their correlated errors) at the centre of the track for each particle, beside the vertices information and the track length. At the end of each record a summary of the MASTERLIST information was supplied.

CHAPTER IV

PRELIMINARY DATA ANALYSIS AND SCANNING EFFICIENCY

4.1 Scanning and Measuring Statistics

Table 4.1 gives the number of events for different types of interactions and decays where they have been sought in this experiment. The table is only for the Durham share of the film from the metal framed target of the inflight films (blocks 2-5) after two scans and two measurements. The different columns are as follows:

SCAN is the number of events found when the scanning was done.

NOTM is the number of events which have been judged as not measurable events because they are difficult to measure and most of them have very bad geometry.

REMS is the number of events judged to be remeasured and these are either failed GEOMETRY or KINEMATICS and no reason was found why they should not pass.

ENOV is the effective number of events after eliminating the not events and the neon interactions.

NFIT is the number of events which gives a fit to a physical channel of any kind. This fit is not always the same physical channel as observed at scanning.

As it is seen and it has been mentioned in various sections that several advantages are to be gained using the track sensitive target. The main advantage is the gain of gamma ray conversions (due to the low radiation length of the neon-hydrogen mixture which is about 45.0 cms) whilst at the same time the target, which is a proton, is unambiguously defined and precision of measurement is maintained. The bubble size in

TYPE	SCAN	NOTM	REMS	ENOV	NFIT
Zero Prong + V°	7641	132	325	3377	2920
Zero Prong + Λ° + 1 γ	1384	27	143	939	769
Zero Prong + Λ° + 2 γ	191	6	41	157	110
Zero Prong + Λ° + 3 γ	37	2	8	32	22
Two Prongs	4267	80	214	4109	3815
Two Prongs + Λ°	742	45	124	546	377
Σ^+ (Σ^+_π) (Σ^+_ρ)	4622	159 120	280 143	2511 1623	2072 1360
Σ^+ + 1 γ	607	36	108	561	417
Σ^+ + 2 γ	56	4	11	45	30
Σ^-	4578	259	506	3963	3198
Three Prongs	3942	74	128	3343	3141
$\pi - \mu - e$	814	—	—	—	—

TABLE (4-1): SCANNING and MEASURING STATISTICS

hydrogen turns out to be smaller than in a conventional bubble chamber which increases the measurement precision and improves the resolution near the vertices. The track sensitive target however as it was used in this experiment suffered from the following drawbacks:-

(1) As discussed in Section 2.3 the detection efficiency of the gamma rays is limited due to the geometry of the chamber.

(2) Since the depth of the track sensitive target is very shallow, about 8.0 cms a relatively large number of K^--meson tracks enter the perspex walls and disappear inside it either with or without an associated V^o in the pure hydrogen region. This is clear from comparing the number of zero prong events with associated V^o found at scan and the number of events which give kinematical fits. The bulk of the difference is due to interactions of the K^--mesons inside the perspex walls. These events were eliminated from the sample.

(3) Despite the seals, neon molecules leaked through them, as time went on, to the pure hydrogen region. This gave rise to some K^--meson interactions with the neon nuclei (background interactions). This number is small experimentally showing that the rate of diffusion was quite small. This was also concluded from determining the muon ranges which were found to be nearly the same for all blocks as stated in Section 4.5. Almost all the background interactions were recognizable and hence have been excluded.

(4) Using the aluminium degrader to slow down the beam momentum gave rise to various side effects, one of these was that the beam momentum at the entrance of the track sensitive target was not well known. This removes a normally tight constraint in the fitting process. Another is that the contamination of the beam increased due to interactions and

decays taking place inside the degrader. The contamination of the beam was about 25%. However since this is due to lightly ionising pions, muons, and electrons the contamination can be recognized. However, despite this the amount of kaon track in the experiment was determined, as a function of momentum, from the easily recognized tau-mode of decay of the negative kaons.

4.2 χ^2 Probability and the Stretch Quantities

Before embarking on detailed analyses the quality of the data has to be checked. As an example the events involving charged Σ-hyperons production is shown below. The χ^2 probability is a measure of the goodness of the fitted hypothesis. It should be uniform for events of the same final state if the errors are estimated correctly. If the errors are overestimated the distribution will peak at high probability; conversely the peak occurs at low values. If the hypothesis is wrong but spuriously leads to a fit then it is expected to be of low probability. The χ^2-probability distributions for the three different channels ($K^- + P \rightarrow \pi^- + \Sigma^+$, $\Sigma^+ \rightarrow \pi^o + P$; $K^- + P \rightarrow \pi^- + \Sigma^+$, $\Sigma^+ \rightarrow \pi^+ + n$; $K^- + P \rightarrow \pi^+\Sigma^-$, $\Sigma^- \rightarrow \pi^- + n$) are given individually in figures 4.1a to 4.1c, where it is seen that the distributions are isotropic apart from a peak at low values of χ^2-probability ($P(\chi^2) < 0.1$).

At low momentum there is little probability of spurious fitting and so the peak at low probability must be due to events where the real errors are considerably higher than the average values assumed. Apart from the low probability peak it would appear that errors are properly calculated.

The stretch quantity on a measured variable $S_i(x)$ is defined by

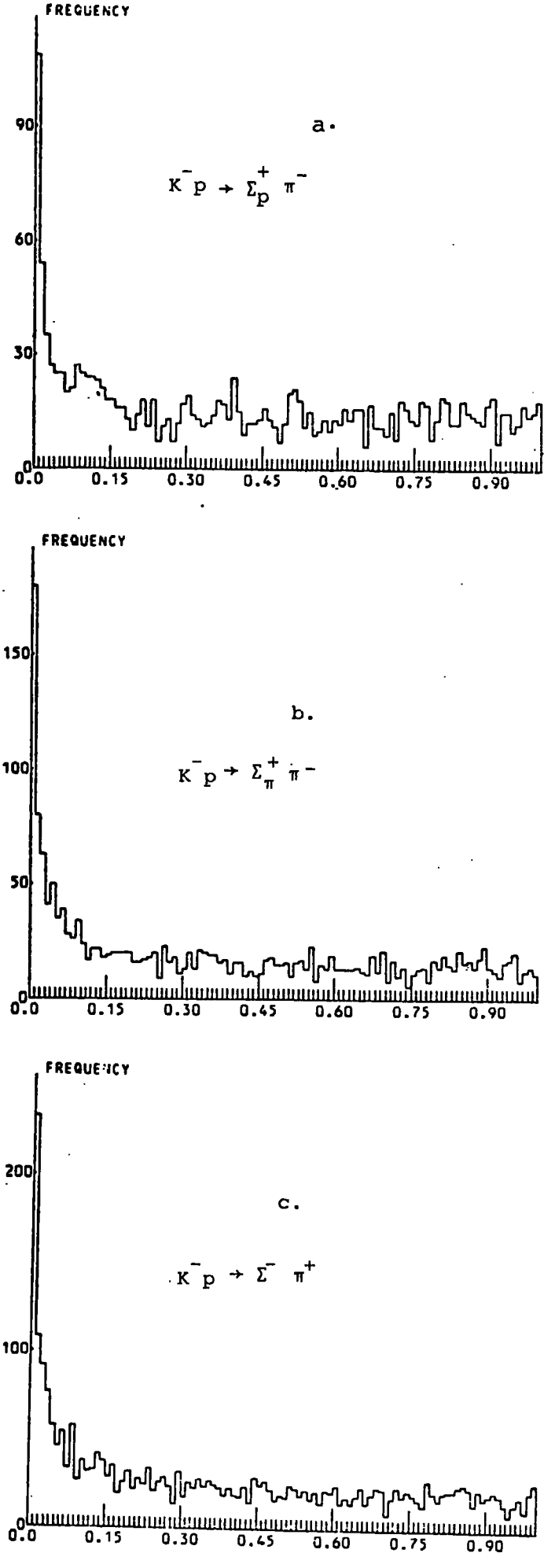

Figure 4.1:

χ^2-Probability distribution for the Σ-hyperons.

$$S_i(x) = \frac{x_i^f - x_i^m}{\sqrt{\sigma_m^2 - \sigma_f^2}}$$

where x_i^f is the fitted value of the measured variable x_i^m, σ_m is the error on the measured value of that variable, and σ_f is the error on the fitted value.

Each of the stretch quantities should have a Gaussian distribution with a mean value of zero and a standard deviation of unity if the errors are correctly estimated. The stretches are shown in figures 4.2a to 4.2f and a summary of the statistical tests is shown in table 4.2. The kurtosis is of the order of 3 which is correct for a Gaussian distribution and the standard deviations are consistent with unity. The mean values are slightly shifted from zero. However these shifts vary from one channel to another and they appear to be fluctuations only.

Quantity	Mean	Standard Deviation	Kurtosis
ϕ_{K^-}	-0.076 ± 0.014	1.14	3.4
$(\tan\lambda)_{K^-}$	-0.14 ± 0.014	1.16	3.45
$(1/p)_{K^-}$	0.055 ± 0.015	1.22	3.47
ϕ_{π}	0.12 ± 0.016	1.29	3.17
$(\tan\lambda)_{\pi}$	0.07 ± 0.015	1.19	3.34
$(1/p)_{\pi}$	-0.2 ± 0.017	1.37	3.15

Table 4.2: A summary of the statistical tests for the charged sigma hyperons.

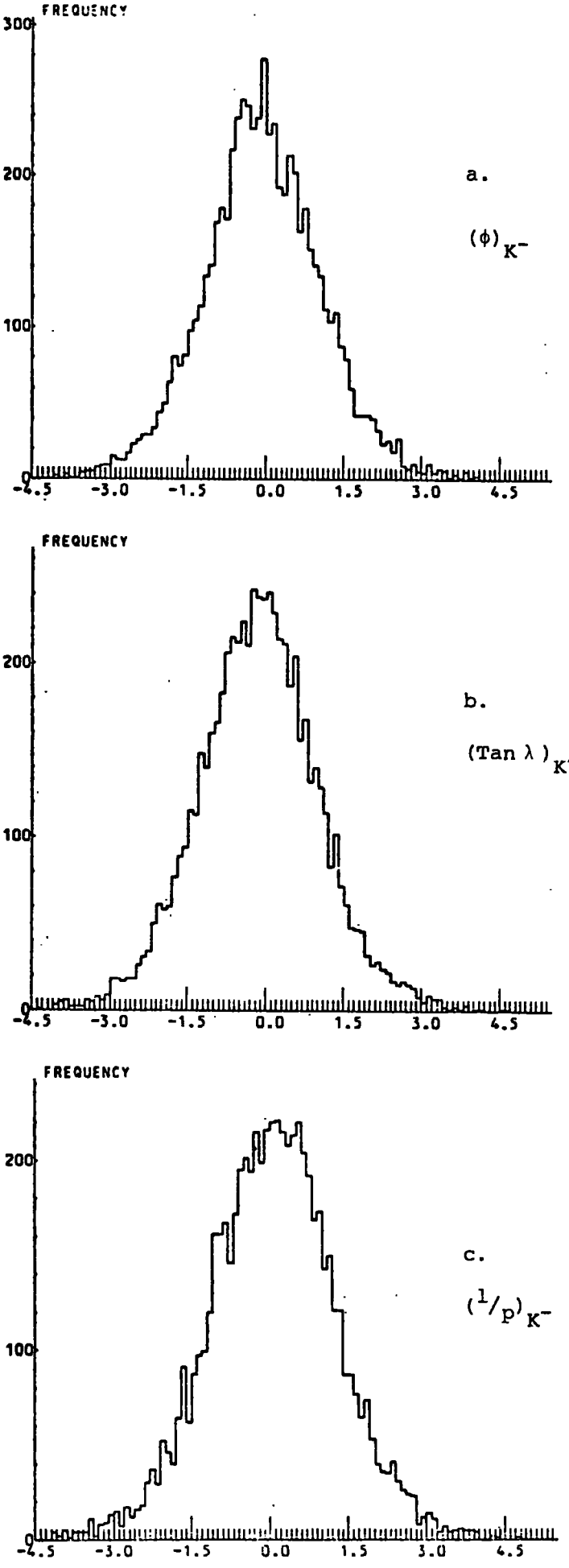

Figure 4.2:

Stretch quantities for the primary $\bar{K}$-meson producing Σ-hyperon.

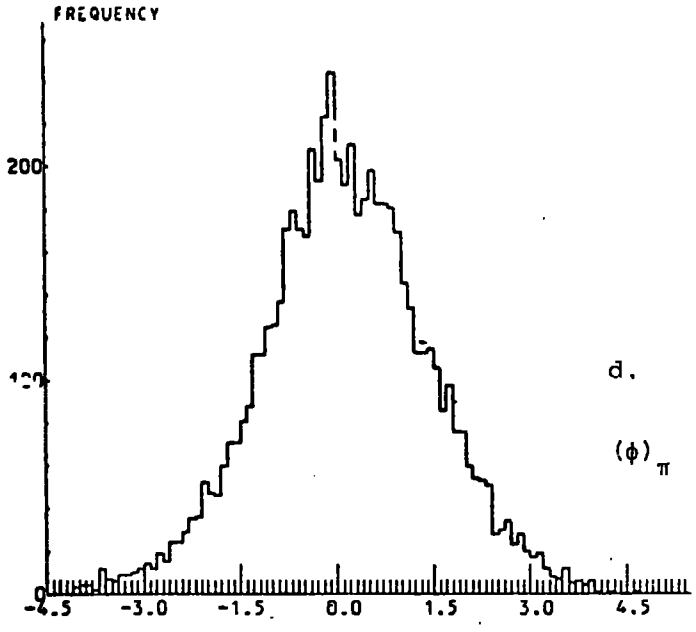

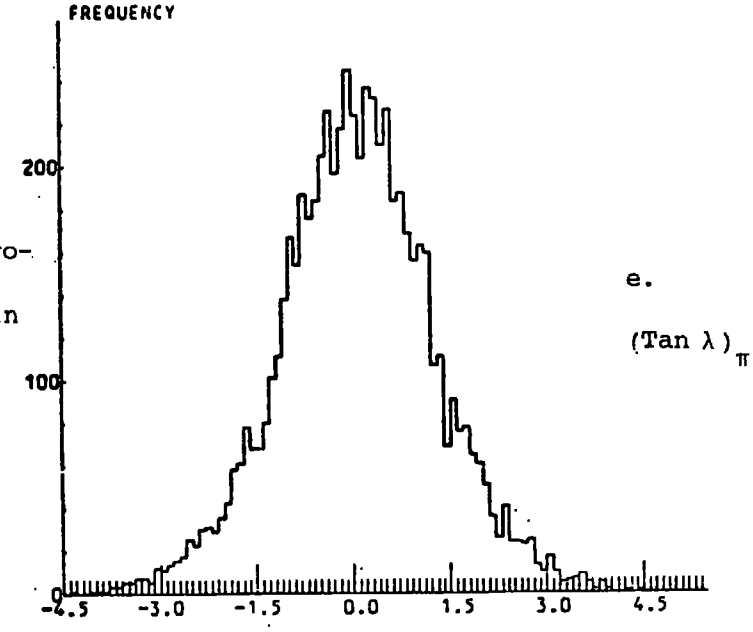

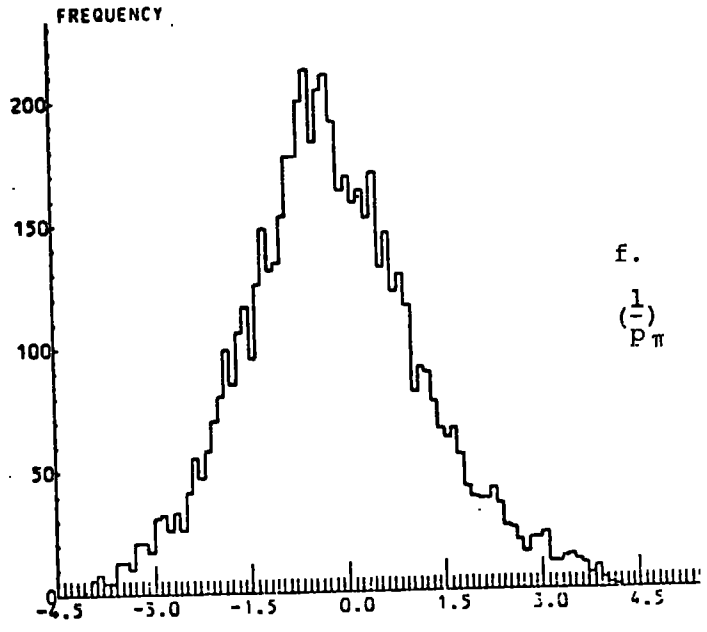

Figure 4.2: Stretch quantities at the production vertex in the case of Σ-hyperons.

4.3 Scanning Efficiency

All bubble chamber experiments involve searching for particular interactions or decays in a certain fiducial volume. Obviously the efficiency with which these events are found is of prime importance. To determine this, the film or a representative portion of it is independently scanned twice (occasionally three times), then by comparing the events found on the separate scans the efficiency can be determined. In this experiment all the film has been scanned twice and a part of it has been scanned a third time. In the following section the determination of the scan efficiency using the double scan is first described. This is followed by the determination of the scan efficiency using the three scans.

4.3.1 Double Scan Method: (4-1)

Events have been divided into different categories according to the number of prongs at the production vertex. Clearly the visibility of an event depends upon this and to some extent on a number of other parameters, such as the position of the interaction in the chamber, the dip angles of the charged secondaries and so on. The categories of events are:-

1. Zero prong events with associated V^os
2. Two prong events with associated Λ^os
3. Two prong events with a kink Σ^-
4. Two prong events with a kink Σ^+
5. Three prong events.

It is assumed that the scan efficiency for each category, k, is constant throughout a single scan, ϵ_1^k for the first scan and ϵ_2^k for the second scan. Consider that:

N_o^k is the true number of events of a certain category. Of these N_1^k is the number of events found on the first scan only and N_2^k is the number of events found on the second scan only. The number of events found on both scans in common is N_{12}^k , then

$$N_1^k = N_o^k \varepsilon_1^k (1 - \varepsilon_2^k)$$

$$N_2^k = N_o^k \varepsilon_2^k (1 - \varepsilon_1^k)$$

$$N_{12}^k = N_o^k \varepsilon_1^k \varepsilon_2^k$$

From these

$$\varepsilon_1^k = \frac{N_{12}^k}{N_{12}^k + N_2^k}$$

$$\varepsilon_2^k = \frac{N_{12}^k}{N_{12}^k + N_1^k}$$

$$N_o^k = \frac{(N_1^k + N_{12}^k)\ (N_2^k + N_{12}^k)}{N_{12}^k}$$

$$= \frac{\text{(all events on first scan)(all events on second scan)}}{\text{(events found on both scans in common)}}$$

The overall efficiency for the two scans is given by

$$\varepsilon_c^k = 1 - \left\{\left(1 - \varepsilon_1^k\right)\ \left(1 - \varepsilon_2^k\right)\right\}$$

Table 4.3 shows the scan efficiencies for categories 1-5 in each block of the film individually and for all blocks combined.

A careful check of the table shows that events were scanned with scan efficiencies which are dependent on the categories of the events. The single scan efficiency increases with the size of event as expected

BLOCK	2	3	4	5	2 - 5
ε_1^1	·77	·69	·727	·792	·706
ε_2^1	·62	·793	·794	·78	·785
ε_C^1	·913	·936	·944	·954	·937
ε_1^3	.748	.735	·82	·763	·766
ε_2^3	·822	·843	·822	·802	·822
ε_C^3	·955	·958	·968	·953	·958

BLOCK	2	3	4	5	2-5
ε_i^2	·411	·373	·691	·639	·597
ε_2^2	·657	·564	·841	·669	·732
ε_C^2	·80	·726	·951	·881	·892
ε_1^4	·739	·773	·753	·796	·764
ε_2^4	·824	·876	·818	·843	·838
ε_C^4	·954	·972	·955	·968	·962

BLOCK	2	3	4	5	2-5
ε_1^5	·852	·861	·855	·871	·86
ε_2^5	·871	·879	·864	·846	·864
ε_C^5	·981	·983	·98	·98	·981

TABLE (4·3) SCAN EFFICIENCIES (ε_i^k) WHERE i DENOTES THE SCAN AND k DENOTES THE CATEGORY

from zero prong events to three prong events. The exception is for two prong events with an associated Λ^o. These events happen much less frequently than all the other categories, especially at the low end of our energies (blocks 2 and 3). As they simulate $\pi^+\pi^-$ events (Σ -hyperon production and pion decay close to the vertex) scanners occasionally forgot to search for the associated Λ^o. Examination of the table also shows that as time went on the scanning efficiencies have improved which can be seen by comparing the second scan efficiency with the first scan efficiency. The low single scan efficiency is due in part to the quality of the pictures where in certain areas of the fiducial volume the illumination is poor, and in part due to the masking of tracks in hydrogen by tracks in the neon-hydrogen mixture. However the overall scan efficiency is satisfactory and for most categories is well above 90%. As expected the scan efficiencies for the third and fourth categories (Σ^- and Σ^+ hyperons) are the same.

4.3.2 Extension of the Double Scan Method

In general if there are n independent scans then the number of classes into which events can be allocated is $2^n - 1$. A portion of the film was scanned three times and so, for these, there are seven independent classes into which events can be divided. These are given in table 4.4; a bar above a number, e.g. $\bar{2}$ means that the event is not found on this scan. For each category of events there are four parameters (ε_1^k, ε_2^k, ε_3^k and N_o^k) to be determined using the seven classes. Employing the method of minimum χ^2 these quantities have been determined for each category k

$$\chi_k^2 = \sum_{i=1}^{7} \frac{\left(N_i^k - N_{i'}^k\right)^2}{N_i^k}$$

The scan efficiencies determined in this way are shown in table 4.6 as EDS and compared with the double scan method. The discrepancies manifested there are dealt with in the next section.

4.3.3 Modified Extension of the Double Scan Method

The fits by the method above are not good. Examination of the numbers in different classes as shown in table 4.5 indicates that the numbers of events found on a single scan and not on the other two are more than expected. This is a characteristic of events seen with low probability. Inspection of the table also shows that the events which are seen on all three scans are seen with high probability. Consequently it is necessary in the analysis of events of a single category to allow for a variation in the probability of being seen (4-2). In the present case of three scans only two levels of probability can be considered, those events which are highly conspicuous and seen with high probability and those events which are seen only with low probability. The scan efficiencies are then recalculated where the scan efficiency for a particular category k is determined by

$$P^k = \frac{N_{OA}^k P_A^k + N_{OB}^k P_B^k}{N_{OA}^k + N_{OB}^k}$$

where N_{OA}^k is the true number of events of this category which are seen with high probability P_A^k and N_{OB}^k is the true number of events which are seen with low probability P_B^k. These scan efficiencies are shown as MEDS in table 4.6.

In these fits the P_A^k and P_B^k are free parameters and as it is described they define two arbitrary discrete efficiencies. In the following subsection a continuous visibility function is tried.

CLASS	SCAN 1	SCAN 2	SCAN 3	EXPECTED NUMBER
1	1	$\bar{2}$	$\bar{3}$	$N_0\ \varepsilon_1\ q_2\ q_3$
2	$\bar{1}$	2	$\bar{3}$	$N_0\ q_1\ \varepsilon_2\ q_3$
3	$\bar{1}$	$\bar{2}$	3	$N_0\ q_1\ q_2\ \varepsilon_3$
4	1	2	$\bar{3}$	$N_0\ \varepsilon_1\ \varepsilon_2\ q_3$
5	1	$\bar{2}$	3	$N_0\ \varepsilon_1\ q_2\ \varepsilon_3$
6	$\bar{1}$	2	3	$N_0\ q_1\ \varepsilon_2\ \varepsilon_3$
7	1	2	3	$N_0\ \varepsilon_1\ \varepsilon_2\ \varepsilon_3$

TABLE (4.4)

CLASS / CATEGORY	$1\ \bar{2}\ \bar{3}$	$\bar{1}\ 2\ \bar{3}$	$\bar{1}\ \bar{2}\ 3$	$1\ 2\ \bar{3}$	$1\ \bar{2}\ 3$	$\bar{1}\ 2\ 3$	$1\ 2\ 3$
V°	20	34	35	57	59	77	243
2 PRONG+Λ°	4	10	7	5	8	4	21
$\Sigma^\pm$	56	59	70	77	86	92	512
3 PRONG	10	18	6	28	18	27	255
TOTAL	90	121	118	169	204	167	1032

TABLE (4.5)

4.3.4 Visibility defined Function of Derenzo and Hildebrand

Instead of defining two arbitrary areas of low and high probability the method of Derenzo and Hildebrand followed (4-3). There instead of using discrete probabilities a continuous visibility function F(V) is used where V, the visibility of an event, is such that $0 \leq V \leq 1$. The visibility includes the inherent characteristics of the event as well as the scanners' efficiency.

Derenzo and Hildebrand used for the visibility function $F(V) = K\, V^{\alpha}\, (1 - V)^{\beta}$ which depends on three parameters α, β, and K. The particular value of this function is that by varying the parameters α and β a large spectrum of shapes F(V) can be obtained. Figure 4.3 shows a family of curves of F(V) illustrating the variety of shapes produced by altering the parameters α and β.

The number of events seen between V and V + dV is given by F(V) dV and the true number of events is given by

$$N_T = \int_0^1 F(V)\, dV$$

In the case of three independent scans, the number of events found on a single scan and not on the other two, double scans and not on the third, and triple scans can be calculated. For example the number of events seen on one scan and not on the other two for a certain category k is

$$N_1^k = \int_0^1 K\, V^{\alpha}\, (1 - V)^{\beta}\; V(1 - V)^2\; dV$$

$$= K \int_0^1 V^{\alpha + 1}\; (1 - V)^{\beta + 2}\, dV$$

$$= K\, I\, (\alpha + 1,\ \beta + 2)$$

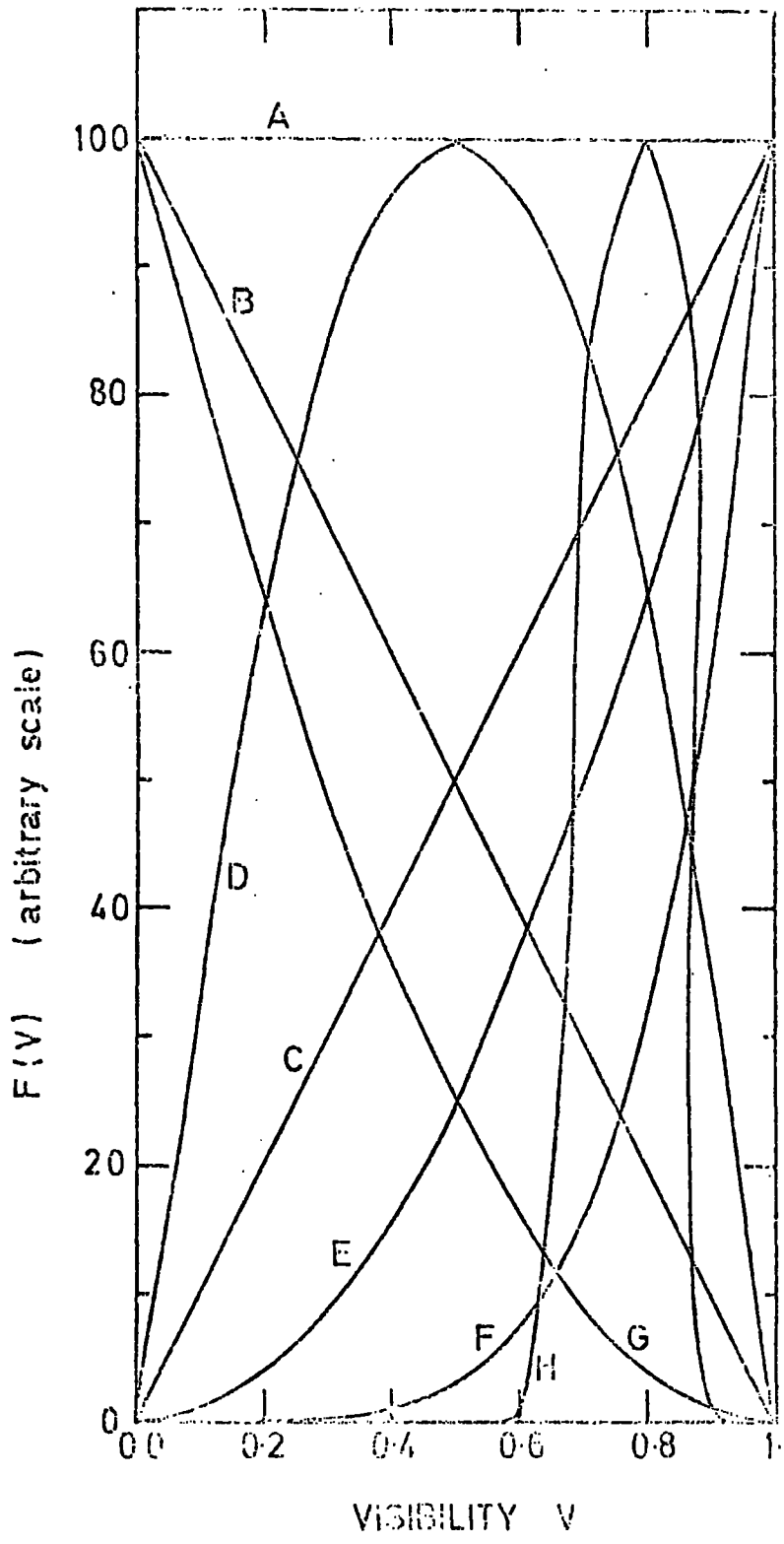

The function;
$F(V) = K V^{\alpha}(1-V)^{\beta}$
family of
curves corresponding to
various values of the
parameters α and β.

A : $\alpha = \beta = 0$
B : $\alpha = 0, \beta = 1$
C : $\alpha = 1, \beta = 0$
D : $\alpha = \beta = 1$
E : $\alpha = 2, \beta = 0$
F : $\alpha = 5, \beta = 0$
G : $\alpha = 0, \beta = 2$
H : $\alpha = 50, \beta = 15$

FIG. (4·3)

where

$$I(\alpha, \beta) = \int_0^1 V^{\alpha} (1 - V)^{\beta} \, dV$$

$I(\alpha,\beta)$ can be given in terms of gamma functions if $\alpha, \beta > -1$

$$I(\alpha,\beta) = \int_0^1 V^{\alpha+1-1} (1 - V)^{\beta+1-1} \, dV$$

$$= \frac{\Gamma(\alpha + 1) \, \Gamma(\beta + 1)}{\Gamma(\alpha + \beta + 2)}$$

For those events seen on two scans only and those seen in common on all three scans.

$$N_2^k = K \, I \, (\alpha + 2, \beta + 1)$$

$$N_3^k = K \, I \, (\alpha + 3, \beta)$$

The results of this analysis are indicated by DH in table 4.6.

The comparison of the overall efficiencies found by using the different methods for all categories (table 4.6) shows that the extension of the double scan method has underestimated the scan efficiencies. All other methods give nearly the same, high values. Since all the films of blocks 2-5 were double scanned and only a portion of the film was scanned three times then the double scan efficiency method has been used.

4.4 Gamma Ray Detection Efficiency

If an event produces n gamma rays and the probability for one of these to materialise is p, then the probabilities of observing 0, 1, 2 ...,n gamma rays are given by the terms of the binomial expansion $(p + q)^n$ where $q = 1 - p$. Hence from a comparison of the experimentally observed

CATEGORY / METHOD	ZERO PRONGS ε^1_c		TWO PRONGS+ Λ° ε^2_c		$\Sigma^\pm$ ε^3_c		THREE PRONGS ε^4_c	
DS	0.73	0.94	0.31	0.655	0.796	0.96	0.863	0.987
	0.79		0.50		0.806		0.91	
EDS	0.63	0.86	0.49	0.708	0.686	0.901	0.702	0.911
MEDS	0.704	0.929	0.312	0.662	0.749	0.94	0.831	0.977
	0.761		0.509		0.761		0.862	
DH	0.729	0.926	0.370	0.603	0.721	0.92	0.827	0.97

TABLE (4.6) THE OVERALL SCAN EFFICIENCY USING DIFFERENT METHODS

numbers of 0, 1, 2, ..., n gamma rays, the probability p can be found.

The expected materialisation probability has been estimated for the track sensitive target system by using Monte Carlo events. Monte Carlo events of the type $K^- + P \rightarrow \Lambda^o + \pi^o$

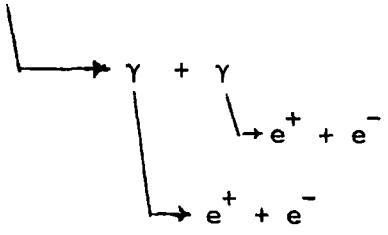

were generated using program FAKE, with the assumptions that (a) the X, Y and Z coordinate distribution of events correspond to real events in the chamber and (b) there is isotropy of the production of π^o-mesons and their decay to gamma rays. The results of the FAKE simulation should be typical of other channels in this experiment leading to the production of a single neutral pion. For example the results should hold for $K^- + P \rightarrow \pi^- + \Sigma^+$ where $\Sigma^+ \rightarrow \pi^o + P$. Radiation lengths in hydrogen and the neon-hydrogen mixture of 1000 cms and 35 cms were assumed. The gamma rays were not forced to materialise in each event, so that events that are generated fall into three categories. The first category in those events which are not associated with seen gamma rays, the second category is those events which are associated with one seen gamma ray each, and the third category is those events which are associated with two gamma rays each. The terms of the binomial expansion are given by, where n = 2

Number of gamma rays	Probability	Number of events from FAKE
0	$G_o = q^2 \equiv (1-p)^2$	649
1	$G_1 = 2Pq \equiv 2p(1-p)$	312
2	$G_2 = p^2$	39

The numerical values of the terms found in the FAKE simulation are in reasonable agreement with the binomial prediction, i.e. $G_1^2/G_oG_2 = 4$. Consequently although FAKE uses a realistic description of the generated events, it is clear that there are no strong correlations between the gamma rays which would upset the binomial description above, (provided as will be seen below that gamma rays of all energies are considered).

By using these faked events the materialisation efficiency of gamma rays, P, is found to be about 20%. Here there is no selection on the gamma ray momentum, and it is assumed that all gamma rays which materialise are seen regardless of their momentum, direction, or their position in the chamber. However, experimentally, gamma rays with momentum below about 20 MeV/C are very difficult to measure and to show that they are pointing to a primary vertex. When gamma rays with this low momentum are removed from the Monte Carlo sample, the effective materialisation probability drops to about 16%. Experimentally the removal of low momentum gamma rays is made at scanning time where the grid size of the fiducial scanning card is related to the 'size' of these gamma rays. The removal of these gamma rays at scanning will be seen to affect the description of the terms G_o, G_1 and G_2 by the binomial distribution. This is because there is a correlation between the energies of the two gamma rays from the π^o decay. Obviously if one gamma ray is of highest momentum the other is of lowest momentum. Even if both gamma rays materialise the event would be classified as a single gamma ray event at scan time. Because there is approximately an order of magnitude difference between the numbers of one gamma ray and two gamma ray events the loss of one gamma ray events from term G_1 to term G_o is not compensated by the gain of events from term G_2 to G_1. So if, for example, $1/5$ of the materialised gamma rays are of low momentum (as the above FAKE simulation indicates)

then $1/5$ of the one gamme ray events will be changed to the zero gamma category. The situation with the two gamma ray events is by no means clear since a detailed knowledge of the correlation between the two gamma ray energies is needed. Consequently the expected number of two gamma ray events where low momentum gamma rays are excluded is difficult to calculate. From the point of view of estimating the materialisation probability from experimental numbers it is safer to use the ratio of one gamma ray events to zero gamma ray events rather than a ratio involving two gamma ray events.

For example in the production of the Σ^+-hyperon by $K^- + P \rightarrow \pi^- + \Sigma^+$ and decay of the Σ^+-hyperon by the mode, $\Sigma^+ \rightarrow \pi^o + P$, two gamma rays are produced. From Table 4.1 the number of events for Σ^+_p decays are:

Zero gamma ray events	=	1623
One gamma ray events	=	561
Two gamma ray events	=	45

This leads to a probability of materialisation of about 15%. Strictly this is a combination of materialisation probability and scanning efficiencies for gamma rays. However as stated in section 3.7, chapter 3, this scanning efficiency is believed to be very high. Consequently the empirical value of materialisation probability can be compared directly with the Monte Carlo value. The agreement is quite good, showing that the neon-hydrogen mixture does reduce the radiation length to about 35 cms. This should be compared with the Monte Carlo results for a conventional chamber of the same size. There the expected value is 0.7%. Consequently the composite chamber is about 20 times better from this point of view. Events of the type $K^- + P \rightarrow \pi^o + \Lambda^o$ where faked rather than $K^- + P \rightarrow \pi^- + \Sigma^+$ ($\Sigma^+ \rightarrow \pi^o + P$) due to the difficulty of faking such events

(which have a total of five production and decay vertices) and allowing both gamma rays from the decay of π^{o}-meson to materialise. This is due to the restriction in FAKE on the number of vertices which is a maximum of four are allowed.

4.5 Concentration of Neon in the T.S.T.

The materialisation probability of pair production in the region of neon-hydrogen mixture is dependent on the neon concentration. This was kept constant in the metal framed target run of about 75% of neon. However this concentration has been increased in the case of the all perspex run as the engineers attempted to raise the neon concentration to as high value as possible. Apart from the deliberate changes in neon concentration a small fall off in concentration is expected since, despite the seals, neon does diffuse into the hydrogen. The effect in the neon-hydrogen mixture can be ignored but the admixture in the hydrogen has to be considered seriously. Some diffusion does occur since events are found during scanning which can only be interpreted as interactions in neon nuclei inside the hydrogen.

To investigate the diffusion of neon into hydrogen and to determine the hydrogen density in the T.S.T. region the ranges of the μ^{+}-mesons from the decay of the π^{+}-mesons at rest were measured. These muons have a unique momentum of 29.79 MeV/C, if the positive pions decayed at rest, and hence have a unique range.

The density of hydrogen will be smaller than is usual in a hydrogen chamber since the operational temperature in the T.S.T. is at 29 K about 10% higher than usual. Roughly this should lead to a drop of about 10% in density.

The ranges of a sample of 660 μ^+-mesons in blocks 2-5 were determined after reconstructing them in the space of the chamber. These ranges were plotted for each of these blocks individually and are given in figures 4.4a to 4.4d.

To determine the average range in each of these blocks the distribution of the ranges of the positive muons was fitted according to

$$f(R) = \frac{1}{S_R\sqrt{2\pi}} \exp\left\{-\frac{1}{2}\frac{(R-\bar{R})^2}{S_R^2}\right\} + K R^{\alpha} (R_m - R)^{\beta}$$

This equation represents a Gaussian distribution superimposed on a background distribution. The Gaussian distribution is represented by the first term with a mean $\bar{R}$ and a standard deviation S_R (the muon ranges were assumed to be normally distributed around the mean due to the measurement error).

The background distribution is represented by the second term of the equation. Here K, α, and β are parameters of the fit beside the mean and the standard deviation of the Gaussian distribution, R_m and R are the maximum measured range and the range of the μ^+-meson respectively. The background function has a wide range of shapes as shown in figure 4.3. The best fit was obtained by varying the parameters until a minimum of χ^2 was obtained. The fitted distributions are shown on each plot together with the fitted background.

The average ranges of the muons in each of the blocks 2-5 are shown in table 4.7. The ordering of block numbers corresponds roughly to time during the exposure. The ranges are very similar and so it is concluded that there was no significant diffusion of neon into the hydrogen during the exposure.

To examine the effects of the hydrogen density the muons from the four blocks were combined and an average range was determined using the same method and this gave an average range of 1.1101 ± 0.0030 cms. Figure 4.5 is the muon ranges distribution for all blocks combined.

The range-energy table initially used in GEOMETRY and KINEMATICS has been modified to allow for about 10% fall in density. It predicts a muon range of 1.167 cms. When this value is compared with the measured one it is found that a correction factor of 1.051 ± 0.0025 must be applied to the nominal hydrogen density.

To determine the neon concentration in the second region of neon-hydrogen mixture a sample of 292 μ^+-mesons ranges taken from blocks 2-5 were measured and were fitted in the same way as the muon ranges in hydrogen. The distribution of the μ^+-mesons ranges is shown in figure 4.6. The fit gave an average muon range of 0.233 ± 0.002 cms. From figure 4.7 this range corresponds to a neon concentration of 75.4 ± 0.6 mole percent (4.4). In turn from figure 4.8 this concentration of neon would give rise to a radiation length of 41.4 ± 0.7 cms for the gamma rays (2.1). This agrees with the determination of the probability of materialisation of gamma rays determined above. Moreover a direct determination of the conversion length of the gamma rays materialising in the neon-hydrogen mixture has been shown to be (36.0^{+20}_{-10}) cms (3.1). From this the radiation length should be 28^{+15}_{-7} cms. This is roughly consistent with the radiation length of 41.4 cms.

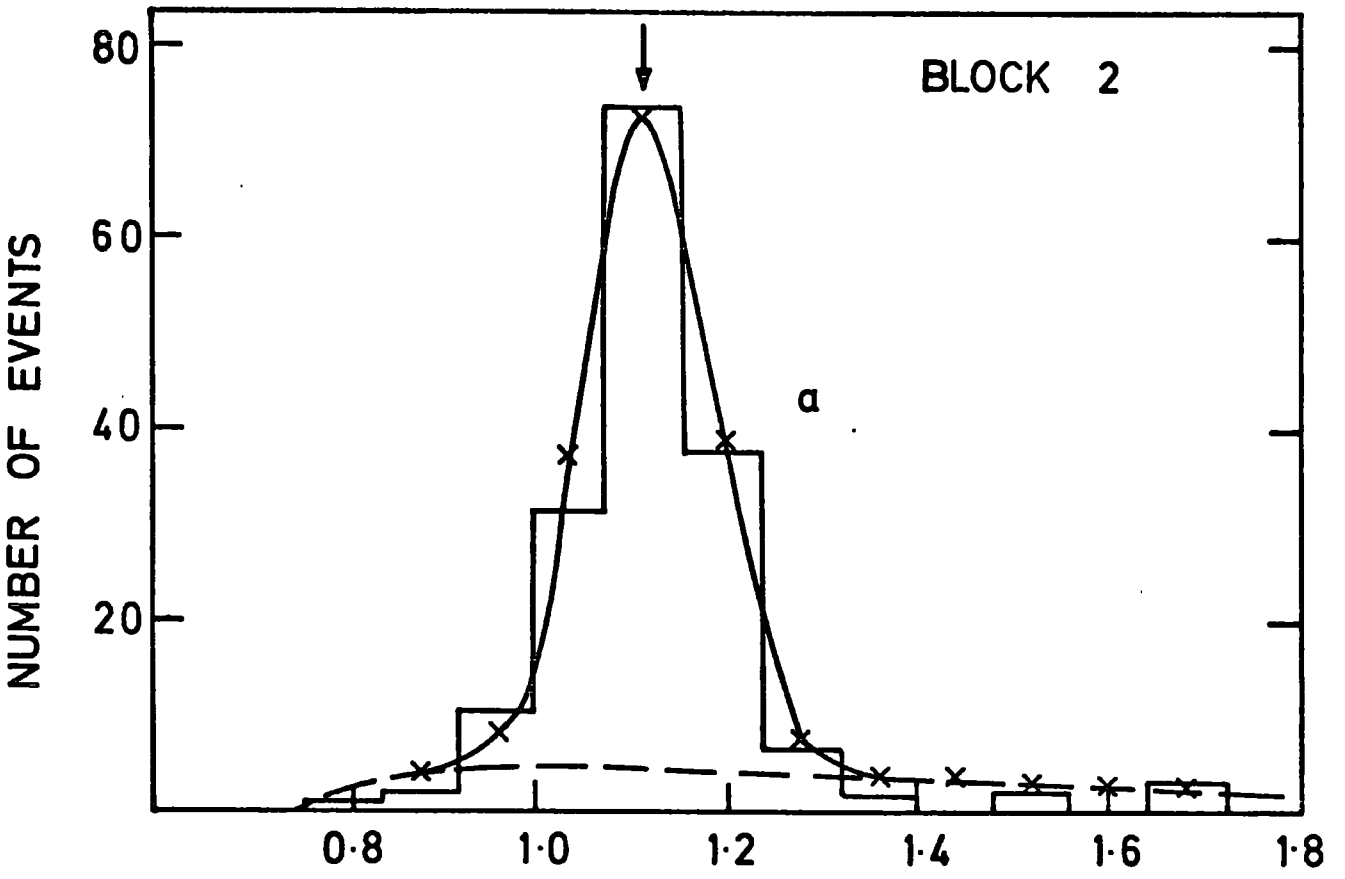

FIG. (4.4) Range of positive muons (cm)

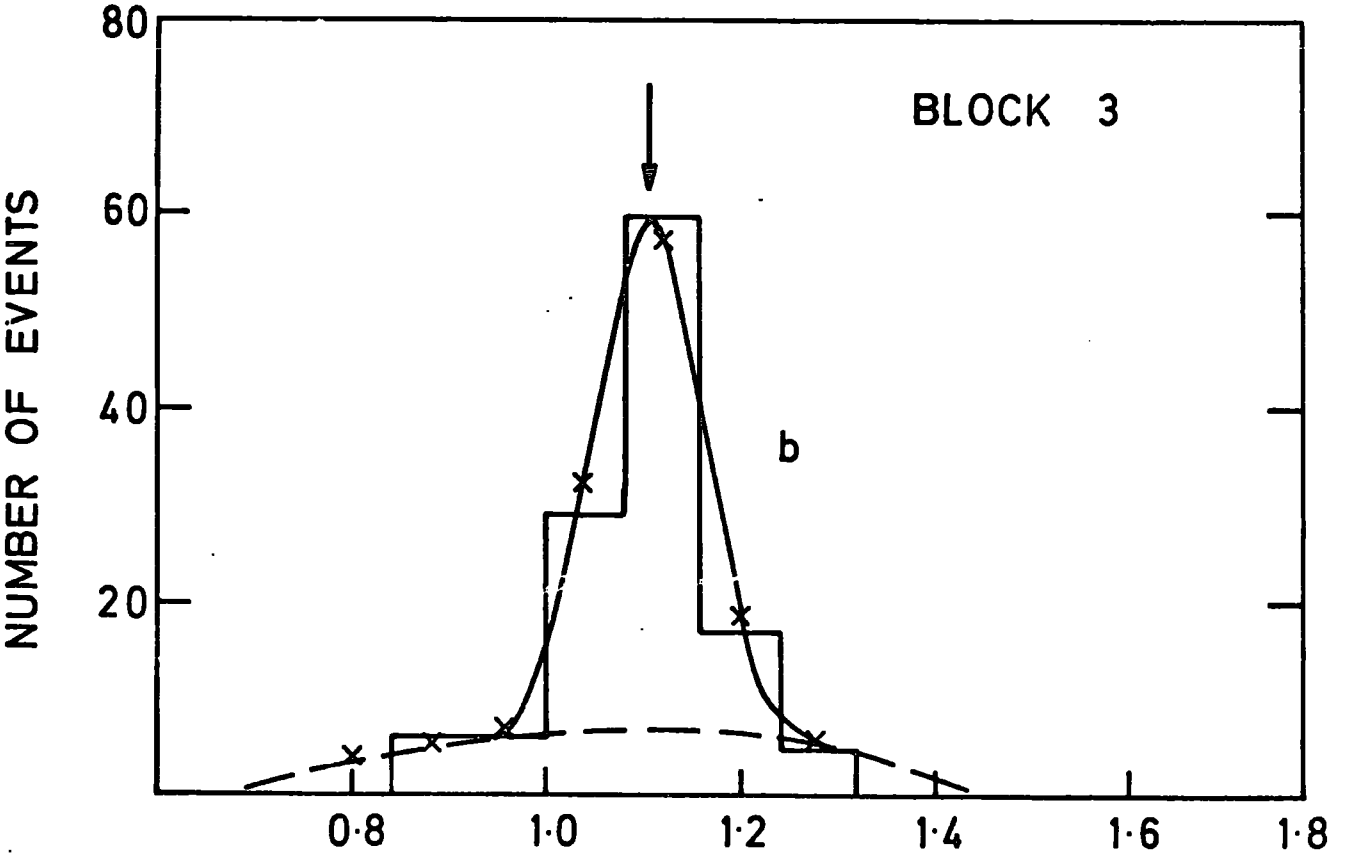

FIG. (4.4) Range of positive muons (cm)

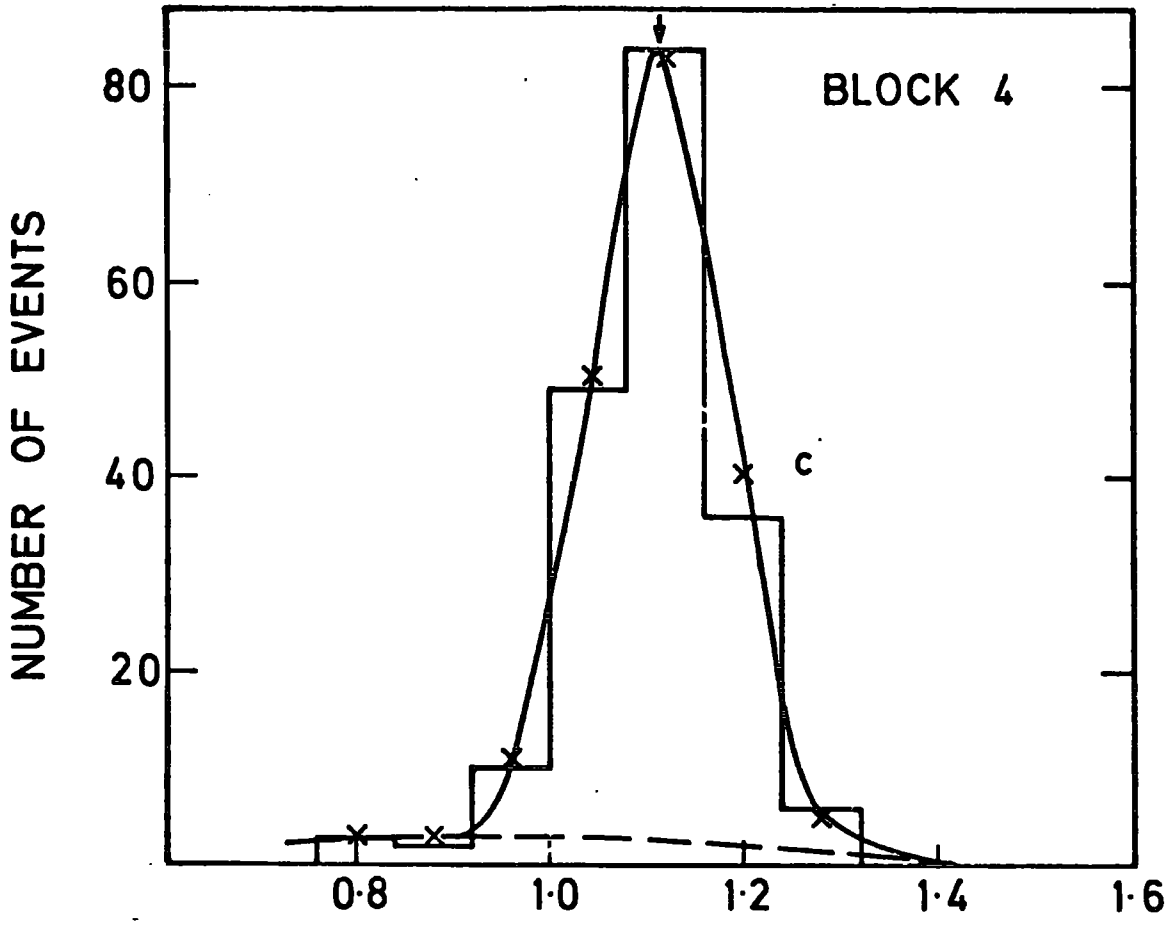

FIG. (4.4) Range of positive muons (cm)

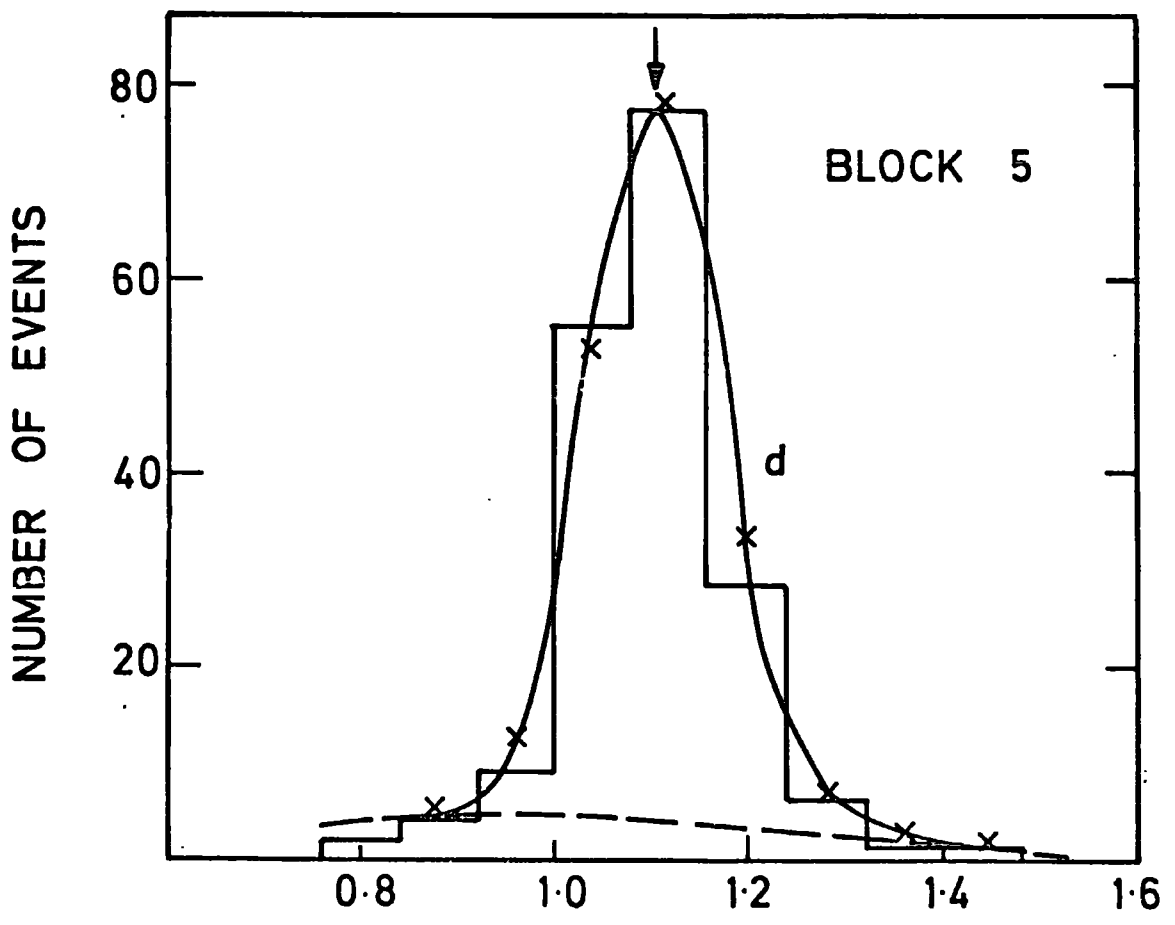

FIG. (4.4) Range of positive muons (cm)

BLOCK	2	3	4	5	2-5
RANGE(cm)	1·121	1·105	1·113	1 106	1·1101
ERROR	± 0.005	± 0·005	± 0.005	± 0·005	± 0.003
NO OF EVENTS	164	123	190	183	660

TABLE (4·7) AVERAGE RANGES OF THE MUONS IN DIFFERENT BLOCKS

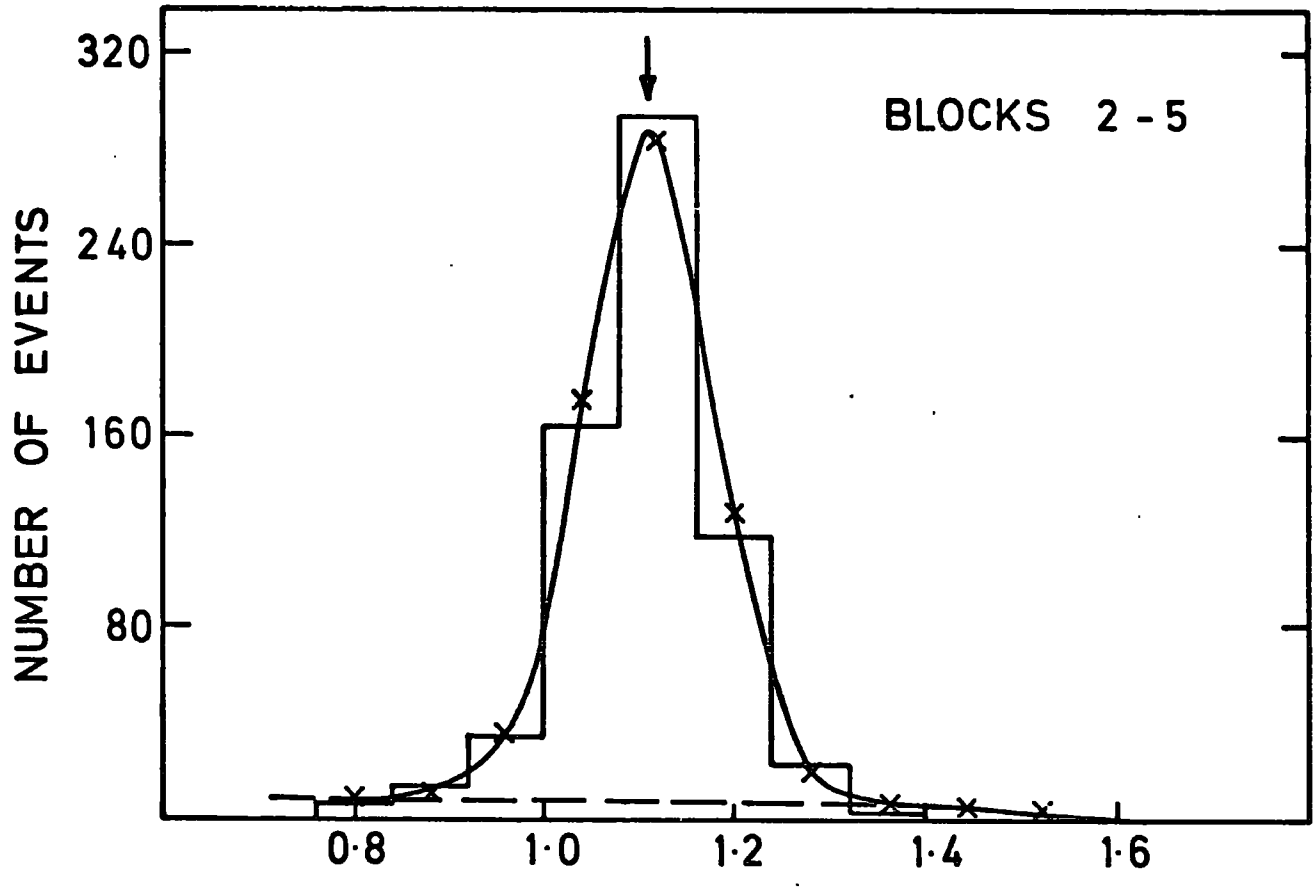

FIG. (4.5) Range of positive muons (cm)

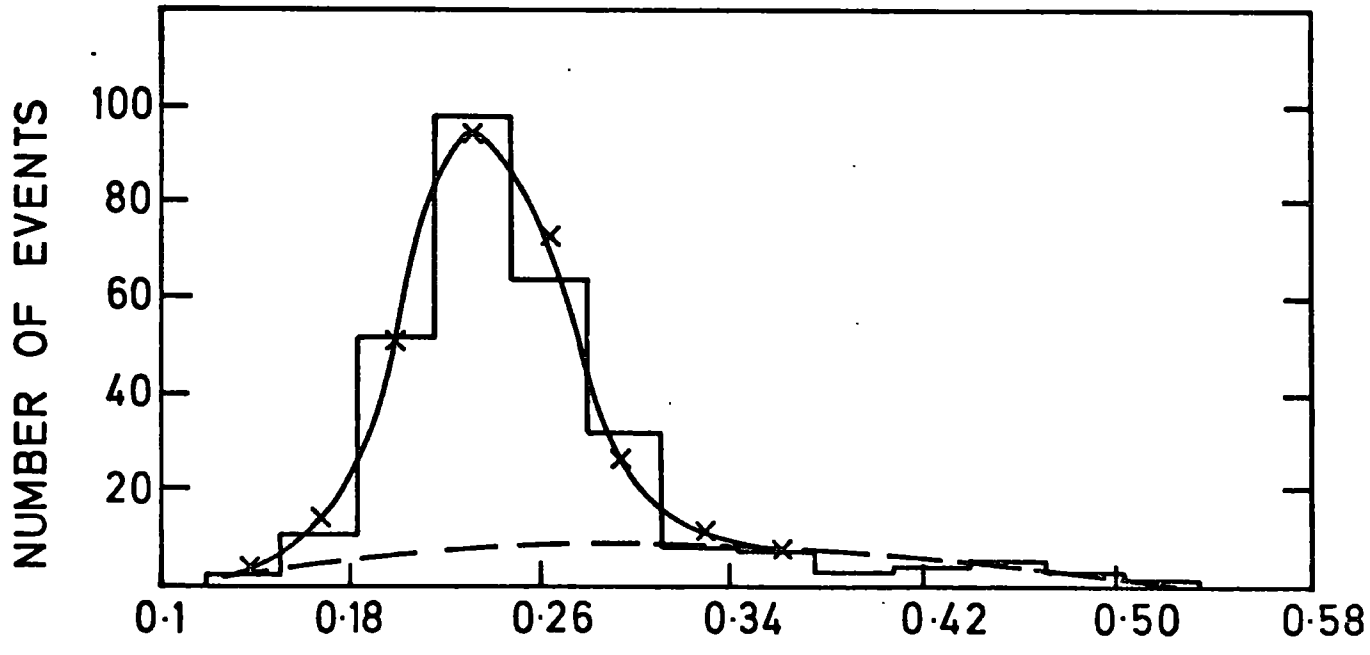

FIG. (4.6) Range of positive muons (cm)

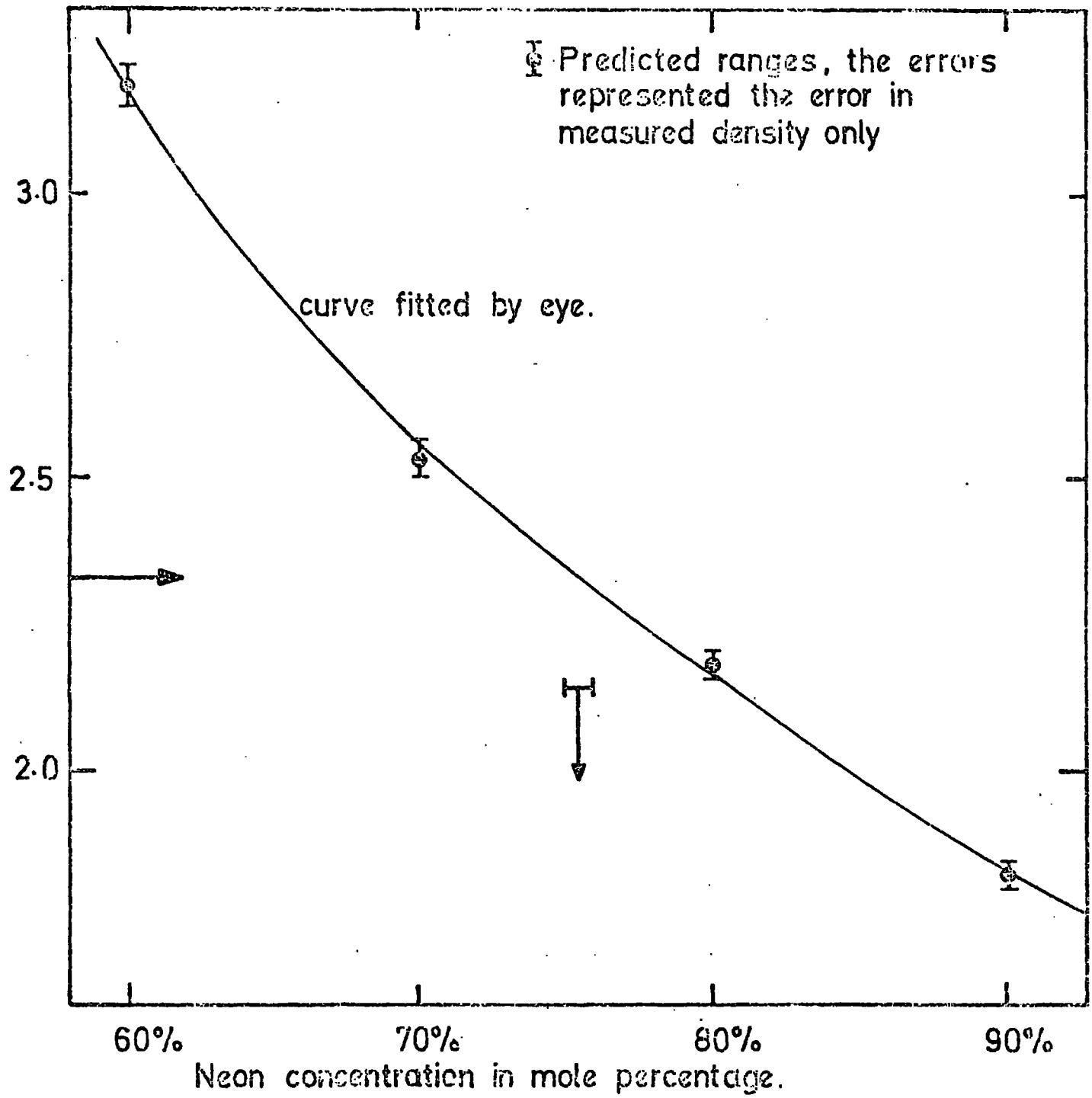
Predicted ranges, the errors represented the error in measured density only
curve fitted by eye.
3.0
2.5
2.0
μ in mm.
60%
70%
80%
90%
Neon concentration in mole percentage.

FIG. (4.7)

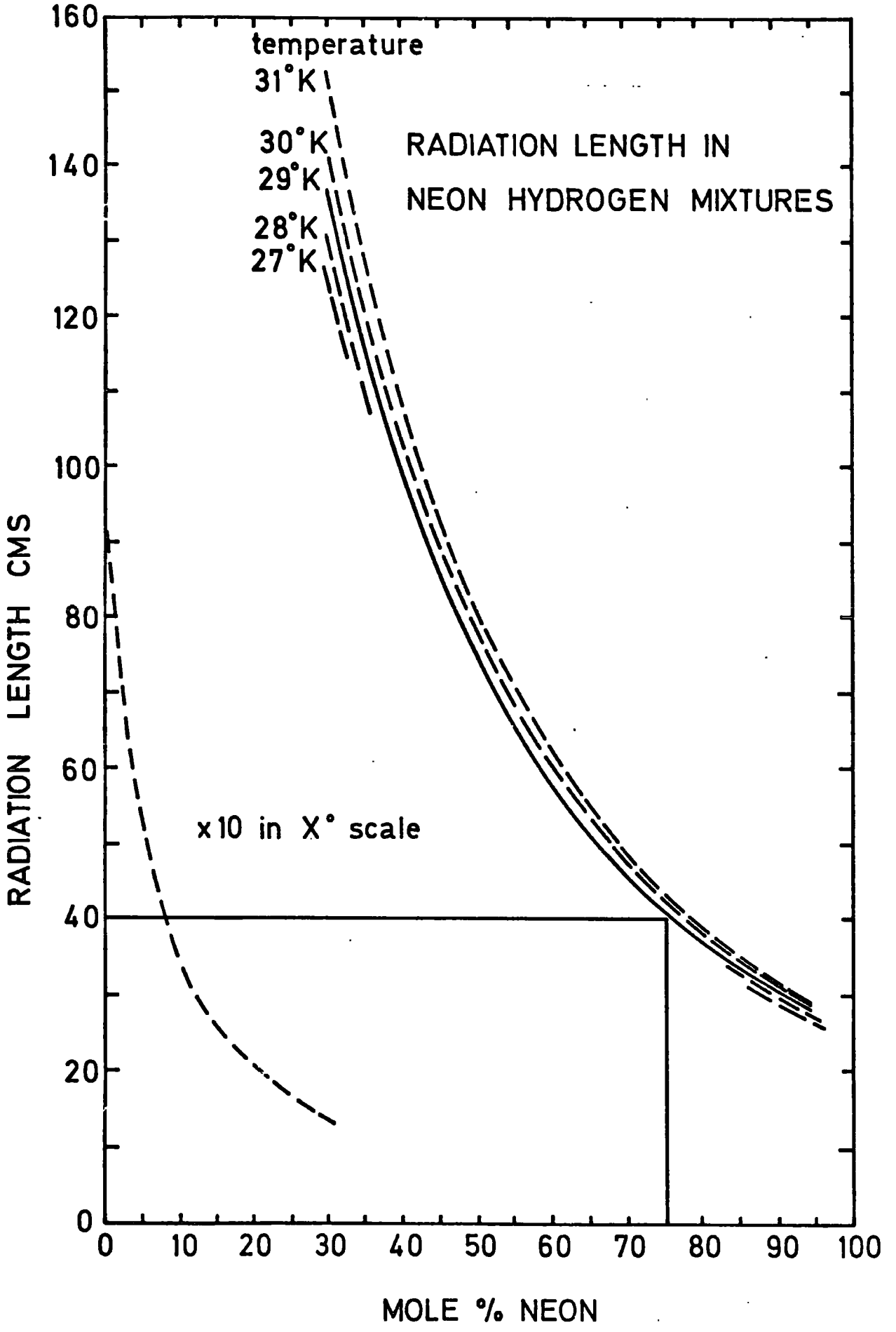

FIG. (4.8) Radiation length X° in neon-hydrogen mixtures.

CHAPTER V

BASIC INFORMATION TO DETERMINE CROSS-SECTIONS - TRACK LENGTHS AND CORRECTIONS FOR LOSSES

5.1 Introduction

In hydrogen bubble chambers the determination of a cross-section, σ , follows from the experimental determination of the interaction length λ , according to

$$\sigma = 1/(N\lambda) \tag{5.1}$$

where N, the number of target nuclei per cm^3, is the product of the density, ρ , and Avogadro's number, N_o.

Hence

$$\sigma = 1/(\rho\, N_o\, \lambda) \tag{5.2}$$

The determination of the density of hydrogen in the T.S.T. has been discussed in the previous chapter. The mean free path is determined from the total length of the primary tracks, ℓ , (to their interactions or their escape from the fiducial volume) and the total number of strong interactions, N_i, that is

$$\sigma = N_i/(\ell\, N_o\, \rho\,) \tag{5.3}$$

In this experiment the cross-section is to be determined as a function of momentum.

The number of strong interactions is subject to scanning losses and various geometrical biases, some of which are introduced by the

shallow nature of the T.S.T. These are discussed later. The total length of the primary tracks in a given momentum interval is not a simple quantity to determine in this experiment. The beam is quite heavily contaminated as discussed in Chapter 4. At the low momenta of the experiment the contamination is recognized by the difference in ionisation between the signal of negative kaons and the background of pions, muons, and electrons. On average the total contamination amounts to about 25%. However the fact that this is a formation experiment requires the measurement of the contamination as a function of momentum. This is much more difficult and it really rules out the estimation of contamination directly as described above. It implies measurement of tracks to determine momentum and this requirement leads to the way in which the amount of kaon track in the contaminated beam is determined and that is by identifying the tau-mode of decay of the kaons.

In this chapter the determination of the primary track length per momentum interval is discussed. This is followed by an account of the corrections to the numbers of events that have to be made in case of the charged sigma hyperons and the elastic scattering channels.

5.2 Primary Track Length using the Tau-mesons

The negative kaon decays in a variety of ways with a mean lifetime of 1.237×10^{-8} sec. One mode, the tau-mode of decay into three charged pions, is seen with high scanning efficiency and is recognized unambiguously. By determining the number of these in each momentum interval and knowing the branching fraction by this mode of decay, $\sim$ 5% (1.20), the total amount of kaon path length in each momentum interval can be determined. The two-body $K^- \rightarrow \pi^- + \pi^o$ where the π^o-meson decays into a gamma ray and a Dalitz pair can simulate the tau-mode. However

at these low momenta, the difference in ionisation between electrons (positrons) and the pions is very clear. Consequently most events of this kind which would form a spurious background are rejected at scanning time. The candidates for tau-decay were measured (including any doubtful $\pi^- e^+ e^-$ events) and fitted to the possible hypotheses. The tau events were accepted after Judging was carried out as described in Chapter 3, Section 3.8. The total number of events which were not measurable (due to bad geometry, poor visibility and so on) and events which failed the fitting procedures after a total of two measurements were all carefully recorded. After measurement the coordinates of the event at the decay vertex and the fitted values (ϕ , $\tan\lambda$, $1/p$) at the centre of the primary K^--meson track were used to determine the track length as a function of primary momentum as follows. Firstly by propagating the primary K^--meson track in the backward direction and then in the forward direction the corresponding values of ϕ , $\tan\lambda$, and $1/p$ could be determined at the entrance to the fiducial volume and the length to decay and the potential length to the exit from the volume found. In this the energy loss and curvature of the tracks were properly taken into account.

Knowing the momentum at the entrance of the fiducial volume and the potential length in hydrogen for each of the primary K^--meson tracks of the tau-decays, the contribution to the total track length expected from all kaons in each momentum interval was calculated. Energy loss was allowed for via the range momentum table and small attenuation by decay and strong interaction were taken into account. This track length was weighted in various ways. The most important of these is to allow for the momentum dependent probability of the decay of the kaon by the tau-mode on an event by event basis. Others include corrections for the scan efficiency, the unmeasurable events, and the events which failed to pass

the programs of GEOMETRY and KINEMATICS. These latter corrections are applied to the overall distribution of the track lengths. The details of the calculation follows.

At the entrance of the fiducial volume there is a number spectrum of $\bar{K}$-mesons with ingoing momenta, P and P + ΔP, and potential path lengths between L and L + ΔL is given by

$$N(L,P)\ \Delta L\ \Delta P \tag{5.4}$$

As these particles pass down the chamber, they lose energy and

(a) leave the fiducial volume

(b) undergo decay and recorded if the mode of decay is that of the tau-meson.

(c) undergo strong interaction and are recorded if they are observed.

At a distance $\ell < L$ along the kaon track the momentum is reduced to $p < P$ where

$$P = a\ R^{b} \tag{5.5}$$

and

$$p = a(R-\ell)^{b} = a\ R^{b}\ (1-\frac{\ell}{R})^{b} = P\ (1-\frac{\ell}{R})^{b} \tag{5.6}$$

Here a and b are known constants and R is the potential range of a kaon from the entrance to the fiducial volume.

If the spectrum N(L,P) is known then the path length in given momentum bins can be computed by propagating down each kaon track (allowing for decay and interaction) and dividing the track into lengths corresponding to the required momentum intervals. By adding the lengths together the total path length in each momentum bin is determined. The bins used are 20 MeV/C wide; any one kaon contributes to 2 or 3 momentum bins. Since the cross-sections are to be determined, in principle it is not possible

to allow for the alteration due to strong interaction. However since the alteration is only of the order of 5%, then approximate cross-sections are sufficient (see Appendix A).

The spectrum N(L,P) is determined from the measured tau-decays. When their measured momenta and lengths are propagated backwards along the kaon tracks they give an entrance spectrum $T(L,P)\Delta L\Delta P$ which is related to the required $N(L,P)\ \Delta L\ \Delta P$ through the probability of decay of the kaon by the tau-mode.

To find the relationship between T(L,P) and N(L,P) a kaon track of potential length L, and momentum P is considered. At distance ℓ along the track the momentum is $p = P(1 - \ell/R)^b$ and so its decay length at the point of decay is

$$\lambda_d = \gamma\beta c\tau = p c\tau / M_{K^-} \qquad (5.7)$$

where τ is the mean life-time of the K^--meson and M_{K^-} is its mass.

Hence the probability of decay along the track of potential length L is

$$\int_o^L \frac{d\ell}{\lambda_d} = \int_o^L \frac{M_{K^-}\, d\ell}{c\tau p} = \frac{M_{K^-} R}{P c\tau (1-b)} \left\{ 1 - \left(1 - \frac{L}{R}\right)^{1-b} \right\} \qquad (5.8)$$

The reciprocal of this is the weighting factor for the track decay. Recalling that the branching ratio for tau-decay, f, is 0.0559, then the weighting factor, W, is

$$W = \frac{c\tau (1-b) P}{f M_{K^-} R} \quad \frac{1}{1 - (1 - \frac{L}{R})^{1-b}} \qquad (5.9)$$

Hence

$$N(L,P) = W T(L,P) \qquad (5.10)$$

After determining N(L,P) the track length distribution in momentum bins is calculated as described above.

Although the account of weighting above is given analytically using a range-energy relation in practice this was done numerically using the range-energy table.

The drawback of this method is the lack of statistics arising from the low value of the branching ratio by the tau-decay mode. This is seen from the comparison of the interaction and decay lengths. Approximately the mean free path for strong interaction in cm is

$$\lambda_i \sim 780\ P \quad (P \text{ in GeV/C})$$

and the decay length in cm is given exactly by

$$\lambda_d = 751\ P\ .$$

So it is seen that the total number of kaon decays is almost equal to the number of strong interactions. But only 5% of the total decays will be through the tau-decay mode and even allowing for the unseen modes of strong interactions (taking place through neutral modes), the number of tau decays will be less than about 1/10 of the strong interactions. However for the individual partial cross-sections the number of tau decays is nearly equal to the number of strong interactions. Consequently the precision of the results depends on the number of the tau decays.

From the track length which is calculated by the above described method, the number of kaon interactions per millibarn is calculated in 20 MeV/C momentum intervals of the primary K^--meson and this is given in Figure 5.1.

When statistics are low the above method leads to a smoothing out of the effects of fluctuations in the number of tau-decays.

Another method of evaluating the number of events per millibarn is described (1.22) . This is a more direct method and it relies only on the number of tau-decays, N_τ, in a momentum interval ΔP_{K^-}. Then the

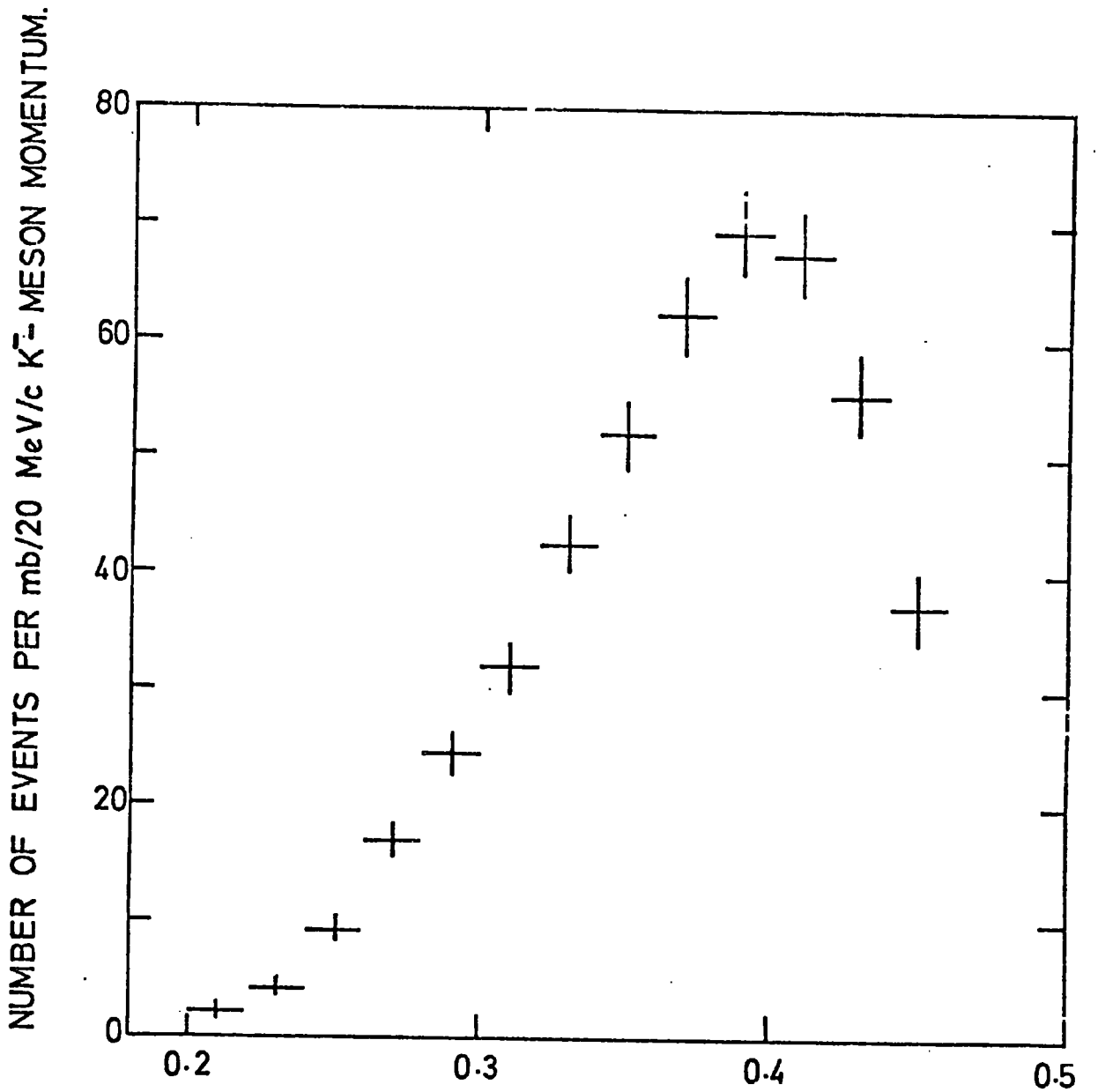

FIG 5·1 PRIMARY TRACK LENGTH [(eV/mb) / 20 MeV/c K^- MOMENTUM]

track length, $TL(P_{K^-}, \Delta P_{K^-})$ is given by

$$TL = (N_\tau \, c \, \tau \, P_{K^-}) / f \, M_{K^-} \tag{5.11}$$

From this track length the number of events per millibarn, eV/mb, is given by

$$eV/mb = TL \times n \tag{5.12}$$

where n is the number of protons per cm^3. Hence

$$eV/mb = (n N_\tau \, c \, \tau \, P_{K^-}) / f \, M_{K^-} \tag{5.13}$$

The number of events per millibarn calculated by this and the previous method are given in Table 5.1 as a function of the primary momentum. At high momenta of primaries and high statistics the two methods should give the same result. On the whole the agreement is satisfactory. The results of the first method are used.

Primary momentum in MeV/C	No. of events per millibarn using the first method	No. of events per millibarn using the direct method
200 - 220	2.3	3.3
220 - 240	4.3	4.3
240 - 260	9.3	9.3
260 - 280	17.0	18.3
280 - 300	24.5	26.4
300 - 320	30.3	28.1
320 - 340	42.6	43.5
340 - 360	52.0	52.2
360 - 380	62.5	61.9
380 - 400	69.5	67.3
400 - 420	67.7	67.4
420 - 440	55.5	49.5
440 - 460	37.3	34.1

Table 5.1: Primary track length in eV/mb using the above described two methods as a function of the primary momentum

Having calculated the number of events per millibarn the cross-section for any particular interaction, σ_i^j, is given by

$$\sigma_i^j = N_i^j / (\text{eV/mb}) =$$

$$\frac{\text{corrected number of interactions}}{\text{number of events per millibarn}} \qquad (5.14)$$

where N_i^j is the number of interactions of type j corrected for losses.

It has been mentioned that the fitted values at the centre of the primary K^--meson track of the tau decay were used to determine the track length and hence the number of events per millibarn. This is true for the track-length determination for the elastic scatterings, and the number of events per millibarn for this channel is given later in Figure 5.14. Meanwhile in the case of the charged sigma hyperons the geometry values (measured values) were used to give Figure 5.1. This is justified from the examination of the pull quantities $P_i(x)$ which are defined by

$$P_i(x) = (x^f - x^m) \qquad (5.15)$$

where x^f and x^m are the fitted and measured values of the variable.

The pull quantities should have each a mean value of zero. The pull on 1/p, where P is the momentum of the primary track is shown in Figure 5.2a to c for the cases of tau-decay events, elastic scattering events, and the charged sigma hyperon events respectively. The mean values of the pulls for the three cases are consistent with zero. These are given below, together with their standard deviations in Table 5.2.

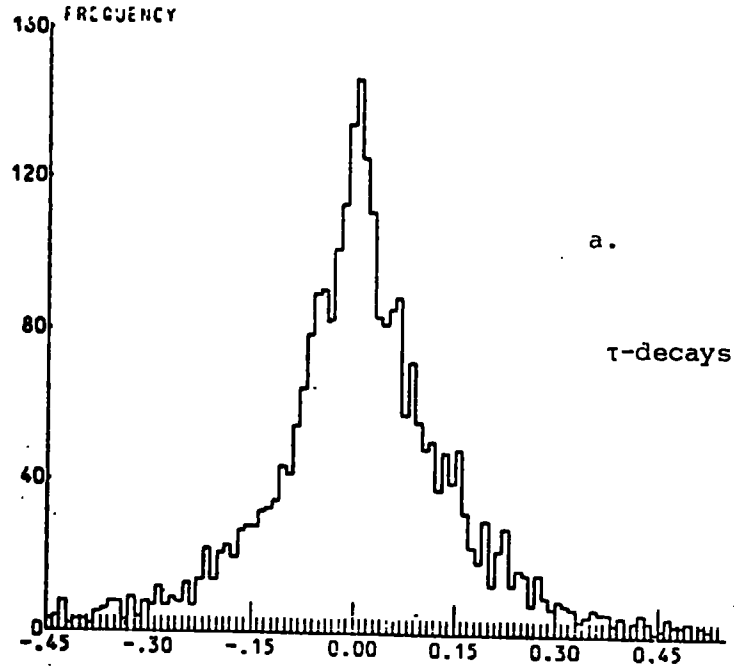

a.

τ-decays

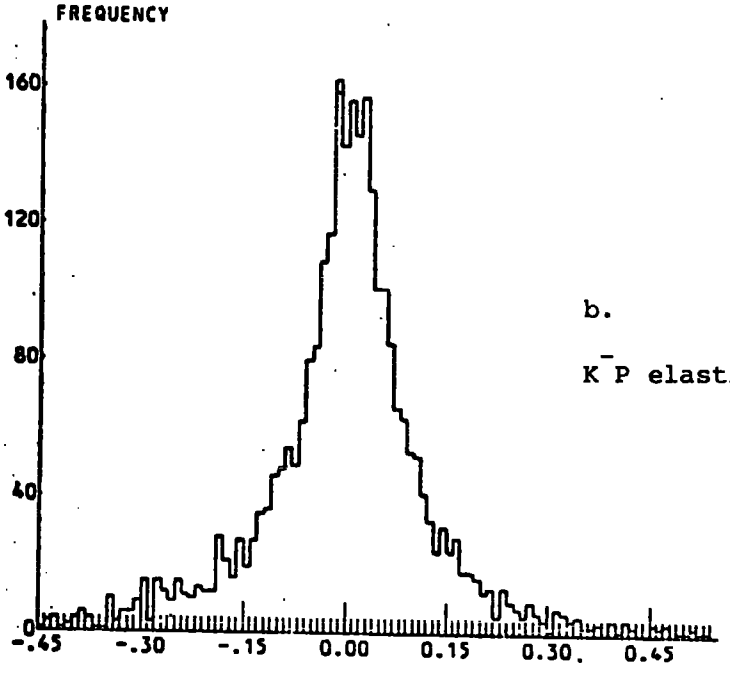

b.

$K^- P$ elastic scatterings

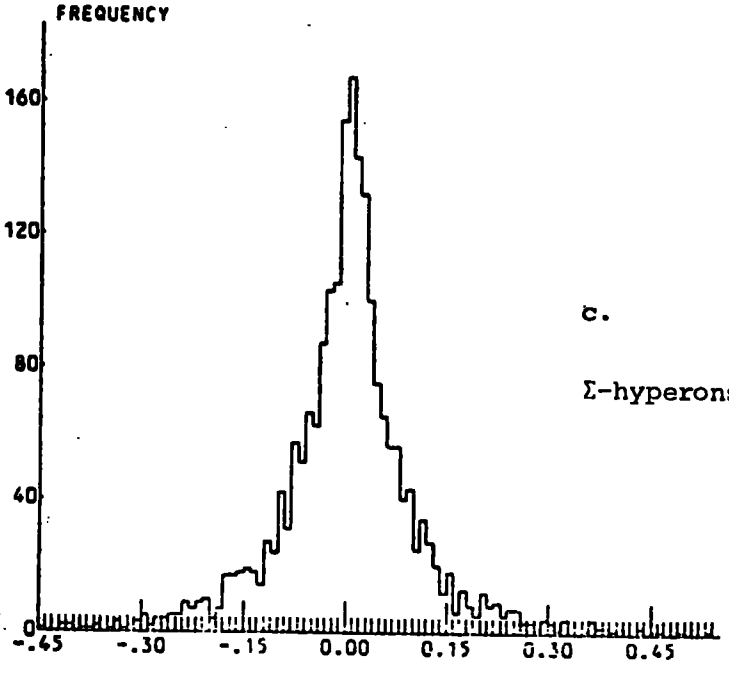

c.

Σ-hyperons

Figure 5.2:

Pull distribution on the primary for the quantity $(1/_p)$

Pull on the primary for $1/p$

Type	Mean	Standard Deviation
Tau-decay	+0.0084	0.20
Elastic Scattering	-0.0034	0.20
Sigma-Hyperon	-0.0007	0.11

Table 5.2: Statistical summary of the pull distribution for $^1/_p$ of the primary to the channels under consideration.

It is clearly seen that the pull on the primary of tau-decays is similar to that of the elastic scattering which suggests that the 4C-fit in these two cases has exactly the same constraining effect. However the pull distribution for the primary of the charged sigma hyperon events is narrower implying that this 4C-fit is less stringent.

This means that the fitted momenta of the primaries in K^-P elastic scattering are very close to fitted values of primaries to tau decays. However the fitted values of momenta for the primaries to Σ-hyperon production events are midway between the geometry values and the fitted values of the tau decay momenta. As a result of these comparison, for K^-P elastic scattering the track length as a function of fitted momentum is used (i.e. using Kinematic Values), whereas for Σ-hyperon production the distribution for unfitted momentum is used (i.e. Geometry Values). In each case the signal and tau-decay reference are subject to similar errors and these tend to cancel.

5.3 Experimental Biases in Σ^+-Hyperon Production and Decay

The reaction producing Σ^+-hyperon at the energies of the experiment is

$$K^- + P \rightarrow \pi^- + \Sigma^+$$

followed by the decay modes

$$\Sigma^+ \rightarrow \pi^0 + P \qquad (\Sigma^+_p)$$

$$\Sigma^+ \rightarrow \pi^+ + n \qquad (\Sigma^+_\pi)$$

The reaction $K^- + P \rightarrow \pi^- + \pi^0 + \Sigma^+$ has a cross-section which is negligible in the region of this experiment.

Before the determination of the cross-section for any channel, the number of observed events has to be corrected for losses. In the case of positive sigma hyperon, the events were treated separately on an event by event basis and selection criteria were imposed to exclude events which are inefficiently seen. This is an important operation for the evaluation of the cross-section for any channel and this must be fully understood so that corrections are estimated properly. But before going into the discussion of the losses it will be illuminating to consider the kinematics of production of the process $K^- + P \rightarrow \pi^- + \Sigma^+$ which are shown in Figures 5.3a to d for three different momenta of the primary K^--meson (202, 302, and 465 MeV/C) (5.1). The quantities involved in these figures are

(i) $\cos \theta^*_{PROD}$, the cosine of the angle between the primary direction and the Σ^+-hyperon direction in the K^-P centre of mass frame.

(ii) θ_{LAB} is the angle between the primary direction and the Σ^+-hyperon direction in the laboratory frame of reference.

(iii) $\left(P_{\Sigma+}\right)_{LAB}$ is the momentum of the Σ^+-hyperon in the laboratory system.

(iv) λ_{DEC} is the mean decay length for the Σ^+-hyperon after it is produced in the laboratory.

(v) D_s is the distance the production vertex has to be from the interface of the T.S.T. walls in order to allow for the decay of the Σ^+-hyperon within one life-time (i.e. $D_s = \lambda_{DEC} \sin\theta_{LAB}$).

It can be seen from Figures 5.3 a, b and c that losses are expected. In the region of $\cos\theta^*_{PROD} \lesssim -0.9$ and $\cos\theta^*_{PROD} \gtrsim +0.8$ the laboratory angle between the primary direction and the Σ^+-hyperon direction is small and difficult to see. For the first limit above the Σ^+-hyperon momentum in the laboratory is so low that the hyperons will not leave a visible track. Losses in production may be examined from the distribution of the angle ϕ_p defined as

$$\phi_p = \cos^{-1} \left| \frac{\hat{Z} \times \hat{K}}{|\hat{Z} \times \hat{K}|} \cdot \frac{\hat{K} \times \hat{\Sigma}}{|\hat{K} \times \hat{\Sigma}|} \right| \qquad (5.16)$$

Losses in decay are manifest in the distribution of the angle ϕ_D defined as

$$\phi_D = \cos^{-1} \left| \frac{\hat{Z} \times \hat{\Sigma}}{|\hat{Z} \times \hat{\Sigma}|} \cdot \frac{\hat{\Sigma} \times \hat{D}}{|\hat{\Sigma} \times \hat{D}|} \right| \qquad (5.17)$$

where $\hat{Z}$ is a unit vector normal to the front glass, $\hat{K}$ is the direction of the incident K^--meson, $\hat{\Sigma}$ is the direction of the Σ^+-hyperon, and $\hat{D}$ is the direction of the charged decay particle from the Σ^+-hyperon. As they are defined ϕ_P and ϕ_D are the angles between the normal to the production or decay planes respectively of the Σ^+-hyperon and a direction in the X Y plane of the chamber. Obviously there is no relation between the geometry of the production or decay and the geometry of the chamber and so the distributions of ϕ_P and ϕ_D should be isotropic. Zero values of ϕ occur

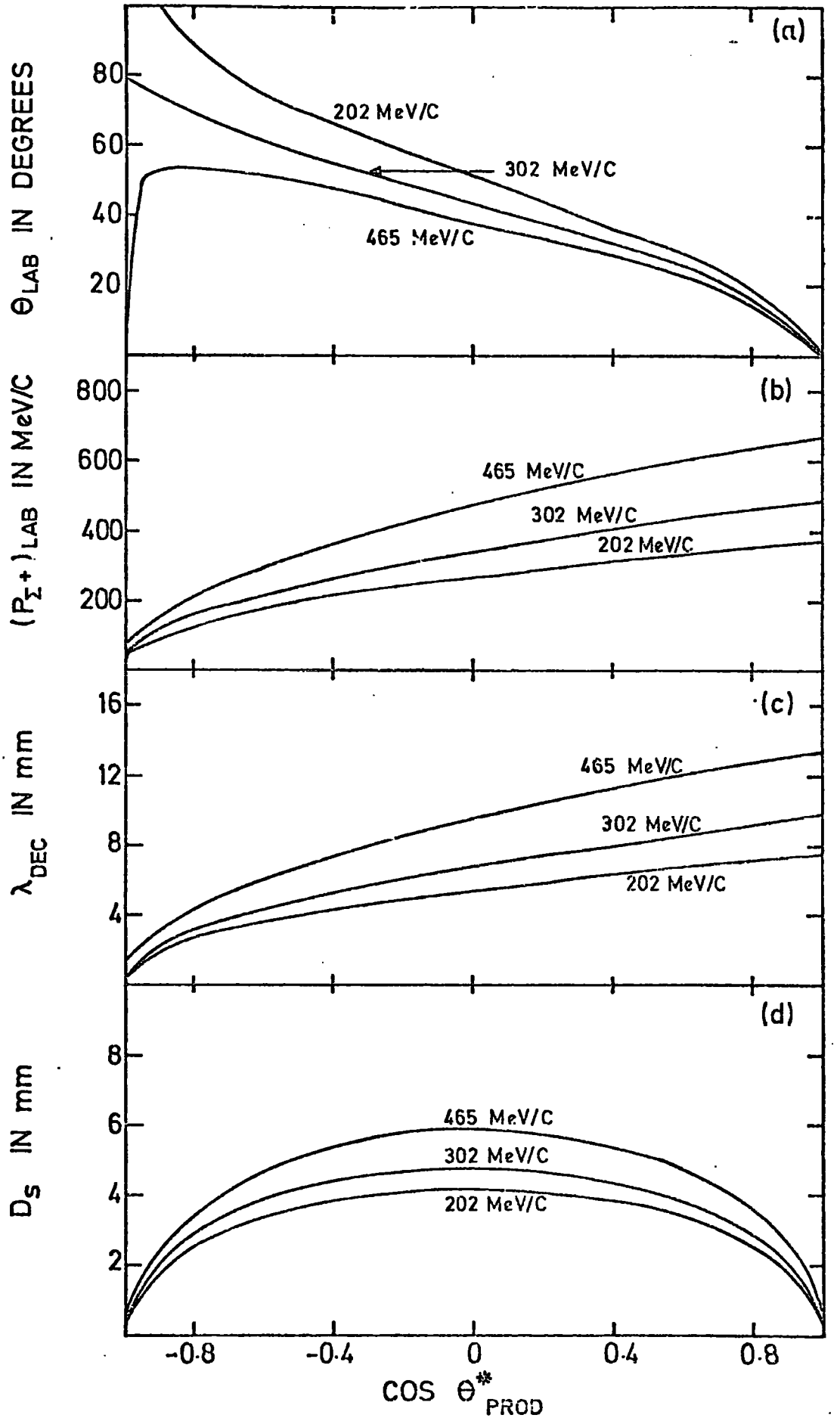

FIG. 5.3 KINEMATICS OF THE REACTION $K^- P \longrightarrow \pi^- \Sigma^+$

when the normal to the production plane or the decay plane lie in the XY plane of the chamber. Such events have poor geometry and are expected to be lost.

Small angles of decay will be difficult to detect and this will be reflected in the angular distribution of the charged decay particle in the rest frame of the parent Σ^+-hyperon particle. As this distribution should be isotropic losses should be easily detected and corrected.

From Figure 5.3d, the value of D_s varies with the primary momentum from about 4.0 mm at 200 MeV/C to 5.8 mm at 465 MeV/C. Losses due to the shallowness of the chamber, if there are any, should be apparent in a comparison of ϕ_P (or ϕ_D) distribution for events near the chamber surfaces and for events far away. For Σ^+-hyperon production and decay the value of D_s for the higher momentum (465 MeV/C) was used to divide the depth of the hydrogen region into three slices as shown in Figure 5.4. The depths of regions I and III are each equivalent to two life-times and this demanded that the proper time of flight of the Σ^+-hyperon to be within two life-times for the events selected in these two regions.

In order to have high acceptance of the events produced in these three regions, events in region II were all accepted if their proper time of flight from the production vertex to the decay vertex met the requirement mentioned above. Meanwhile events in regions I and III were accepted if the direction of the produced Σ^+-hyperon is away from the perspex walls (to avoid the complications of disappearing in these walls). Also the above selection on the proper time of flight was imposed. Consequently in region II the full cone of production should be seen and in regions I and III either the lower or higher half cone of production respectively is seen.

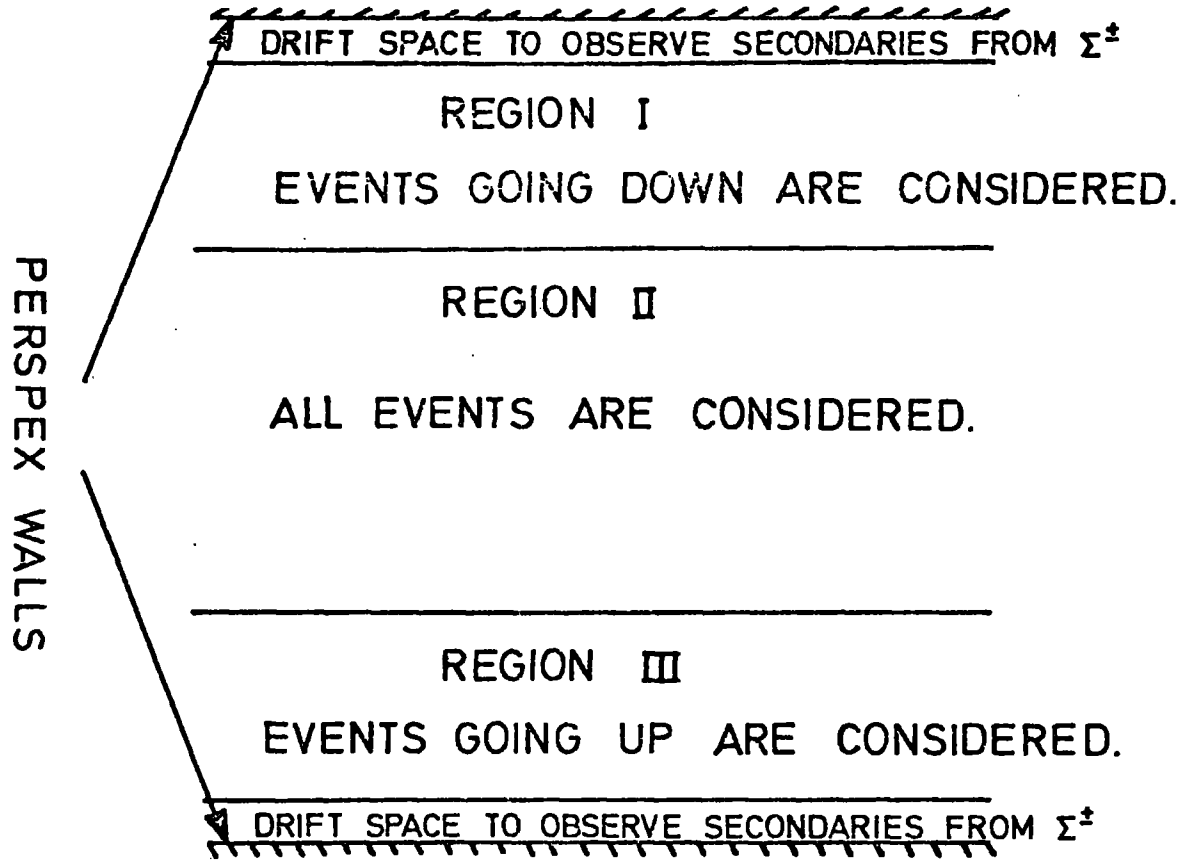

FIG.5.4: THE DEPTH OF THE HYDROGEN REGION OF THE T.S.T DIVIDED INTO THREE REGIONS AS EXPLAINED IN THE TEXT.

Examination of the above mentioned distributions (ϕ_P, ϕ_D, and $\cos \theta^*_D$) were tried using all the data available without dividing the depth of the hydrogen chamber of the T.S.T., these distributions are given in Figures 5.5, 5.6 and 5.7 for the two decay modes of the Σ^+-hyperon. Losses at ϕ angles up to about 20^o are apparent. If the shallow chamber has any effect, then by dividing it into regions where the full cone of production is ensured to be seen then the same distributions should show better behaviour than the corresponding previous ones. These distributions are given on the same figures for the two decay modes of the Σ^+-hyperon in region II.

Comparing the two sets of distributions shows that they are behaving in the same way and hence it is concluded that the shallow chamber has nearly no effect on the observation of the Σ^+-hyperon events. This is expected since the distance D_s needed to observe the full cone in this case to within two life-times is less than 1.2 cm (taking the value corresponding to 465 MeV/C primary momentum), unlike the Λ^o-hyperon events where the distance needed to observe the full cone of production within one life-time is 2.56 cms at 500 MeV/C primary momentum (3.1). The small value of D_s in the case of Σ^+-hyperon is a reflection of the short mean life-time of the Σ^+-hyperon.

Consequently in the case of the Σ^+-hyperon events, losses are due to visibility effects only (and not the shallow chamber) and these will be discussed in the next sections, but before this, in the following section, the definition of the fiducial volume is described.

5.3a Definition of the Fiducial Volume

The fiducial volume was finally defined for the events to be chosen for the analysis. Here two factors were considered. The fiducial volume

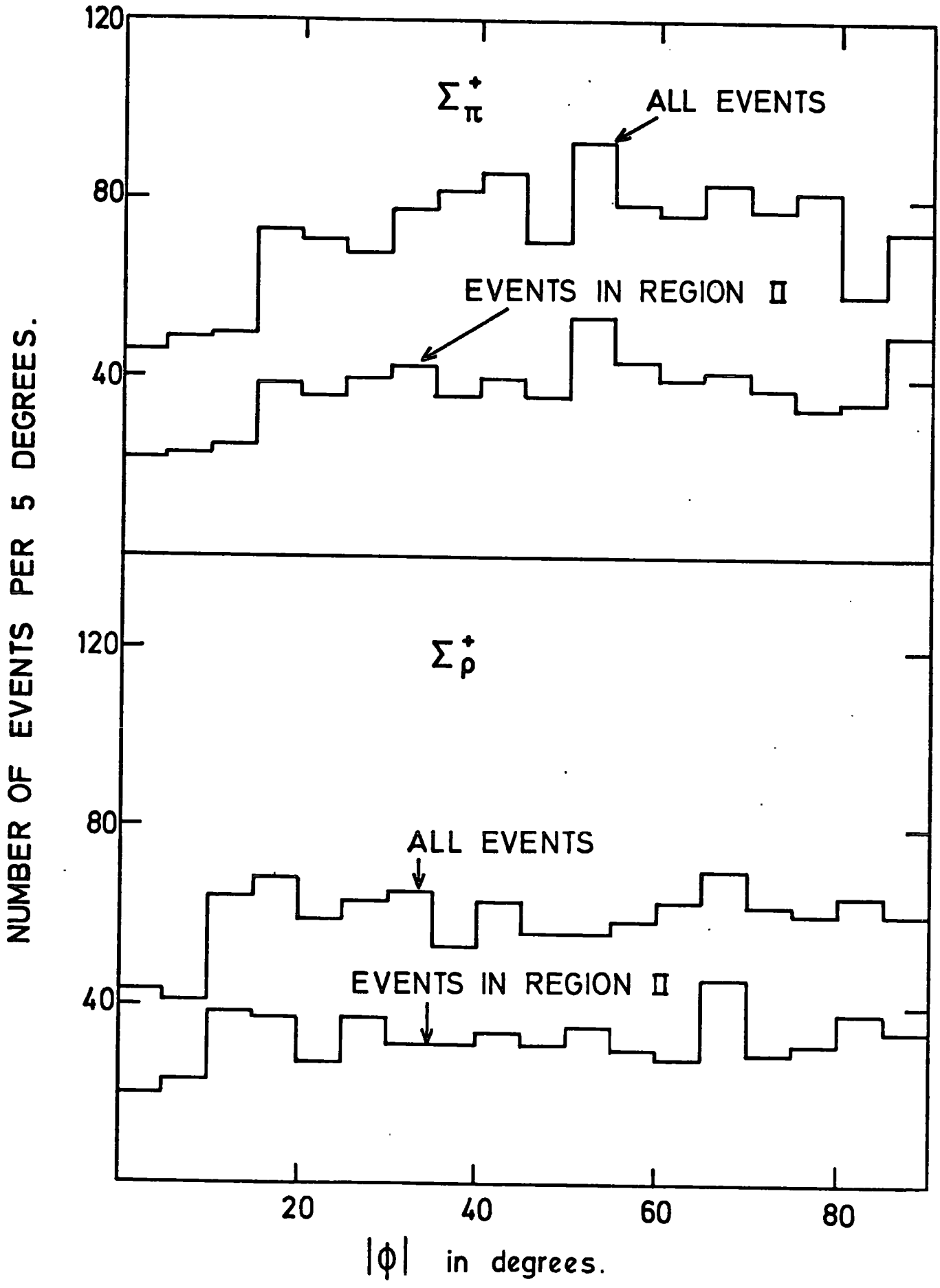

FIG. 5.5 THE DISTRIBUTION OF $|\phi_\rho|$ FOR THE TWO DECAY MODES OF THE $\Sigma^\pm$ HYPERON.

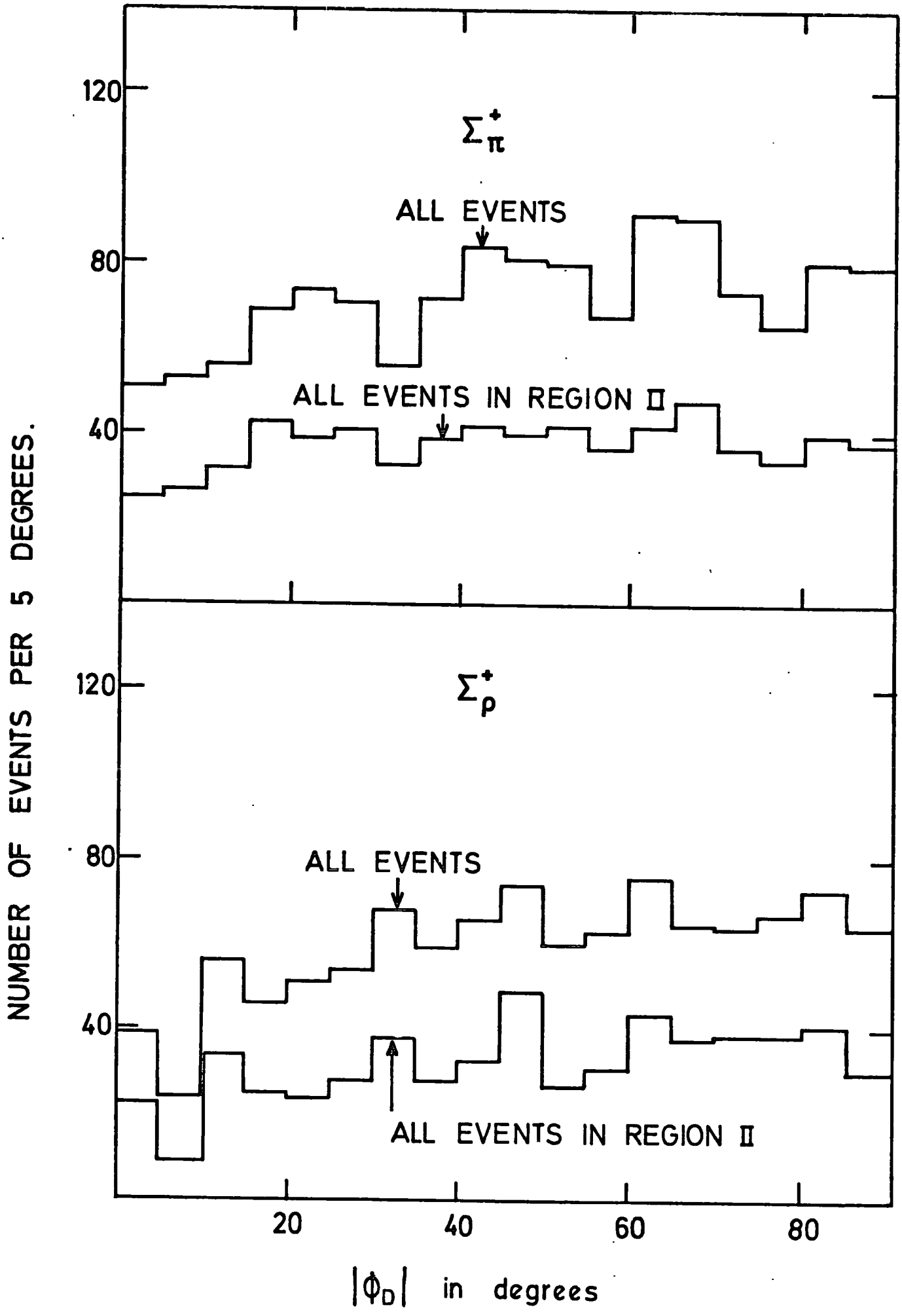

FIG. 5.6 THE DISTRIBUTION OF $|\phi_D|$ FOR THE TWO DECAY MODES OF THE $\Sigma^\pm$ HYPERON.

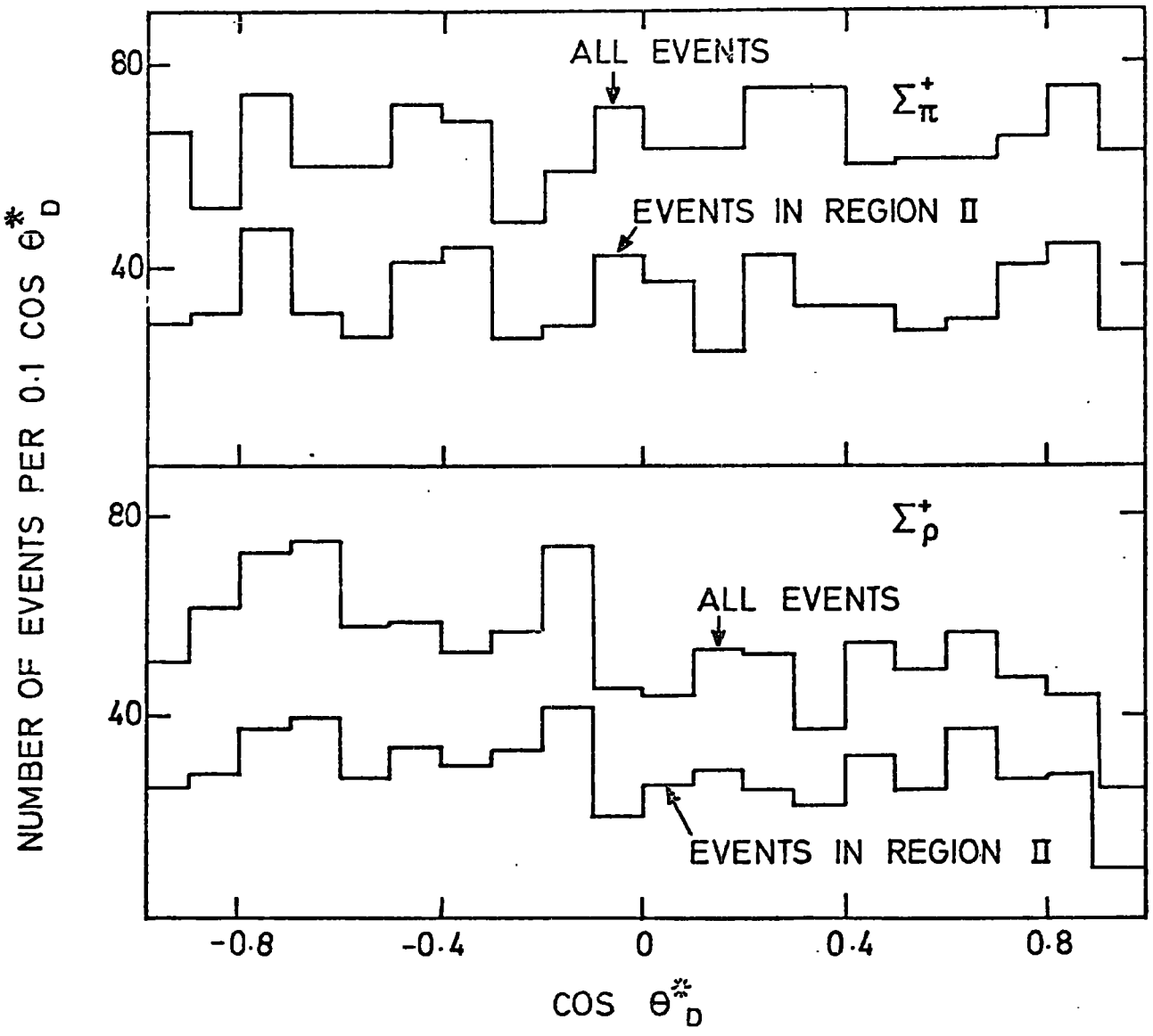

FIG. 5.7 THE DECAY ANGULAR DISTRIBUTIONS FOR THE TWO DECAY MODES OF THE $\Sigma^\pm$ HYPERON EVENTS.

must be chosen where the effects of the perspex walls are at a minimum. This is achieved by moving away from the perspex walls a sufficient distance. However the distance chosen should be such as not to reduce the numbers of events too much. To determine the distance the hydrogen T.S.T. region was divided into small slices each 2 mm deep from the perspex walls where a depth of 2 mm was always left so that the secondaries from the charged sigma hyperon would have sufficient length to be observed. For all the events in a 2 mm depth the average weight was determined to allow for the losses outside the T.S.T. of decaying Σ-hyperon. This weighting factor is plotted as a function of the distances of the 2 mm cells away from the perspex walls in Figure 5.8a and b for both charged sigma hyperons. After 2 mm (for Σ^+-hyperon production and decay) and 4 mm (for Σ^--hyperon) both weights are below 2 and quickly approach the value of 1.30 (Σ^+-hyperon) and 1.25 (Σ^--hyperon), this drift length for the Σ^--hyperon is a factor of 2 larger than that of Σ^+-hyperon which reflects the factor of 2 in their mean life-times.

It is clear that by allowing a depth of 4 mm away from the perspex walls the main effect of the walls is obviated. For normalisation purposes this was done for both $\Sigma^\pm$-hyperons in exactly the same way and the fiducial volume was defined 4 mm away from the interface of each of the perspex walls.

5.3.1 Life-time Correction

If the decay of the Σ^+-hyperon occurs either very close to the production vertex (so that the Σ^+-hyperon does not leave a visible track) or the decay occurs outside the fiducial volume (and the Σ^+-hyperon has probably decayed inside one of the perspex walls) then the interaction appears as a two-prong event and it will be classified with the ordinary

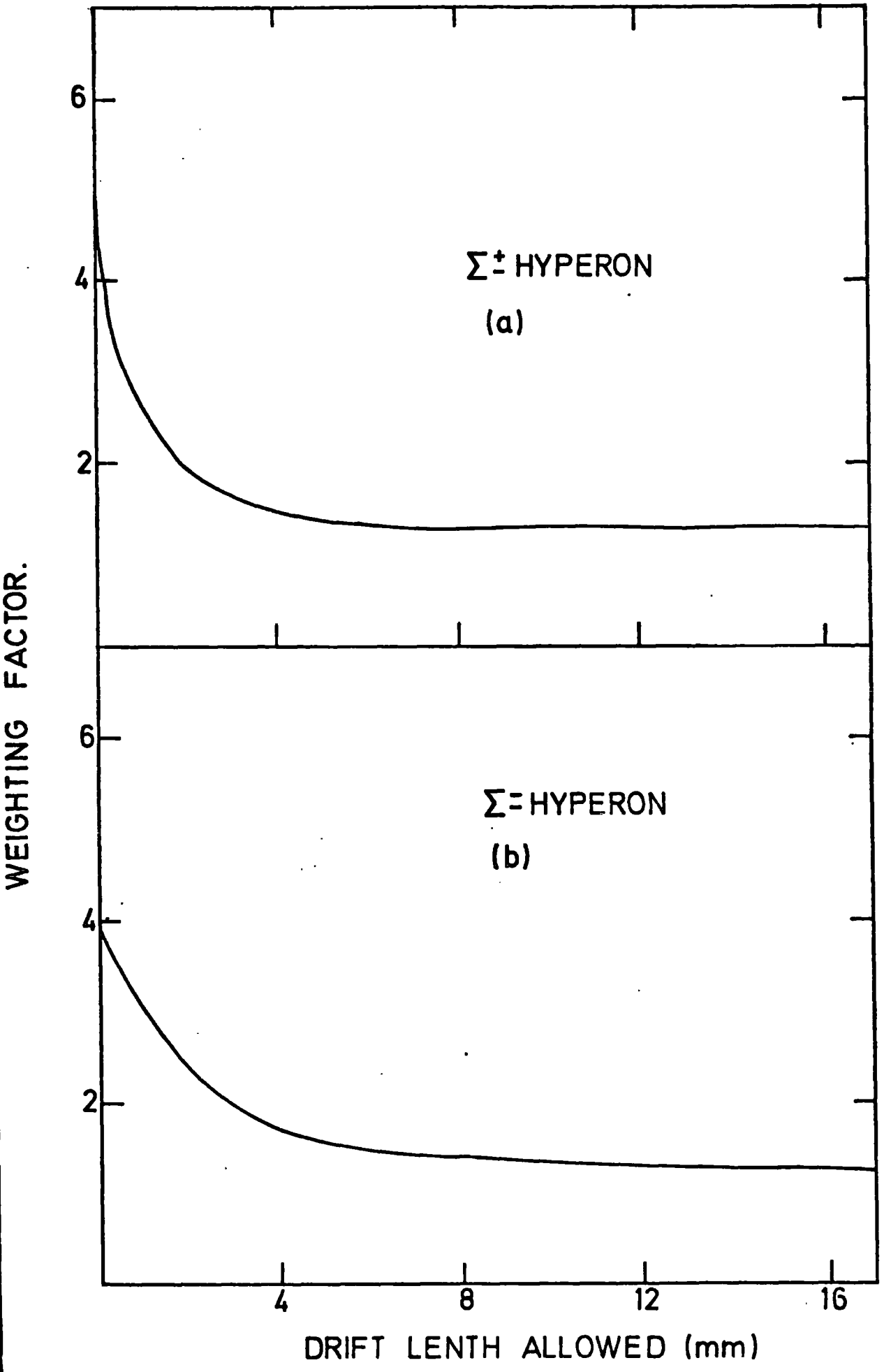

FIG. 5.8 WEIGHTING FACTOR AS A FUNCTION OF THE DRIFT LENGTH FROM THE PERSPEX WALL (Σ-HYPERONS SELECTED GOING TOWARDS THE PERSPEX WALL.)

two-prong events. Corrections can be made for these losses by imposing a minimum cut-off proper time and weighting each event according to

$$W = \left\{ \exp(-t_o/\tau_+) - \exp(-t_p/\tau_+) \right\}^{-1} \qquad (5.18)$$

where τ_+ is the mean life-time of the Σ^+-hyperon, t_o is the minimum cut-off proper time for the Σ^+-hyperon, and t_p is the potential proper time to leave the fiducial volume. If the Σ^+-hyperon comes to rest inside its potential length then t_p is set equal to a very large value. The energy loss suffered by the Σ^+-hyperon when traversing the hydrogen is taken into account in calculating the potential proper time. Figure 5.9a and b show the proper decay time distributions for the two decay modes of the Σ^+-hyperon (Σ^+_p and Σ^+_π) without any selection or corrections. The straight lines drawn on the distributions correspond to the value of the mean life-time of $\tau_+ = 0.80 \times 10^{-10}$ sec which is the world average for the Σ^+-hyperon (1.20). The lines were fitted to the distributions for the region $0.2 \times 10^{-10} \leqslant t \leqslant 2.0 \times 10^{-10}$ sec. It is clear from the distributions that the value of t_o, the minimum proper time, is 0.2×10^{-10} sec.

A weighting factor for both modes of decay of the Σ^+-hyperon combined was determined according to equation (5.18) using all the events with proper time of flight $t > 0.2 \times 10^{-10}$ sec. All the events below this value were removed from the sample. The advantage of this selection is to remove events in a homogeneous way from the whole range of the production angular distribution which means that this distribution is not distorted by this selection. This gives a weighting factor of 1.3 ± 0.001 for all the events selected which is the plateau value in figure 5.8a.

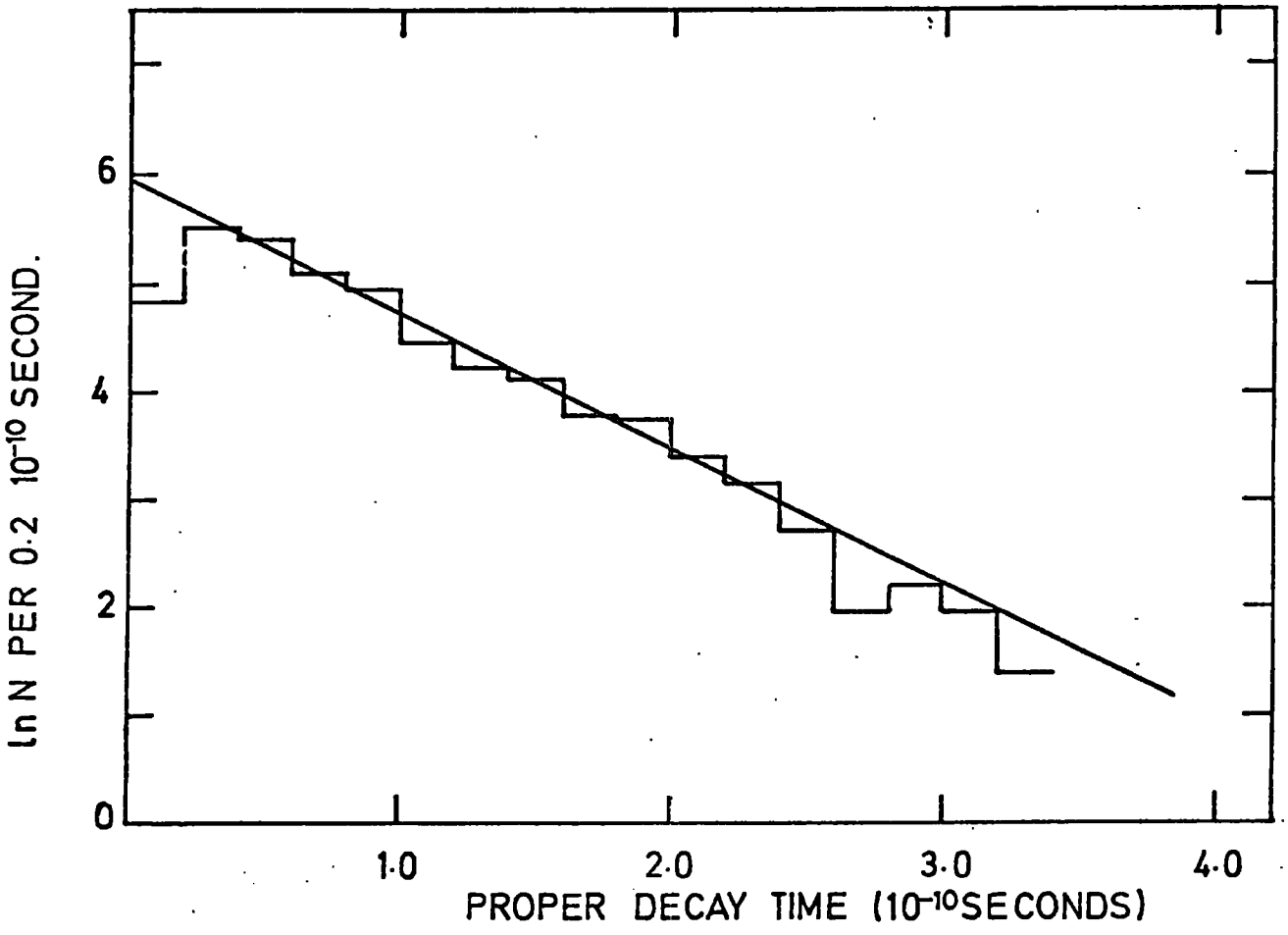

FIG.(5·9)a DECAY TIME DISTRIBUTION FOR THE OBSERVED Σ_p^+ EVENTS

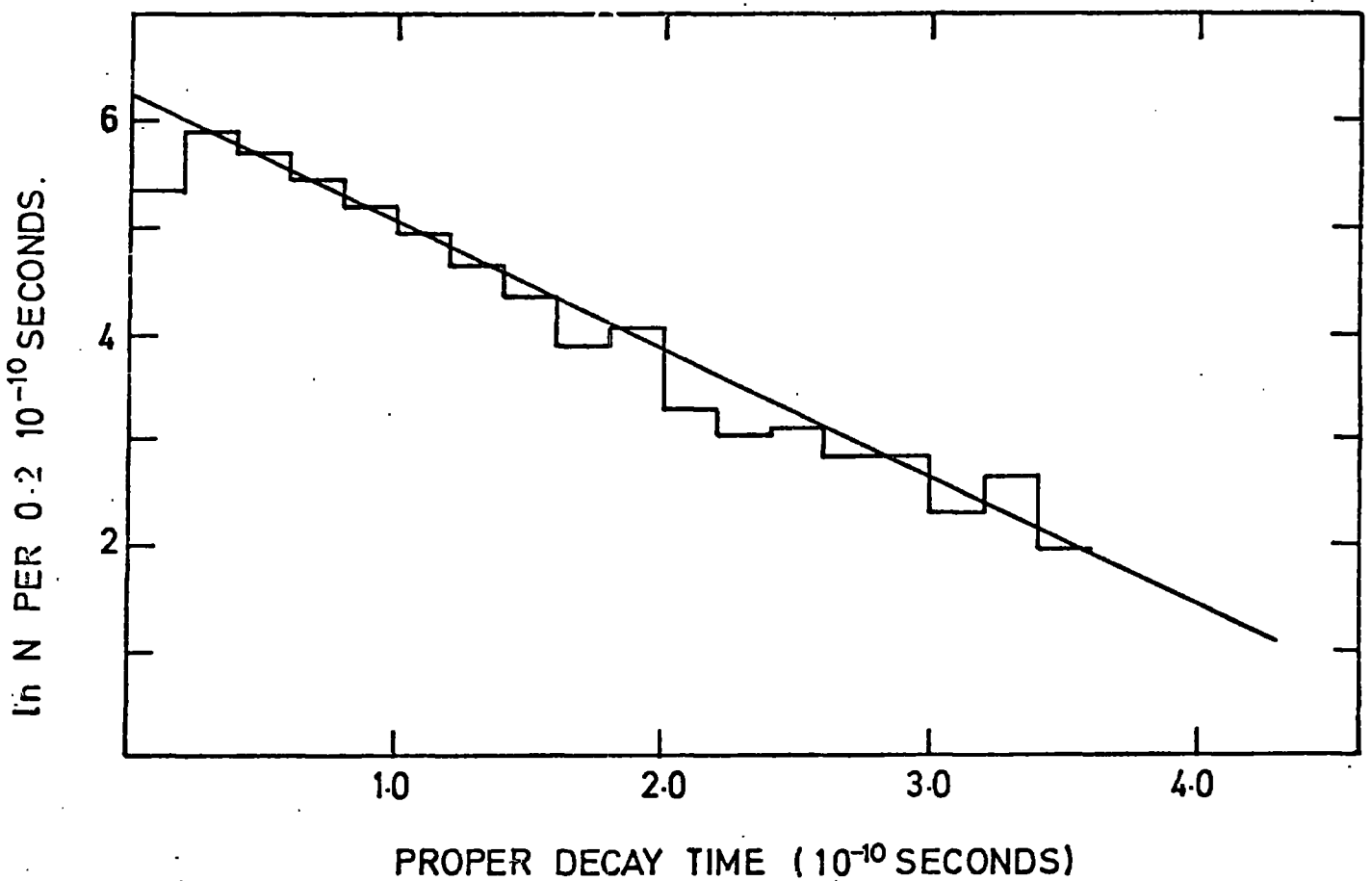

FIG.(5·9)b DECAY DISTRIBUTION FOR THE OBSERVED Σ^+_π EVENTS

5.3.2 Corrections to the production Angular Distribution and $|\phi_p|$ corrections

For interactions by primary kaons at rest in the chamber the Σ^+-hyperon is produced with a momentum of about 180 MeV/C which leads to a range of about 1.2 cms. As the primary momentum is increased from zero the resulting Lorentz transformations will lead to an increase in the laboratory momentum of the forwardly produced Σ^+-hyperon and to a reduction of the backwardly produced Σ^+-hyperon. From Figure 5.3b, Σ^+-hyperon produced at 180^o in the centre of mass frame will have a laboratory momentum of less than 100 MeV/C for all primary kaon momenta. In general for all primary kaon momenta, Σ^+-hyperons will be produced with very low momenta if they are emitted backward in the centre of mass frame, hence they do not produce visible tracks. Such events will be classified in the two-prong categories.

In general with the quite rapid decay of the Σ^+-hyperon, the Σ^+-hyperon track is small. Scanning visibility is highest when the Σ^+-hyperon makes a large angle to the kaon track. Σ^+-hyperons forwardly produced in the centre of mass sytem are transformed to small angles in the laboratory frame. Here the Σ^+-hyperon may look like a continuation of the kaon track and the event may be classified as a two-prong event. Hence with both these effects, losses are anticipated for very forward and very backward Σ^+-hyperons. A detailed calculation of these losses requires the knowledge of the production angular distribution of the Σ^+-hyperon. These distributions are treated in the next chapter. For the present purpose events are excluded from the sample if $\cos \theta^*_{PROD} < -0.9$ or $\cos \theta^*_{PROD} > +0.8$ where θ^*_{PROD} is the same angle as defined before.

Events were excluded from the Σ^+_p mode of decay and Σ^+_π mode of decay if ϕ_p is less than 10 degrees and 15 degrees respectively where

these bins were found to be depleted. This introduces a weighting factor of 1.125 ± 0.04 for Σ^+_p decay mode and 1.20 ± 0.05 for the Σ^+_π mode of decay.

5.3.3 Losses at Small Decay Angles

The detection of the Σ^+-hyperon depends mainly on observing the decay vertex of this type of event. This is sometimes difficult to detect when the angle between the Σ^+-hyperon track and its charged decay track is very small in the laboratory frame. In the decay mode $\Sigma^+ \rightarrow N + \pi$, the nucleon N, will follow the direction of the parent sigma hyperon (to within 10^o) with similar momentum (to within 25%) (5.2). For the proton mode of decay of the Σ^+-hyperon (Σ^+_p) the seen decay track will have these characteristics and so confusion between the Σ^+-hyperon and the proton may occur. For the pion mode of decay the pion track is more isotropically distributed and moreover the ionisation of the pion track is clearly different from that of the parent sigma-hyperon and so this effect is not serious. Experimentally the difficulty arises when trying to detect the projected decay angle on the scanning table. Events are also lost in the case of Σ^+_p decay mode if the proton is emitted backward in the rest frame of a low momentum Σ^+-hyperon. Here its velocity in the Σ-hyperon frame is comparable, but opposite to the velocity of the centre of mass, so that in the laboratory frame the momentum of the proton is too low to leave a visible track. This loss depends on the angular distribution of the charged decay particle in the rest frame of the sigma-hyperon which should be isotropic and also on the angular distribution of the azimuthal angle ϕ_D defined before. Because of the difference in the kinematics of the decay (5.2), events of these two decay modes have been treated separately in estimating decay losses.

In this a two dimensional plot of cos θ_D^* and ϕ_D, which is shown in Figure 5.10a and b for the Σ_π^+ and Σ_p^+ decay modes respectively, was used. In each case a central region was defined for each decay mode where this region is expected to give good visibility and be free of biases. The bounds of the region were defined by extending them until loss became apparent in both ϕ_D and cos θ_D^*. Events inside these boundaries are accepted for further analysis and events outside these boundaries are removed from the sample. The accepted number of events have to be weighted by a factor, W_D.

$$W_D = \frac{\text{Total area under consideration}}{\text{Area defined by the boundaries}} \qquad (5.19)$$

The two dimensional plot was used in this case to take account of the possible correlation between these two variables. Otherwise the correction for this loss might be overestimated by double counting if the two distributions had been taken individually. It should be noted that in some previous work individual corrections, with the possibility of overestimation through corrections, have been made (1.22).

Events were selected in the case of the Σ_π^+ - hyperon mode of decay between $-1.0 \leqslant \cos\theta_D^* \leqslant +1.0$ and $\phi_D \geqslant 20^\circ$ which gives a weighting factor of 1.28 ± 0.04. In the case of the Σ_p^+ mode events are selected if they are between $-1.0 \leqslant \cos\theta_D^* \leqslant +0.9$ and $\phi_D \geqslant 30^\circ$; this gives a weighting factor of 1.58 + 0.06.

A useful check on these corrections can be made by determining the branching ratio of Σ^+-hyperon decay to proton, B, which is defined as

$$B = \frac{\Sigma^+ \rightarrow \pi^0 + P}{\Sigma^+ \rightarrow \pi^0 P + \Sigma^+ \rightarrow \pi^+ n} \qquad (5.20)$$

From reference 1.20 this should be (51.6 ± 0.7)%. Using only events

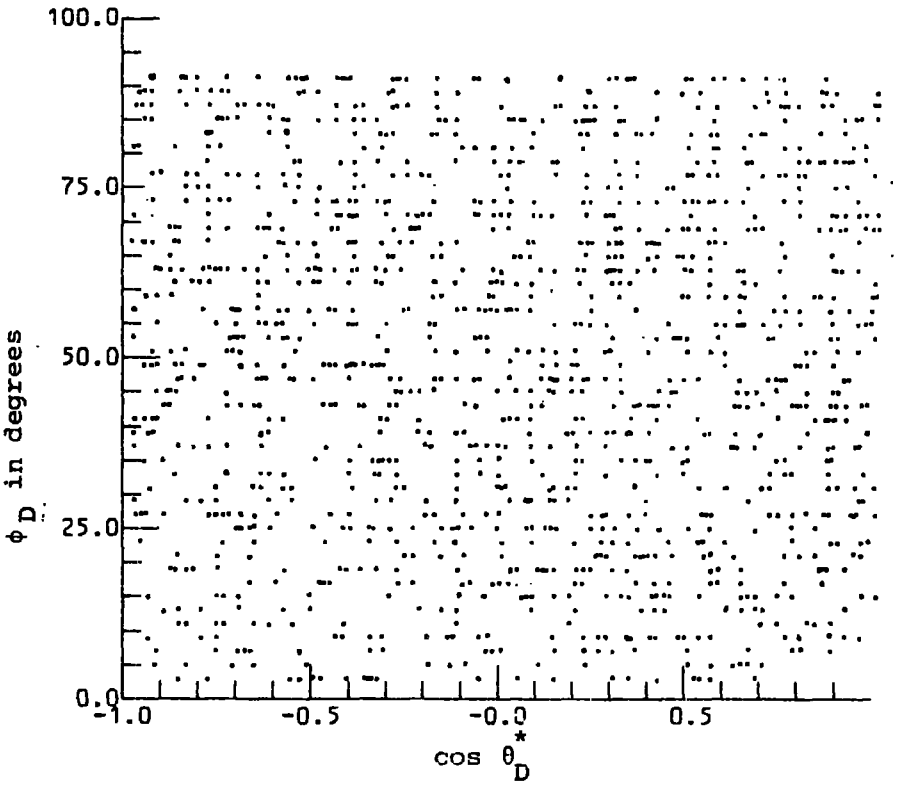

Figure 5.10a: The two dimensional plot of cos θ^*_D against ϕ_D for the Σ^+_π- events

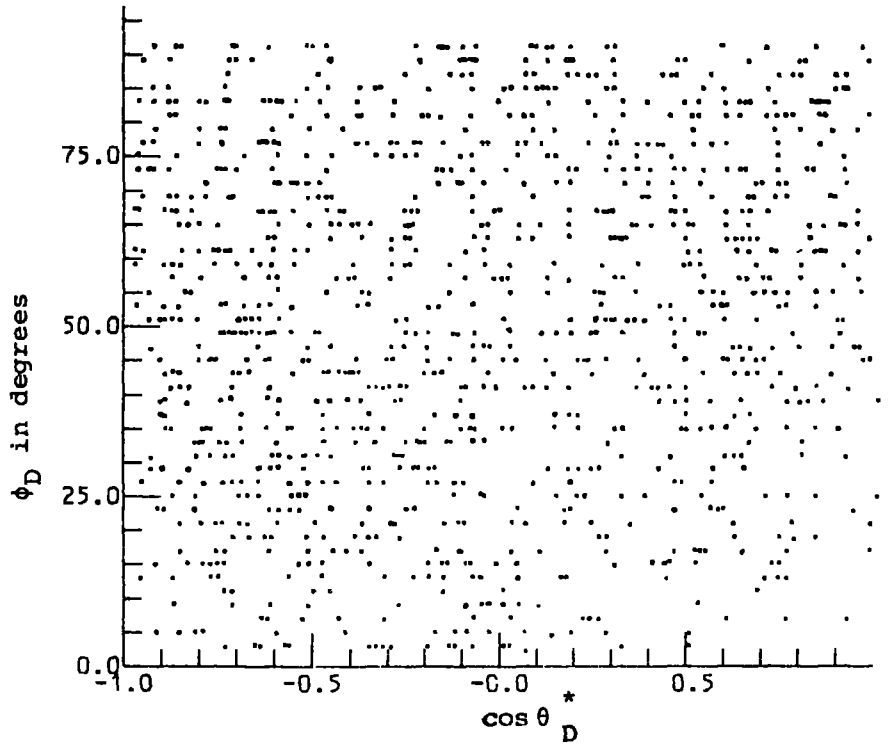

Figure 5.10b: The two dimensional plot of cos θ^*_D against ϕ_D for the Σ^+_p -events

according to the angular ranges above and scale to the full angular range the value of B is

$$B = (46.4 \pm 2.09)\ \%$$

This implies a loss of proton decays. This loss must be such that it affects Figure 5.10b more or less uniformly. The source of this is probably due to loss of small decay angles in the laboratory system. For example in Figure 5.11 the observed $\cos \theta_D^*$ distribution for Σ_p^+ is shown and compared with the distribution expected if all the laboratory angles below certain values are lost. This is given in Figure 5.12. This effect which is only pronounced for Σ_p^+ decay is not a loss of small laboratory angles but affects almost all the $\cos \theta_D^*$ range. This loss cannot be detected in Figure 5.10b. This loss and its corresponding weighting factor can be calculated by comparing the horizontally and vertically projected angles of decay. Although the decay takes place in the three dimensional chamber space, it is detected by its horizontally projected decay angle on the scanning table. This is where the loss occurs. The vertically projected decay angle plays no role in the detection. Consequently for the observed events, the vertically projected angle should be unbiased, whereas the horizontally projected angle should show the loss described above. The detection efficiency of the decay increases with increasing horizontally projected angle up to a certain value where it becomes constant and very high. Meanwhile the vertically projected angle of decay is detected equally everywhere with an overall detection efficiency equal to that of the horizontally projected angles. So the distribution of the vertically projected angles is not distorted but has to be scaled by a factor to estimate the total number of events. Hence the comparison of the vertically and horizontally projected decay angles should allow the estimation of the loss of small decay angles

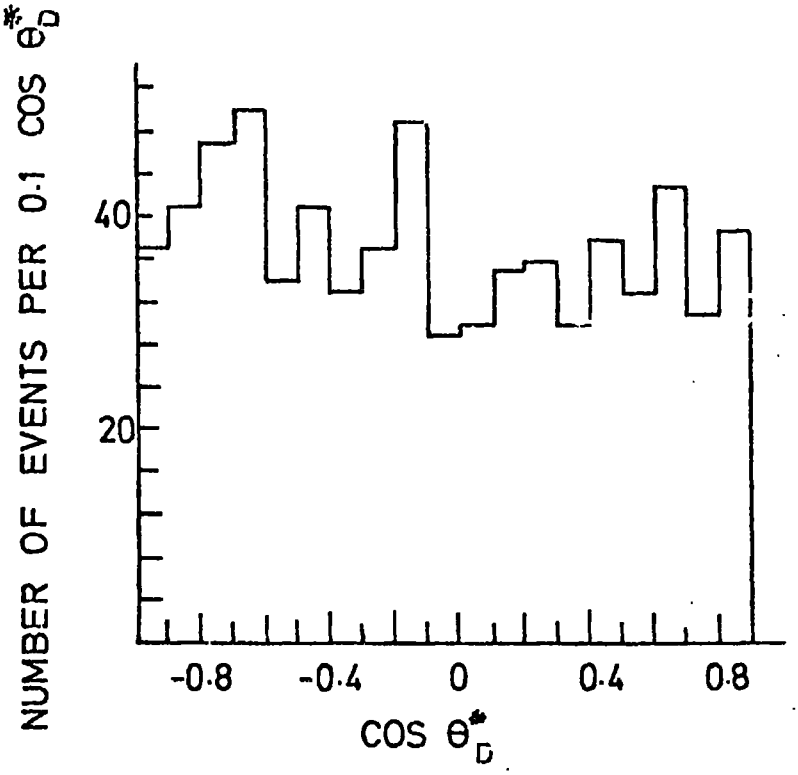

FIG. 5.11 THE OBSERVED COS θ^*_D DISTRIBUTION FOR $\Sigma\hat{\rho}$ EVENTS.

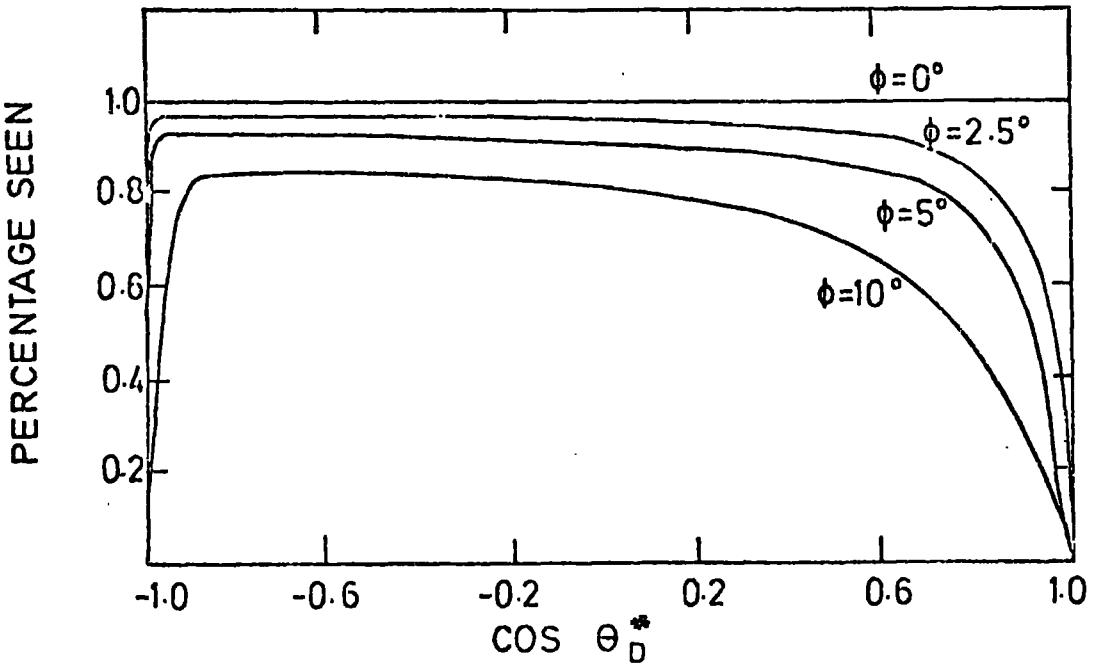

FIG 5.12 THE DISTRIBUTION OF THE COSINE OF THE DECAY ANGLE IN THE $\Sigma^{\pm}$ HYPERON CENTRE OF MASS SYSTEM FOR THE PROTON IF THE LABORATORY ANGLES BELOW CERTAIN VALUES ARE LOST.

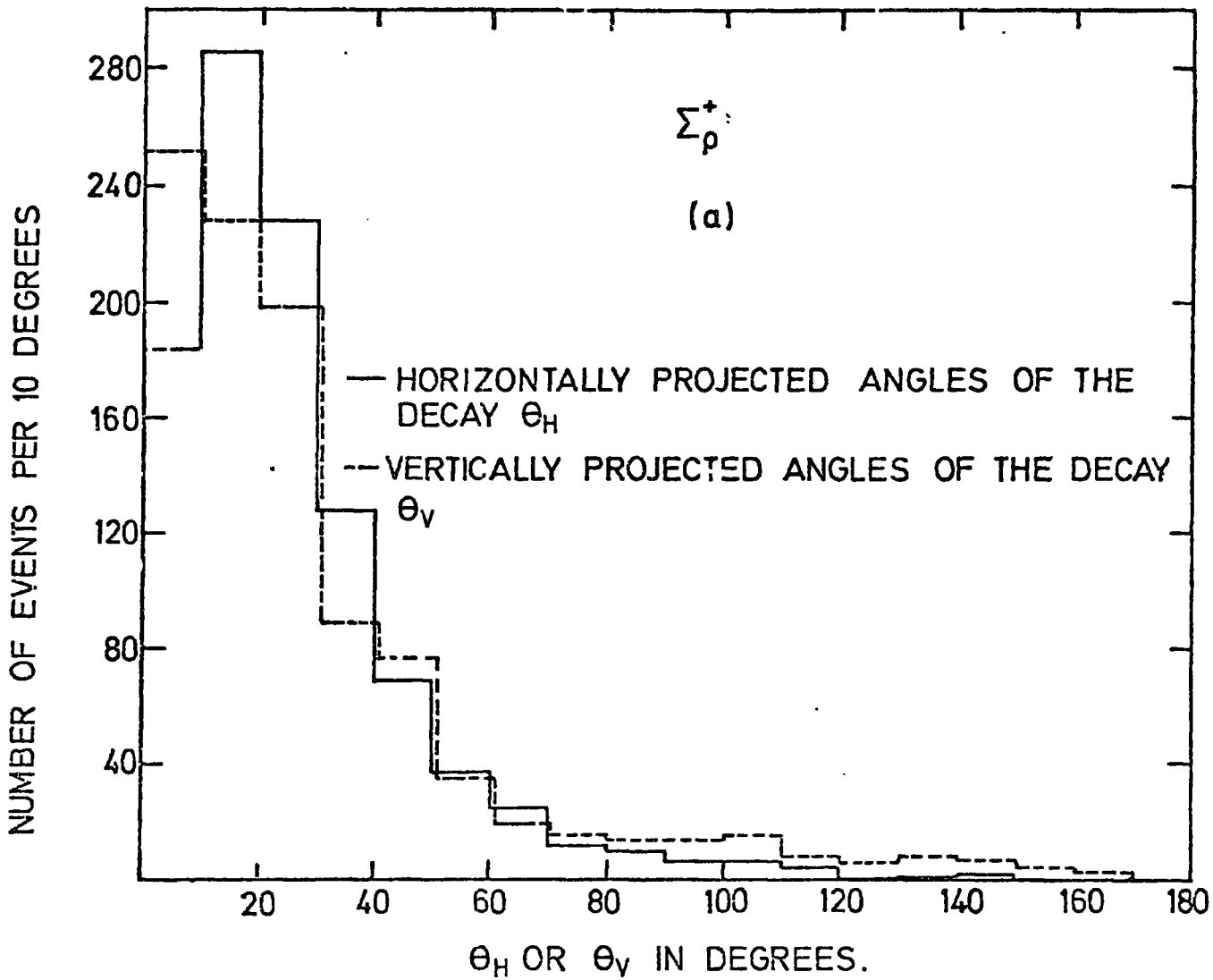

FIG. 5·13 a THE DISTRIBUTION OF THE HORIZONTALLY AND VERTICALLY PROJECTED ANGLES OF DECAY FOR THE Σ_p^+ MODE OF DECAY.

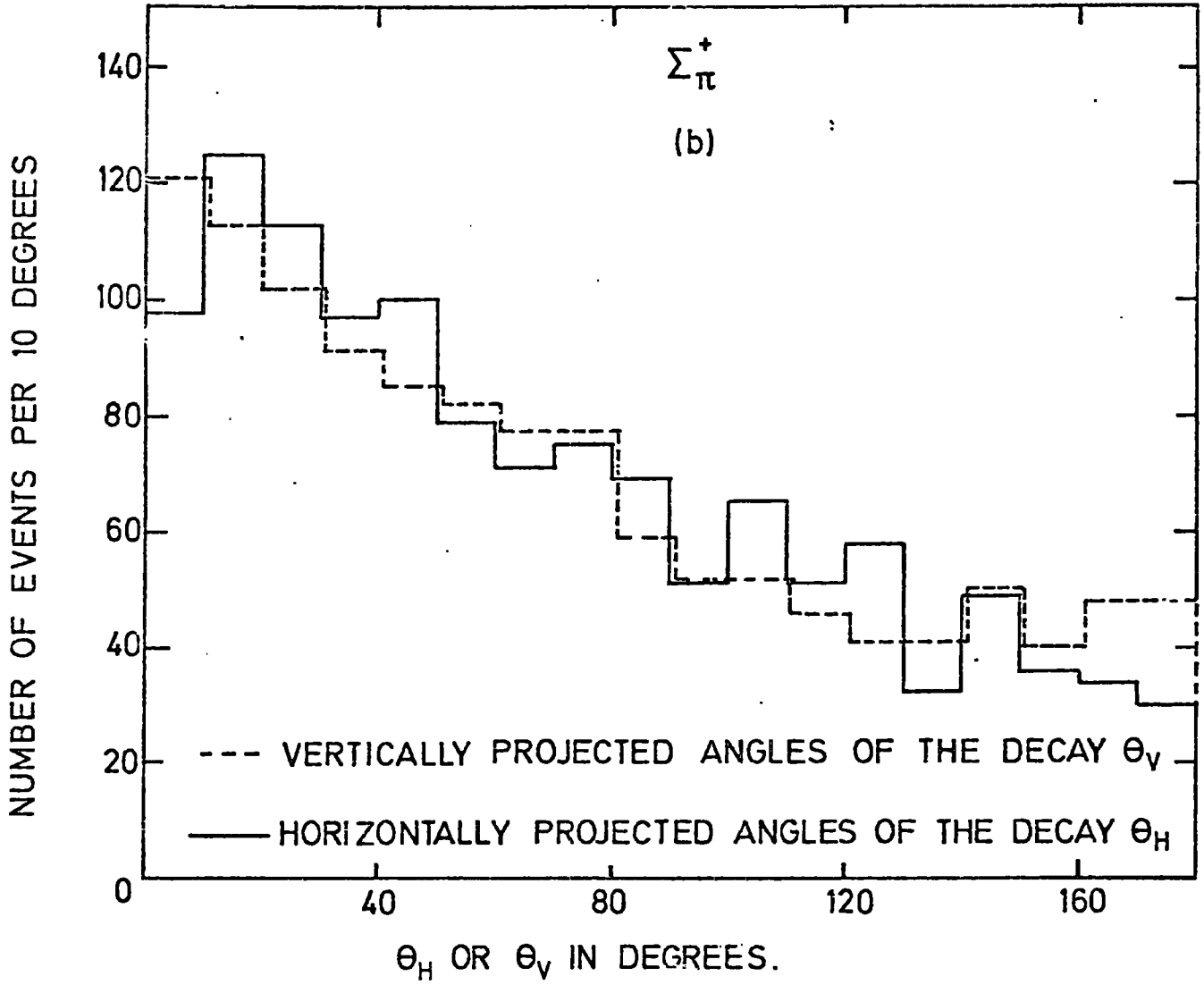

FIG. 5·13(b) THE DISTRIBUTION OF THE HORIZONTALLY AND VERTICALLY PROJECTED ANGLES OF DECAY FOR THE Σ^+_π MODE OF DECAY.

which is spread over the whole cos θ_D^* range in the case of Σ_p^+ mode of decay. Figure 5.13a is the horizontally projected angles distribution of the decay for the Σ_p^+ mode of decay. The vertically projected angles distribution is shown as a dotted curve on the same figure. This gave a weighting factor of 1.13 ± 0.04 for the Σ_p^+ mode of decay. As a comparison the Σ_π^+ mode of decay gives a weighting factor of 1.02 ± 0.03 quite consistent with unity.

5.3.4 Corrections for Scanning and Measuring Losses

Having corrected for all previous biases where events have been eliminated from the sample because they are seen in a less efficient way, the Σ^+ events which are used have to be corrected for losses during scanning, for losses due to the failure in the programs GEOMETRY and KINEMATICS and for events which cannot be measured. Losses during scanning are corrected for via the scan efficiency for the Σ^+-hyperon. This efficiency is very high and amounts to a weighting factor of 1.04 ± 0.004. The other corrections above is made using the information of Table 4.1, Chapter 4. The events which are not measurable and those which failed the two remeasurements were merged together and were assumed to be spread uniformly over the momentum range and angular ranges of the experiment. This gives a weighting factor of 1.22 ± 0.03.

The assumption on which this weighting factor is based may be criticized. It is true that there are some unmeasured events which are associated with particular angles of production or decay already they have been corrected for via the weighting factor for angular losses. The remaining events were not measured or failed (REMS in Table 4.1) for random reasons. In a rough estimation of these two classes in the lower end of the momentum range (5.3) of the primary, it is found that

the number of not measured events are divided nearly equally between those rejected for random reasons and those for particular reasons. If this is taken into account then the cross-section to be presented finally will be overestimated by about 4%.

As a check on the way events have been weighted the ratio B defined as before was calculated from the corrected numbers of Σ^+_p mode of decay events and Σ^+_π mode of decay events. This gives a value of (49.5 ± 2.23)% which is within a standard deviation of the world average value of (51.6 ± 0.7)%. This gave confidence in the way losses were determined.

5.3.5 Summary

The corrections made for the two decay modes of the Σ^+-hyperon are summarised in Table 5.3

Correction \ Mode of Decay	Σ^+_p	Σ^+_π
Life-time	1.300 ± 0.001	1.300 ± 0.001
Azimuthal Angle ϕ_p	1.125 ± 0.040	1.200 ± 0.050
Small Decay Angles	1.580 ± 0.060	1.280 ± 0.040
Horizontal Projected Angle	1.130 ± 0.040	1.020 ± 0.030
Scanning Losses	1.040 ± 0.004	1.040 ± 0.004
Measuring Losses	1.220 0.030	1.220 ± 0.030

Table 5.3: Summary of the corrections made to the two decay modes of the Σ^+-hyperon.

5.4 Experimental Biases in Σ^--Hyperon Production and Decay

The reaction producing Σ^--hyperons at the energies of this experiment is

$$K^- + P \rightarrow \pi^+ + \Sigma^-$$

which is followed by the decay mode

$$\Sigma^- \rightarrow \pi^- + n$$

The reaction $K^- + P \rightarrow \pi^+ + \pi^0 + \Sigma^-$ has a negligible cross-section in the region of this experiment. As in the case of the Σ^+-hyperon events, the Σ^--hyperon events were treated separately on an event by event basis to account for the losses. Selection criteria were imposed to produce a sample of events, bias free, for the calculations of the cross-sections and production angular distributions. The kinematics of production of the process $K^- + P \rightarrow \pi^+ + \Sigma^-$ and the different tests for the effects due to the shallowness of the chamber are given in Appendix B, together with the description of some losses affecting the detection of Σ^--hyperon events. This has been done because it is very similar to the way Σ^+-hyperon events were treated. Here only a brief account will be given to the losses and their corresponding correction factors. Losses which are different to the Σ^+-hyperon will be discussed in some detail. The losses affecting the Σ^--hyperon events are given in the next sections.

5.4.1 Life-time Correction

This loss is very similar to the loss of events described in Section 5.3.1 for the Σ^+-hyperon and events were corrected according to equation (5.18). This gives a weighting factor of 1.24 ± 0.006.

5.4.2 Corrections to the Production Angular Distribution and the Losses in ϕ_p.

The kinematics of production of the Σ^--hyperon are very similar to that of the Σ^+-hyperon. The selections of Section 5.3.2 were imposed on the Σ^--hyperon events. This introduces a weighting factor of 1.20 ± 0.03 because of the section on ϕ_p.

5.4.3 Losses Due to Small Decay Angles

This loss is the same as the loss of events for Σ^+_π mode of decay described in Section 5.3.3. Selections of the events were made exactly in the same way as for the Σ^+_π of the above-mentioned section. This gives a weighting factor of 1.28 ± 0.04.

5.4.4 Losses Due to the Absorption of Σ^--Hyperon

Those Σ^--hyperons identified by their pion decay are necessarily in flight. However any Σ^--hyperon which is produced with low momentum is likely to come to rest. Then it will interact with a target proton producing neutral particles rather than decay. In this case the event will be classified with the two-prong events. This is more likely to happen when the Σ^--hyperon is emitted backwards in the centre of mass system so that in the laboratory frame it will have very low momentum. This effect is strongly dependent on the angular distribution for the Σ^--hyperon production which has been considered in a previous section. The probability that the Σ^--hyperon would interact in flight with a proton of liquid hydrogen is highly unlikely because the available track length for Σ^--hyperon is very small. This bias is not significant.

5.4.5 Corrections for Scanning and Measuring Losses

These have been corrected for in exactly the same way as Σ^+-hyperon in Section 5.3.4. This is done by using the scan efficiency which gives a weighting factor of 1.044 ± 0.004 and the information of Table 4.1 which gives another weighting factor of 1.24 ± 0.03.

5.4.6 Summary

The summary of the corrections made to the Σ^--hyperon events is given in Table 5.4.

Correction	Value
Life-time	1.24 ± 0.006
Azimuthal Angle ϕ_p	1.20 ± 0.03
Small Decay Angles	1.28 ± 0.04
Scanning	1.044± 0.004
Measuring	1.24 ± 0.03

Table 5.4: Summary of the corrections made for the Σ^--hyperon events

5.5 Experimental Biases in the K^-P Elastic Scattering

As mentioned in Chapter 3, Section 3.2, the two-prong elastic scattering events were scanned for together with nonelastic scattering two-prong events in the second scan. The two-prong elastic scattering events form the bulk of all the two-prong events and represent roughly one-half of all interactions. About 25% of all the two-prong events only were measured. These were chosen from the whole momentum range and

they are distributed roughly equally throughout the momentum blocks 2-5. In this section the track length for the two-prong elastic scattering, based on the tau-mode of decay as in the case of Figure 5.1, was worked out only for the portion of the film where the two-prong events were measured and this is shown in Figure 5.14. Then the biases affecting the detection of the two-prong elastic scattering events are described where events inefficiently seen have been eliminated from the sample and were corrected for so that cross-sections can be determined. These biases are described in the following sections.

5.5.1 Correction Due to the Decay of Scattered K^--meson

These are events where the K^--mesons decay after they suffer a scatter on the target proton and they are normally classified among the two-prong events followed by the decay of the negative track into one-prong (Σ^--hyperon). This loss can be corrected for by introducing a weighting factor based on the known K^--meson decay ratio (1.20).

$$N_o = N W = N/(\exp(-t_p/\tau_{K^-})) \qquad (5.21)$$

where the weighting factor $W = 1/\exp(-t_p/\tau_{K^-})$, N is the number of observed events, N_o is the true number of events corrected for the decay after the scattering of the primary K^--meson, t_p is the proper time taken by the K^--meson, after it scattered, to leave the fiducial volume or the proper time for it to come to rest, and τ_{K^-} is the mean life-time of the K^--meson. This weighting factor has a value of 1.058 ± 0.002.

5.5.2 Correction for Nearly Vertical Scattering Plane

Losses of events may occur when the plane containing the two

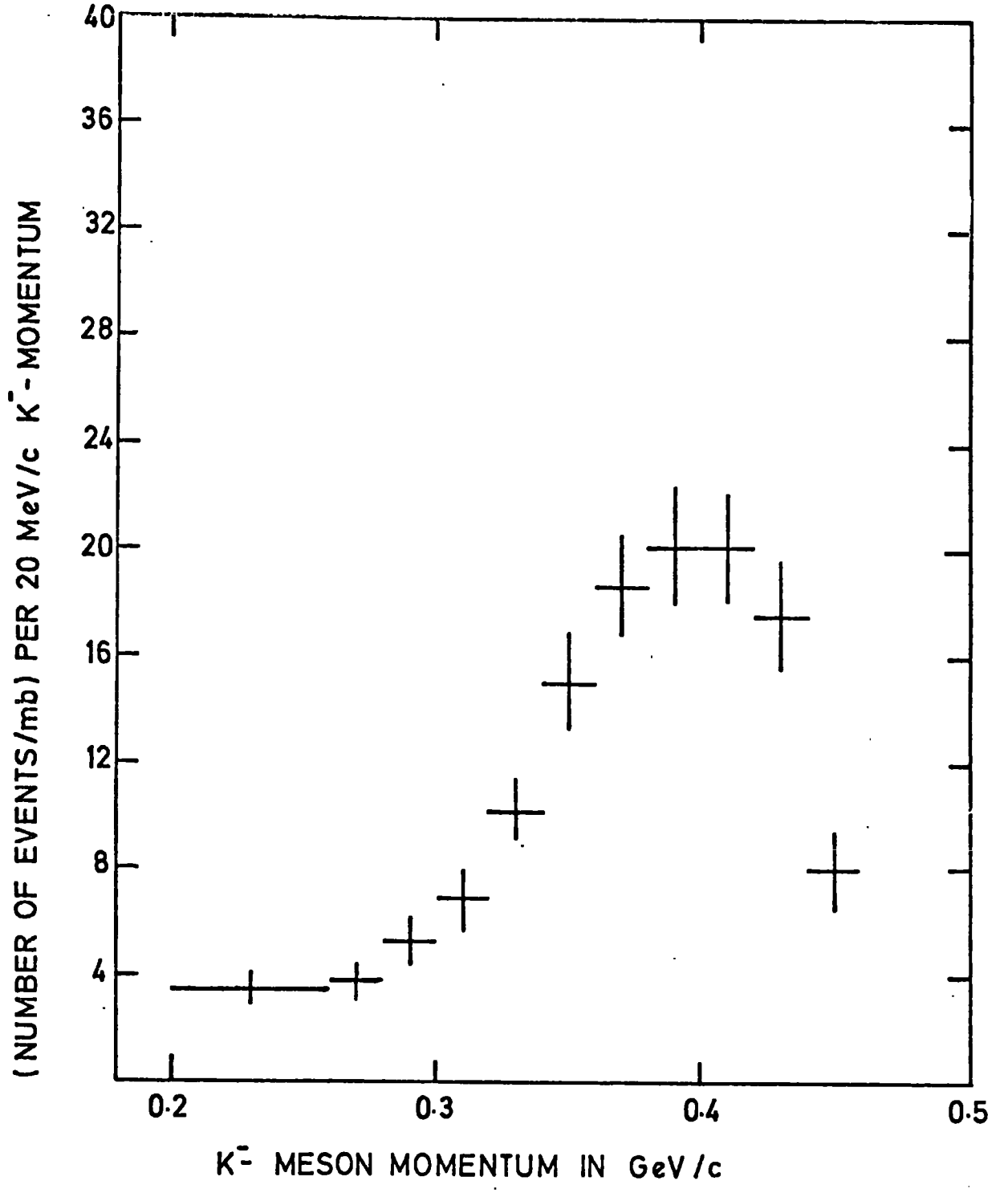

FIG. 5.14 PRIMARY TRACK LENGTH [(eV/mb)/20 MeV/c K^- MOMENTUM] FOR ELASTIC SCATTERING.

secondary tracks is nearly vertical to the scanning plane. This effect is detected in the distribution of the angle ϕ defined as follows

$$\phi = \cos^{-1} \left| \frac{\hat{Z} \times \hat{K}_{in}}{|\hat{Z} \times \hat{K}_{in}|} \cdot \frac{\hat{K}_{in} \times \hat{K}_{out}}{|\hat{K}_{in} \times \hat{K}_{out}|} \right| \qquad (5.22)$$

where $\hat{Z}$ is the unit vector normal to the front glass, $\hat{K}_{in}$ is the direction of the incident K^--meson, and $\hat{K}_{out}$ is the direction of the outgoing K^--meson. This distribution should be isotropic if there are no losses due to this effect. Figure 5.15 shows the distribution of ϕ for the K^-P elastic scattering events where it is seen that events are lost at small values of the azimuthal angle ϕ. By increasing the angle ϕ the distribution is found to reach a plateau at $\phi = 15^o$. Consequently all events with $\phi > 15^o$ were accepted for further analysis. This selection yields a weighting factor of 1.20 ± 0.02.

5.5.3 Correction for Small Angles of Scattering

Losses of the K^-P elastic scattering events occur when the angle of scattering of the K^--meson is small and the recoil proton carries off little momentum to leave a visible track. These events, which are normally lost, are only important in the forward direction. These losses are dependent on the angular distribution of the scattered K^--meson with respect to the primary K^--meson in the centre of mass system. The angular distributions in momentum bins of the primary are described in the next chapter and these are used for the calculation of the cross-sections in these momentum bins of the primary.

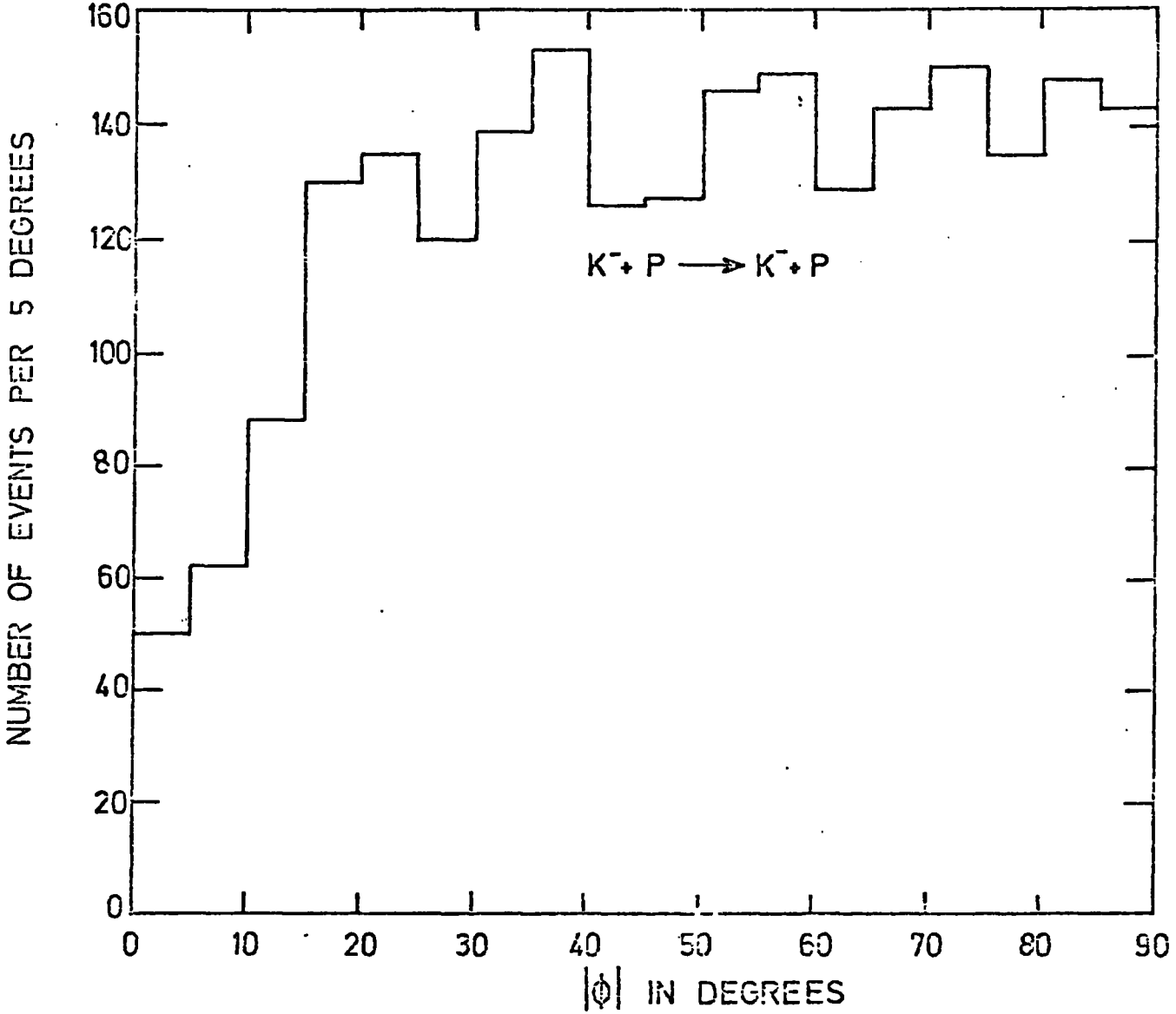

FIG. 5·15 THE DISTRIBUTION OF THE AZIMUTHAL ANGLE $|\phi|$ DEFINED BY EQUATION 5·22 FOR THE ELASTIC SCATTERING EVENTS.

5.5.4 Corrections for Scanning and Measuring Losses

These have been corrected for in the same way as previously for both $\Sigma^{\pm}$-hyperons. This yields a weighting factor of 1.17 ± 0.03 for scanning losses and a weighting factor of 1.08 ± 0.02 for the measuring losses.

5.5.5 Summary

A summary of the corrections made to the elastic scattering events is given in Table 5.5.

Correction	Value
Decay of Scattered K^--meson	1.058 ± 0.002
Nearly Vertical Scattering Plane	1.20 ± 0.02
Scanning	1.17 ± 0.03
Measuring	1.08 ± 0.02

Table 5.5: Summary of the corrections made to the elastic scattering events.

CHAPTER VI

CROSS-SECTIONS, ANGULAR DISTRIBUTION AND POLARISATION

6.1 Introduction

The work described in this thesis is concerned mainly with the properties of K^-P interactions leading to the production of the charged sigma hyperons and to elastic scattering for primary momenta between 200 MeV/C and 460 MeV/C.

In chapter five there were described the corrections for the several losses from these channels which must be made before the cross-section for a particular channel can be found. In the following, the calculations of the cross-sections for the production of the Σ^+-hyperon, Σ^--hyperon, and the K^-P elastic scattering are presented. This is followed by the determination of the ratio γ = Σ^--hyperon/Σ^+-hyperon production, which is independent of losses, at different momenta of the primary K^--meson using a method independent to that used for the determination of the cross-section. The production angular distributions, as a function of the primary kaon momentum, are determined and presented and an anlysis in terms of Legendre polynomials is made. Finally the polarisation of the Σ^+-hyperon at production is found.

6.2 Cross-Sections

Having evaluated the weight and the number of events per millibarn (normalisation factor), the cross-sections for the production of the Σ^+-hyperon, Σ^--hyperon, and the K^-P elastic scattering were calculated in the momentum range 200 MeV/C to 460 MeV/C of the primary K^--meson. This momentum range was divided into intervals of varying widths and in

each the cross-sections for the three channels were calculated. Variable bin widths were used to obtain approximately equal numbers of events in each bin. The cross-sections are presented in Table 6.1 for Σ^+-hyperon, Table 6.2 for Σ^--hyperon and Table 6.3 for the K^-P elastic scattering. The value of each momentum bin is quoted alongside the different numbers of events in the different stages after the selections have been imposed. Column four gives the number of events weighted for the losses and selections which were imposed in chapter five. This number determines the cross-sections. In the case of the Σ^+-hyperon where there are two modes of decay (Σ^+_p and Σ^+_π) each with different weighting factors (due to different selections) then a weighted mean for the two weighting factors was calculated. This weighted mean was used to raise the number of events from the fits to the angular distributions to get the corrected number of events. The cross-sections are shown as well on Figures 6.1a, 6.2a and 6.3a for the Σ^+-hyperon, Σ^--hyperon and K^-P elastic scattering respectively. For the sake of clarity the cross-sections for these three channels are plotted alone from the determination of this experiment and followed by figures 6.1b, 6.2b and 6.3b where the values of the cross-sections determined from previous experiments in the same region have been superimposed for the comparison. For the K^-P elastic scattering cross-sections (Figure 6.3b) only the latest determination is included. It is clear that the agreement is good except in the region of primary momentum of 280 MeV/C to 310 MeV/C. Meanwhile in the case of the charged sigma hyperons the disparity between the cross-sections determined in this experiment and the previous determinations is quite apparent.

The production of the resonance $\Lambda(1520)$ should occur at a momentum of about 395 MeV/C in the isospin channel I = 0. Since all three channels described in this chapter involve both I = 0 and I = 1, then evidence of the production of the resonance $\Lambda(1520)$ should be seen.

P_{K^-} in MeV/C I	Number of events remaining after selection II	Number of events from the fits to the angular distributions III	Number of events corrected for losses IV	Cross-section in mb for Σ^+-hyperon V
200 - 280	230	250	721	21.93 ± 1.93
280 - 320	292	314	905	16.02 ± 1.24
320 - 360	373	437	1260	13.31 ± 0.88
360 - 380	239	262	756	12.11 ± 1.02
380 - 400	306	338	975	14.02 ± 1.09
400 - 420	246	277	799	11.79 ± 0.99
420 - 460	276	298	859	9.26 ± 0.72

Table 6.1: Σ^+-hyperon cross-section as a function of K^--meson momentum

P_{K^-} in MeV/C I	Number of events remaining after selection II	Number of events from the fits to the angular distributions III	Number of events corrected for losses IV	Cross-section in mb for Σ -hyperon V
200 - 280	179	201	498	15.15 ± 1.43
280 - 320	197	214	531	9.40 ± 0.82
320 - 360	245	257	637	6.37 ± 0.51
360 - 380	199	215	533	8.53 ± 0.76
380 - 400	213	241	598	8.60 ± 0.74
400 - 420	176	205	508	7.50 ± 0.70
420 - 460	170	193	479	5.16 ± 0.47

Table 6.2: Σ^--hyperon cross-section as a function of K^--meson momentum

P_{K^-} in MeV/C I	Number of events remaining after selection II	Number of events from the fits to the angular distributions III	Number of events corrected for losses IV	Cross-section in mb for K^-P elastic scattering V
200 - 280	185	203	325	45.22 ± 4.79
280 - 320	356	378	605	49.38 ± 4.84
320 - 360	508	564	903	35.79 ± 2.83
360 - 380	338	384	615	32.90 ± 3.12
380 - 400	371	442	708	35.10 ± 3.26
400 - 420	388	448	718	35.57 ± 3.39
420 - 460	401	495	793	30.92 ± 2.68

Table 6.3: K^-P elastic scattering cross-section as a function of K^--meson momentum

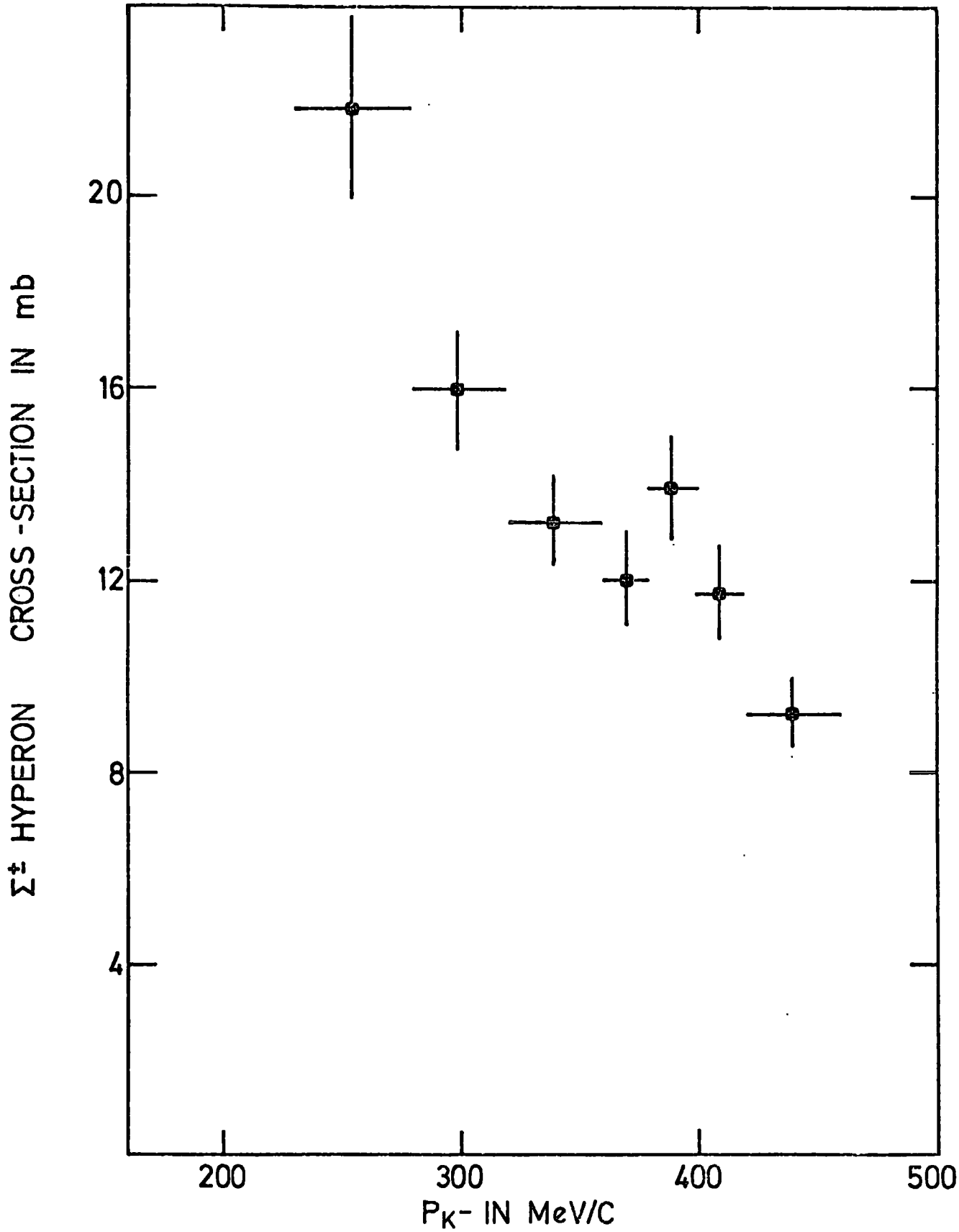

FIG. 6·1a CROSS SECTION FOR THE REACTION $K^{\mp} P \longrightarrow \pi^{\mp} + \Sigma^{+}$ AS A FUNCTION OF THE PRIMARY MOMENTUM.

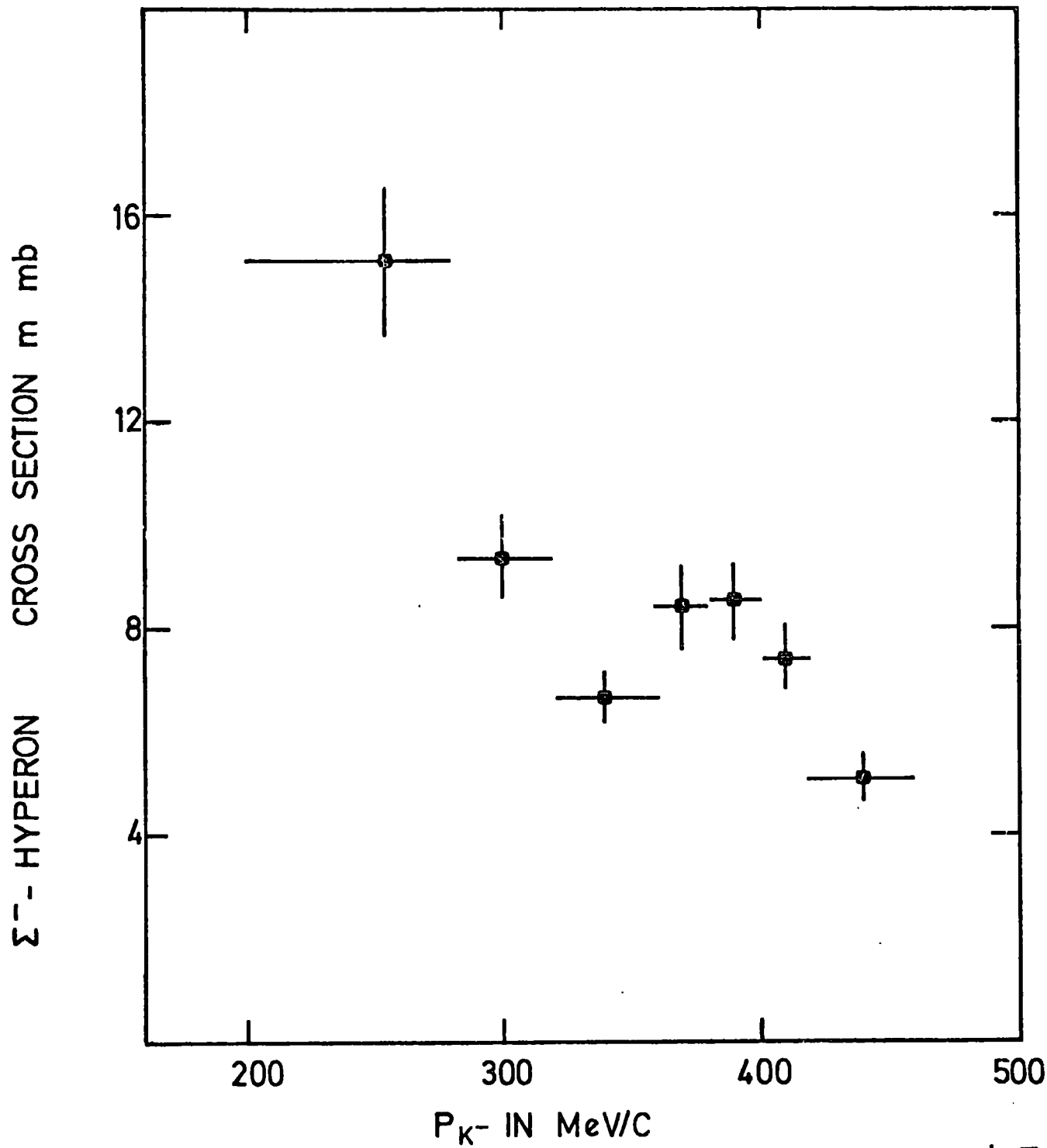

FIG. 6.2 a CROSS SECTION FOR THE REACTION $K^- + P \rightarrow \pi^+ + \Sigma^-$ AS A FUNCTION OF THE PRIMARY MOMENTUM.

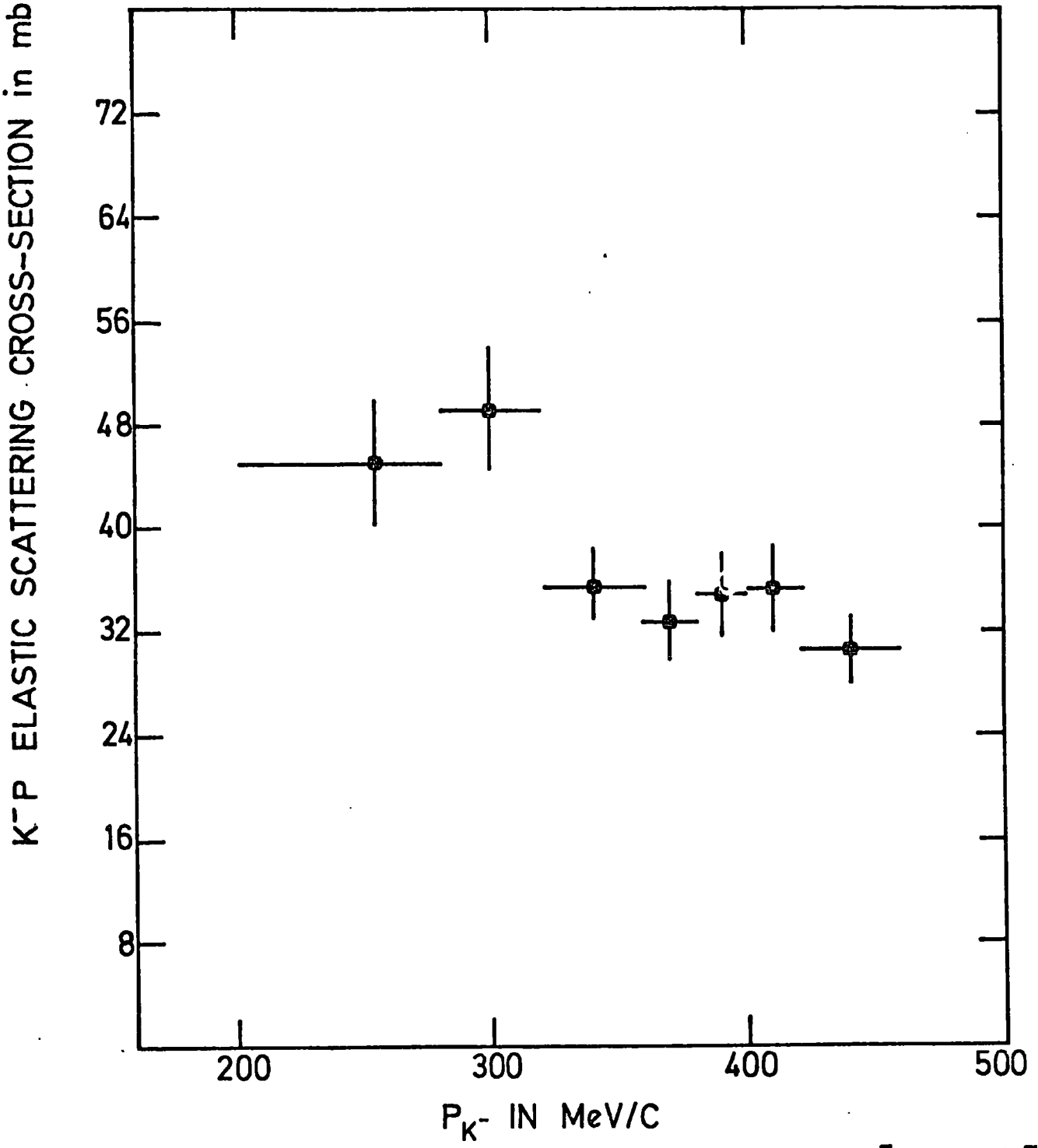

FIG. 6.3 a CROSS-SECTION FOR THE REACTION $K^- + P \rightarrow K^- + P$ AS A FUNCTION OF THE PRIMARY MOMENTUM.

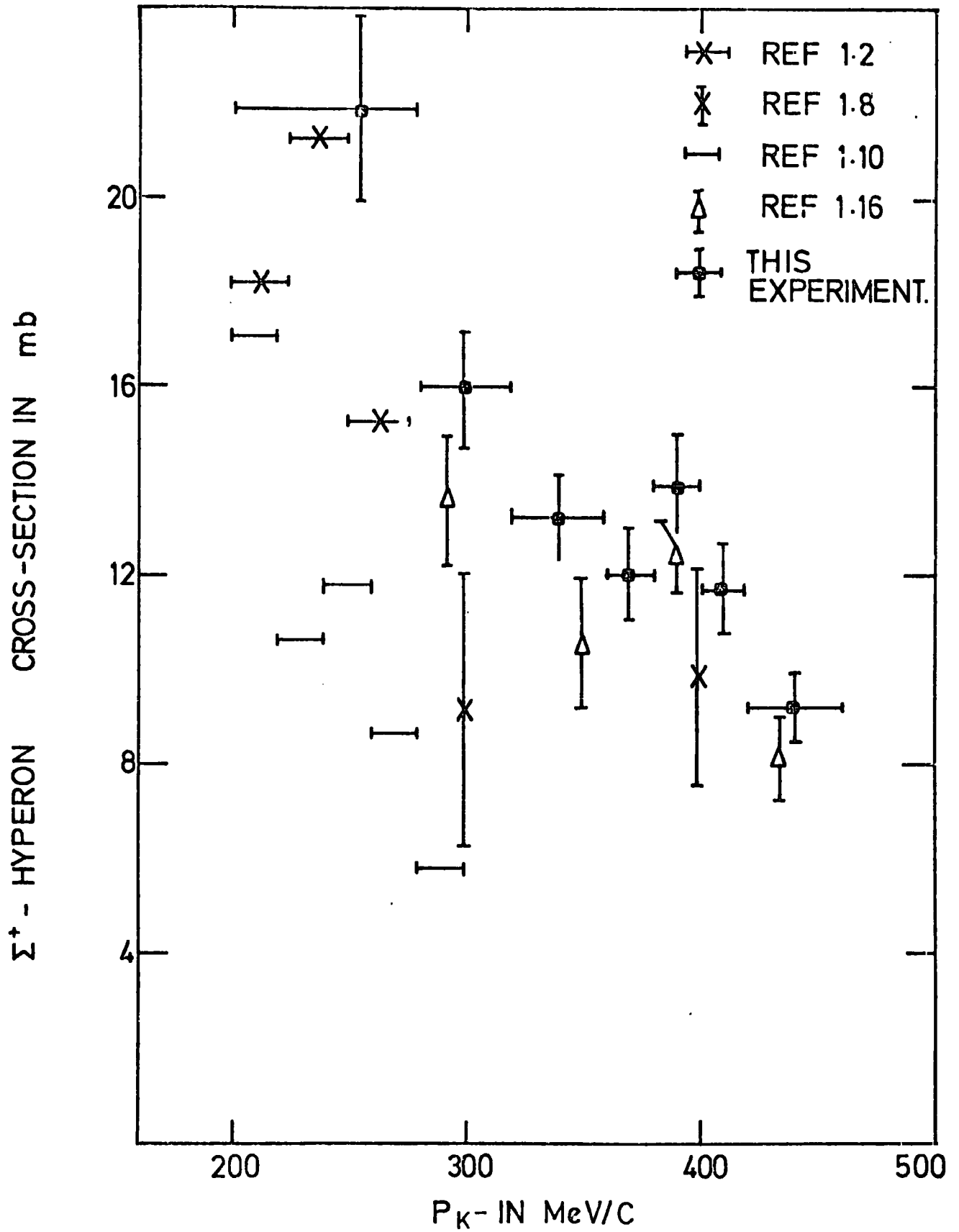

FIG. 6·1 b CROSS SECTION FOR THE REACTION $K^- + P \longrightarrow \pi^- + \Sigma^+$ TOGETHER WITH PREVIOUS DETERMINATIONS.

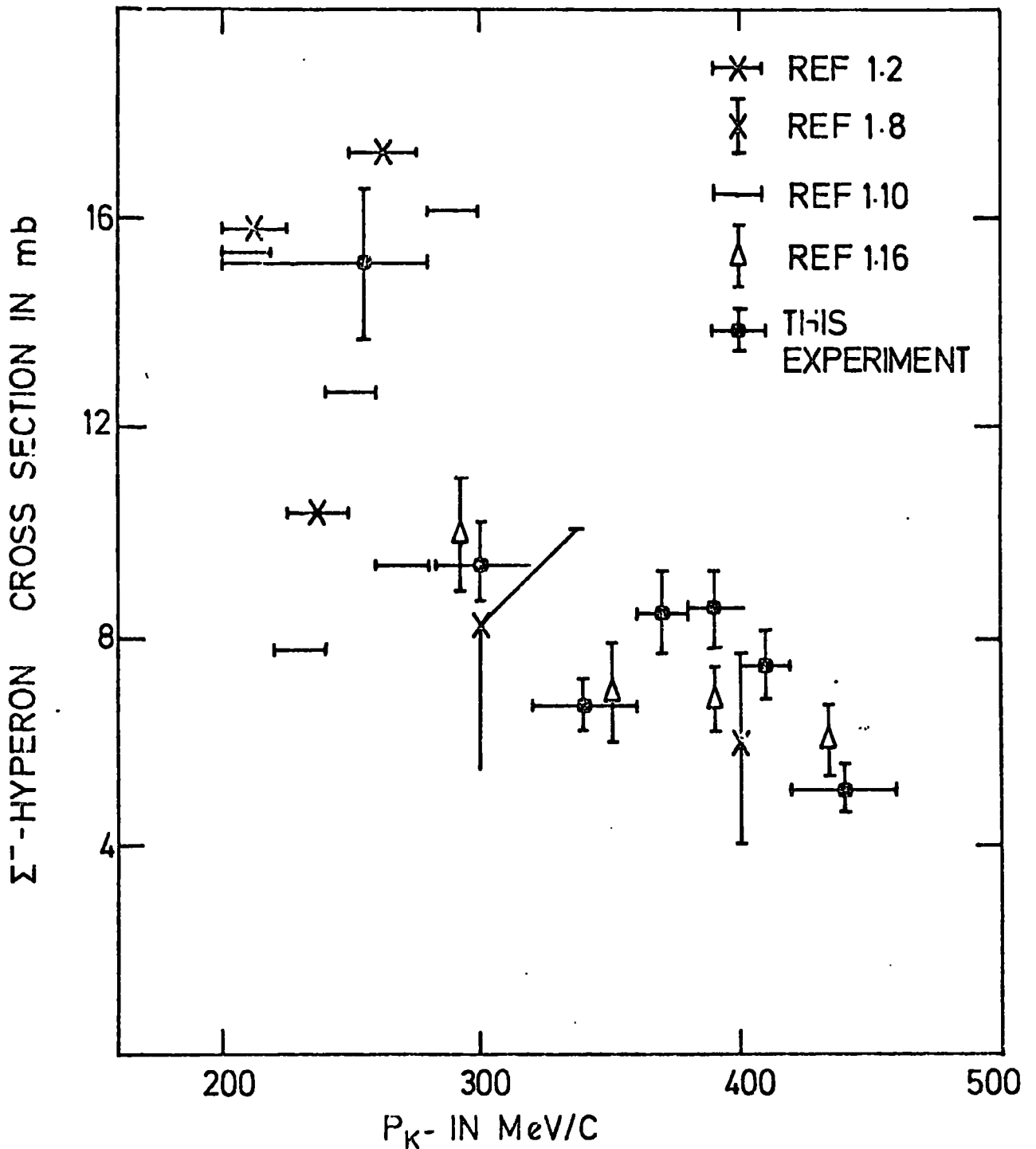

FIG.6·2 b CROSS-SECTION FOR THE REACTION $K^- + P \rightarrow \pi^+ + \Sigma^-$ TOGETHER WITH PREVIOUS DETERMINATIONS.

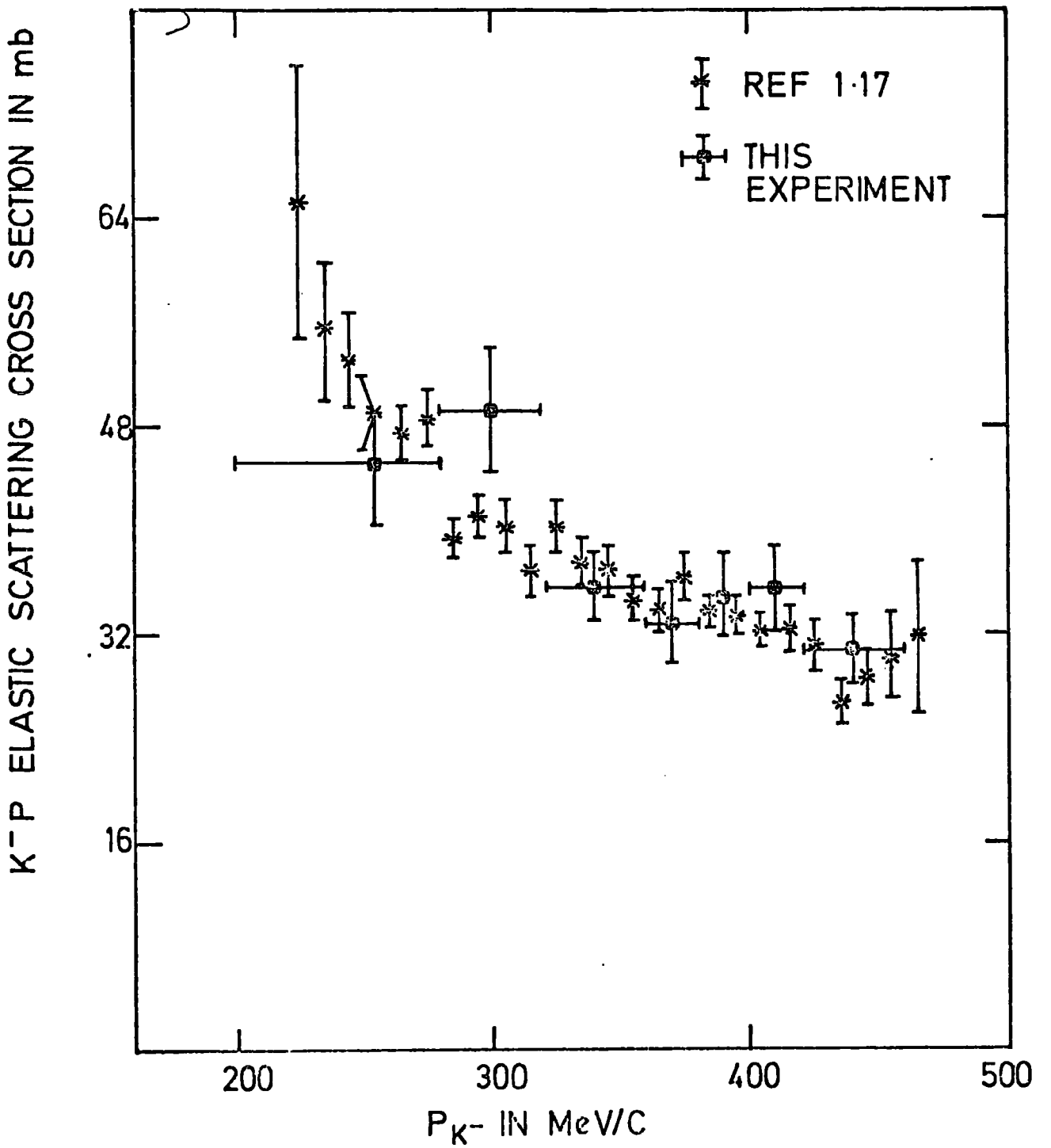

FIG. 6·3 b CROSS SECTION FOR THE REACTION $K^- + P \rightarrow K^- + P$ TOGETHER WITH THE MOST RECENT DETERMINATION.

It is quite clearly present for Σ^--hyperon production and is probably to be seen in the other two channels. The apparent difference in the breadth of the resonance in the charged sigma hyperon channels is discussed later (see Section 7.2).

6.3 The Ratio γ = Σ^--Hyperon/Σ^+-Hyperon

The quantity γ can be determined from the pion decays of Σ^- and Σ^+ hyperons which are very similar from the point of view of scanning and measuring. Consequently in the ratio it is expected that biases of scanning and measuring will largely cancel. In both cases there will be some short track length cut-off (representing different fractions of the total production because of the different life-times). Once the Σ-hyperon track can be seen, however, the pion decay modes offer very similar patterns to be detected and measured. The branching ratio (1.20) for the $\Sigma^+ \rightarrow p + \pi^0$ must then be used to get the real total number of Σ^+-hyperon events. Since the Σ^--hyperon interacts when it comes to rest, while the Σ^+-hyperon decays, there is an upper limit for the time of observation for the former, but not the latter.

To ensure that the Σ-hyperon does not come to rest before it decays a restriction of the Σ-hyperon momentum at the production vertex had to be imposed. This minimum momentum was dictated by the fact that events were only considered if they were seen between two limits (a minimum cut-off length and a maximum cut-off length). The probability of the Σ-hyperon decay between these two limits was calculated for both charged sigma hyperons for different minimum cut-off lengths and a fixed upper limit of the Σ-hyperon length. These probabilities are shown in Figure 6.4 as functions of the momenta of the charged sigma hyperons. The minimum cut-off length relevant to the experiment is ℓ_0 = 0.2 cm.

6.3.1 Σ^+_π-Hyperon Events

A Σ^+-hyperon is seen with momentum at the production vertex, P_V, and this Σ^+-hyperon is required to survive longer than the minimum cut-off length, ℓ_o , and decay before it has travelled ℓ_f , the maximum cut-off length. The momentum at the production vertex was restricted to values where the residual range, R_V, is always larger than the maximum cut-off length. In this case

(a) if $R_V < \ell_o$ the event is not counted

(b) if $R_V > \ell_o$ but $R_V < \ell_f$ it probably decays at rest, i.e. lived longer than the time equivalent to R_V and in this case the probability of the event between the two limits is not known. The event is not counted in this case either.

(c) if $R_V > \ell_f$ the Σ^+-hyperon has decayed in flight and the probability of the hyperon decaying between the two limits is

$$f_{\Sigma^+} = \left\{\exp\left(-m_+ \ell_o/PC\tau_+\right)\right\} \left\{1 - \exp\left(-m_+\ell_f/PC\tau_+\right)\right\}$$

$$= \left\{\exp\left(-t_o^+/\tau_+\right)\right\} \left\{1 - \exp\left(-t_f^+/\tau_+\right)\right\} \qquad (6.1)$$

where

m_+ is the Σ^+-hyperon mass with a momentum P, τ_+ is the Σ^+-hyperon life-time and C is the velocity of light. The energy loss due to traversing the liquid hydrogen by the Σ^+-hyperon was taken into account in calculating the minimum and maximum times t_o^+ and t_f^+ .

6.3.2 Σ^--Hyperon Events

These events have been treated in the same way as the Σ^+-hyperon events.

(a) if $R_V < \ell_o$ the event is not counted.

(b) if $R_V < \ell_f$ and $R_V > \ell_o$, then the Σ^--hyperon decayed in flight before R_V and in this case the event is not counted either.

(c) if $R_V > \ell_f$ then the Σ^--hyperon decayed in flight and the probability of the Σ^--hyperon decaying between the two limits is given by

$$f_{\Sigma^-} = \left\{\exp\left(-m_- \ell_o/PC\tau_-\right)\right\}\left\{1 - \exp\left(-m_-\ell_f/PC\tau_-\right)\right\}$$
$$= \left\{\exp\left(-t_o^{-\prime}/\tau_-\right)\right\}\left\{1 - \exp\left(-t_f^-/\tau_-\right)\right\} \qquad (6.2)$$

where

m_- is the Σ^--hyperon mass with momentum P and τ_- is its life-time, C is the velocity of light.

The energy loss of the Σ^--hyperon in hydrogen was taken into account in calculating t_o^- and t_f^- .

The γ-ratio calculated in this way is given in Table 6.4 together with the ratio calculated by dividing the cross-sections derived earlier using the same primary momentum intervals.

It is apparent from Table 6.4 that an individual value of γ , determined from the ratio of numbers of events, is different from the value calculated from the ratio of cross-sections. This reflects that in the former only pion modes of decay of Σ^+-hyperons are used and a branching ratio is used to take account of the unused Σ_p^+ decays. In the latter both pion and proton modes of decay are used. However on average the γ values from the ratio of pion decays and from the cross-sections are identical within error. This confirms that the losses, for which the cross-sections have been corrected, have been properly identified, and the corrections properly estimated and applied. Consequently it is felt that no important systematic effects have been neglected in determining

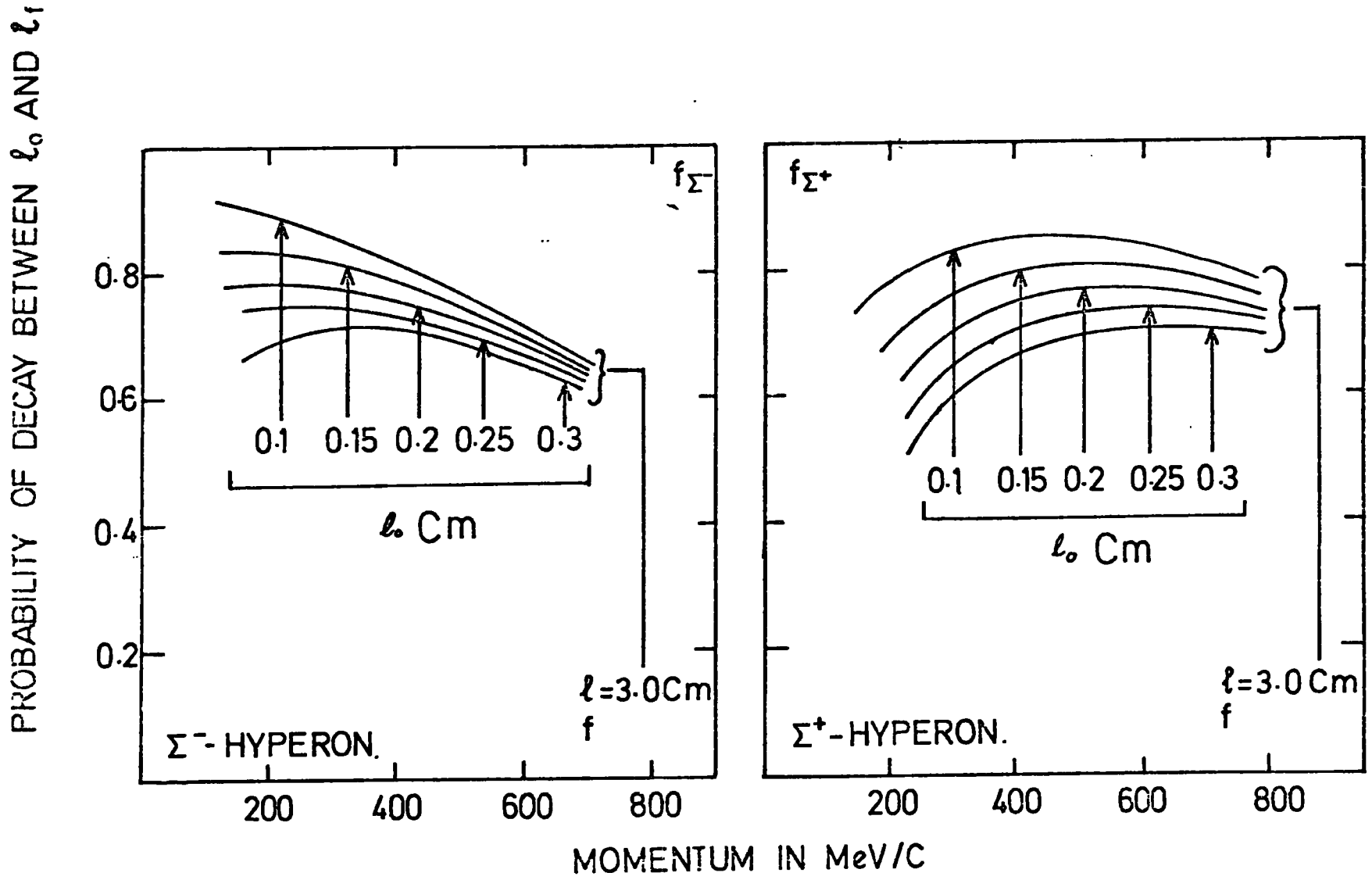

FIG. 6·4 PROBABILITY OF DECAY OF THE Σ·- HYPERONS AS FUNCTION OF THE Σ- HYPERON MOMENTUM.

P_{K^-} in MeV/c	γ-ratio from the cross sections	γ-ratio from Σ_π decay modes
200 - 280	0.69 ± 0.09	0.62 ± 0.07
280 - 320	0.59 ± 0.09	0.56 ± 0.05
320 - 360	0.51 ± 0.07	0.54 ± 0.04
360 - 380	0.70 ± 0.11	0.66 ± 0.07
380 - 400	0.61 ± 0.11	0.66 ± 0.07
400 - 420	0.64 ± 0.11	0.59 ± 0.05
420 - 460	0.56 ± 0.10	0.49 ± 0.06

Table 6.4: γ-ratio (Σ^-/Σ^+) as a function of the primary K^--meson momentum.

the corrected cross-sections.

This comparison is based on the assumption that the production angular distributions of Σ^+ and Σ^--hyperons are identical. It will be seen in the next section that this is not necessarily true for all ranges of momentum. The effect of this on the comparison will be considered then.

6.4 Production Angular Distribution

In Chapter 5 the production angular distributions of the charged sigma hyperons and the K^-P elastic scattering were used to account for the losses which occur at $|\cos \alpha^*| \sim 1.0$. Here α^* is the centre of mass angle of the outgoing π-meson at the production vertex with respect to the incident K^--meson direction in the case of the charged sigma hyperon production. Losses may be seen in the vicinity of $\cos \alpha^*_{\pi K} \sim \pm 1.0$. Note that these correspond to backwardly and forwardly emitted sigma hyperons respectively. In the case of K^-P elastic scattering α^* is the centre of mass angle of the outgoing K^--meson with respect to the primary K^--meson direction. The production angular distribution was studied for each of several primary momentum intervals where the same primary momentum bins have been used as for the determination of the expansion coefficients of the cross-sections.

In order to determine the expansion coefficients of the angular distribution the angular distribution in each momentum bin of the primary was represented in terms of a Legendre polynomials of the type

$$\frac{dN}{d(\cos \alpha^*)} = \sum_{n=0}^{n_{max}} A_n P_n (\cos \alpha^*) \qquad (6.3)$$

where A_n is the coefficient and $P_n(\cos \alpha^*)$ is the Legendre polynomial of order n. Fits to the different angular distributions were made using

MINUIT (6.1) which exploits a minimum χ^2 method. The production angular distributions are shown in Figures 6.5, 6.6 and 6.7 for the Σ^+-hyperon, Σ^--hyperon, and K^-P elastic scattering respectively. The results of the fits to the angular distributions using the above mentioned expression with $n_{max} = 3$ (where it was found that this is sufficient) are drawn as curves on the same figures.

The values of A_n/A_o are obtained by fitting the experimental distributions between $-0.80 \leqslant \cos\alpha^* \leqslant +0.80$ to avoid the areas of loss. The coefficients A_n/A_o for the three channels as a function of the primary momentum are given in Tables 6.5, 6.6 and 6.7. These coefficients are shown also on Figures 6.8, 6.9 and 6.10 for the Σ^+-hyperon, Σ^--hyperon, and K^-P elastic scattering respectively.

The fitted curves of the production angular distributions have been drawn between $-1.0 \leqslant \cos\alpha^* \leqslant +1.0$ on Figures 6.5 to 6.7.

P_{K^-} in MeV/C	A_1/A_o	A_2/A_o	A_3/A_o
280 - 320	-0.42 ± 0.28	-0.34 ± 0.29	-0.29 ± 0.53
320 - 360	-0.87 ± 0.26	0.62 ± 0.22	-0.41 ± 0.38
360 - 380	-0.32 ± 0.36	0.79 ± 0.28	0.24 ± 0.51
380 - 400	-0.34 ± 0.33	1.19 ± 0.20	- 0.024± 0.43
400 - 420	0.08 ± 0.17	1.35 ± 0.21	0.07 ± 0.20
420 - 460	-0.06 ± 0.36	0.77 ± 0.26	0.02 ± 0.48

Table 6.5: Legendre polynomial coefficients for

$K^-P \rightarrow \pi^- + \Sigma^+$

P_{K^-} in MeV/C	A_1/A_o	A_2/A_o	A_3/A_o
280 - 320	0.19 ± 0.35	-0.26 ± 0.35	-0.33 ± 0.54
320 - 360	-0.06 ± 0.30	-0.51 ± 0.32	-0.67 ± 0.50
360 - 380	0.09 ± 0.35	-0.50 ± 0.37	-0.51 ± 0.51
380 - 400	0.69 ± 0.31	0.73 ± 0.25	0.61 ± 0.45
400 - 420	0.35 ± 0.38	0.81 ± 0.28	0.53 ± 0.50
420 - 460	0.69 ± 0.39	1.165± 0.27	0.08 ± 0.48

Table 6.6: Legendre polynomial coefficients for

$K^- P \rightarrow \pi^+ \Sigma^-$

P_{K^-} in MeV/C	A_1/A_o	A_2/A_o	A_3/A_o
280 - 320	-0.02 ± 0.15	-0.13 ± 0.21	-0.10 ± 0.22
320 - 360	0.27 ± 0.12	0.16 ± 0.17	0.38 ± 0.19
360 - 380	0.28 ± 0.13	0.97 ± 0.14	-0.19 ± 0.17
380 - 400	0.54 ± 0.13	1.01 ± 0.15	0.56 ± 0.17
400 - 420	0.31 ± 0.26	0.85 ± 0.19	-0.08 ± 0.34
420 - 460	0.23 ± 0.13	0.76 ± 0.15	-0.10 ± 0.17

Table 6.7: Legendre polynomial coefficients for

$K^- P \rightarrow K^- P$

P_{K^-} in MeV/C	A_1/A_o I	A_1/A_o II	A_1/A_o III
280 - 320	-0.42 ± 0.28	-0.34 ± 0.35	-0.20 ± 0.23
320 - 360	-0.87 ± 0.26	-0.55 ± 0.19	-0.61 ± 0.15
360 - 380	-0.32 ± 0.36	-0.70 ± 0.37	-0.41 ± 0.25
380 - 400	-0.34 ± 0.33	-0.48 ± 0.35	-0.25 ± 0.13
400 - 420	0.08 ± 0.17	0.10 ± 0.20	-0.09 ± 0.14
420 - 460	-0.06 ± 0.36	0.34 ± 0.40	-0.02 ± 0.12
P_{K^-} in MeV/C	A_2/A_o I	A_2/A_o II	A_2/A_o III
280 - 320	-0.34 ± 0.29	-0.60 ± 0.39	-0.25 ± 0.23
320 - 360	0.62 ± 0.22	0.55 ± 0.19	0.61 ± 0.15
360 - 380	0.79 ± 0.28	0.92 ± 0.27	0.87 ± 0.18
380 - 400	1.19 ± 0.20	1.10 ± 0.24	1.12 ± 0.13
400 - 420	1.35 ± 0.21	1.31 ± 0.20	1.01 ± 0.13
430 - 460	0.77 ± 0.26	0.77 ± 0.27	0.78 ± 0.18
P_{K^-} in MeV/C	A_3/A_o I	A_3/A_o II	A_3/A_o III
280 - 320	-0.29 ± 0.53	-0.21 ± 0.57	0.27 ± 0.36
320 - 360	-0.41 ± 0.38	-0.50 ± 0.23	-0.14 ± 0.27
360 - 380	0.24 ± 0.51	-0.17 ± 0.50	0.22 ± 0.34
380 - 400	-0.02 ± 0.43	-0.11 ± 0.47	0.11 ± 0.17
400 - 420	0.07 ± 0.20	0.37 ± 0.24	0.06 ± 0.15
420 - 460	0.02 ± 0.48	0.09 ± 0.55	0.09 ± 0.17

Table 6.8: Legendre polynomial coefficients for the different data sets of the production of Σ^+-hyperon.

I = Events from the Durham share of the film for the two modes of decay of the Σ^+-hyperon

II = Events from the Durham and Birmingham shares of the film for the Σ^+_p mode of decay

III = Events from the Durham and Birmingham shares of the film for the two decay modes of the Σ^+-hyperon.

P_{K^-} in MeV/C	B_1/A_o	B_2/A_o	B_3/A_o
280 - 320	0.15 ± 0.15	-0.07 ± 0.11	-0.02 ± 0.09
320 - 360	0.49 ± 0.10	-0.39 ± 0.08	0.07 ± 0.06
360 - 380	0.35 ± 0.13	-0.23 ± 0.12	0.17 ± 0.10
380 - 400	0.54 ± 0.11	-0.01 ± 0.11	0.19 ± 0.10
400 - 420	0.39 ± 0.12	-0.01 ± 0.12	0.04 ± 0.10
420 - 460	0.46 ± 0.12	0.21 ± 0.11	0.07 ± 0.09

Table 6.9: Polarisation Legendre coefficients as a function of incident momentum for the reaction $K^- + P \rightarrow \pi^- + \Sigma^+$.

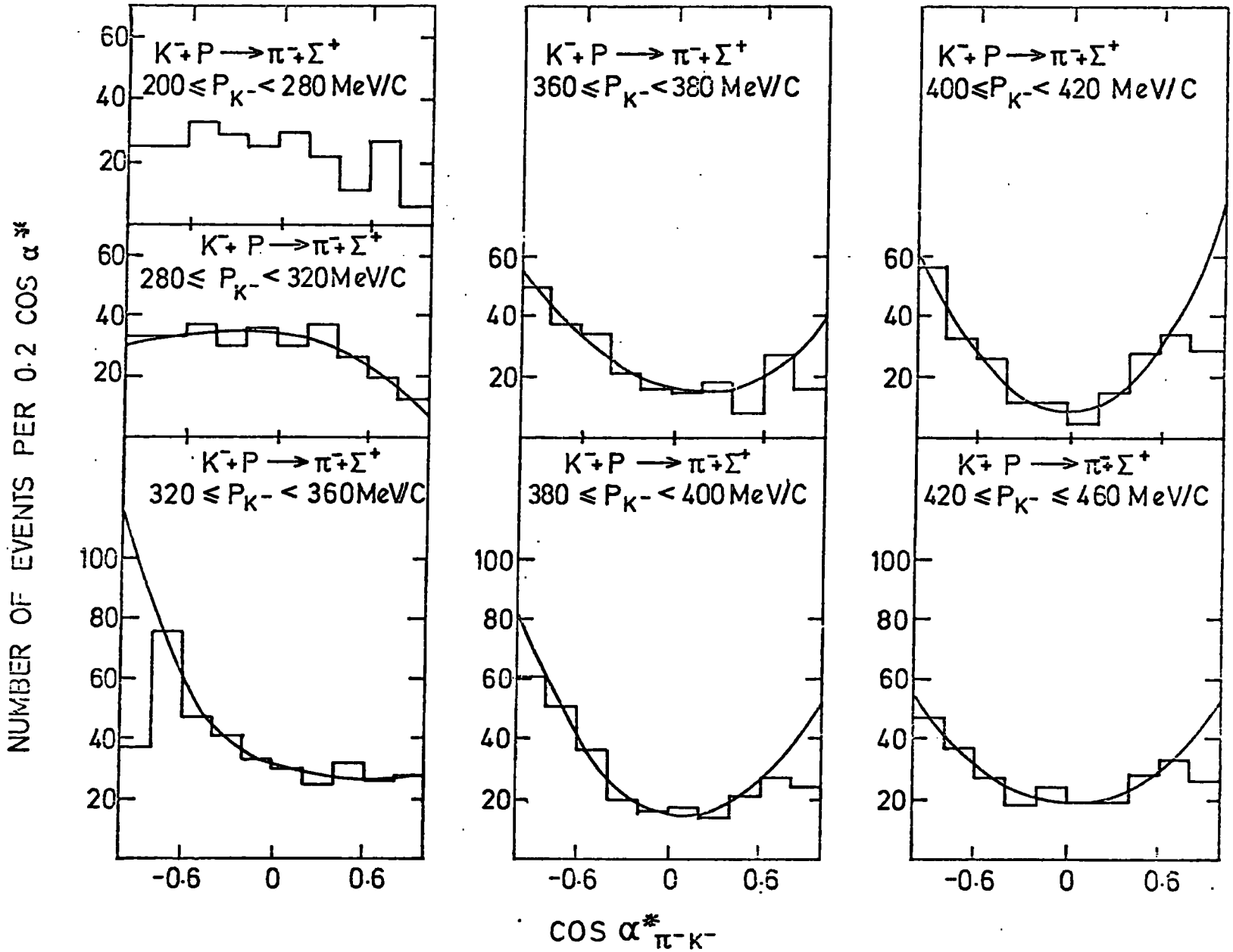

FIG 6·5 PRODUCTION ANGULAR DISTRIBUTION OF THE REACTION $K^- + P \rightarrow \pi^- + \Sigma^+$

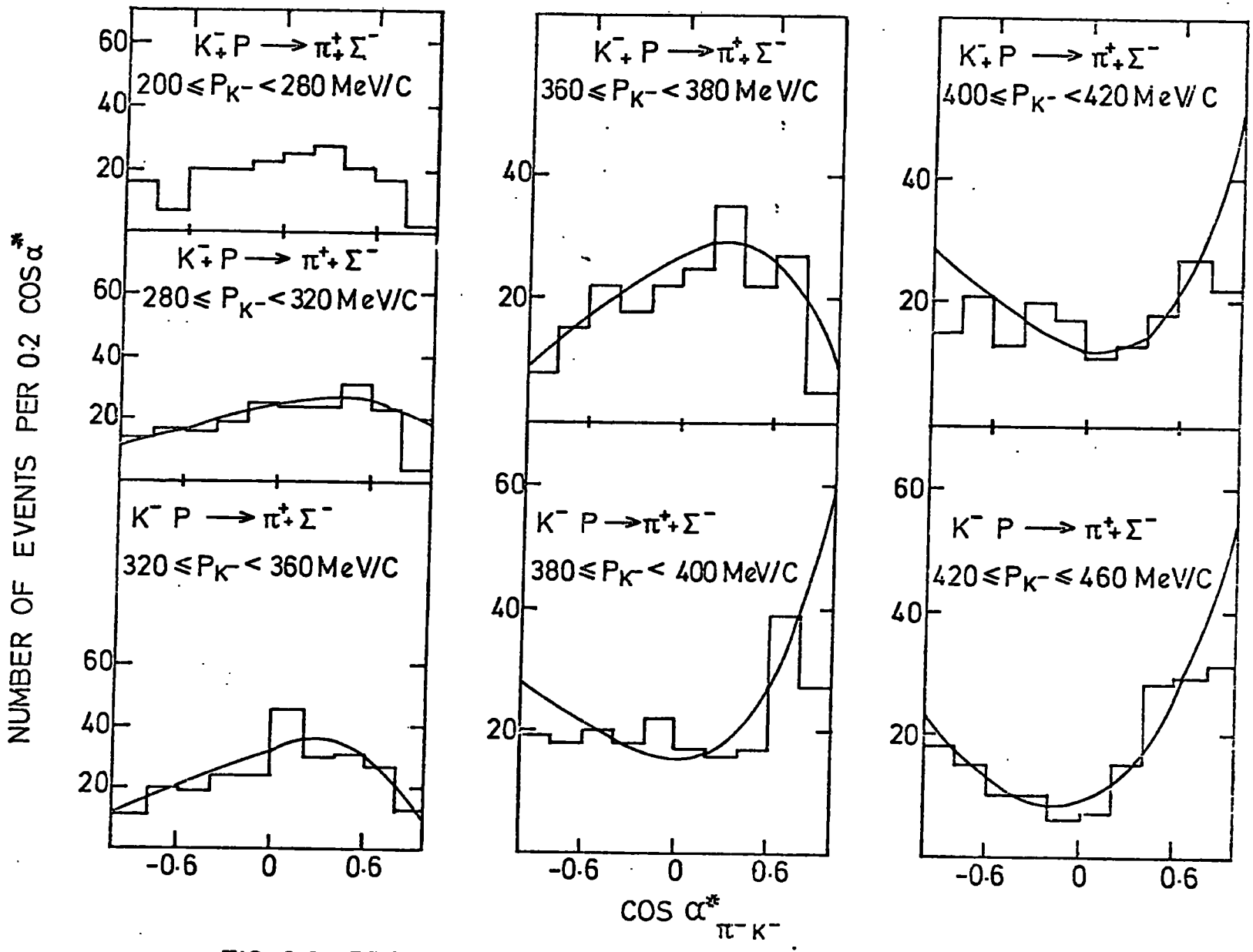

FIG 6.6 PRODUCTION ANGULAR DISTRIBUTION OF THE REACTION $K^- + P \rightarrow \pi^+ + \Sigma^-$

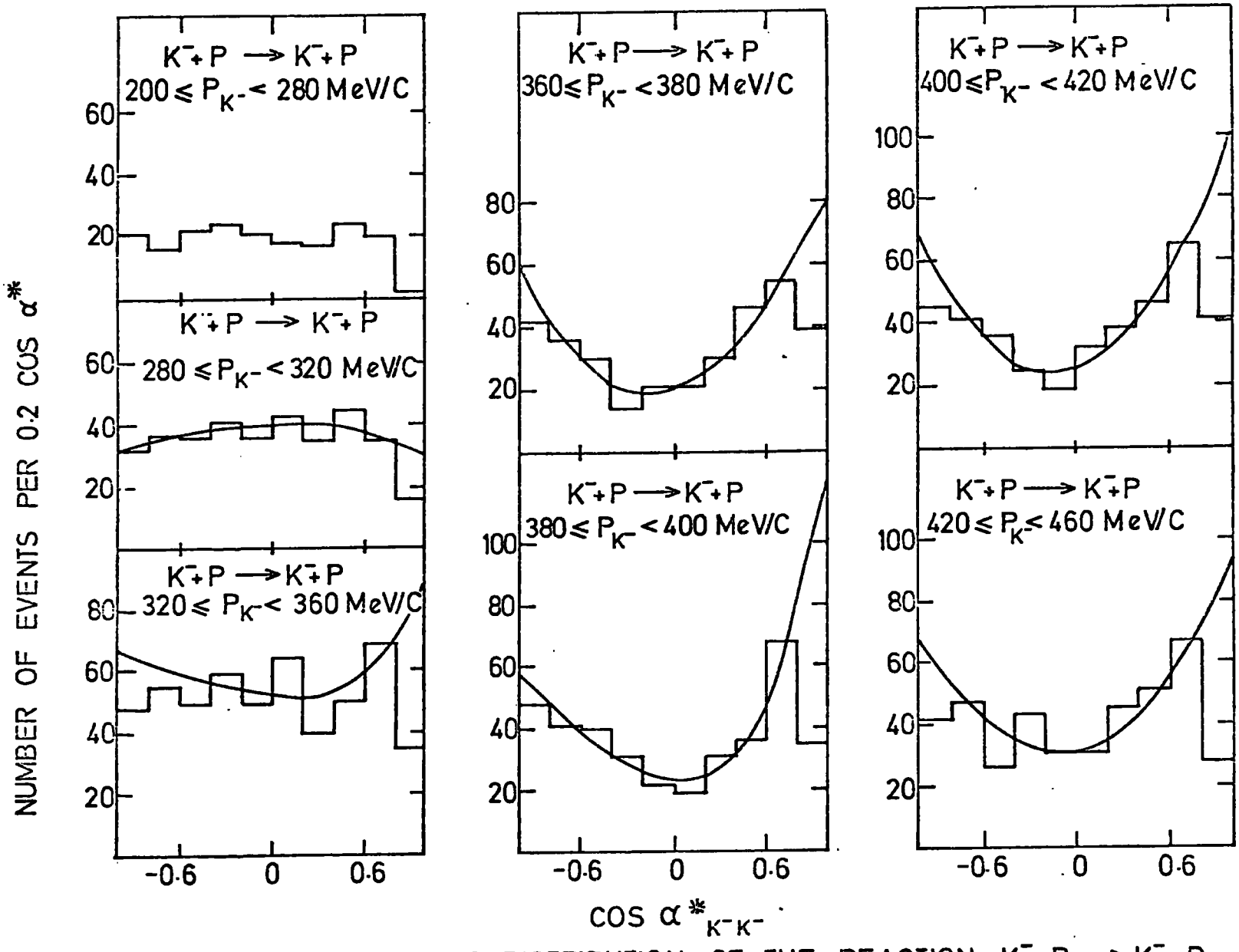

FIG. 6·7 ANGULAR DISTRIBUTION OF THE REACTION $K^- + P \longrightarrow K^- + P$

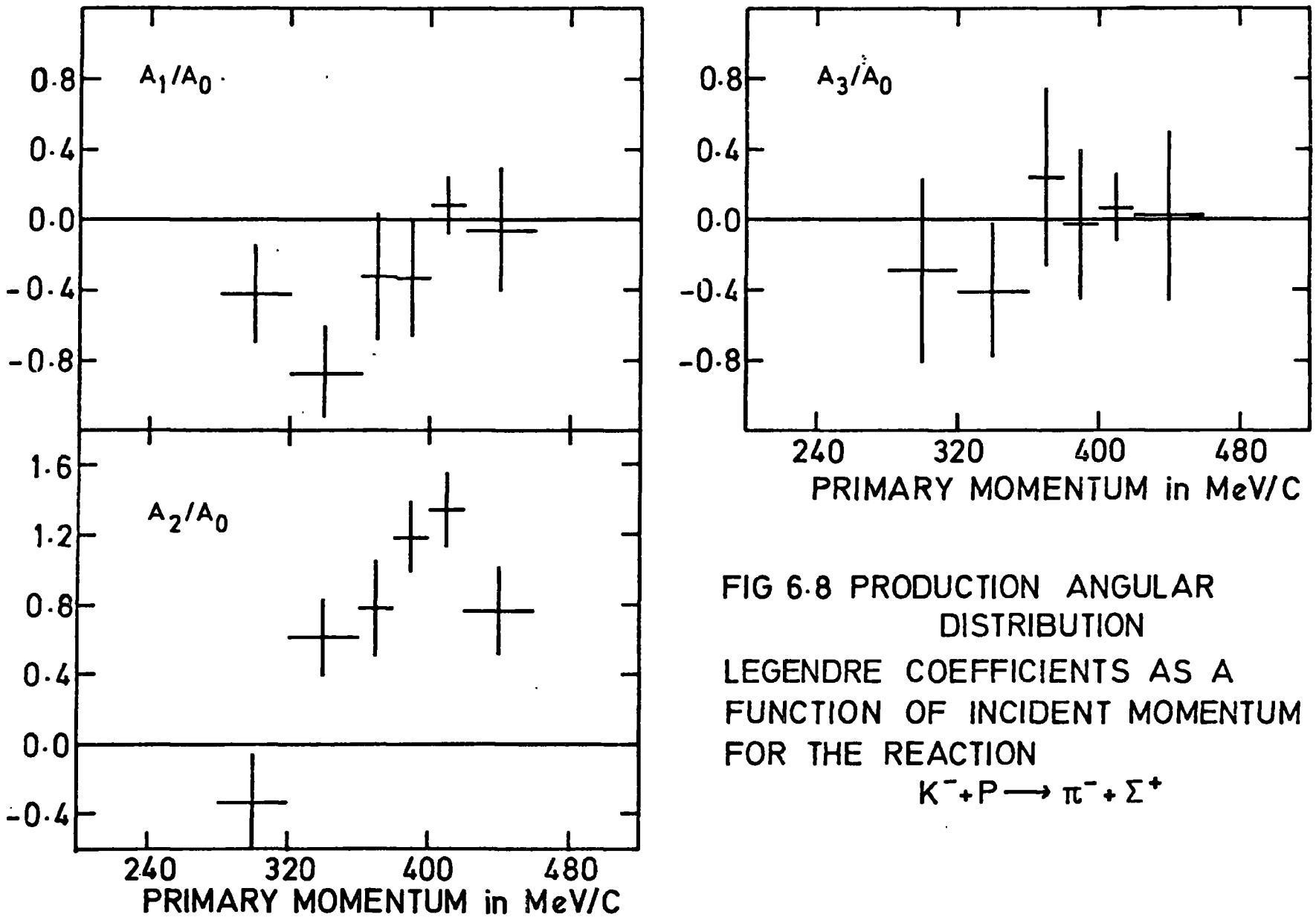

FIG 6·8 PRODUCTION ANGULAR DISTRIBUTION

LEGENDRE COEFFICIENTS AS A FUNCTION OF INCIDENT MOMENTUM FOR THE REACTION

$K^- + P \longrightarrow \pi^- + \Sigma^+$

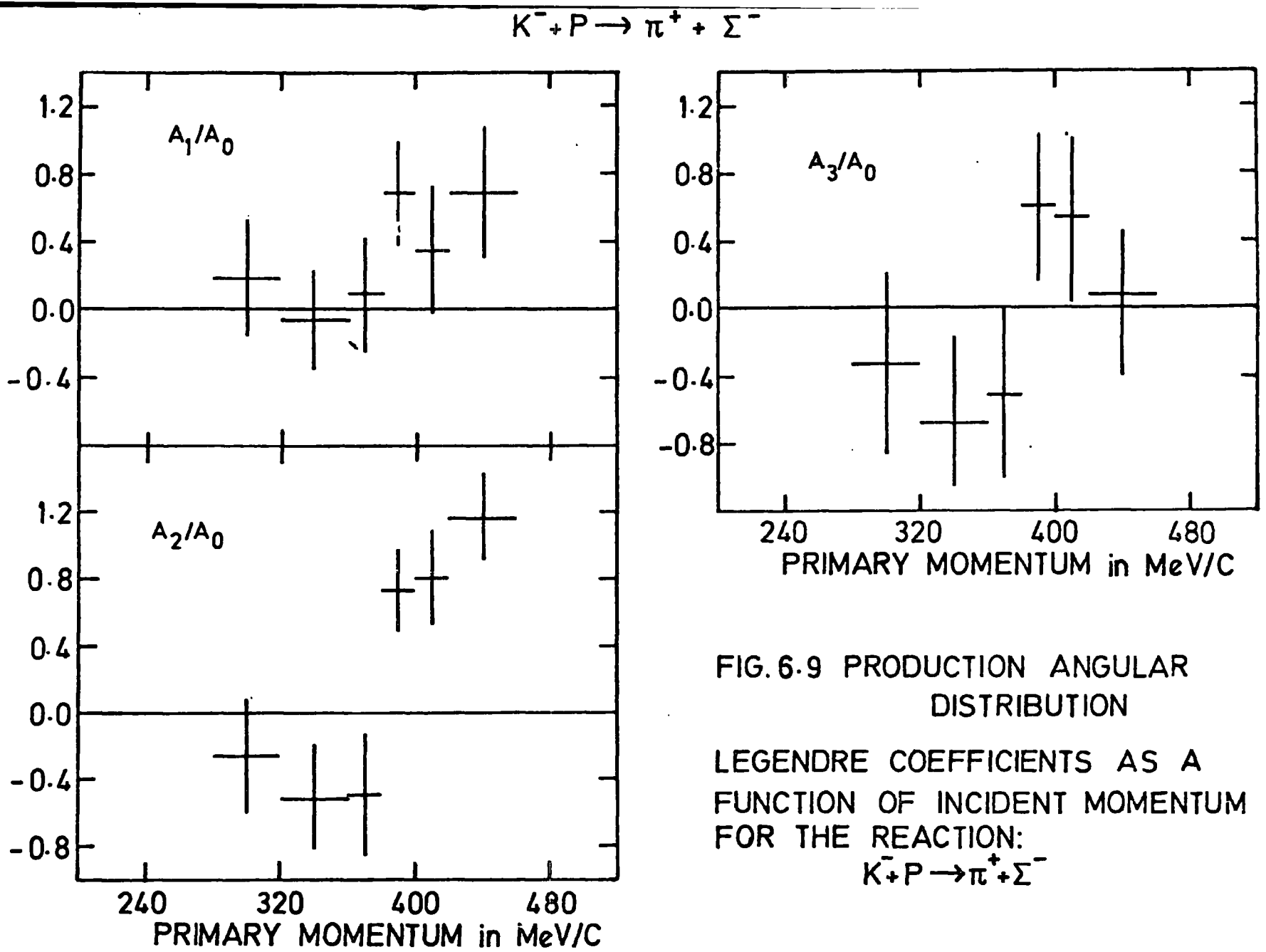

FIG. 6·9 PRODUCTION ANGULAR DISTRIBUTION

LEGENDRE COEFFICIENTS AS A FUNCTION OF INCIDENT MOMENTUM FOR THE REACTION:

$K^- + P \rightarrow \pi^+ + \Sigma^-$

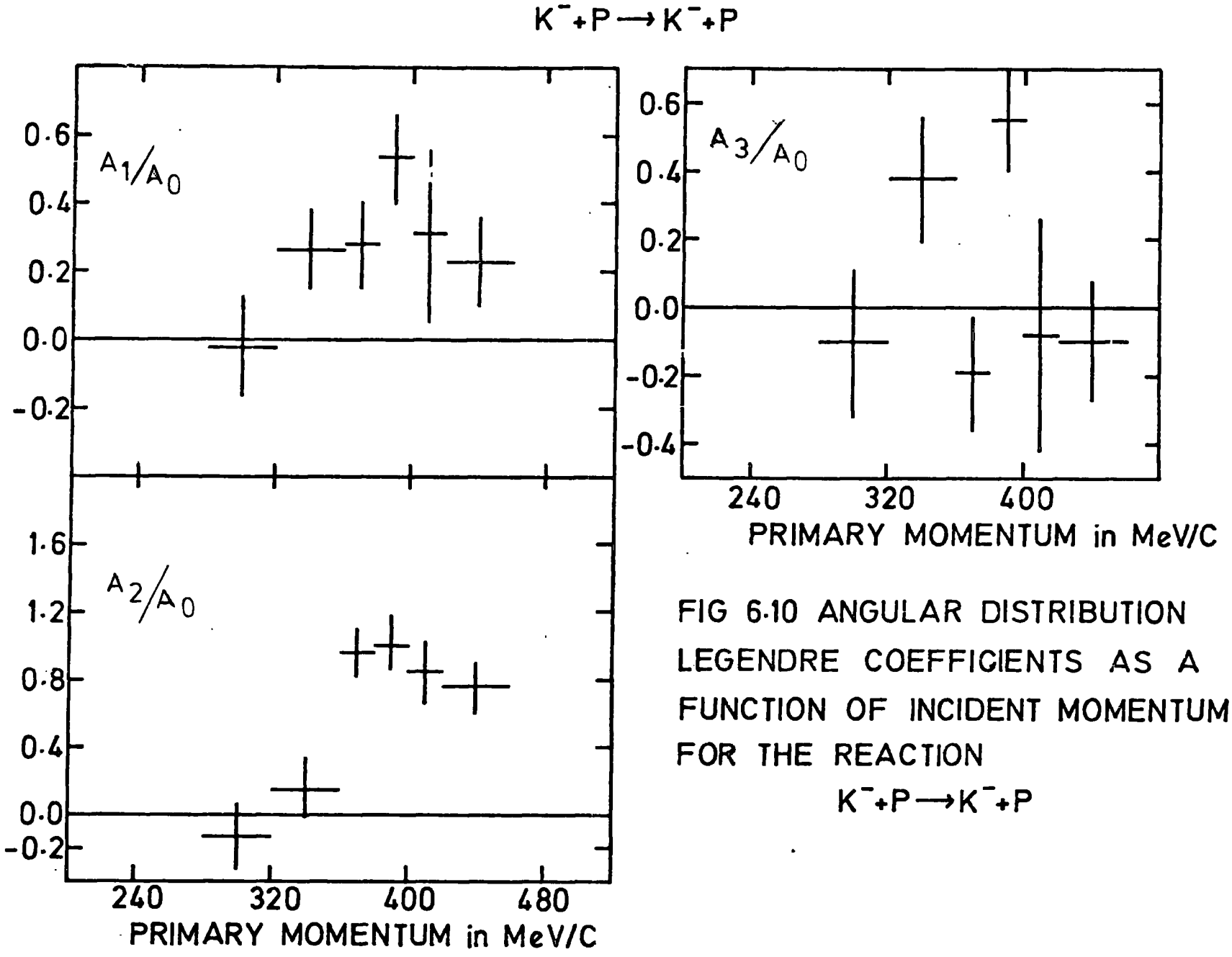

FIG 6.10 ANGULAR DISTRIBUTION LEGENDRE COEFFICIENTS AS A FUNCTION OF INCIDENT MOMENTUM FOR THE REACTION

$K^- + P \rightarrow K^- + P$

As can be seen from the above tables and their associated figures, the angular distributions in the three channels show a strong $\cos^2\alpha^*$ dependence in the primary momentum region about 390 MeV/C due to the $\Lambda(1520)$ resonance and this usually disappears in the regions below and above the resonance. The structure in A_1/A_o specially apparent in the case of elastic scattering in the region of the $\Lambda(1520)$ resonance is due to the interference of a small background P-wave with the resonant D-wave. The coefficient A_2/A_o has a very marked behaviour and it is the result of the resonant D-wave.

Examination of the angular distribution figures shows that probably the P-wave starts to show itself in the region of the primary momentum $P_{K^-} > 200$ MeV/C. The production angular distribution for the region $200 \leq P_{K^-} < 280$ MeV/C in the case of the Σ^+-hyperon was fitted only to a P-wave where the coefficient A_1/A_o was found to be in good agreement for this region if the values of A_1/A_o of Figure 6.8 were extended smoothly to the lower region. Also as it is seen from the figures of A_n/A_o that the coefficient A_3/A_o for the three channels is very small and can be considered as being consistent with zero.

The γ-ratio was considered in the previous section where a comparison was made assuming that the angular distributions of production of Σ^+ and Σ^--hyperons are identical. It can be seen from Figure 6.5 and 6.6 that this is not always true. However the differences occur at values of $\cos\alpha^*$ of ± 1.0 where the solid angle of production is small. Consequently the effects of losses at these extreme values of $\cos\alpha^*$ will have little effect on the γ-ratio.

6.5 Σ^+-Hyperon Polarisation

The polarisation of the Σ^+-hyperon produced by the reaction $K^- + P \rightarrow \pi^- + \Sigma^+$ can be measured by making use of its parity non-conserving

weak decay. Although there are two modes of decay of the Σ^+-hyperon (Σ^+_p and Σ^+_π) the polarisation of the hyperon is determined through its proton mode of decay (Σ^+_p).

Given the polarisation $\underline{P}$ of the Σ^+-hyperon, the angular distribution of the decay proton from the parent Σ^+-hyperon integrated over the azimuth in the rest frame of the hyperon is

$$\frac{dN}{d(\cos b)} = \frac{N_T}{2} \quad (1 + \alpha_o \underline{P} \cos b) \tag{6.4}$$

Here N_T is the total number of events, α_o is the decay asymmetry parameter for the Σ^+_p mode of decay ($\alpha_o = -0.979$) and b is the angle between the proton and the polarisation directions. Since the production of the Σ^+-hyperon is due to a parity conserving strong interaction, the hyperon may only be polarised in a direction normal to the production plane. Consequently the angle b is given by

$$\cos b = \hat{n} \cdot \hat{p} \tag{6.5}$$

where $\hat{p}$ is the unit vector in the direction of the decay proton in the Σ^+-hyperon rest frame and $\hat{n}$ is the unit vector normal to the production plane. This is defined by

$$\hat{n} = \frac{\vec{K} \times \vec{\Sigma}}{|\vec{K} \times \vec{\Sigma}|} \tag{6.6}$$

where $\vec{K}$ and $\vec{\Sigma}$ are the momentum vectors (or directions) of the incident K^--meson and outgoing Σ^+-hyperon respectively.

The joint distribution of both the centre of mass production angle α^* (defined previously) and the angle b can be expressed by the following expansion

$$\frac{d^2N}{d(\cos\alpha^*)\,d(\cos b)} = \frac{N_T}{4}\left\{1 + \sum_{\ell=1}^{n}\frac{A_\ell}{A_0}\,P_\ell(\cos\alpha^*) \quad +\right.$$

$$\left. \alpha_0\cos b\,\sum_{\ell=1}^{n}\frac{B_\ell}{A_0}\,P_\ell^1(\cos\alpha^*)\right\} \qquad (6.7)$$

In this the production angular distribution is defined by the Legendre polynomial coefficients A_ℓ which were explained and determined earlier, and the variation of the polarisation with the production angle is contained in the value of the coefficients B_ℓ of the associated Legendre polynomials $P_\ell^1(\cos\alpha^*)$. The values of B_{ℓ/A_0} can be projected from the experimental distribution of equation (6.7) by multiplying both sides by $P_\ell^1(\cos\alpha^*)\cos b$ and integrating over $\cos\alpha^*$ and $\cos b$. Then the following relation is obtained

$$B_{\ell/A_0} = \frac{3(2\ell+1)}{\alpha_0\,\ell(\ell+1)}\;\frac{1}{N_T}\sum_{J=1}^{N_T}(\cos b)_J\;P_\ell^1(\cos\alpha^*)_J \qquad (6.8)$$

where the integral has been replaced by a sum over the finite sample of N_T events.

The criteria for selecting events for the determination of the Σ^+-hyperon polarisation are the same as those used in the analysis of the angular distributions (Section 6.4). There the polynomial coefficients for the angular distributions were determined over a range of momentum bins. In the polarisation analysis momentum bins and selection criteria are unchanged except for the further selection that since only the Σ_p^+ mode of decay can be used to increase statistics; events from both the Durham and Birmingham samples of the film have been used. To test the compatibility of both samples of data the production angular distributions

for the combined data in the different momentum intervals were fitted to Legendre polynomial expansions. This determined the A_ℓ/A_o values for both the Σ^+_p mode of decay and for the combined Σ^+_p and Σ^+_π modes of decay. These A_ℓ/A_o values were compared with the values determined using the Durham events. The values are given in Table 6.8 where it is seen that there are no significant differences. Since the values of A_ℓ/A_o are to be used in the determination of the Σ^+-hyperon polarisation, then these values obtained from the largest statistics were used: that is for the combined sample of Durham and Birmingham events using both modes of decay.

The B_ℓ/A_o values are found for the Σ^+_p mode of decay, through equation (6.8). These were determined directly on an event by event basis and they are given in Table 6.9. The B_ℓ/A_o values are shown on Figure 6.11. The polarisation of the Σ^+-hyperon was determined using the A_ℓ/A_o and B_ℓ/A_o values through the following formula

$$\underline{P}\ (\cos\alpha^*) = \frac{\sum_\ell (B_\ell/A_o)\ P^1_\ell\ (\cos\alpha^*)}{1 + \sum_\ell\ (A_\ell/A_o)\ P_\ell\ (\cos\alpha^*)} \qquad (6.9)$$

in the different momentum intervals. The polarisation determined in this way is plotted on Figure 6.12 as a function of $\cos\alpha^*$ for each primary momentum bin. For comparison there is shown on Figure 6.12a the values of $\alpha_o\ \underline{P}$ taken from reference 6.2 at a momentum of 410 - 510 MeV/C.

It is seen that the agreement between the polarisation in the last momentum bin (420 - 460 MeV/C) determined above and Figure 6.12a is good. The polarisation of the Σ^+-hyperon in the lower momentum bins of the primary (the two momentum bins 380 - 400 MeV/C and 400 - 420 MeV/C) are also in good agreement with a previous determination (6.3).

The errors on the polarisation values cannot be determined directly from the A_ℓ/A_o and B_ℓ/A_o values since these are correlated.

Instead an envelope which represents a variation of one standard deviation in the values of A_ℓ/A_0 and B_ℓ/A_0 was determined in each of the primary momentum intervals. These envelopes are shown on Figure 6.12 as dotted curves drawn by hand. These were calculated using the following formula

$$\Delta \underline{P}\ (\cos\alpha^*) = \left[\left\{ \frac{\sum_\ell \Delta\ (B_\ell/A_0)\ P_\ell^1\ (\cos\alpha^*)}{\sum_\ell (B_\ell/A_0)\ P_\ell^1\ (\cos\alpha^*)} \right\}^2 + \left\{ \frac{\sum_\ell \Delta\,(1 + (A_\ell/A_0)\ P_\ell\ (\cos\alpha^*)}{1 + \sum_\ell\ (A_\ell/A_0)\ P_\ell\ (\cos\alpha^*)} \right\}^2 \right]^{\frac{1}{2}} \underline{P}\ (\cos\alpha^*) \qquad (6.10)$$

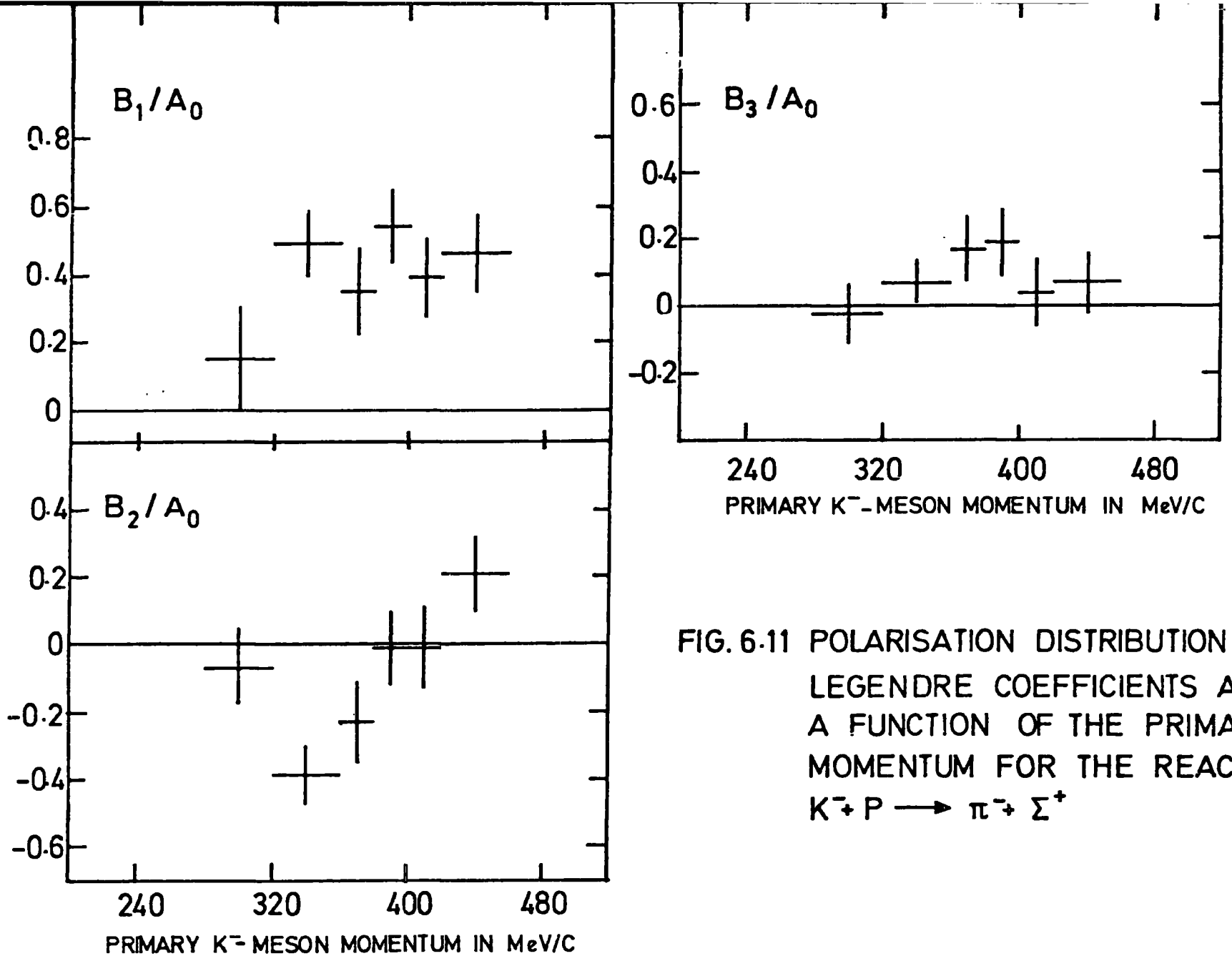

FIG. 6·11 POLARISATION DISTRIBUTION LEGENDRE COEFFICIENTS AS A FUNCTION OF THE PRIMARY MOMENTUM FOR THE REACTION $K^- + P \longrightarrow \pi^- + \Sigma^+$

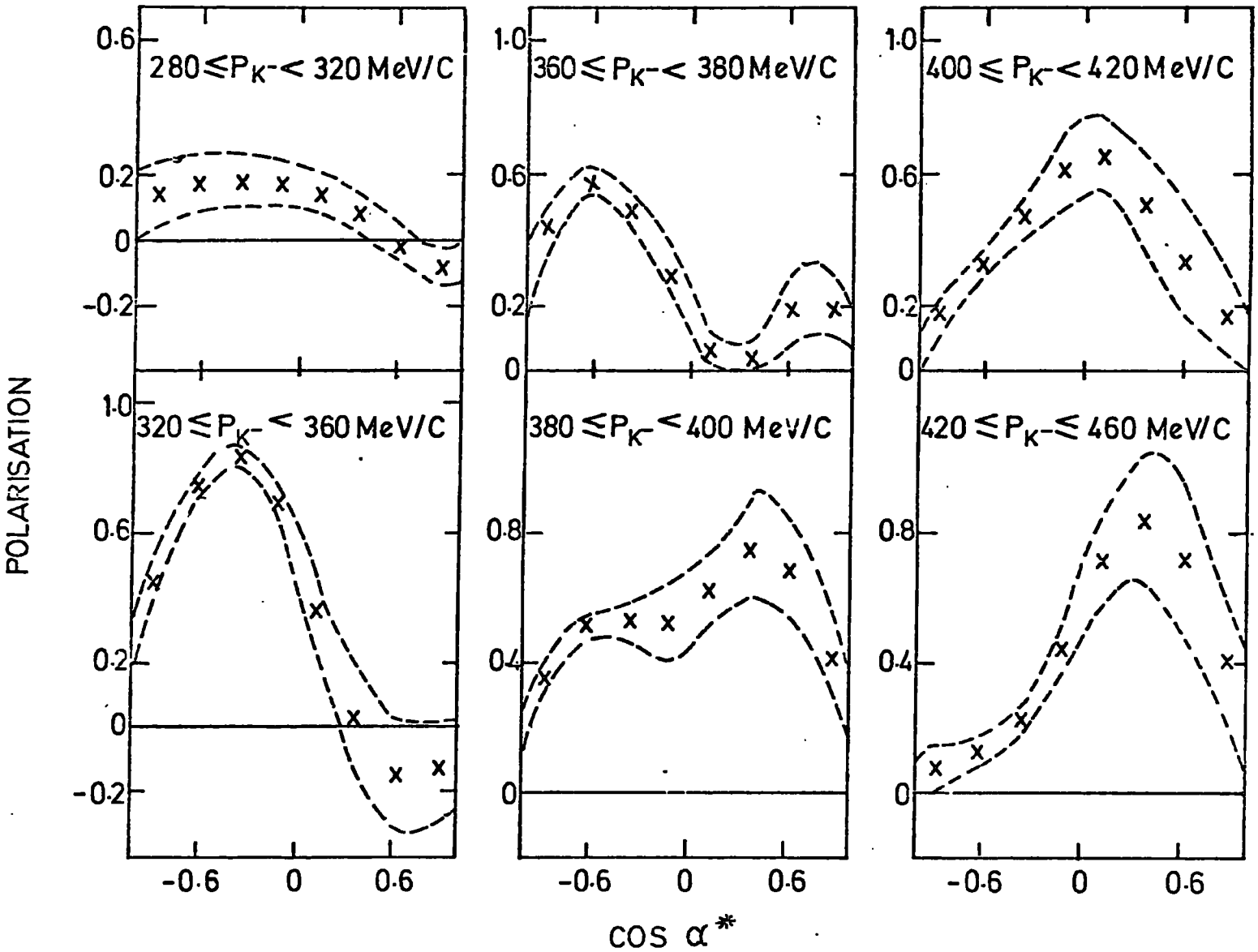

FIG. 6·12 Σ^+ - HYPERON POLARISATION DISTRIBUTION AS A FUNCTION OF COS α^* IN DIFFERENT PRIMARY MOMENTUM INTERVALS FOR THE REACTION $K^- + P \rightarrow \pi^- \Sigma^+$

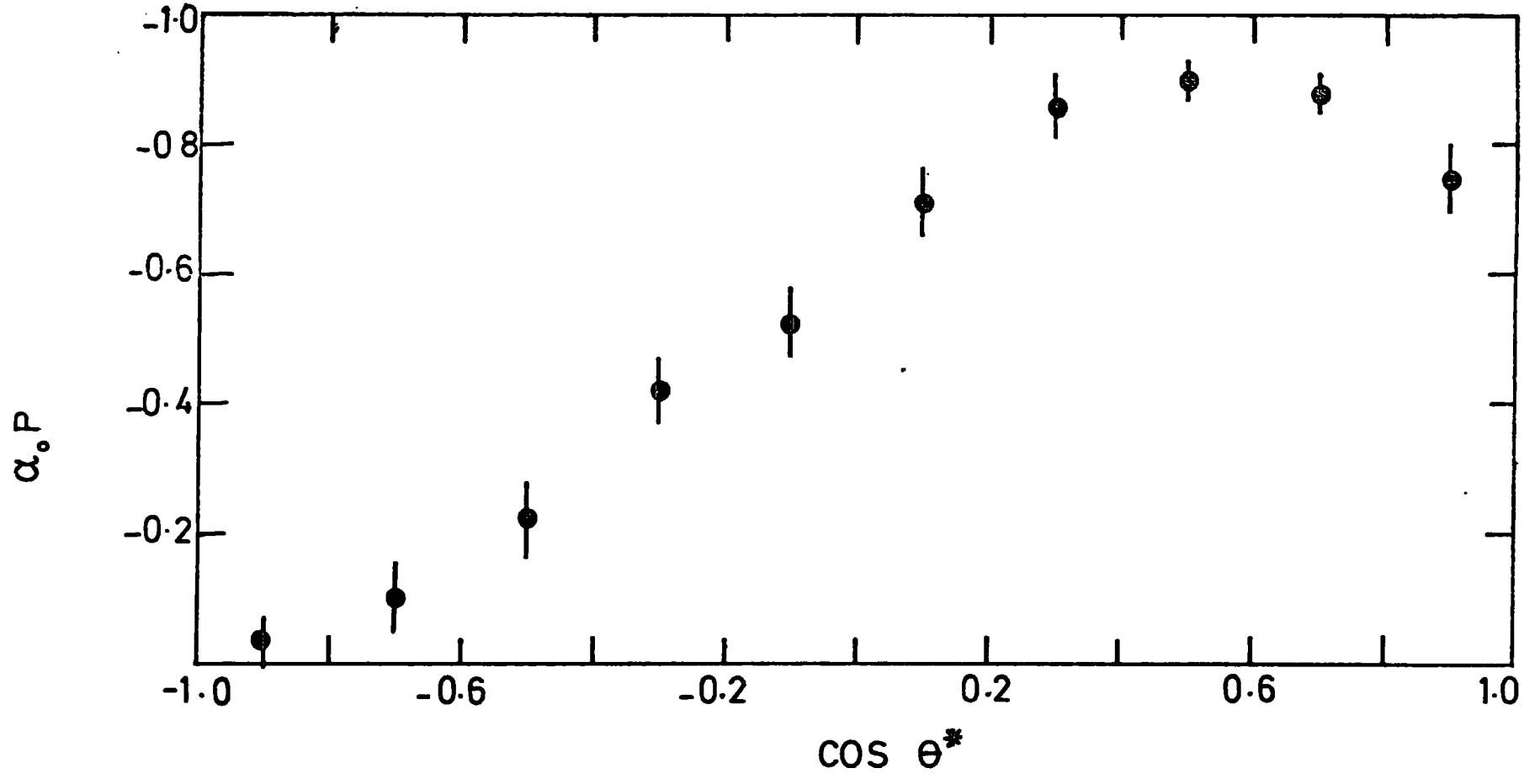

FIG. 6·12 a $\alpha_o P$ AS A FUNCTION OF COS θ^* FOR $\Sigma^+ p$ EVENTS FROM REFERENCE 6·2 WHERE α_o IS THE DECAY ASYMMETRY PARAMETER ($\alpha_o = -0.979$) P IS THE HYPERON POLARISATION AND θ^* IS THE PRODUCTION ANGLE OF THE π^- WITH RESPECT TO THE INCIDENT K^- IN THE CENTRE OF MASS SYSTEM

CHAPTER VII

ISOSPIN CROSS-SECTIONS OF THE SIGMA HYPERONS AND GENERAL CONCLUSIONS

7.1 Introduction

In the last chapter the variation of the cross-sections for $\Sigma^{\pm}\pi^{\mp}$ production with the primary incident momentum has been found (Figures 6.1a and 6.2a) and the production angular distributions analysed. Both show evidence of structure at about 395 MeV/C primary momentum corresponding to the formation of the $\Lambda(1520)$ resonance. As explained in chapter one, the charged sigma channels involve the superposition of isospin 0 and 1 amplitudes, and the main purpose of the present chapter will be the extraction of the separate isospin contributions. Recalling that

$$\langle \pi^-\Sigma^+ |T| K^-P \rangle = \frac{1}{2} T_1^{\Sigma} + \frac{1}{\sqrt{6}} T_o^{\Sigma}$$

$$\langle \pi^+\Sigma^- |T| K^-P \rangle = -\frac{1}{2} T_1^{\Sigma} + \frac{1}{\sqrt{6}} T_o^{\Sigma}$$

and

$$\langle \pi^o\Sigma^o |T| K^-P \rangle = -\frac{1}{\sqrt{6}} T_o^{\Sigma}$$

then the separate isospin contributions are expressed by the relations

$$|T_1^{\Sigma}|^2 = 2\left\{(\sigma_+ + \sigma_-) - 2\sigma_o\right\} \qquad (7.1)$$

$$|T_o^{\Sigma}|^2 = 6\,\sigma_o \qquad (7.2)$$

Here $|T_I^{\Sigma}|^2$ is the cross-section for a $\Sigma\pi$ final state with isospin I and σ_+ σ_-, and σ_o are the measured cross-sections for $\pi^-\Sigma^+$, $\pi^+\Sigma^-$, and $\pi^o\Sigma^o$ respectively. The measurement of σ_o is not described in this thesis, but the treatment of the available data will be dealt with in Section 7.3. Also a brief account of the behaviour of the cross-sections in terms of pure

isospin amplitudes will be given. Finally at the end of the chapter general conclusions about the work of this thesis are given.

7.2 Reconsideration of the cross-sections for $\Sigma^{\pm}$-hyperons production

The behaviour of the charged $\Sigma\pi$ cross-sections will be displayed in a slightly different way to that of Figures 6.1a and 6.2a. Any cross-section integrated over angles can be expressed as a partial wave expansion

$$\sigma = \pi\lambda\!\!\!^{-2} \left\{ |S_1|^2 + |P_1|^2 + 2|P_3|^2 + 2|D_3|^2 + \text{higher terms} \right\} \tag{7.3}$$

where $\lambda\!\!\!^{-}$ is the centre of mass de Broglie wavelength ($\lambda\!\!\!^{-} = h/P^*$ where P^* is the centre of mass momentum), S, P, D are the partial wave amplitudes for ℓ = 0, 1, 2 and the subscripts denote twice the total angular momentum J. For the isospin zero contribution to $|D_3|^2$ we expect a resonant Breit-Wigner variation as a function of total centre of mass energy, E. There is no evidence to suppose that the other partial waves depend sharply on E, so that the main variation apart from the resonance might be expected to arise from $\pi\lambda\!\!\!^{-2}$. Accordingly the cross-sections are more conveniently shown as the variation of $\sigma/\pi\lambda\!\!\!^{-2}$ with E, rather than directly in terms of laboratory momenta as in the last chapter. The data already given in Figures 6.1a and 6.2a are plotted again in Figure 7.1. The presence of the $\Lambda(1520)$ contribution is now very clearly marked for both charged sigma channels. The variation outside the resonance peaks is less well established since there are so few points. Towards lower energies the $\pi^-\Sigma^+$ cross-section in terms of $\pi\lambda\!\!\!^{-2}$ seems to have little change while the $\pi^+\Sigma^-$ cross-section may rise sharply. It is clear, since for K^-P at rest (E = 1.432 GeV) the ratio of $\pi^+\Sigma^-$ to $\pi^-\Sigma^+$ is 2.34 (ref. 1.18), that the observed rising of σ_- is qualitatively correct. However cross-sections

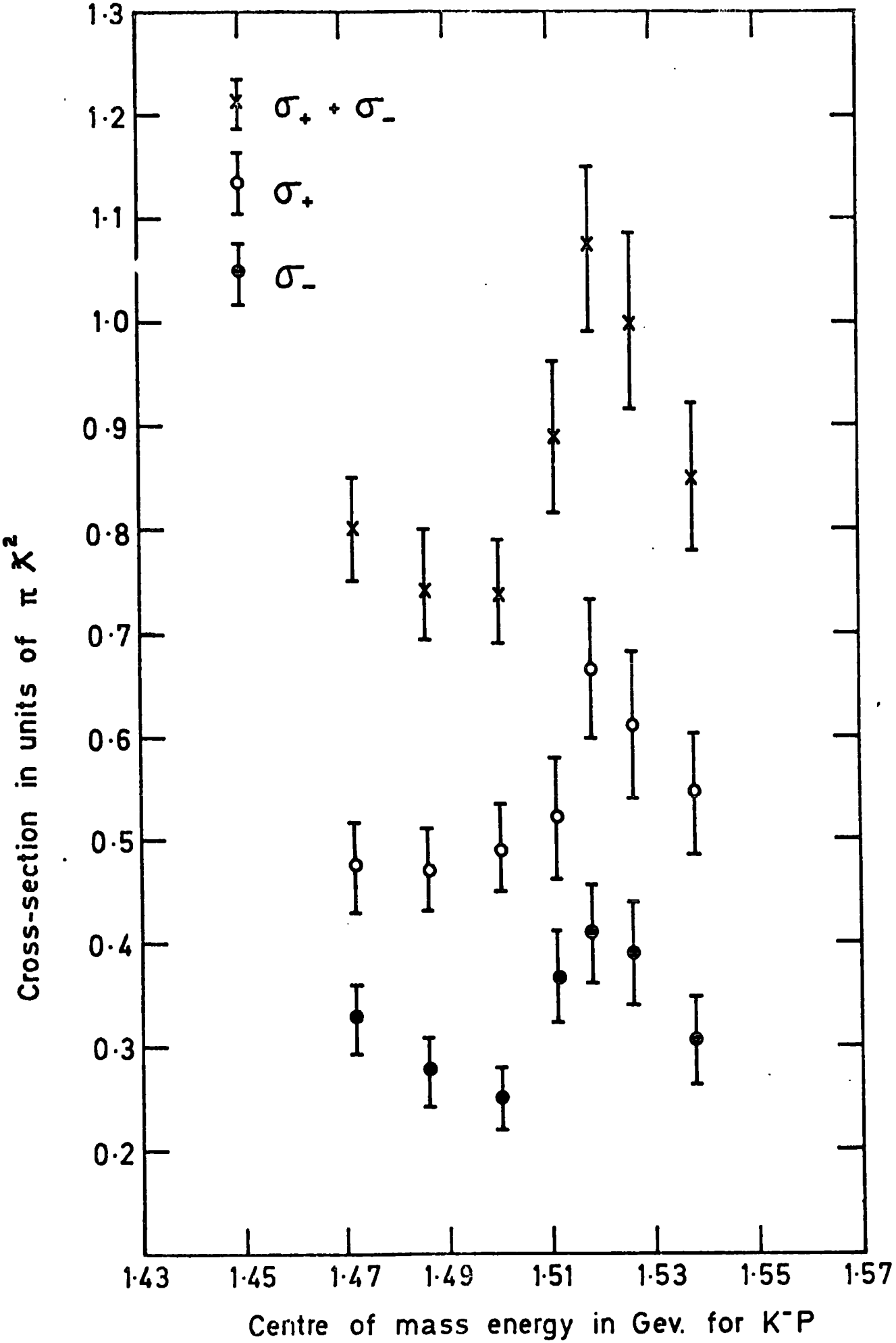

FIG. 7·1 The cross-sections of the reactions $K^-P \rightarrow \pi^-\Sigma^+$ and $K^-P \rightarrow \pi^+\Sigma^-$ in units of $\pi \lambda^2$ as a function of the cm energy.

at the lowest energy should be treated with some caution. This is not surprising as they are derived from data of low statistics at the edge of the measured momentum distribution in this experiment, where any spread due to measurement error would have its largest effect.

However in equation (7.1) the sum of the cross-sections for the production of charged sigma hyperons are required. Consequently individual data points are now based on the joint statistics which will tend to even out some of the fluctuation.

7.3 The cross-sections for Σ^o-hyperon Production

The cross-sections for Σ^o-hyperon production, together with those for Λ^o-hyperon production, have been determined and analysed for this experiment (reference 3.1) and the $\pi^o\Sigma^o$ cross-section in terms of $\pi\lambda^2$ is shown in Figure 7.2. Once again the resonant structure at 1520 MeV is seen in this pure isospin 0 channel. Compared to the cross-sections for $\Sigma^{\pm}$-hyperons production this cross-section is about three times smaller. Consequently the effects of low statistics are more important here and particularly so in equation (7.1). There the precision of the isospin cross-sections will be determined essentially by the Σ^o-hyperon cross-section, especially outside the resonance region, despite the relatively good precision of the cross-section for $\Sigma^{\pm}$-hyperon production.

To avoid this it is proposed to use the higher quality data of Mast et al (reference 1.17). In that experiment the cross-sections for Σ^o-hyperon production are given but the $\Sigma^{\pm}$ cross-sections are yet to be published. The Σ^o-hyperon cross-section of Mast et al are given in Figure 7.3. A comparison with Figure 7.2 shows that the momentum resolution of Mast et al experiment is higher than the present one in that the experimental width of the $\Lambda(1520)$ is narrower. This arises from the different

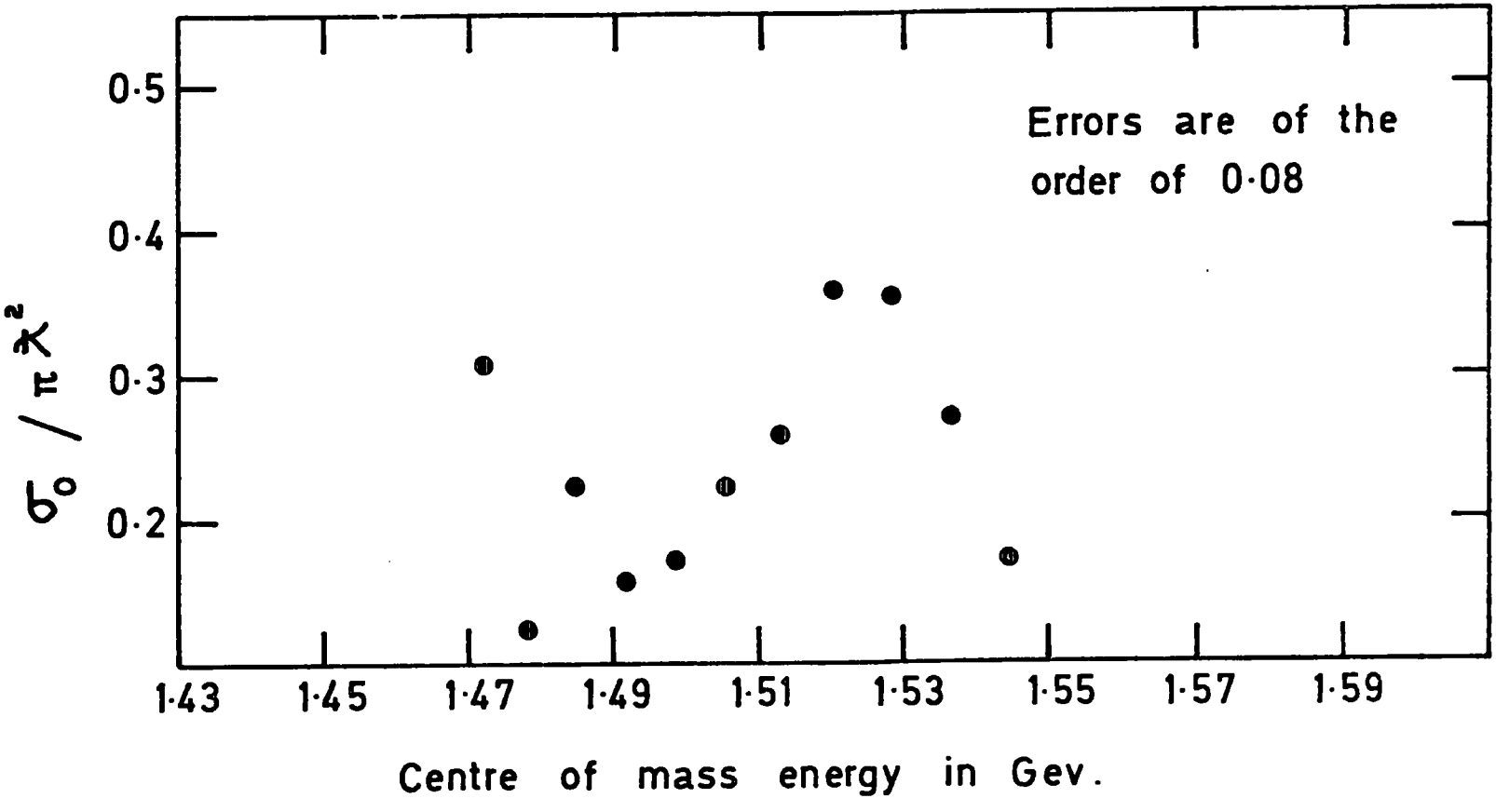

FIG. 7·2 Cross-section of the reaction $K^- P \rightarrow \pi^\circ \Sigma^\circ$ in units of $\pi \lambda^2$ as a function of cm energy from this experiment.

resolutions of primary momentum in the two experiments. Consequently if this σ_o is used in equation (7.1) systematic errors will be introduced where there is structure in the cross-sections from the different resolutions. A compromise which avoids this is to use the Durham data in the resonance region to give the appropriate momentum resolution and the data of Mast et al outside the resonance where the resolution is less important. Firstly the whole of Mast et al data (Figure 7.3) is fitted with a Breit-Wigner curve and background to determine the background shape. Then this background shape plus the Durham data in the resonance region is used for the variation of σ_o with energy (Figure 7.4).

The data points in Figure 7.3 were fitted to a linear background with two constants and a Breit-Wigner form for the resonance

$$\frac{\sigma_o}{\pi\lambda^2} = A + BE + \frac{CF\,\Gamma_o^2}{(E - 1.52)^2 + \frac{F^2\,\Gamma_o^2}{4}} \qquad (7.4)$$

where A and B are the constant of the linear background which were assumed parameters of the fit, C is a normalising constant. Γ_o is the width of the $\Lambda(1520)$ modified by F which is given by

$$F = \left(\frac{P}{P_o}\right)^5 \quad \frac{(P_o R)^4 + 3(P_o R)^2 + 9}{(P R)^4 + 3(P R)^2 + 9} \qquad (7.5)$$

This allows the variation of width with momentum across the resonance, P being the final state momentum in the centre of mass. The subscript, o, denotes the value at the resonance energy and R is the radius of interaction taken to be 4.0 GeV^{-1}. F is a combination of the dependence of the resonance width on energy due to the D-wave centrifugal barrier (hence the power 5 from $2\ell + 1$) and the matching of the wave function through the barrier.

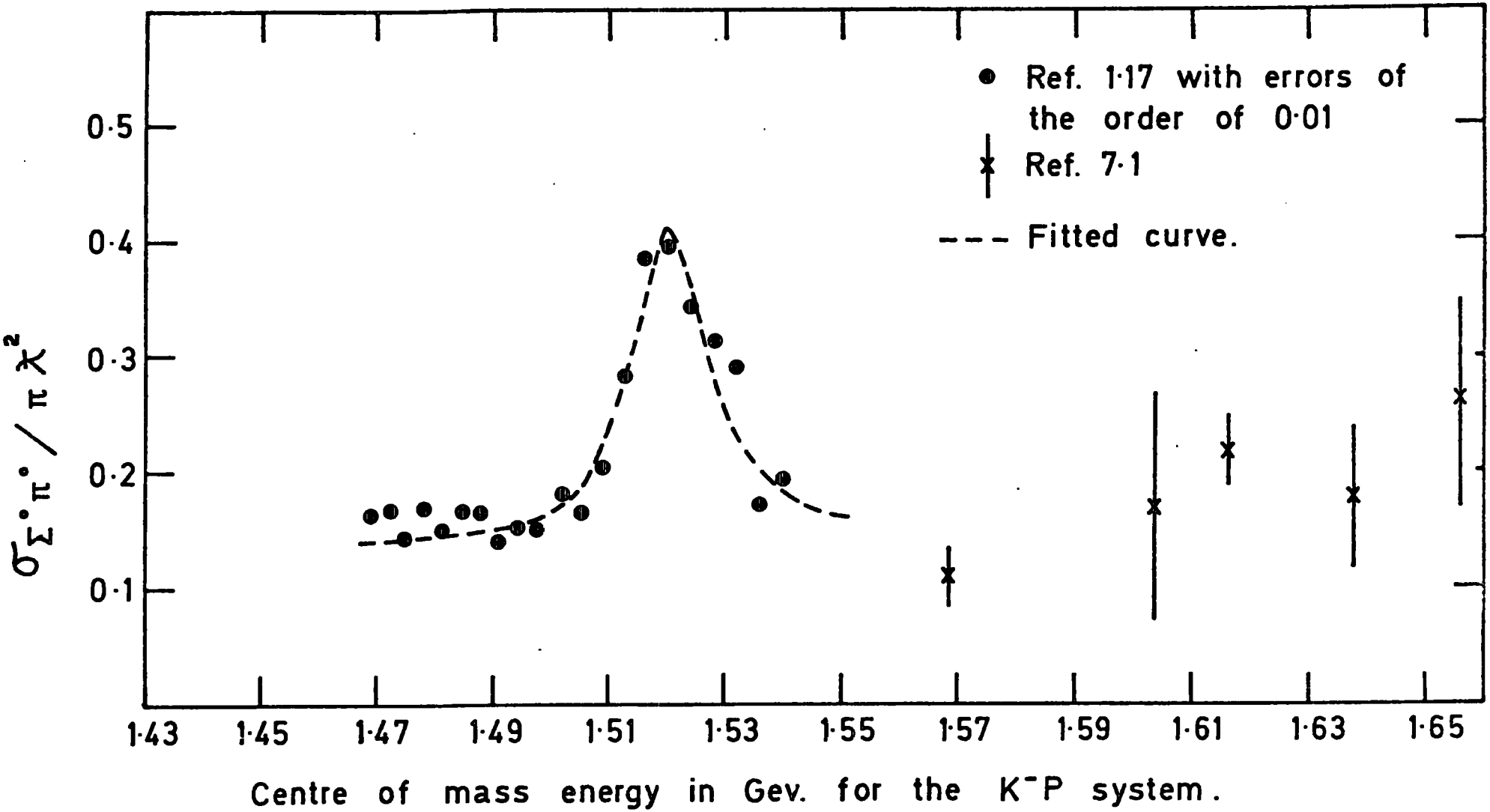

FIG. 7·3 Cross-section of the reaction $K^-P \rightarrow \pi^0\Sigma^0$ in units of $\pi\lambda^2$ as a function of cm energy.

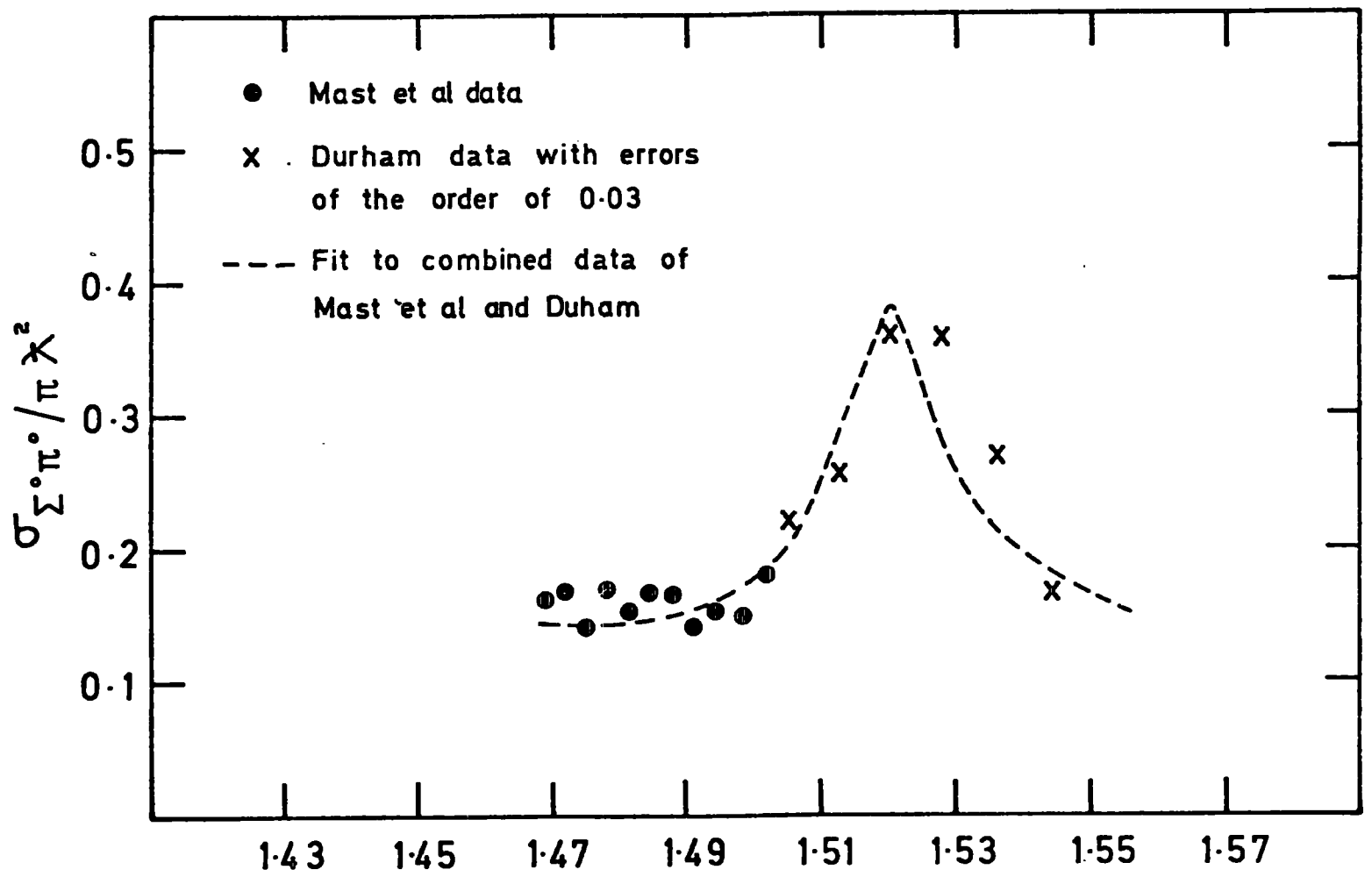

FIG.7·4 The cross-section of the reaction $K^-P \rightarrow \pi^\circ\Sigma^\circ$ in units of $\pi\lambda^2$ as a function of the cm energy.

The linear background required by the fit was 0.132 + 0.0065 E which is practically constant and the width Γ_0 needed was 0.016 GeV which is in good agreement with the natural width of 0.015 GeV.

The same linear background was fixed for the fit to Figure 7.4 but the Breit-Wigner parameters were redetermined due to the different energy resolutions in the peak region. The width Γ_0 needed in this case was 0.018 GeV.

Using the errors quoted in reference 1.17 in the fit to the points of Figure 7.3, the χ^2 for the fit was 92 with 21 degrees of freedom. In view of the obvious constant cross-sections outside the resonance peak this high value of χ^2 implies that the errors are underestimated. Scaling all the published errors by a factor of two gives an acceptable χ^2 of 23, so it is assumed that the model of a linear background and a Breit-Wigner is appropriate.*

7.4 Determination of the isospin cross-sections

Having evaluated the variation of σ_0 ($\pi^0\Sigma^0$ cross-section) with energy then the I = 1 cross-section for the $\pi\Sigma$ was determined using equation (7.1). The I = 0 cross-section was determined using the data of reference 1.17. These two cross-sections are given in Figure 7.5 as a function of the centres of mass energy together with the I = 1 cross-section for the $\pi^0\Lambda^0$. Table 7.1 is a summary of the different isospin cross-sections involved and also shows the ratio

$$R = |T_1^{\Sigma}|^2 / |T_1^{\Lambda}|^2$$

---

* A background of the form $AE^2 + BE + C$ was tried where A, B and C are constants. This fit gave a minimum background at the resonance peak.

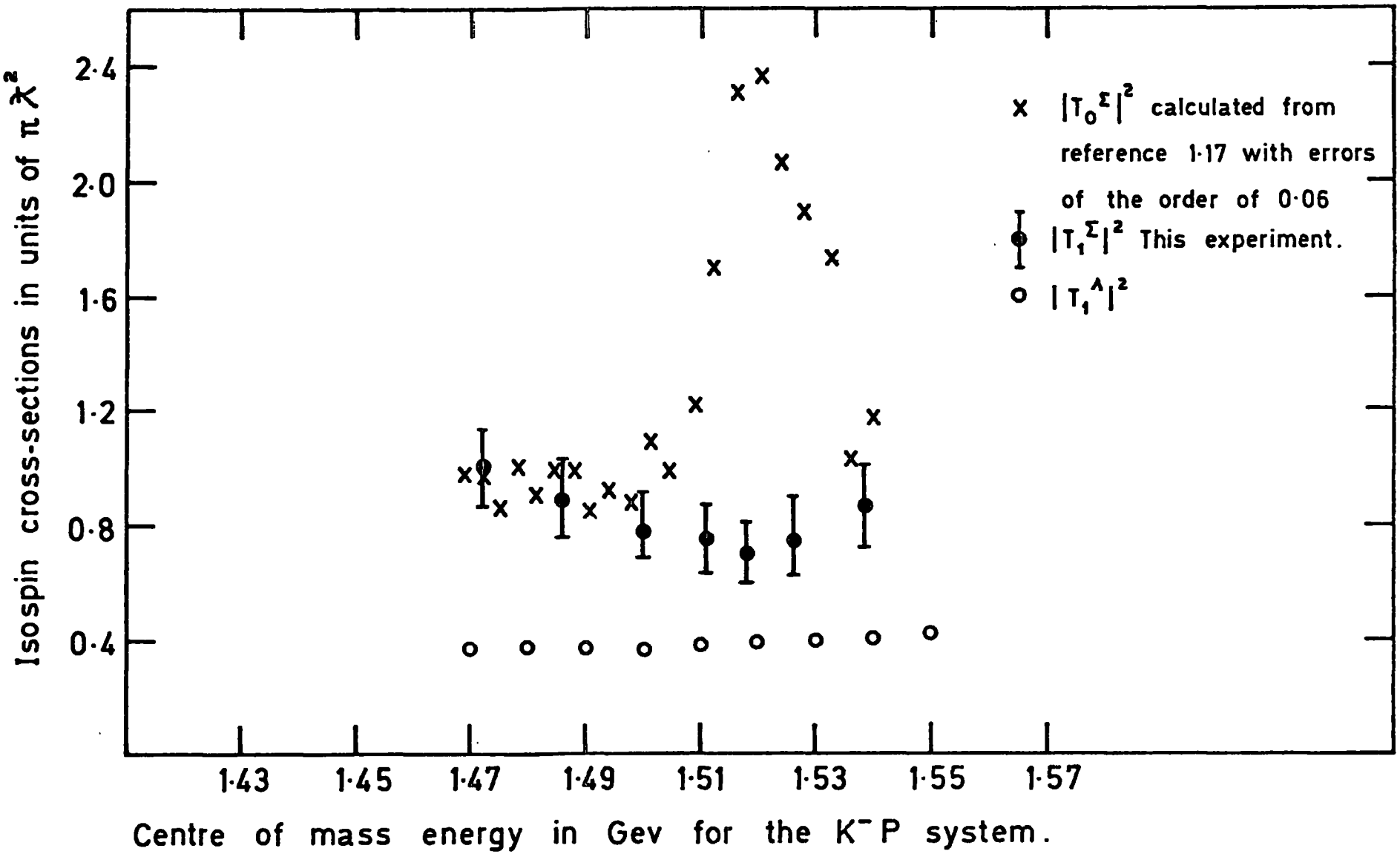

FIG. 7·5 The cross-sections of $I=0$ and $I=1$ of the reaction $K^-P \rightarrow \pi\Sigma$ in units of $\pi\lambda^2$ as a function of cm energy.

E in GeV	$(\sigma_+ + \sigma_-)/\pi\lambda^2$	$\sigma_o/\pi\lambda^2$	$\lvert T_1^{\Sigma}\rvert^2$	$\lvert T_1^{\Lambda}\rvert^2$	R
1.472	0.80 ± 0.05	0.15	1.00 ± 0.13	0.37 ± 0.032	2.7 ± 0.4
1.486	0.75 ± 0.05	0.15	0.90 ± 0.12	0.37 ± 0.026	2.4 ± 0.4
1.500	0.74 ± 0.05	0.17	0.80 ± 0.11	0.37 ± 0.024	2.2 ± 0.3
1.511	0.89 ± 0.07	0.26	0.74 ± 0.12	0.38 ± 0.015	1.9 ± 0.3
1.518	1.07 ± 0.08	0.36	0.70 ± 0.10	0.39 ± 0.012	1.8 ± 0.3
1.526	1.00 ± 0.085	0.31	0.76 ± 0.13	0.39 ± 0.014	1.9 ± 0.3
1.538	0.85 ± 0.07	0.21	0.86 ± 0.14	0.40 ± 0.03	2.2 ± 0.4

Table 7.1: The isospin I = 1 cross-sections for $\pi\Sigma$ and $\pi\Lambda$ as a function of E.

It is seen from Table 7.1 that the error bars on the values of $|T_1^{\Sigma}|^2$ are quite large for this experiment, so it is felt that the apparent variation of $|T_1^{\Sigma}|^2$ with energy is of no significance. Hence the variation of the ratio R is of no significance, the average value of R is 2.16 ± 0.13.

From SU(3) the interaction of the $\bar{K}$-meson with a proton is one of the general octet-octet interaction. This interaction can involve the multiplets resulting from $8 \otimes 8$, i.e. the multiplets $27 \oplus 10 \oplus 10^* \oplus 8_F \oplus 8_D \oplus 1$. Using the expansion coefficients with Y = 0 I = 1 (Y is the hypercharge) then the transition amplitudes related to those in terms of multiplets are (from SU(3) isoscalar factors).

$$|\Sigma\pi\rangle = \frac{\sqrt{6}}{3}\,\underline{8}_F + \frac{\sqrt{6}}{6}\,\underline{10} - \frac{\sqrt{6}}{6}\,\underline{10^*} \qquad (7.6)$$

$$|\Lambda\pi\rangle = \frac{\sqrt{30}}{10}\,\underline{27} + \frac{\sqrt{5}}{5}\,\underline{8}_D - \frac{1}{2}\,\underline{10} - \frac{1}{2}\,\underline{10^*} \qquad (7.7)$$

In this low energy region it is perhaps reasonable to assume that

the higher multiplets do not contribute very much and can be neglected, then equations (7.6) and (7.7) will be reduced to

$$|\Sigma\pi> \quad = \quad \frac{\sqrt{6}}{3} \quad \underline{8}_F$$

$$|\Lambda\pi> \quad = \quad \frac{\sqrt{5}}{5} \quad \underline{8}_D$$

giving, when the $\bar{K}P$ formation amplitudes are included

$$R = |<\Sigma\pi|T|PK>|^2 \Big/ |<\Lambda\pi|T|PK>|^2 = 1.85 \frac{|\underline{8}_F|^2}{|\underline{8}_D|^2}$$

It will be seen that the experimental value of R at the energy E = 1.52 GeV is very close to this ratio, if the symmetric, $\underline{8}_D$, and asymmetric, $\underline{8}_F$, octet amplitudes are approximately equal.

6.5 General Conclusions

In this thesis work has been described which is based on the 1.5 metre B.N.L.B.C. This chamber has been modified into a composite chamber by dividing a hydrogen filled inner chamber from a neon-hydrogen filled outer chamber. The purpose of this has been to attempt to improve the conversion efficiency of the gamma rays by changing the radiation length from that of hydrogen ($\chi \sim 10$ metres) to that of the neon-hydrogen mixture ($\chi \sim 45$ cm). This improved conversion efficiency was then expected to help resolve problems associated with the production of π^0-mesons. For example with good conversion efficiency the well known ambiguity of $\Lambda^0\pi^0$ with $\Sigma^0\pi^0$ would be clearly resolved. This aspect of the chamber has been used in a previous description of the neutral channels of this experiment (reference 3.1). In the present work with charged channels this feature has not had the same importance. However as part of the general work, properties of the composite chamber of relevance to this have been described.

Firstly from a comparison of the ranges of the μ-mesons (from $\pi - \mu - e$ decay at rest) in both hydrogen and the neon-hydrogen mixture it has been possible to determine the composition of the neon-hydrogen mixture. The increased stopping power of the neon-hydrogen mixture reduced the range of the μ-meson from 1.1101 ± 0.0026 cm in hydrogen to 0.233 ± 0.002 cm in neon-hydrogen. From this the composition of the mixture is (75.4 ± 0.6)% neon by number of molecules. This proportion of neon should lead to a radiation length of 41.4 ± 0.7 cm and consequently for the path lengths available in the modified B.N.H.B.C. the conversion efficiency of gamma rays is expected (by Monte Carlo calculation) to be 16%. Experimentally this has been checked by examining the materialisation of gamma rays from the production and decay of Σ^+-hyperons by the proton mode ($\Sigma^+ \rightarrow P\,\pi^0$, $\pi^0 \rightarrow \gamma + \gamma$). The experimental value of the conversion efficiency is 15% in good agreement with the expected value. Although this conversion efficiency is still low it does represent an improvement by a factor of 20 over a hydrogen chamber. Indeed the large B.E.B.C. chamber has been modified in a similar way to use this advantage. However in the smaller B.N.H.B.C. the hydrogen filled T.S.T. has had to be relatively shallow (about 8 cm thick) and this has introduced several problems.

These problems have been discussed and solved in chapters four and five. The shallow chamber imposes short track lengths and other geometrical limitations such as enhanced loss of decay of Λ^0-hyperons outside the T.S.T. These have a direct effect on the cross-sections. However by careful analysis of the data these problems have been identified and corrections made to overcome them. That these have been successful was shown in chapter six where the γ-ratio ($K^- p \rightarrow \pi^+ \Sigma^- / K^- p \rightarrow \pi^- \Sigma^+$) has been determined in two different ways firstly, by taking the ratio of the

cross-sections (which include all the corrections) and secondly by scaling or both from the largely uncorrected ratio of the decays ($\Sigma^- \rightarrow \pi^- n / \Sigma^+ \rightarrow \pi^+ n$). These two channels are so similar that apart from life-times geometric effects and losses should be the same. The agreement between the values, one with corrections and one without, show that the geometric effects of this shallow chamber have been largely identified and properly corrected.

After considering these technical aspects of this T.S.T. chamber, the $\Sigma^{\pm}$ channels and the elastic scatterings have been examined in some detail. Firstly the cross-sections for these channels have been determined in the momentum region of 200 to 460 MeV/C. This range includes the momentum interval, centred at 390 MeV/C, where the $\Lambda(1520)$ should be produced. This isospin singlet (as also isospin triplets) can of course be produced in the charged channels. It is quite clearly seen in the Σ^- channel and enhancements occur at the appropriate momentum for Σ^+ and elastic scatterings. For the latter the enhancement represents a small signal on a very large background and hence it is difficult to resolve. The cross-sections are in agreement with previous determinations, although the Σ cross-sections are generally higher at low momentum. The Σ cross-sections were further analysed to separate them into isospin 0 and isospin 1 cross-sections. As expected the resonant signal appears entirely in the isospin 0 channel. This is the first time that such an analysis has been made and it represents the bringing together of accurate Σ^0 cross-sections (from Mast et al) and the quite accurate $\Sigma^{\pm}$ cross-sections of this thesis. The isospin 1 cross-section was compared with the isospin 1 cross-section ($K^- p \rightarrow \pi^0 \Lambda^0$) and found to be 2.16 ± 0.13 larger. The expected ratio from SU(3) symmetry is 1.85.

Differential cross-sections were analysed in chapter six where fitting by an expansion in terms of Legendre polynomials was made. The

most significant term of the expansion (A_ℓ/A_0) occurs for $\ell = 2$ for both Σ^+ and Σ^--hyperons and elastic scattering. This corresponds again to the $\Lambda(1520)$. Finally the polarisation of the Σ^+-hyperon was determined through its weak decay by the proton mode. Experimentally the quantity $\alpha_0 P$ is found and by taking the well known value of α_0 the polarisation P was found. This was investigated as a function of primary momentum. Good agreement was found between these results and those of Bangerter et al (reference 6.3) and Reucroft et al (reference 6.2).

It was explained in chapter one that this experiment was being conducted in three phases. The first phase was to be an evaluation of the use of a T.S.T. composite chamber and to show that this chamber could be used for low momentum kaon physics. This has been successfully demonstrated in this thesis by showing that in the region of the $\Lambda(1520)$ accurate, unbiased, results can be obtained. The second and third phases, to obtain new data and results at very low momenta ($P < 200$ MeV/C) and in the hitherto unworked region of 400 - 600 MeV/C, are now underway.

APPENDIX A

THE EFFECT OF STRONG INTERACTIONS ON WEIGHTING OF THE TRACK LENGTH

In Chapter 5 (Section 5.2), the weight that gives the initial number of kaons from the number of seen tau decays, W, was found. This weight was derived, where the contribution from the strong interactions has not been taken into account in the analytical treatment. The effect of this is described in the following:

Assume that $\lambda_T(P)$ is an effective mean free path for strong interactions and weak decays, then

$$\frac{1}{\lambda_T(P)} = \frac{1}{\lambda_i(P)} + \frac{1}{\lambda_d(P)} = AP^{-S} \qquad (A.1)$$

where λ_i and λ_d are the mean free path for interaction and decay respectively. The dependence on momentum is approximated but adequate for the calculation, and S can be found from the variation of the total K^-p cross-sections with momentum which is 1.13. The residual range corresponding to the momentum is given by

$$R = KP^n$$

where n = 3.6 and from this relation the momentum of a particle after a distance ℓ from a point where $P \equiv P_o$ with $R \equiv R_o$ is

$$P(\ell) = P_o \left(1 - \frac{\ell}{R_o}\right)^{1/n} \qquad (A.2)$$

so that

$$\frac{1}{\lambda_T(\ell)} = A P_o^{-S} \left(1 - \frac{\ell}{R_o}\right)^{-S/n}$$

The attenuation of the beam is given by

$$-dN(\ell) = N(\ell)\, A\, P_o^{-S} \left(1 - \frac{\ell}{R_o}\right)^{-S/n} d\ell$$

which yields

$$N(\ell) = N_o \exp\left[-\int_o^{\ell} \left(1 - \frac{\ell}{R_o}\right)^{-S/n} d\ell/\lambda_T(P_o)\right] \quad (A.3)$$

where N_o is the original number of kaons.

Since $\frac{\ell}{R_o}$ is small in our momentum region, it is allowed to expand $\left(1 - \frac{\ell}{R_o}\right)^{-1/n}$ in a binomial series which leads equation A.3 to

$$N(\ell) = N_o \exp\left[-\frac{\ell}{\lambda_T(P_o)}\left(1 + \frac{S}{2n}\frac{\ell}{R_o} + \frac{S(1+S)}{6n}\frac{\ell^2}{R_o^2}\right)\right]$$

Also $\frac{\ell}{\lambda_T} \ll 1$, so the exponential can be expanded too and therefore

$$N(\ell) = N_o \left[1 - \frac{\ell}{\lambda_T(P_o)}\left(1 + \frac{S}{2n}\frac{\ell}{R_o} + \frac{S(S+1)}{6n}\frac{\ell^2}{R_o^2}\right) + \frac{1}{6}\left(\frac{\ell}{\lambda_T(P_o)}\right)^2 \cdots\right]$$

(A.4)

Now, the number of decays in length $d\ell$ at ℓ is

$$-dN_d = N(\ell)\, d\ell/\lambda_d(\ell)$$

where

$$\lambda_d^{-1}(\ell) = \frac{m}{c\tau P} = \frac{m}{c\tau P_o}\left(1 - \frac{\ell}{R_o}\right)^{-1/n}$$

which substitution has been made from A.2. Assuming L is the potential length, then the number of decays within the chamber becomes

$$N_d = \int_o^L N(\ell)\ (1 - \frac{\ell}{R_o})^{-1/n}\ d\ell/\lambda_d(P_o) \qquad (A.5)$$

Integrating A.5 after substituting A.4 for $N(\ell)$ gives

$$N_d = \frac{N_o L}{\lambda_d(P_o)} \left[1 - \frac{L}{2\lambda_T} + \frac{L}{2nR_o} + \frac{L^2}{18\lambda_T^2} + \frac{n+1}{6n^2}\ \frac{L^2}{R_o^2} - \frac{S}{6n}\ \frac{L^2}{\lambda_T R_o} \cdots \right]$$

Therefore, the observation of a τ-decay with entry momentum P_o and potential length L implies a total number of kaons entering with those characteristics given by

$$W_i\ (P_o, L) = \frac{\lambda_d(P_o)}{BL} \left[1 - \frac{L}{2\lambda_T} + \frac{1}{2nR_o} \cdots \right]^{-1}$$

where B is the branching ratio ($\sim 5\%$).

To calculate the amount of tracklength per momentum interval, define $\ell(P_1)$ and $\ell(P_2)$ as the lower and upper edge of a length corresponding to the momentum interval $P_1 \to P_2$. On average $W_i(P_o, L)$ kaons contribute a pathlength of L_i between $\ell(P_1)$ and $\ell(P_2)$ such that

$$L_i(P_1, P_2) + \int_{\ell(P_1)}^{\ell(P_2)} N(\ell)\ d\ell \qquad (A.6)$$

$$= \int_{\ell(P_1)}^{\ell(P_2)} W_i(P_o, L) \left[1 - \frac{\ell}{\lambda_T(P_o)} - \frac{S}{2n}\ \frac{\ell^2}{\lambda_T R_o} \cdots \right]$$

where substitution has been made from A.4.

Integrating A.6 gives

$$L_i(P_1,P_2) = W_i(P_o,L)\left[\ell\left(1-\frac{\ell}{2\lambda_T}\right)+\frac{1}{6}\left(\frac{1}{3\lambda_T^2}-\frac{S}{n}\frac{1}{\lambda_T R_o}\right)\ell^2\ldots\right]_{\ell(P_1)}^{\ell(P_2)}$$

It can be seen from the above relation that the effect of the strong interactions in the amount of track length is of the order of $\frac{\ell}{2\lambda_T}$ which is $\sim 5\%$ for 50 mb total cross-section.

APPENDIX B

THE DETAILS OF SECTION 5.4

B.1 Biases in Σ^--Hyperon Production and Decay

In Chapter 5, Section 5.4, the biases affecting the Σ^--hyperon events have been given very briefly. Here the same biases are discussed in more detail.

The kinematics of production of the process $K^- + P \rightarrow \pi^+ + \Sigma^-$ are shown in Figure B.1a to d for three different momenta of the primary K^--meson (202, 302, and 465 MeV/C). The quantities involved in these figures are the same as it was defined before for the Σ^+-hyperon in Section 5.3.

It can be seen from Figures B.1a to c that losses are expected at both ends of $\cos\theta^*_{PROD}$. In the region of $\cos\theta^*_{PROD} < -0.90$, the Σ^--hyperon momentum in the laboratory is so low that the hyperon will not leave a visible track or it will lose energy very quickly and come to rest to be absorbed rather than decay. In the region of $\cos\theta^*_{PROD} > +0.8$ the laboratory angle between the primary direction and the Σ^--hyperon direction is so small that it will be difficult to isolate the production vertex. Losses concerned with the detection of the Σ^--hyperon at the production vertex may be examined by the distribution of the angle ϕ_p defined in equation (5.18).

Losses in the decay are examined by the distribution of the angle ϕ_D defined in equation (5.19) and the decay angular distribution of the charged decay particle in the rest frame of the Σ^--hyperon where these two distributions should be isotropic.

To check the effects due to the shallowness of the chamber the

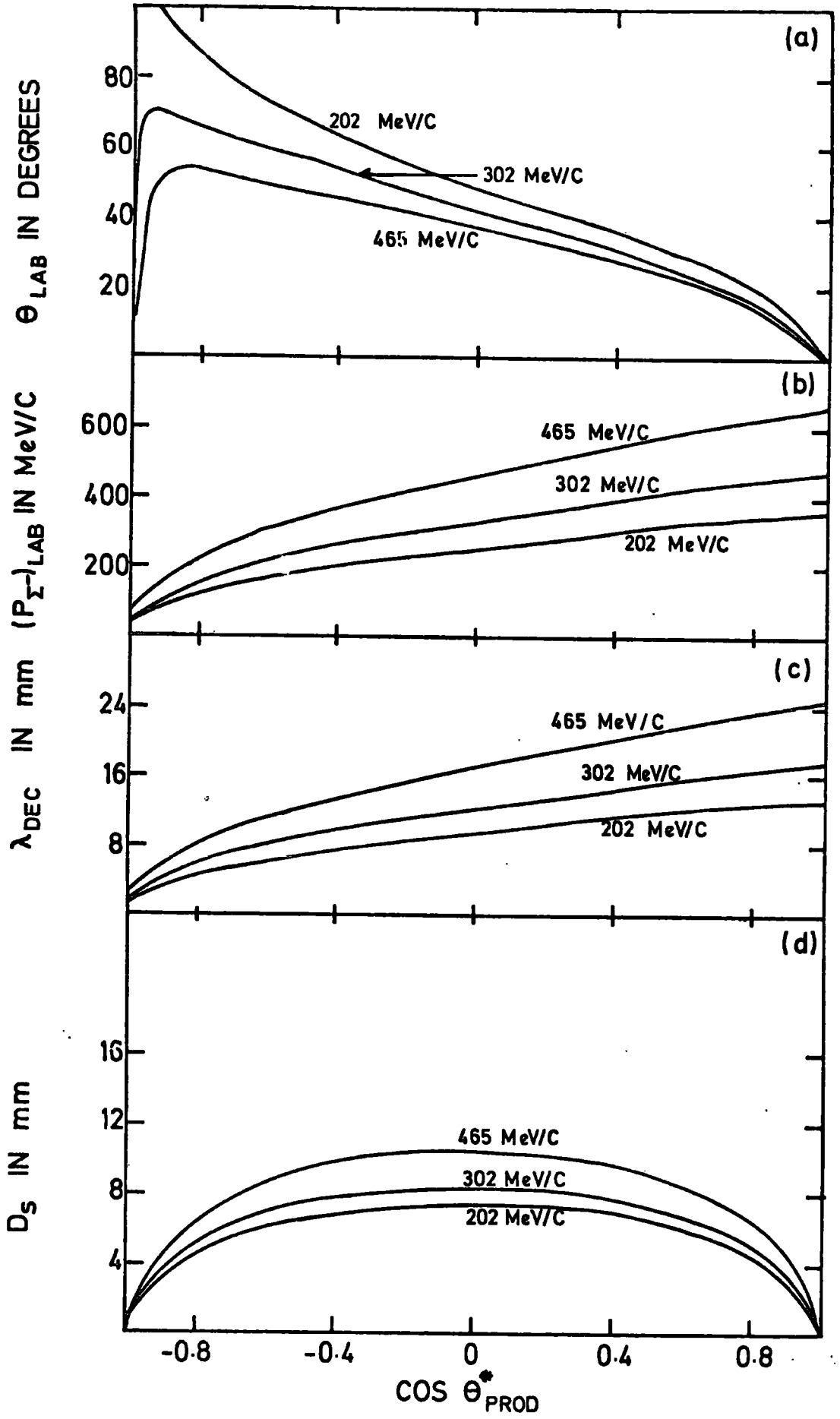

FIG.B·1 KINEMATICS OF THE REACTION $K^-P \longrightarrow \pi^+\Sigma^-$

value of D_S corresponding to the highest momentum (465 MeV/C) was used to divide the depth of the hydrogen region into three slices as in the case of the Σ^+-hyperon events (with the same requirements described before in each of these three slices individually).

The distributions of ϕ_P, ϕ_D, and $\cos \theta_D^*$ using all the events without dividing the depth of the hydrogen chamber of the T.S.T. were compared with those with the depth of the hydrogen chamber divided into three regions. These distributions are shown in Figures B.2a to c, where it is seen that the two sets of distributions are behaving nearly in the same way. It is concluded again that the shallow chamber has very little effect on the observation of the Σ^--hyperon events and losses are due to visibility effects only. These losses are described in the following sections.

B.2 Life-time Correction

If the decay of the Σ^--hyperon occurs either very close to the production vertex so that it will not leave a visible track or the Σ^--hyperon has lived long enough to go outside the fiducial volume and it has probably decayed or absorbed inside one of the perspex walls, then the interaction will be misclassified as a two-prong event. Corrections to these losses were made by imposing a minimum cut-off proper time which was found empirically from Figure B.3 where the proper time of flight of the Σ^--hyperon is drawn against $\ell n\, N$ in proper time bins of 0.2×10^{-10} sec without any selection. The straight line drawn on the distribution corresponds to the value of the mean life-time of $\tau_{\Sigma^-} = 1.48 \times 10^{-10}$ sec and it agrees with the world average value for the Σ^--hyperon. The line was fitted to the distribution for the region 0.2×10^{-10} sec $< t < 2 \times 10^{-10}$ sec. It is clear from this distribution that the value of t_o, the minimum proper

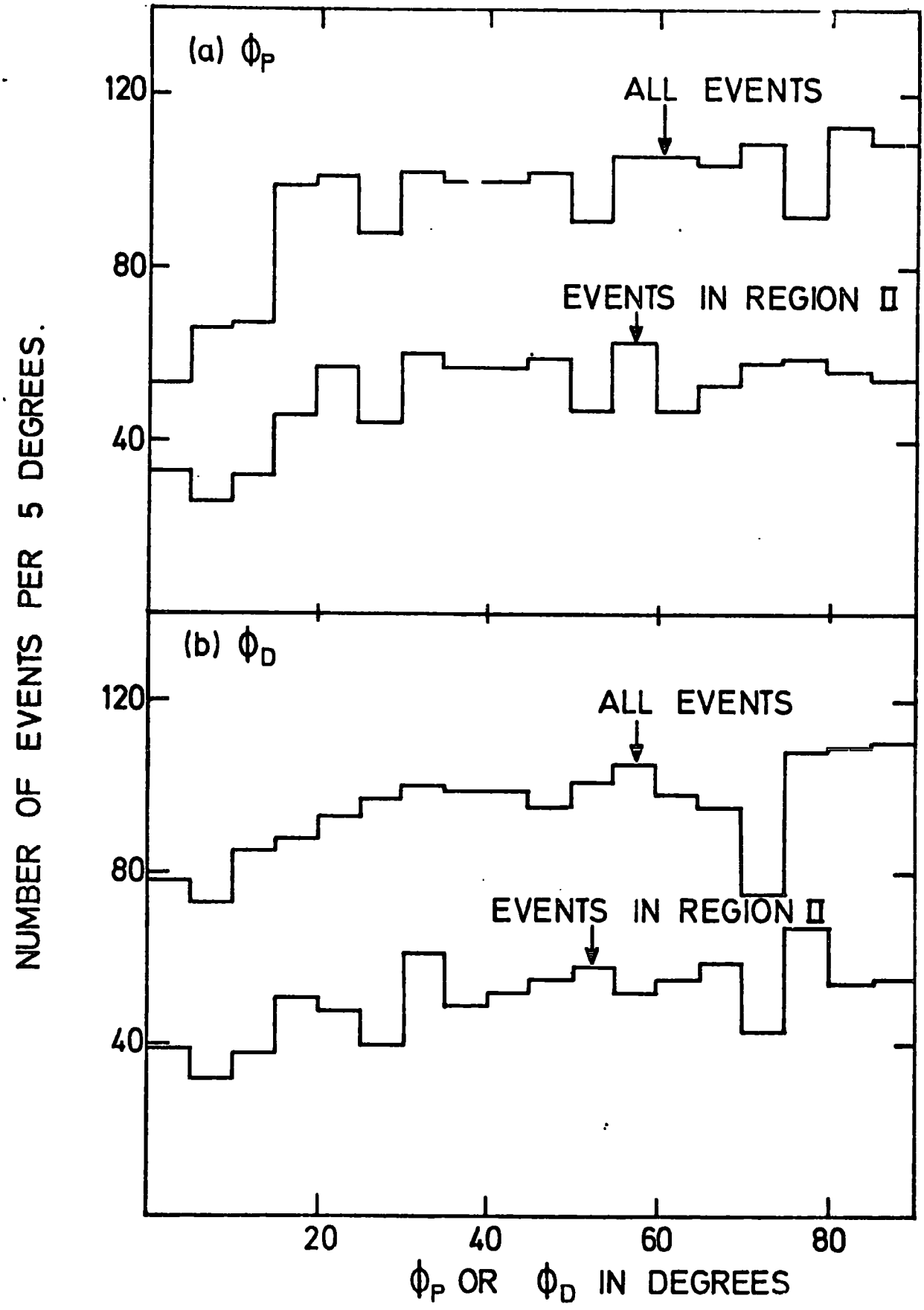

FIG B·2 THE AZIMUTHAL ANGLES ϕ_P OR ϕ_D FOR THE Σ^--HYPERON EVENTS.

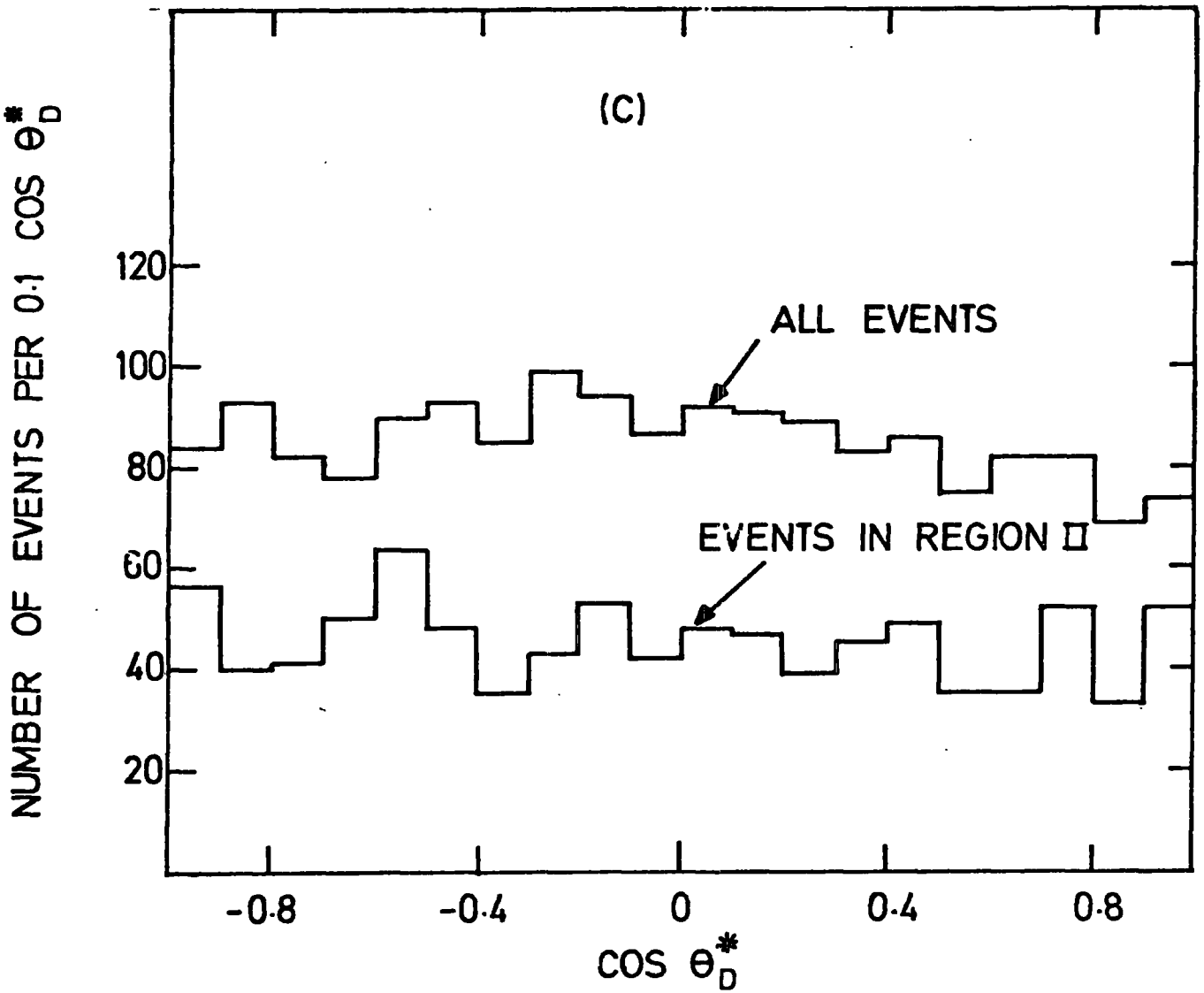

FIG. B·2 THE ANGULAR DISTRIBUTION OF THE π^- - MESON FROM THE Σ^- - HYPERON IN THE REST FRAME OF THE Σ^- - HYPERON.

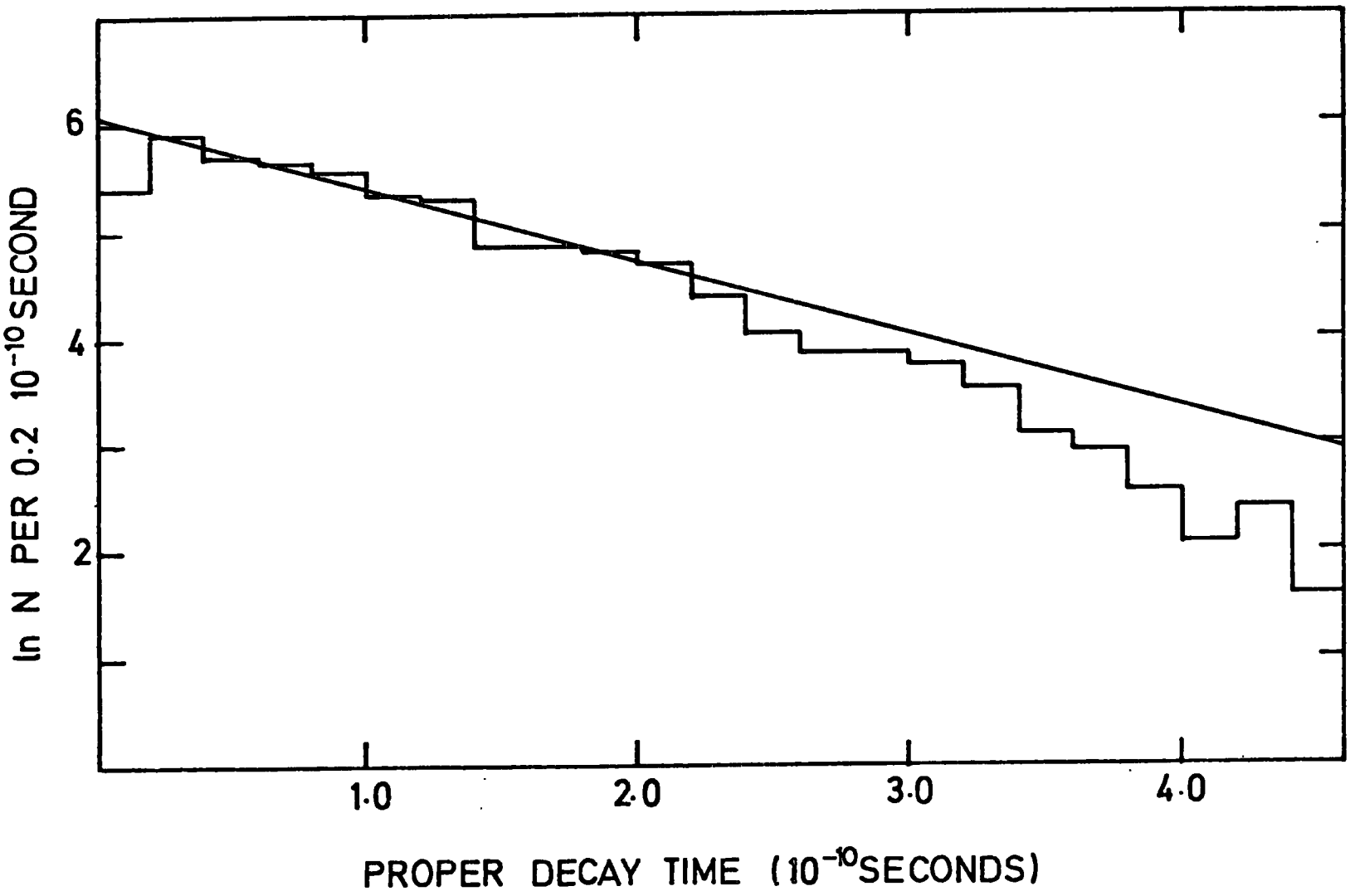

FIG. (B.3) DECAY TIME DISTRIBUTION FOR THE OBSERVED Σ^-- EVENTS

time is 0.2×10^{-10} sec. Equation (5.18) was used to correct for these losses where t_p in this case is the proper time to leave the fiducial volume. If the Σ^--hyperon comes to rest inside its potential length, then t_p is the proper time of flight to come to rest. The energy loss suffered by the Σ^--hyperon when traversing the hydrogen is taken into account in calculating the proper time of flight. The fall off of the distribution of Figure B.3 at high values of t is due to the target slice being very shallow (geometrical effect). Here long Σ^--hyperon tracks which contribute mainly to the higher values of t may enter the perspex and are classified as two-prong events. Another cause of this fall-off is due to the fact that some of these long Σ^--hyperon tracks were discarded at the scanning stage to help the scanners not to record unnecessary two-prong elastic scattering events followed by the decay of the K^--meson into one-prong.

B.3 Corrections to the production Angular Distribution and ϕ_p corrections

The interactions of primary Kaons at rest in the chamber produce Σ^--hyperons with a unique momentum of about 180 MeV/C. As the primary momentum is increased from zero the resulting Lorentz transformations will lead to an increase in the laboratory momentum of the forwardly produced Σ^--hyperon and to a reduction of the backwardly produced Σ^--hyperons. From Figure B.1b, for all primary kaon momenta in this experiment, Σ^--hyperons will be produced with very low momenta if they are emitted in the backward direction in the centre of mass system. Hence they either do not leave visible tracks or they lose energy very quickly and interact with the proton rather than decay. Such events will be classified in the two-prong category.

With the quiet rapid decay of the Σ^--hyperon, the Σ^--hyperon track is small. Scanning visibility is highest when the Σ^--hyperon makes a large angle to the kaon track. Σ^--hyperons forwardly produced in the centre of mass frame are transformed to small angles in the laboratory system. Here the Σ^--hyperon may look like a continuation of the kaon track. Hence with both these effects losses are anticipated for very forward and very backward Σ^--hyperons. Corrections for these losses have been made through the fits to the angular distributions of production as described previously. But for the purpose of making other corrections, areas where losses are expected were removed from the sample. The selection was to accept events if $\cos \theta^*_{PROD} \geq -0.9$ and $\cos \theta^*_{PROD} \leq +0.8$. Events outside this range were excluded from the sample. Examination of the azimuthal distribution of ϕ_P for the selected events shows a loss of events for $\phi_P < 15^o$. Consequently events are accepted if $\phi_P > 15^o$.

B.4 Losses Due to Small Decay Angles

This loss of events is related to the decay vertex and it is dependent on the kinematics of the decay of the Σ^--hyperon. The kinematics of the decay of the Σ^--hyperon are very much the same as that of the Σ^+_π mode of decay and the characteristics of the events (Σ^--hyperon) are the same as stated in Section 5.3.3. As a result of this, events have been treated in the same way where a two dimensional plot of $\cos \theta^*_D$ and ϕ_D was examined. This is shown in Figure B.4. In this plot, as before, a central area was chosen which gives events free of biases, then this area was extended in both $\cos \theta^*_D$ and ϕ_D until this loss became apparent. This defined the boundaries of events to be used for further analysis. Events outside these boundaries were eliminated from the sample and the events accepted were scaled according to equation (5.19).

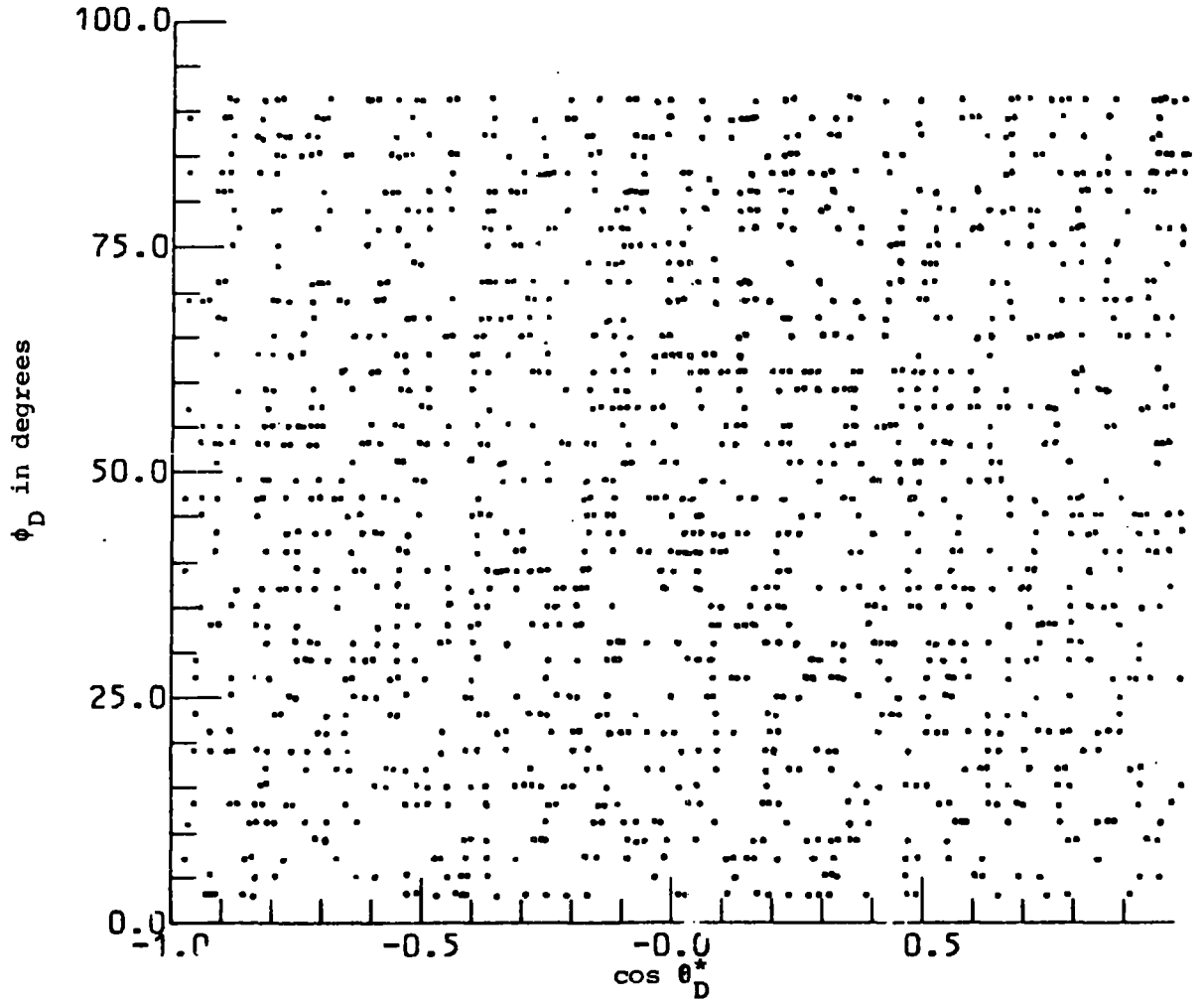

Figure B.4: The two dimensional plot of cos θ^*_D against ϕ_D for the Σ^--hyperon events.

B.5 Losses Due to the Absorption of Σ^--Hyperon and Losses Due to Scanning and Measuring

These losses have been described previously in Section 5.3.4 for the scanning and measuring losses and in Section 5.4.4 for the absorption of the Σ^--hyperon.

REFERENCES

Chapter 1

1.1 D.V. Bugg, Phys. Rev. 168, 1466 (1968)

1.2 W.E. Humphrey and R.R. Ross, Phys. Rev. 127, 1305 (1962)

1.3 J.K. Kim, Ph.D. Thesis, Coulombia University (1966)

1.4 M.F. Kaplon, Proceedings of the 1958 Annual International Conference on High Energy Physics at CERN, CERN Scientific Information Service, Geneva, 171 (1958)

1.5 P. Nordin et al., Bul. Am. Phys. Soc., (II), 4, 288 (1959)

1.6 P. Eberhard et al., Phys. Rev. Lett. 2, 312 (1959)

1.7 S.C. Freden et al., Phys. Rev. 118, 564 (1960)

1.8 P. Nordin, Phys. Rev. 123, 2168 (1961)

1.9 D.H. Davis et al., Phys. Rev. Lett. 6, 132 (1961)

1.10 M. Sakitt et al., Phys. Rev. 139, B 719 (1965)

1.11 G.P. Thomas and P.L. Jain, Nucl. Phys. B13, 385 (1969)

1.12 M. Csejthey-Barth et al., Phys. Lett., 16, 89 (1965)

1.13 G.S. Abrams and B. Sechi-Zorn, Phys. Rev., 139, B454 (1965)

1.14 W. Kittel et al., Phys. Lett., 21, 349 (1966)

1.15 D. Berley et al., Phys. Rev. D1, 1996 (1970)

1.16 M.B. Watson et al., Phys. Rev. 131, 2248 (1963)

1.17 T.S. Mast et al., Phys. Rev. 183, 1200 (1969)
Phys. Rev. Lett. 21, 1715 (1968)
Phys. Rev. D7, 5 (1973)
Phys. Rev. D7, 3212 (1973)
Phys. Rev. D11, 3078 (1975)
Phys. Rev. D14, 13 (1976)

1.18 D.N. Tovee et al., Nucl. Phys. B33, 493 (1971)

1.19 A.D. Martin, Phys. Lett. 65B, 346 (1976)

1.20 Review of particles properties, Particle Data Group, Reviews of Modern Physics, Vol.48, No.2, Part II

1.21 J.K. Kim, Phys. Rev. Lett. 27, 356 (1971)

1.22 R. Armenteros et al., Nucl. Phys. B21, 15 (1970)

1.23 T. Bowen et al., Phys. Rev. D2, 2599 (1970)

1.24 A.S. Carroll et al., Phys. Rev. Lett. 37, 806 (1976)

1.25 Referring to Figure 1.1, the abbreviations and references are:

LBL 1965:	see reference 1.17
HYBUC 1973:	R. Settles, private communication
BMY 1965:	see reference 1.15
CHS 1967:	see reference 1.22
CHM 1970:	H. Oberlack, private communication
Tenn. Mass 1969:	E. Hart, private communication
BNL 1964:	D. Berley et al., Phys. Rev. Letters 15 64 (1965)
CHS 1964:	R. Armentoros et al., Nucl. Phys. B 8, 233 (1968)
Mary'd 1964:	R.P. Vhlig et al., Phys. Rev. 155, 1448 (1967)
LBL 1964:	D.F. Kane, Phys. Rev. D 5, 1583 (1972)
Ch. LBL 1970:	D. Merrill et al., Berkeley APS Meeting 1973
RHEL-ICL:	G. Kalmus, private communication
CERN 1968:	M. Ferro-Luzzi, CERN/D.Ph. 11 Phys. 71-9
Saclay 1969:	M. Ferro-Luzzi, ibid
LBL 1962:	D.O. Huwe, Phys. Rev. 181, 1824 (1969)
CRS 1967:	P.J. Litchfield et al., Nucl. B 30, 125 (1971)
CH 1969:	M. Ferro-Luzzi, ibid
UCLA 1962:	P.M. Dauber, UCLA Report 90024 (Thesis) (1966)
K:	see reference 1.3
CK:	J. Chan and J. Kadyk, private communcation of an unpublished Berkeley experiment

Chapter 2

2.1 C.M. Fisher, External Report RL - 73 - 053

2.2 T.W. Dombeck, Ph.D. Thesis, North Western University, Evanston, Illinois (1972).

D.R.S. Boyd, Ph.D. Thesis, University of Edinburgh, Scotland, U.K. (1973)

2.3 Parameters of 1.5 metre Hydrogen Bubble Chamber, XERN/TC/NBC, 64 - 1 (1964)

2.4 G.H. Trilling, Proceedings of the International Conference on Bubble Chamber Technology, Argonne National Laboratory, 1173 (1970)

2.5 H. Leutz and P.R. Williams, 1973, International Conference on Instrumentation for High Energy Physics, Frascati, 60, (1973)

Chapter 3

3.1 M.T. Fallahi, Ph.D. Thesis, University of Durham (1978)

3.2 The Geometrical Reconstruction of Bubble Chamber Tracks, J.W. Burren and J. Sparrow NJRL/R/14

3.3 A Kinematical Fitting Program for the Analysis of Bubble Chamber Events, A.G. Wilson NIRL/M/38

Chapter 4

4.1 Y.K. Lim, J.E. Laby and V.D. Hopper, Supp. Nuovo Cimento, 15, 382 (1960)

4.2 C.J. Waddington, Supp. Nuovo Cimento, 19, 37 (1961)

4.3 S.E. Derenzo and R.H. Hildebrande, Nucl. Inst. and Meth., 69, 287 (1969)

4.4 J.G.V. Guy, J.W.G. Wignall and C.M. Fisher, External Report RL-73-035

Chapter 5

5.1 Oxford Kinematical Tables up to 30000 MeV, the National Institute for Research in Nuclear Science, Rutherford High Energy Laboratory (1961)

5.2 R.A. Salmeron, Kinematical Tables for Two-Body Decays from 0.05 to 25.0 GeV/C, Nuclear Physics Division, CERN, Geneva (1963)

5.3 N.H. Bedford, University of Durham, Private Communication

Chapter 6

6.1 MINUIT Long Write-up CERN Computer Program Library, F. James and M. Reos, D506, D516 (1971)

6.2 S. Reucroft et al, Phys. Rev. D15, 5 (1977)

6.3 R.O. Bangerter et al, Phys. Rev. 187, 1821 (1969)

Chapter 7

7.1 Compilation of cross-sections of K^--induced reactions, CERN/HERA 70-6 (1970)

ACKNOWLEDGEMENTS

I would like to thank Professors A.W. Wolfendale and B.H. Brandsden, who, as sequential heads of the Physics Department, made available the facilities of the department during my work for this thesis. I wish to express my appreciation and indebtedness to Dr. J.V. Major, who supervised the work in this thesis. His encouragement, guidance and many helpful suggestions were invaluable.

I wish to thank Dr. D. Evans for his many discussions and comments during the course of this work. My thanks are due also to all my colleagues in the High Energy Nuclear Physics Group for their direct or indirect help through the discussions and comments at the various stages of the work, in particular Mr. A.P. Lotts and Dr. P.S. Jones.

I would like to thank the scanning and measuring staff for their work on this experiment, in particular Mrs. M. Garnett.

Lastly, but by no means least, I wish to express my deepest gratitude to my brother, Yehya A. Hamam, for he has not only taken the burden of the financial support throughout this work, but he has been always my greatest encouragement throughout the difficult periods.

To all these and many others who have helped and encouraged me I am much indebted.